

NASA TECHNICAL TRANSLATIONS

NASA TT F-16,501

BALLISTIC RANGES AND THEIR APPLICATION
IN EXPERIMENTAL RESEARCH

N. A. Zlatin, G. I. Mishin

(NASA-TT-F-16501) BALLISTIC RANGES AND
THEIR APPLICATIONS IN EXPERIMENTAL RESEARCH
(Scientific Translation Service) 392 p HC
\$10.25 CSCL 14B

N75-33061

Unclas

G3/09 42252

Translation of "Ballisticheskiye ustanovki i
ikh primeneniye v eksperimental'nykh issle-
dovaniyakh". Moscow, "Nauka" Press, 1974,
pp. 1-344



NATIONAL AERONAUTICS AND SPACE ADMINISTRATION
WASHINGTON, D. C. 20546 OCTOBER 1975

ANNOTATION

This book provides a systematic presentation of the theory and practice of high-speed ballistic ranges, surveys the modern methods used to study high-speed phenomena, and examines the results of studies of the processes taking place during high-speed motion of bodies of various shapes in gaseous and solid media. The book is intended for scientists, engineers, physicists, and technical personnel of the scientific research institutes studying the aerodynamics, gasdynamics, and mechanics of continua, and also for graduate students and upper-level students in the physical and mechanical sciences.

PRECEDING PAGE BLANK NOT FILMED

EDITORS' FOREWORD

The latest achievements in aerodynamics, gasdynamics, and dynamics of solid media have been possible only as a result of the successes in developing experimental techniques, particularly the ballistic methods. However, to date, no books have appeared in the Soviet scientific literature which acquaint the interested reader with the fundamentals and details of these methods or with the results of studies being made using these methods. The present volume is the first attempt to satisfy this need.

We present a systematic discussion of the theory and practice of high-speed ballistic test facilities, survey the modern methods for studying high-speed phenomena, and examine the results of studies of the processes taking place during high speed motion of bodies of different shapes in gaseous and solid media.

The book is based on the results of developments and studies performed by the authors. Along with the obvious advantages, this has its drawbacks, since in this approach we may inadvertently fail to examine some aspects of the problems associated with application of the ballistic methods. The team of authors will be grateful to anyone who points out such omissions, and also those who may offer critical comments regarding the subjects discussed in the book.

The present volume was already prepared when Mir Press published in late 1971 the translation of the collection of articles entitled Physics of High Speed Processes (Kurtzzeitphysik, Vienna - New York, 1967). It appears to us that this collection of articles and the present volume complement one another quite well in regard to several questions, and the bibliographies of the two books provide quite exhaustive information on these questions from the original studies of Soviet and foreign investigators.

We hope that the present volume will be useful to the scientists, engineers, physicists, and technical personnel of the scientific research institutes studying the aerodynamics, gasdynamics, and mechanics of continua, and also to the graduate students and upper-level students in the physical and mechanical specialties.

Chapters I and II were written by the late N. N. Popov, Chapter III — by G. I. Mishin, Chapter IV — by N. A. Zlatin, and Chapter V — by A. P. Krasil'shchikov.

N. A. Zlatin
G. I. Mishin

TABLE OF CONTENTS

	Page
EDITORS' FOREWORD	1v
INTRODUCTION	1
CHAPTER I. HIGH-VELOCITY LAUNCHERS	7
§1.1. Preliminary Remarks	7
§1.2. Launch Physical Principles and Light-Gas Launcher Classification	10
§1.3. Single-Stage Gasdynamic Launchers	14
§1.4. Multistage Gasdynamic Launchers	18
§1.5. Electrodynamic Launchers	34
§1.6. Characteristics of Some High-Velocity Launchers and Features Associated with Their Field of Application	40
CHAPTER II. FUNDAMENTALS OF LIGHT-GAS LAUNCHER DESIGN	46
§2.1. Preliminary Remarks	46
§2.2. Equations of Gas Motion and Methods of Their Solution	49
§2.3. Numerical Solution of the Lagrange Problem for Various Cases	65
§2.4. Corrections for Real Gas Properties, Friction, and Heat Transfer	85
§2.5. Influence of Forcing Pressure on Gas Flow Velocity in Barrel	89
§2.6. Light-Gas Launcher Optimal Parameter Selection	96
§2.7. Remarks on Charge Selection	116
§2.8. Sabots, Projectiles, and Diaphragms	121
§2.9. Approximate Light-Gas Launcher Analysis Method	127
CHAPTER III. MEASUREMENT APPARATUS AND TECHNIQUES	141
§3.1. Preliminary Remarks	141
§3.2. Passage Time Recording	143
§3.3. Synchronizing Equipment	150
§3.4. Measuring Flying Body Velocity	160
§3.5. Determining Flying Model Trajectory Parameters	163

3.6.	Time Interval Measurements	168
3.7.	Visualization Methods and Photographic Systems	178
3.8.	Pulsed Light Sources	185
3.9.	Electrical Fast-Acting Shutters	187
3.10.	Pulsed Radiography	207
3.11.	Telemetry Methods	212
CHAPTER IV. DYNAMICS OF SOLID MEDIA		221
4.1.	Preliminary Remarks	221
4.2.	Nondeformable Body Penetration into Plastic (Metal) Halfspace	223
4.3.	Qualitative Analysis of the Cavity Formation Process During High-Velocity Impact of Deformable Bodies	234
4.4.	Formulation and Analysis of the Problem of Modeling the Deformable Body Encounter Process	242
4.5.	Comparison of "Original" and "Model" Process Parameters	248
4.6.	Modeling Curve	251
4.7.	Evaluation of Thermal Phenomena Role in Metallic Body Interaction	257
4.8.	Failure of Metal Bodies During "Short" Impact	267
CHAPTER V. AEROBALLISTIC INVESTIGATION METHODS		275
5.1.	Preliminary Remarks	275
5.2.	Characteristics of the Ballistic Method of Aerodynamic Investigation	276
5.3.	Ballistic Stands	284
5.4.	Aeroballistic Tunnels	293
5.5.	Gasdynamic Parameters for Ballistic Ranges. Modeling Region	306
5.6.	Technique for Determining Drag Coefficient	312
5.7.	Measurement of Other Aerodynamic Characteristics	327
5.8.	Results of Some Aerodynamic Studies	332
REFERENCES		362

INTRODUCTION

In the course of technical progress, the scientists and engineers are faced with new and increasingly complex problems. Resolution of these problems is impossible without the use of modern research methods which correspond to the level of the tasks. Thus, in the fifties, the rapid development of energy, space, aviation, and certain other branches of new technology required study of processes characterized by speeds of the order of several kilometers or tens of kilometers per second. Such processes include, for example, spacecraft motion in various gaseous media, interaction of spacecraft with meteoritic bodies, and so on. It is obvious that, in order to study these processes, it was first necessary to develop methods for imparting high velocities to bodies of different, but known, shapes and sizes. It was then necessary to develop equipment to record those parameters of these high-speed processes which are of interest to the investigators. Finally, it was necessary to construct physically valid models of the processes in question and formulate computational schemes.

/7*

It is well known that the conventional artillery and gun systems can give solid bodies velocities which do not exceed 1000 - 1500 m/sec. If we elongate the gun barrel in these systems (to 160 calibers or more) and use powder charges whose weight is an order of

* Numbers in the margin indicate pagination in the original foreign text.

magnitude greater than the weight of the body being launched, the launch velocity can be increased to about 2000 - 2500 m/sec. However, further increase of the muzzle velocity using conventional powder systems is not possible in principle. The reason is that the powder gases have high molecular weight (about 28), i.e., they are characterized by relatively low sound speed and, consequently, low expansion (discharge) velocity. Therefore, it was necessary to find a fundamentally different solution of the problem.

And such a solution was found. The use of light gases (hydrogen and helium) for acceleration of the bodies was proposed. Filling the launcher breech with a light gas and use of a powder charge to increase the gas pressure and temperature make it possible to reduce the molecular weight of the working gas mixture to 14 - 15, and raise the muzzle velocity to about 3000 m/sec. /8

An important step in light-gas development was the use of a piston to separate the launcher breech into two volumes (the "two-stage" principle). One of these volumes was used for the powder charge, and the other — adjacent to the barrel — was filled with the light gas. When the powder charge was ignited, the piston began to move, compressed the light gas, and the latter, as it expanded, imparted velocity to the projectile.

The idea of using the two-stage principle for high-speed launching was very fruitful. By the middle of the fifties, there were several dozen two-stage light-gas launchers in various countries. The experimental studies made using these facilities made it possible to find optimal designs for the various light-gas launcher components. Launch velocities of 10 km/sec, and even higher, were achieved in some of these ranges.

Such velocities exceed markedly the speed of sound in the working gas. This means that the wave effects arising in the working gas will play a major role in the light-gas launchers. Consequently, calculation of the structural and ballistic parameters of the light-gas launchers cannot be based on the classical ballistics methods,

which neglect the wave processes, and require the development of a more general approach. Therefore, the subject matter of the new branch of internal ballistics — high-velocity light-gas launcher theory — is the solution of the general equations of gasdynamics by modern computational mathematics techniques.

The first and second chapters of the present volume are devoted to presentation of the fundamentals of high-velocity light-gas launcher theory, and the principles involved in calculating their structural and ballistic parameters.

The modern ballistic ranges are a complex consisting of a power or light-gas launcher, which imparts to the projectile (model) the required velocity and a definite mode of motion, and the instrumentation, located along some segment of the model motion trajectory.

The nature of the ballistic method, both when studying the collision of solid bodies and when conducting aeroballistic studies, is a result of the fact that the model displaces in space and the duration of the observed processes is short. Therefore, high-speed recording and measuring techniques must be used.

/9

At present, several highly effective methods, based on the latest achievements of electronics, optics, radiography, high-voltage engineering, and so on, have been developed for studying high-speed processes. In examining these methods, we must first of all note high-speed photography in visible light, accomplished basically with the aid of spark and laser light sources, which make it possible to obtain pictures with nanosecond exposure duration.

The electro-optical shutters are convenient tools for studying self-luminous objects. As for high-speed processes of low brightness, here the use of electron-optic converters opens up wide possibilities. These converters make it possible to obtain photographs with exposures lying in the picosecond range.

Pulsed radiography of high-speed processes in nontransparent media is now highly advanced. The modern pulsed radiography equipment makes it possible to obtain high quality pictures with exposures of a few nanoseconds.

The electronic synchronizing and timing circuits have achieved significant progress. They provide reliable control of the complex recording equipment, and make it possible to study the development of the phenomenon in time with high precision.

The principles used in constructing the instrumentation and the measurement techniques used on ballistic ranges are described in Chapter III.

The solid body collision problem must be listed among those whose solution requires use of the high-speed launcher, together with the apparatus for recording high-speed processes.

The problem of the collision of two (or more) bodies is one of the oldest problems, and study of the solid body collision process in order to establish the laws governing this process has attracted scientists and engineers for many centuries. The interest in this problem has increased markedly in the last decades. While previously, the collision velocities used ranged from about one meter per second (forging practice) to about 1 kilometer per second (artillery), at the present time, the development of geophysics, astrophysics, high-pressure physics, and several new engineering branches requires clarification of the laws governing the collision of solid bodies at encounter velocities varying over a wide range — up to 100 km/sec. For example, the previously mentioned velocities of meteoric body encounter with spacecraft may reach these high values.

On the basis of very general physical considerations, we would expect that the laws governing the collision of solid bodies at velocities on the order of 10 km/sec and higher will differ significantly from the laws which hold for velocities of 1 to 1000 m/sec.

/10

And this is indeed the case. Studies of many Soviet and foreign scientists have shown that wave phenomena and hydrodynamic and thermal effects (melting, thermal explosion) play a definite role in high-velocity impact of solid bodies. The basic physical laws governing the collision of metallic bodies have been established, and models of the process have been proposed.

Chapter IV is devoted to discussion of these question.

Another area of ballistic range application is that of aerodynamic investigations, whose origins go back to the artillery engineers in the nineteenth century in their studies of external ballistics.

Advances in the aeroballistic method have been particularly rapid in very recent years, in connection with solving the problems of rocket and space engineering.

In contrast with the other aerodynamic research study methods, in which we study the interaction of an accelerated flow with a stationary model or a model performing limited motion, the ballistic experiment is, in essence, a flight test under laboratory conditions. This technique has several advantages, and the ballistic test results add significantly to the wind tunnel data. The most important advantages of the aeroballistic method are: wide range of Reynolds and Mach number variation, possibility of obtaining high Mach and Reynolds numbers and high stagnation enthalpies, absence of any model supports, undisturbed approaching flow, precise and reliable control of all the approaching flow parameters, and the possibility of studying unsteady aerodynamic phenomena.

The ballistic ranges intended for aerodynamic and gasdynamic studies can be divided into two types. The first includes the ranges which are termed aeroballistic stands. In these ranges, the test model is launched into stationary air ("open" ranges) or into a chamber in which the gas pressure and composition, and sometimes the temperature as well, can vary ("closed" ranges).

The second type includes the ranges in which the model is launched counter to the supersonic flow of a wind tunnel. Such ranges are termed aeroballistic tunnels. Experiments with Mach numbers as high as 83 have been conducted in ranges of this type. Mach numbers of this order have not been realized in any other facilities. /11

The ballistic method is used at the present time to determine the aerodynamic characteristics of models in air and other media, study the physical and chemical phenomena accompanying the motion of bodies at supersonic and hypersonic velocities, and so on. The possibilities of the ballistic method for study of the gasdynamic and physical processes in the near and far hypersonic wake are promising.

Chapter V presents schemes of ballistic ranges of various types, describes the experimental techniques, and evaluates some results illustrating the capabilities of the aeroballistic research method.

CHAPTER I

HIGH-VELOCITY LAUNCHERS

§ 1.1. Preliminary Remarks

A new trend has developed in the last few decades in the field of artillery engineering — the creation of high-velocity launch facilities, i.e., devices for launching bodies with velocity exceeding 2500 - 3000 m/sec. Because of the fact that light gases (hydrogen or helium) are used in these facilities, they are usually termed light-gas guns and light-gas or gasdynamic ranges. In the following, the high-velocity launchers in which hydrogen or helium is used as the driver gas are designated in abbreviated form as LGL. At the present time, LGL are used to impart velocities exceeding 10,000 - 12,000 m/sec to bodies. The LGL are used to conduct scientific studies in the field of solid body collision aerodynamics and physics. /12

In addition to the LGL, in laboratory studies we use high-velocity launchers in which the body is accelerated by electrodynamic forces, and also by shaped charges of various construction. Because of the fact that primarily the power and light-gas launchers are used in the modern ballistic ranges and stands, our attention in the following will be concentrated on the gasdynamic methods for accelerating bodies.

We shall discuss the general status of LGL theory, analysis, design, development, and use.

I. Two basic trends can be noted in the field of LGL design theory. The first is characterized by the tendency to obtain approximate analytic relations describing the projectile motion under very "general" assumptions (see, for example [1 - 4]). The second trend is characterized by the tendency to obtain a precise picture of the motion in all its complexity, with the aid of numerical methods. If the exact solution is available, we can obtain an approximate solution with the aid of certain approximations (see, for example [5 - 9]).

/13

II. In designing the LGL, we use various computational methods, both very approximate and quite rigorous. However, in most cases, the calculation results differ significantly from the experimental results (particularly markedly in determining the maximal gas pressure). The explanation for this lies in the fact that even the most advanced technique for gasdynamic calculation of the ballistic ranges must be based on several unavoidable assumptions (one-dimensional flow, absence of viscosity, and so on). Therefore, experiment plays a definitive role in high-velocity launcher development, and only with the aid of experiment can we introduce the required refinements into the computational technique and ensure LGL component operability and service life.

III. The launcher efficiency can be evaluated if we recall that the LGL are machines which are characterized by a definite thermodynamic cycle, as a result of which the thermal energy contained in the powder, capacity battery, and so on, is transformed into the kinetic energy of the projectile. The efficiency of such devices can be evaluated by the ratio:

$$\eta = \frac{mV^2}{2Q},$$

where m — projectile mass, V — projectile velocity, and Q — amount of thermal energy supplied.

The efficiency of the various launchers correlates well with the velocity imparted to projectiles by these launchers. This indicates that the existing launchers have achieved a definite level of advancement from the viewpoint of the gasdynamics and thermodynamics requirements. Therefore, we can consider that, at the present time, the primary problem is launcher development to improve their operational qualities.

IV. The field of LGL use can be evaluated by examining the relationship between the ratio of the powder charge weight ω to the projectile weight q and the launch velocity (Figure 1.1). We see from the figure that, in order to achieve high launch velocities, it is necessary to use heavy charges. For example, for projectile weight 5 grams, a powder charge weighing 2500 grams is necessary to achieve a velocity of 8000 m/sec. Therefore, the high-velocity launchers have found widest application under laboratory conditions for launching relatively small bodies (weighing from 0.01 to 10 grams)*. The use of launchers of this type to launch heavy bodies requires the construction of special stands. There are only a few such stands in the entire world; however, their number is increasing all the time.

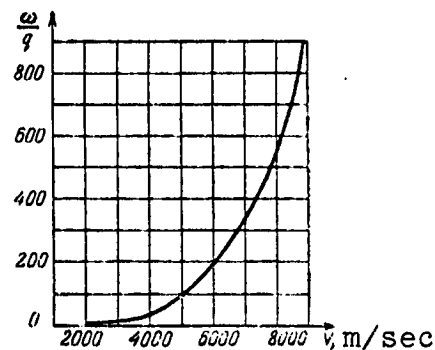


Figure 1. Ratio of powder charge weight to projectile weight versus launch velocity

At the present time, the LGL has passed the first stage of its development, and is a tool which is widely used in laboratory studies of phenomena taking place during the motion and collision of bodies with velocities of 4000 - 10,000 m/sec.

* We recall that in conventional artillery, the ratio ω/q varies from 0.1 to 1.5.

§ 1.2. Launch Physical Principles and Light-Gas Launcher Classification

The light-gas launcher is a particular case of the artillery weapon, which consists of two basic parts: the barrel (including the charge, projectile, and so on), and the carriage on which the barrel is mounted.

In the light-gas launcher, as in any artillery piece, launching of the projectile (body) is accomplished by the gas expanding in the barrel. Energy is supplied to this gas either by burning powder or as a result of precompression by a special piston, heating by an electrical discharge, and so on.

The process of launching from any barrel can be represented schematically as in Figure 1.2, which shows a barrel having the length L , and also two position of the projectile — the initial position at the distance L_c from

the breech, and the final position, when the body has traveled the entire acceleration path L_{ba} .

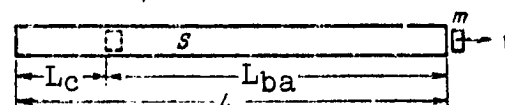


Figure 1.2. Launching a body
from a cylindrical tube

In order to understand the physical basis of the launching process with the aid of expanding gas, and establish the factors which determine the launch velocity V , we need only examine the very simple case of instantaneous power charge combustion.

Using the energy conservation law, we can write:

$$\frac{m_1 a^2}{\kappa(\kappa-1)} \eta = \frac{m V^2}{2} + S \int_0^L \frac{\rho u^2}{2} dL,$$

where S — barrel area, ρ — gas density, u — gas velocity, m_1 — gas mass, m — projectile mass, a — sound speed in the gas, κ — adiabatic exponent. In this equation, the ideal gas internal energy multiplied by the expansion process thermal efficiency η appears on

the left side, while the kinetic energy of the projectile and of the gas traveling in the barrel appears on the right.

The integral in this equation is easily transformed:

$$S \int_0^L \frac{\rho u^2}{2} dL = S \frac{\rho_{av} u_{av}^2}{2} L = \frac{m_1}{2} b_1 V^2,$$

where $S \rho_{av} L = m_1$, and the average gas velocity u_{av} is expressed in terms of the projectile velocity V (b_1 — coefficient of proportionality):

$$u_{av}^2 = b_1 V^2.$$

After transformation, we obtain easily from this equation the well known ballistics formula:

$$V = a \sqrt{\frac{2\eta}{x(x-1) \left(\frac{m}{m_1} + b_1 \right)}}. \quad (1.1)$$

This formula shows that even in the limiting case, when the process thermal efficiency is equal to unity, i.e., when the gas expansion takes place without losses in an infinitely long barrel and the projectile is infinitely light (or the launch gas mass is infinitely large, i.e., $\frac{m}{m_1} \rightarrow 0$), the launch velocity cannot be higher than:

$$V_{\text{limit}} = a \sqrt{\frac{2}{x(x-1) b_1}}. \quad (1.2)$$

In practice, the projectile velocity does not exceed the value*:

$$V \approx (1.8 - 2.5) a. \quad (1.3)$$

Thus, the projectile velocity is determined primarily by the sound speed in the launch gas. This is easily understood if we recall that the sound speed characterizes the ideal gas internal energy E .

/16

*This will be shown in detail later, in Chapter II.

In fact,

$$E = c_p T = \frac{a^2}{\kappa(\kappa-1)}. \quad (1.4)$$

Here, we have used the well known expression for the speed of sound in a gas:

$$a^2 = \kappa R T \quad (1.5)$$

and the Meyer equation:

$$c_p - c_v = R.$$

If we introduce the universal gas constant R^* , equal to:

$$R^* = R \cdot \mu,$$

(1.5) takes the form:

$$a^2 = \frac{\kappa R^* T}{\mu}.$$

Thus, the sound speed in an ideal gas is determined by the gas temperature T and molecular weight μ . Consequently, in order to increase the launch velocity, we must increase the temperature of the launch gas and reduce its molecular weight.

We see from (1.1) that, in the general case, the projectile velocity is determined not only by the sound speed, but also by the adiabatic exponent κ , efficiency η , coefficient of proportionality b_1 and the ratio m_1/m .

If we use dimensional analysis, we can write an expression for the projectile velocity analogous to (1.1), but having the more general form:

$$V = \eta \cdot a \cdot f\left(\frac{m_1}{m}, \kappa, \frac{L_{ba}}{L_c}\right) + V_0 \quad (1.6)$$

where V_1 — transport velocity of the entire gas as a whole, ϕ — overall correction factor; $f(m_1/m, \kappa, L_{ba}/L_c)$ — a function of the ratio m_1/m , κ , and the ratio of the barrel length L_{ba} to the breech chamber length L_c (this ratio basically determines the firing efficiency).

In the following, we shall use the formula for the projectile velocity in this form.

The primary objective of launch theory is to determine the influence of all the above-listed parameters on the projectile velocity (i.e., determine the function f) and show the most promising directions for launcher development. /17

Formula (1.6) shows immediately the three basic directions in which development of launchers with high launch velocity can proceed:

- 1) increase the sound speed in the launching gas, which requires increasing the gas temperature T and reducing its molecular weight μ ;
- 2) increase the transport velocity V_1 ; in practice, this is achieved by using a hydrodynamic (or plastic) piston, accelerating the gas in the barrel by electrodynamic forces, and so on;
- 3) increase the coefficient ϕ by reducing all forms of losses.

All these approaches are reflected in the construction of existing launchers.

Let us turn now to classification of the high-velocity launchers.

The launchers can be divided into two classes on the basis of the principle used in accelerating the projectile.

I. Gasdynamic launchers in which the model is accelerated by a gas (LGL).

II. Electrodynamic launchers in which the model is accelerated by forces arising from the interaction of currents or from a magnetic field. The electrodynamic launchers are subdivided into contact and induction types.

The gasdynamic light-gas launchers are subdivided on the basis of construction principle into single-stage and multistage types. In the single-stage launchers, the energy is supplied directly to the working gas, either by combustion or by an electrical discharge; the primary advantage of these launchers is their simplicity. In the multistage launchers, the energy supply to the working gas takes place through intermediate stages -- for example, a piston is accelerated and its kinetic energy is then transformed into compressed gas potential energy, and so on.

The gasdynamic launchers are divided into three groups on the basis of the principle of energy supply to the working gas:

- a) launchers with mechanical compression (piston or shock wave);
- b) launchers with electrical heating;
- c) launchers with combustion.

The classification in final form is shown in Figure 1.3. This classification covers practically all the known high-velocity launcher schemes.

Turning to a brief description of the various launchers, we emphasize that the objective of this description is not examination of all known schemes (which is not possible at the present time). We shall examine only the most typical schemes.

§ 1.3. Single-Stage Gasdynamic Launchers

The simplest LGL are the single-stage gasdynamic devices, whose scheme is quite similar to that of the conventional firearm.

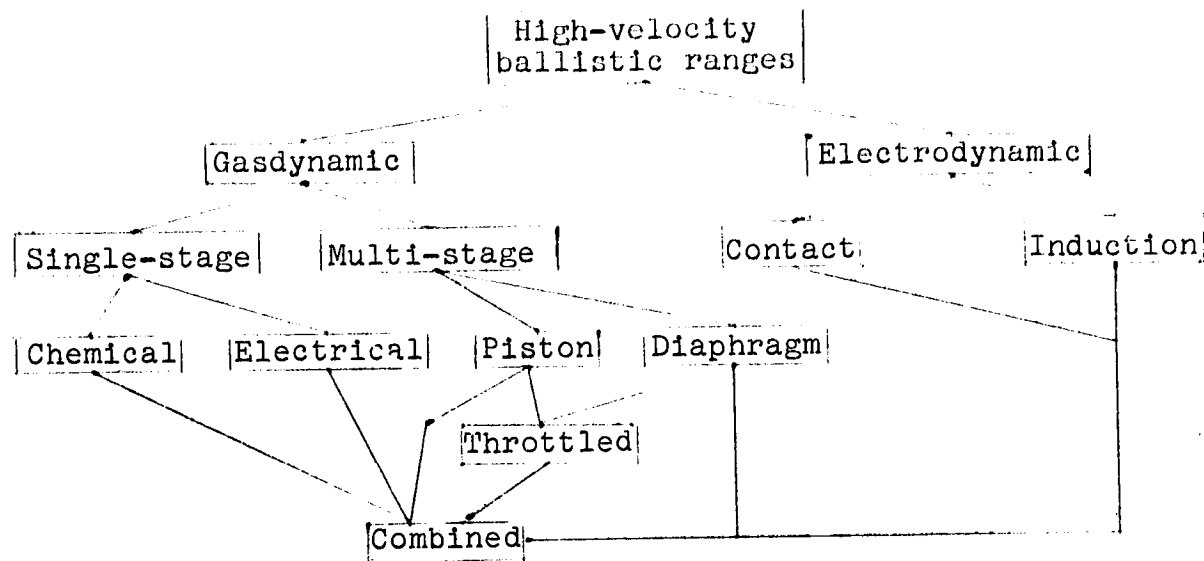


Figure 1.3. Ballistic range classification

The simplest and apparently the first light-gas launcher was that in which the working gas was a light gas (hydrogen) heated by a powder charge. In this case, as the powder burns, a mixture is obtained with molecular weight less than that of the powder gases, but with somewhat lower temperature. The maximal velocity attained in launching bodies from launchers of this type was close to the velocity attained by the conventional powder systems, and therefore these systems did not find practical application.

/19

The next step in single-stage launcher development was the use, as the working gas, of a mixture consisting of oxygen, hydrogen, and helium (OHHM — oxygen, hydrogen, helium mixture).

Figure 1.4 shows the basic characteristics of this working gas as a function of the percentage helium content in the mixture. We see from the figure that the maximal sound speed and, consequently, the maximal launch velocity are obtained with $\epsilon \approx 70 - 75\%$. In this case, $a_0 \approx 2330$ m/sec.

In equipment using OHHM, a launch velocity of 3500 — 4000 m/sec may be achieved. Figure 1.5 shows a diagram of this equipment.

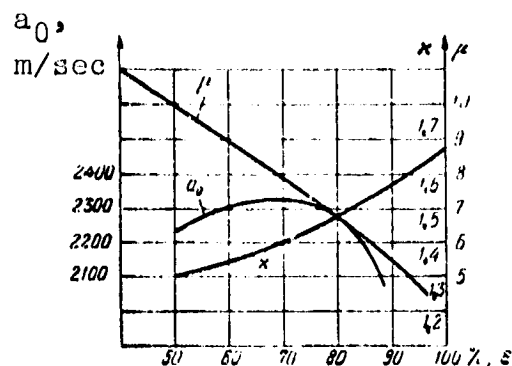


Figure 1.4. Characteristics of OHHM as function of percentage helium content

The most promising among the launchers of the subject type is the launcher with electrical preheating of the light gas. Storage and capacitor batteries, induction coils, and so on, can be used as energy sources for such launchers. In the electrical preheating case, the gas temperature may reach $10,000^{\circ}\text{K}$ or more. In this case, the working gas temperature limitations are associated only with heat transfer through the walls and questions of service life.

Figure 1.6 shows an electrically pulsed launcher in which mechanical energy is stored in flywheels, and the electrical energy source is a unipolar generator [16]. The launcher operates as follows: the motor spins up the flywheels and the unipolar generator to the specified speed, after which the main switch triggers, and energy is stored in the induction coil; when the energy storage process is completed, the primary switch

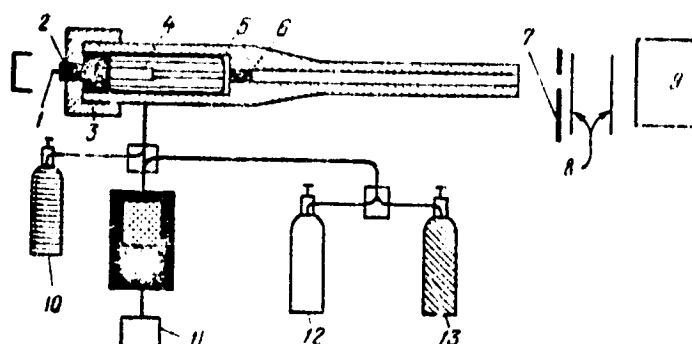


Figure 1.5. Launcher using OHHM:

1 — electrical primer; 2, 3 — breechblock; 4 — igniter; 5 — cartridge; 6 — model; 7 — gas cutoff barrier; 8 — frame-targets; 9 — model catcher; 10 — oxygen bottle; 11 — compressor; 12 — hydrogen bottle; 13 — helium bottle

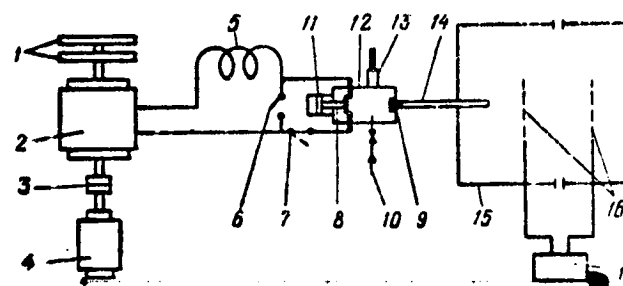


Figure 1.6. Electropulsed launcher:

1 — flywheel; 2 — homopolar generator; 3 — clutch; 4 — motor; 5 — induction coil; 6 — primary switch; 7 — secondary switch; 8 — internal switch; 9 — model; 10 — gas inlet valve; 11 — air cylinder and piston, which break the contact in the working chamber; 12, 13 — pressure sensor; 14 — (Caption continued on following page)

opens and current now flows only through the closed contact inside the chamber. Then the contact in the chamber opens. The energy stored in the induction coil is released in the chamber. The process lasts about 30 - 50 μ sec.

In other electropulsed launchers, a battery of capacitors or other energy source is used in place of the unipolar generator and the induction coil. The capacitor battery provides shorter charging time; however, it is considerably more expensive than the induction coil, and has larger dimensions.

Figure 1.7 shows a general view of the electropulsed chamber in cross section.

A realistic temperature from the viewpoint of barrel service life for the electropulsed launchers can apparently be considered to be $T \approx 8000^\circ \text{K} - 10,000^\circ \text{K}$, and therefore the maximal launch velocity for units of this type, when using hydrogen, is $V = 8000 - 12,000$ m/sec, and when using helium — $V = 7000 - 9000$ m/sec.

The actual launch velocity depends on the specific characteristics of the electropulsed chamber, particularly on the gas pressure

Figure 1.6 (continued)

barrel; 15 — vacuum chamber; 16 — targets; 17 — electronic chronograph

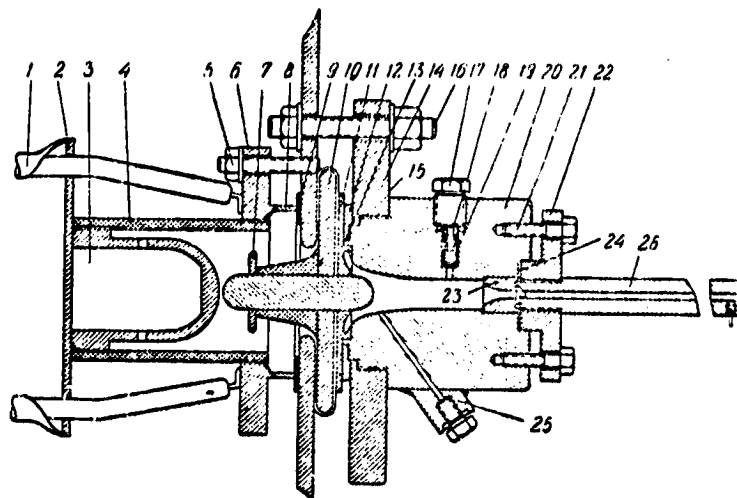


Figure 1.7. Electro-impulse chamber:

1 — cable; 2 — collecting electrode; 3 — electrode; 4 — activation chamber housing; 5 — pin; 6 — flange; 7 — protective ring; 8 — sealing ring; 9 — gasket; 10 — collecting electrode; 11 — insulation; 12 - 14 — seals; 15 — flange; 16 — pin; 17 — plug; 18 — gasket; 19 — crusher gauge; 20 — chamber; 21 — bolt; 22 — flange; 23 — sleeve; 24 — seal; 25 — ignition wire lead-in; 26 — barrel

and the relationship between the projectile mass and the gas mass, and will be lower than the limiting value because of the considerable increase of the gas molecular weight due to electrode erosion (usually $V = 5 - 6$ km/sec).

§ 1.4. Multistage Gasdynamic Launchers

The multistage light-gas launchers differ in principle from the conventional artillery guns in that they include additional stages, whose objective is preheating and compression of the light gas. The most typical LGL of this type is the two-stage piston launcher.

Figure 1.8 shows a piston launcher. The light gas in chamber 4 is compressed by the piston 2, which is driven by powder gases. After the pressure in the light-gas chamber reaches the magnitude p_ϕ , the rim of the projectile 5 is severed, and firing takes place.

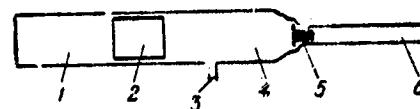


Figure 1.8. Piston-type launcher:

1 — charge; 2 — piston; 3 — gas inlet; 4 — gas chamber; 5 — projectile; 6 — barrel

For preliminary analysis of the piston-type launcher operation, it is necessary to have several relations, which are obtained under the assumption that: a) the expansion-compression processes behind and ahead of the piston are equilibrium processes; b) the driving pressure p_ϕ is equal to the maximal pressure allowable in the launcher:

$$p_\phi = p_{\max}.$$

Using the equation of state, and introducing the entropy function Φ by the well known relation:

$$\Phi = \frac{p}{\rho^{\gamma}}, \quad (1.7)$$

it is easy to express the light-gas temperature at the end of compression in terms of its initial parameters:

$$\frac{T_{\max}}{T_0} = \left(\frac{p_{\max}}{p_0} \right)^{(\gamma-1)/\gamma} \cdot \left(\frac{\Phi_{\max}}{\Phi_0} \right)^{1/\gamma} = \left(\frac{a_{\max}}{a_0} \right)^2. \quad (1.8)$$

We see from Formula (1.8) that, in the piston launcher, it is advantageous to have a high compression ratio p_{\max}/p_0 , and accomplish the compression process with the maximal possible increase of the entropy Φ_{\max}/Φ_0 . In this case, for given p_{\max}^* , κ , and initial gas temperature T_0 , the gas temperature and, therefore, the sound speed in the gas will be maximal.

We shall introduce some relations which will be required later on.

The piston launcher operating principle is based on the fact that the light-gas potential energy at the end of compression:

$$E = \frac{m_1 a_{\max}^2}{\kappa(\kappa - 1)} \quad (1.9)$$

(where a_{\max} — sound speed in the gas at the end of compression, and m_1 — mass of the light gas) is stored initially in the form of kinetic energy of the piston.

The piston kinetic energy is:

$$E_p = \frac{G_p v_{p \max}^2}{2g}, \quad (1.10)$$

where G_p — piston weight, and $v_{p \max}$ — maximal piston velocity. /23

Therefore, we can write:

$$\frac{G_p v_{p \max}^2}{2} = b \frac{m_1 a_{\max}^2}{\kappa(\kappa - 1)} g, \quad (1.11)$$

where b is a coefficient. We see from (1.11) that:

$$G_p = \frac{2bm_1}{\kappa(\kappa - 1)} \left(\frac{a_{\max}}{v_{p \max}} \right)^2 g. \quad (1.12)$$

* It is obvious that the maximal pressure is determined by launcher strength.

The gas charge mass is

$$m_1 = \Pi m,$$

where m — projectile mass, Π — parameter selected from the gas-dynamic analysis (usually, $\Pi \approx 3 - 6$).

On the basis of (1.6), a_{\max} equals

$$a_{\max} = \frac{V}{\varphi f \left(\Pi, \kappa, \frac{L_{ba}}{L_c} \right)};$$

consequently, (1.12) can be written as

$$G_p = \frac{2b\Pi q}{\kappa(\kappa-1)\varphi^{2/2}} \left(\frac{V}{V_{p\max}} \right)^2, \quad (1.13)$$

where $q = mg$ is the projectile weight.

Formula (1.13) relates the piston weight G_p with the launcher parameters: q , V , $V_{p\max}$, and also through f with Π , κ , and L_{ba}/L_c .

Finally, it is easy to establish the connection between the launcher dimensions and the initial light-gas pressure.

It is obvious that the gas charge mass:

$$m_1 = \rho_0 W_c,$$

where ρ_0 is the light-gas density, and W_c is the gas chamber volume before compression, since

$$\rho_0 = \frac{\kappa p_0}{a_0^2},$$

where a_0 is the sound speed in the light gas prior to compression, then:

$$m_1 = \frac{\kappa p_0}{a_0^2} W_c. \quad (1.14)$$

The quantity m_1 is intimately related with the projectile mass m , and their ratio:

$$\Pi = \frac{m_1}{m}$$

is usually specified from the gasdynamic analysis, as mentioned above. /24

Consequently, the initial light-gas pressure:

$$p_0 = \frac{m \Pi a_0^2}{\pi V_c}. \quad (1.15)$$

Formula (1.15) limits the initial light-gas pressure.

Since the quantity p_{\max} is determined by the structural characteristics of the launcher forechamber, the quantity p_{\max}/p_0 for the piston-type LGL is essentially determined by the projectile mass m , gas chamber volume W_c , and initial gas temperature rise, since this determines a_0^* . The existence of the relationship between p_0 and W_c (or, what is the same, the gas chamber dimensions) makes it possible to divide the piston type LGL into two subgroups:

- a) launchers with low compression ratio,
- b) launchers with high compression ratio.

In the low-compression-ratio LGL, the initial light-gas pressure ranges from 60 to 120 atm** (the compression ratio for $p_{\max} \approx 10\,000$ atm is of the order of 100). These launchers have minimal dimensions, but their launch velocity does not exceed 4000 m/sec, which follows from (1.3), if we consider that for this compression ratio the speed of sound in hydrogen increases only to about 2500 - 2800 m/sec.

In launchers with high compression ratio, the initial light-gas pressure is usually close to 10 atm, and the compression ratio is

* $a_0 = \sqrt{\gamma g R T_0}$.

** The pressure in the standard bottles is 135 - 150 atm.

of the order of 1000. The dimensions of these launchers for the same projectile weight exceed those of the low pressure ratio launchers by 5 to 10 times; moreover, their launch velocity is considerably higher -- of the order of 6000 - 7000 m/sec or even higher -- when using a hydrodynamic piston.

With (1.7, 1.13, 1.15) available, we can turn to detailed examination of the existing multistage LGL.

Launchers with heavy nondeformable piston. Launchers of this type are used most successfully for investigations with projectile speeds of 2500 - 4000 m/sec. The primary difficulty in developing such LGL lies in decelerating the piston in the forward position. Usually the piston launchers with heavy metallic piston are designed so that the piston approaches the end of the ballistic barrel with zero velocity. In this first approach, the compressed light gas forms a cushion and plays the primary role in stopping the piston.

If the piston is not equipped with a special wedging device, it will bounce back under the pressure of the light gas. As a rule, the light gas can, at this time, leak out of the launcher through the barrel, and the powder gases again send the piston forward; if special devices are not provided, the piston may acquire considerable velocity and damage the launcher during the second impact. /25

At the present time, two basic methods for preventing impact are normally used: the first is to use a shock absorber made from a soft material, such as aluminum or polyethylene, the second is to equip the piston with a special small pin which blocks the residual light gas as the pin enters the barrel, and thus creates a cushion. As a rule, the choice of heavy piston construction to prevent impact is made experimentally.

The initial gas pressure is usually selected in the range between 60 and 120 atm, in order to facilitate stopping the piston in the LGL with a heavy metal piston. Therefore, these launchers have a low compression ratio.

We noted previously that the launchers with low compression ratio have minimal dimensions (if we do not consider the single-stage launchers). Usually, the gas chamber length in the low-compression-ratio launcher does not exceed 10 - 30 calibers.

The desire to increase the launch velocity in the heavy piston launchers led to use of launchers with high compression ratio, and the damage occurring because of piston impact in the extreme forward position required reduction of the piston weight.

As a result, a new type of piston launcher has been developed — the light-piston LGL. As a rule, these launchers have a high compression ratio; moreover, in these launchers, the compression process takes place with increase of the entropy.

Launcher with light piston. Formula (1.8) shows that increase of the gas entropy in the compression process leads to increase of the temperature for the same compression ratio; consequently, it is advantageous to compress the gas in the launcher with the aid of an irreversible process.

One of the simplest compression processes with entropy increase is compression by a piston which creates shock waves. Specifically, a shock wave arises ahead of a piston traveling with acceleration. The coordinates x, t of the point of shock wave occurrence in the x, t plane are connected with the piston acceleration and the gas parameters by the following well known formulas [25]:

$$x_1 = x_0 + \frac{2}{\kappa + 1} \frac{a^2}{A},$$

$$t_1 = t_0 + \frac{2}{\kappa + 1} \frac{a}{A}.$$

In these formulas, A is the initial piston acceleration, equal to: 26

$$A = \frac{S_g}{G_r} (p_{z0} - p_{r0}),$$

10

where S — piston area, G_p — piston weight, and p_{l0} and p_{r0} are the pressures at the initial moment to the left and right of the piston.

In the heavy piston case, the quantity A is small, and the point of shock wave occurrence lies outside the light-gas chamber; the short gas chamber length in these launchers facilitates this situation. In this case, the compression takes place practically isentropically.

When a light piston is used, the acceleration magnitude may be such that the shock wave occurs near the piston. The presence of shock waves is a characteristic feature of the light-piston launchers.

As the shock wave reaches the front wall of the light-gas chamber, it reflects from the wall, and then a series of reflections from the wall and piston take place. There will be abrupt entropy increase during each reflection, and the entropy ratio in practice may reach:

$$\frac{\Phi_{\max}}{\Phi_0} \sim 2-3.$$

We shall present, as an example, the parameters of an American light-piston launcher [3]. Fast-burning powder is used in this launcher.

The basic launcher data are:

Piston barrel diameter	22 mm
Piston barrel length	1515 mm (69 calibers)
Piston weight	19 g
Powder gas pressure (max)	17,000 atm
Light gas pressure (max)	44,000 atm
Initial light gas pressure	60 atm
Ballistic barrel diameter	5.6 mm
Model weight	0.3 g
Model velocity	7300 m/sec
Powder charge	125 g
Ballistic barrel length	915 mm (165 calibers)

Figure 1.9 shows the velocity of a projectile launched from this gun as a function of the powder charge weight, and Figure 1.10 shows a photo of the ballistic light-piston launcher.

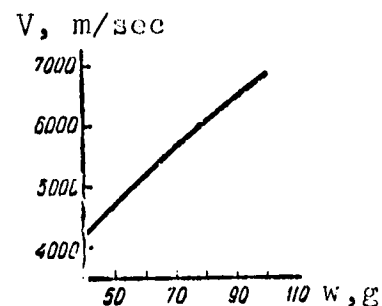


Figure 1.9. Projectile velocity versus powder charge weight

The possibility of compressing the gas with increase of the entropy is not the only advantage of the light-piston launchers. No less important is the



Figure 1.10. Ballistic launcher with light piston

fact that use of the light piston eliminates piston impact during repeated arrivals at the extreme forward position. In fact, experiment has shown that the impact of a light plastic piston is not damaging, even with a velocity of the order of 1000 m/sec.

/27

The disadvantage of the light piston is the fact that the piston can normally be used only once, and must be considered as a firing element. In addition, we have mentioned that the light-piston launchers have larger dimensions.

At first glance, it might seem that it would be easy to convert all piston launchers to the light-piston type. However, it follows directly from (1.12) that this is not always possible in practice. In fact, the piston weight G_p is connected with the compressed light gas parameters, since the maximal piston velocity is usually limited. Thus, for the powder-driven systems, the maximal practically achievable piston velocity is 1000 - 1800 m/sec. For systems in which the piston is driven by OHM, this quantity may be larger — of the order

of 2500 m/sec. Therefore, conversion in the piston launcher to a light piston is possible only when the piston kinetic energy is sufficient for compression of the light gas.

A long gas chamber, usually more than 60 calibers, is characteristic for the LGL with light piston. In some launchers this length reaches 100 or even 150 calibers.

Diaphragm-type launchers. In the diaphragm-type launcher, the high-pressure region (powder gases or OHHM) is separated from the light gas by a diaphragm. When the diaphragm ruptures, a shock wave travels through the light gas and heats the gas. /28

With regard to gasdynamic scheme, the diaphragm-type launcher is identical with the shock tube. Figure 1.11 shows a diaphragm-type launcher.

The advantages of this launcher are its relative simplicity and the possibility of achieving greater increase of the entropy function than when using the light piston. A disadvantage of the diaphragm-type launcher is the reduced launch velocity stability, since it is difficult to achieve good repeatability of the diaphragm opening process and, consequently, stability of the shock wave parameters.

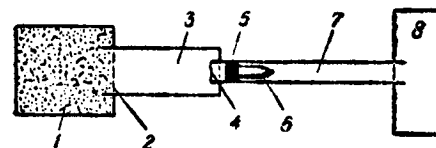


Figure 1.11. Diaphragm-type launcher:

1 — shock chamber; 2 — diaphragm; 3 — light-gas chamber; 4 — diaphragm ahead of model; 5 — sabot; 6 — model; 7 — barrel; 8 — ballistic target

Throttled launcher. The use of shock waves is not the only way to realize the gas compression process with increase of the entropy. A more complete thermodynamic cycle, during which the gas entropy increases, can also be used for this purpose.

The following is such a cycle. Gas with the parameters p_0 and T_0 is obtained by some process; then, this gas expands into an evacuated space (Figure 1.12). In this case, the pressure decreases to the value p_1 , while the gas temperature



Figure 1.12. Schematic of expansion into evacuated space:

1 — valve

remains unchanged. In fact, the equation of the first law of thermodynamics has the form:

$$dQ = dE + p dW.$$

Since $p = 0$, then $dQ = dE = c_v dT$; assuming no thermal losses, $dQ = 0$, and consequently $dT = 0$, i.e., $T = \text{const.}$

Let us determine the increase of the entropy function.

After flowing through the valve, the gas pressure:

$$p_1 = \frac{W_0}{W + W_0} p_0 = p_0 \frac{W_0}{W_1}, \quad W_1 = W + W_0.$$

Prior to flowing through the valve, the entropy function was:

$$\Phi_0 = -\frac{p_0}{\rho_0^{\kappa}} = -\frac{p_0 W_0^{\kappa}}{m_1^{\kappa}},$$

where m_1 - gas mass. After flowing through the valve,

$$\Phi_1 = -\frac{p_1 W_1^{\kappa}}{m_1^{\kappa}},$$

consequently,

$$\frac{\Phi_1}{\Phi_0} = \frac{p_1 W_1^{\kappa}}{p_0 W_0^{\kappa}} = \left(\frac{W_1}{W_0}\right)^{\kappa-1}.$$

The functional dependence of Φ_1/Φ_0 or W_1/W_0 for various values of κ is shown in Figure 1.13. We see from the figure that the entropy function increases by a factor of 2 - 3 during expansion into the vacuum.

The use of expansion into a vacuum is a promising direction in light-gas launcher development; however, to realize this process, we must first have a gas with high initial temperature T_0 . Therefore, this process leads to the need for developing combined multi-stage launchers.

Combined launchers. Analysis of the two-stage gasdynamic launchers has shown that the light-gas temperature must be increased in order to further increase their effectiveness.

In the two-stage launchers, the temperature increases only as a result of a single compression of the gas.

However, (1.8) includes T_0 — the initial gas temperature: the higher this temperature, the higher T_{\max} will obviously be.

Various techniques for preheating the gas, and also for accelerating the projectile in the barrel as a result of additional energy input can be used in the combined launchers.

The simplest preheating technique is to use OHHM in place of light gas. In this case, the OHHM ahead of the piston is ignited before igniting the primary charge which drives the piston. As a result, we obtain a mixture which may have various temperatures, κ , and μ , depending on the composition.

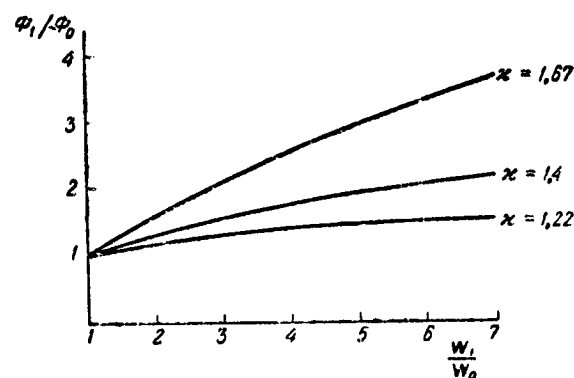


Figure 1.13. Entropy function increase during gas expansion into an evacuated space

Use of OHHM as the working light gas in the piston-type launchers has several advantages, the most important of which is the following. At temperature of order 3000 - 5000° K (depending on the pressure), water vapor begins to dissociate strongly, and therefore in the compression process, part of the piston kinetic energy transforms into energy of dissociation of the gas. Then, when the compression terminates and the model begins to travel in the barrel, the gas temperature falls sharply, and recombination of the molecules begins. Since the recombination process lasts for a time of order 10^{-5} - 10^{-8} sec, association can be completed in the barrel, which is equivalent to heat addition to the gas in the process of its expansion.

Figure 1.14 illustrates the nature of the gas temperature variation in time, with and without account for dissociation. An obvious drawback of this preheating method is the increase of the light gas molecular weight.

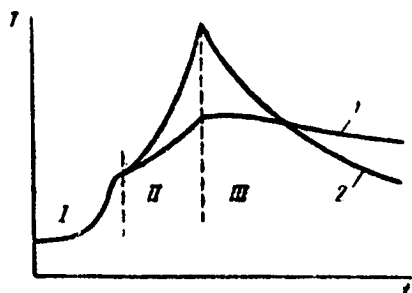


Figure 1.14. Temperature as a function of time:

1 — with dissociation; 2 — without dissociation; I — preheating zone (combustion of OHM); II — zone of compression by piston; III — expansion in barrel

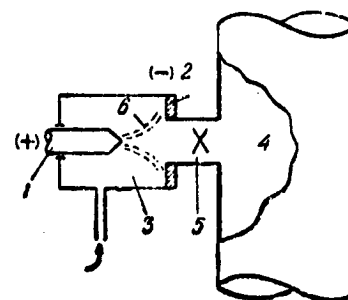


Figure 1.15. Plasmatron preheating:

1, 2 — electrodes; 3 — plasmatron chamber; 4 — evacuated gas chamber; 5 — valve; 6 — arc

A more complex method for initial preheating of the gas is the use of a special heater installed outside the launcher. In this case, the light gas is passed through the preheater (usually electrical), and then fills the barrel. The gas flow lasts for several minutes in order to thoroughly heat the barrel.

/31

Another preheater type is also possible (Figure 1.15). In this case, the light gas passes through a plasmatron, in which it is heated to approximately 1000° K. The plasmatron power is such that the filling process must be accomplished in 1 - 2 sec. The heated gas expands into the ballistic range evacuated chamber. However, this preheating method requires very large powers.

Table 1.1 shows the plasmatron power required for heating various weight quantities of helium to 1300° K in one second (plasmatron efficiency $\eta = 0.5$, helium $c_v = 1.25$ cal/kg \cdot deg).

Finally, rather than the plasmatron, we can use an electropulsed chamber, in which the heating of the gas is accomplished by an electrical discharge, after which the diaphragm ruptures and the gas flows into the evacuated barrel.

In these launchers, preheating is accomplished prior to initiation of compression by the piston. The disadvantages of this compression scheme are the comparatively large thermal losses and the increased powder charge weight, since the work performed by the piston increases in proportion to the initial gas temperature. However, the energy addition can be accomplished inside the compression chamber. In this case, the electrical energy is supplied at the most critical launch time, which, first of all, reduces the thermal losses markedly, and, second, the possibility appears of maintaining a constant pressure equal to the maximal value over some segment of the barrel, as a result of the heat input. The heat input process can obviously be continued with the aid of special dischargers located along the barrel.

Figure 1.16 shows the barrel pressure in the combined launcher as a function of time, with and without discharge.

The drawback of this launcher scheme is the necessity for a powerful pulsed electrical energy source.

The example presented above, characterizing the electrical powers required for preheating, shows that it is also advisable to seek mechanical techniques for preheating the gas. It is easy to imagine several different possible multistage launcher configurations in which only the mechanical and chemical forms of energy are used.

TABLE 1.1*

kgf	0,1	0,25	0,5	0,0	2,0
kw	1040	2600	5200	10400	22000

*Translator's note.
Commas in numbers represent decimal points.

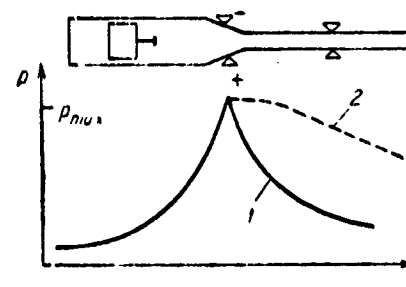


Figure 1.16. Pressure versus time in combined launcher (schematic):

1 — pressure as a function of time without discharge; 2 — pressure with discharge

The operating principle of these launchers is as follows. Multiple compression of the light gas is accomplished, and after each compression, the gas expands into an evacuated space (compression chamber of the next stage).

The compression can be accomplished either with the aid of shock waves or with the aid of heavy and light pistons (Figure 1.17). For example, the launcher consisting only of the chambers 5 and 6 will be a launcher with shock preheat; if a piston is placed in chamber 5, we have a piston-type dual-preheat launchers.

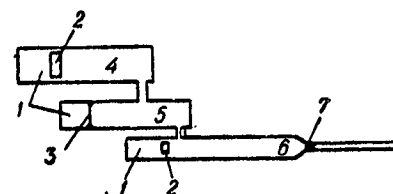


Figure 1.17. Multi-stage launcher:

1 — powder charges;
2 — piston; 3 — diaphragm; 4 — first (piston) stage; 5 — second (shock) stage; 6 — working (piston) stage; 7 — projectile

Finally, the use of reactive projectiles in the launchers is possible in principle (Figure 1.18). It is interesting to compare the operation of the launchers considered above. In Figure 1.19, the ordinate is the temperature, and the abscissa is the pressure. Let the initial gas pressure p_0 and temperature T_0 be the same in all cases. Also, let the maximal pressure p_{\max} be the same. Curve 1 corresponds to the heavy-piston launcher; in this case, the cycle is characterized by the maximal temperature T_1 .

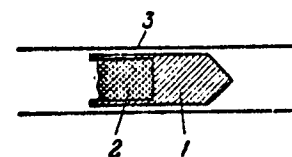


Figure 1.18. Active-reactive projectile:

1 — projectile; 2 — charge; 3 — barrel

Curve 2 corresponds to the light-piston launcher; the cycle is characterized by the maximal temperature T_2 , where $T_2 > T_1$, since compression takes place with increase of the entropy.

Curve 3 corresponds to the diaphragm-type launcher. This curve lies above curves 1 and 2, since the gas entropy increase in this

case is greater; however, the current cannot reach p_{\max} , since the shock wave cannot provide as large compression ratios as the piston-type launcher. Therefore, T_3 may also be lower than T_2 or T_1 . At the same time, we recall that if the shock wave can compress the gas to $p = p_{\max}$, the temperature T_4 will be higher than T_2 .

In the launcher with shock preheating, the relation characterizing the process in the shock unit coincides with curve 3. The expansion into the vacuum (pressure reduction at constant temperature) is described by the segment 5, and the compression by the piston is described by curve 6. It is obvious that T_6 will be higher than both T_3 and T_4 .

Now, we can examine the cycle of the launcher with multistage piston compression. The compression in the first stage corresponds to curve 1; the expansion into the vacuum is represented by curve 7; the new compression by the piston is represented by curve 8. It is obvious that, if we restrict ourselves to two compression stages, the compression temperature will be lower than T_6 . However, the compression process can be continued — curves 9 and 10; this is still another stage, etc. Consequently, in principle, this method can be used to obtain temperatures as high as desired for a given maximal pressure, but here major difficulties may arise in synchronizing the system. We must also consider the large thermal losses in the leakage process.

Of particular interest is the LGL with plastic piston. Generally speaking, the plastic-piston LGL is a heavy-piston launcher; however, because of the importance of this launcher type, it is better to examine it separately.

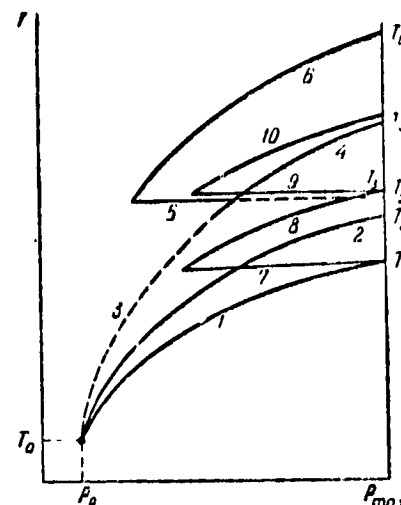


Figure 1.19. Comparison of working cycles of ballistic ranges of different types

For this, we must examine steady incompressible fluid flow through a channel of variable section. Since the same amount of fluid must pass through each channel section per unit time, it is obvious that:

$$S\rho u = S_0\rho u_0 = \text{const}, \quad (1.16)$$

where S — channel section area, u — velocity, ρ — density (subscripts 0 relate to the initial section).

From (1.16),

$$u = u_0 \frac{S_0}{S}, \quad (1.17)$$

consequently, the jet velocity increases as the section areas ratio.

Take an elongated piston made from a relatively incompressible plastic material. If we assume that the piston passes through the convergent part of the barrel without deceleration, its leading edge velocity must increase in accordance with (1.17).

Exact calculation of the piston motion in the bore can be performed by the methods of hydrodynamics, if we know the viscous properties of the material from which the piston is made. However, in practice, it is more convenient to introduce into (1.17) an experimentally determined coefficient.

Figure 1.20 shows a schematic relationship characterizing the piston leading edge velocity variation: in segment I, the velocity is V_0 ; in segment II, the velocity $V = V_0 \frac{S_0}{S} b$; and in segment III, the velocity $V_1 = V_0 \frac{S_0}{S_{ba}} b$.

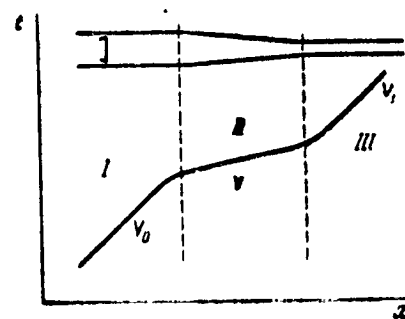


Figure 1.20. Motion of hydrodynamic piston

The ability of the incompressible plastic piston to increase its leading edge velocity when passing through a restriction is used in piston launchers as follows. The converging channel is profiled

so that, in some segment, the leading edge velocity will follow the model velocity in the barrel bore. The gas pressure on the model can be maintained constant in this segment, and therefore the model velocity increases*.

Launch velocities up to 11,000 m/sec have been achieved by launchers of this type in the U.S.A. [10].

In calculations of the piston-type launchers, we usually neglect the influence of piston motion on the model motion. The justification for this simplification is associated with the fact that the piston velocity in these launchers is usually not high. However, in practice, the piston motion does influence the projectile velocity and, in the first approximation, we can consider that the piston forward wall velocity is simply added to the model velocity (i.e., it can be considered a transport velocity); then,

/35

$$V = V_1 + \varphi af = V_t + \varphi af,$$

where V — model velocity; V_t — transport velocity, approximately equal to the piston wall velocity; φaf — gasdynamic launch velocity.

In the case of a heavy or light (but not plastic) piston, its velocity when approaching the forward position is low, and can be neglected. In the hydrodynamic plastic piston case, this velocity is about 1000 m/sec, and must be taken into consideration.

Figure 1.21 shows photos of a plastic piston before and after firing.

§ 1.5. Electrodynamic Launchers

We have examined briefly the gasdynamic launchers, in which projectile acceleration was accomplished by an expanding gas.

* In practice, we use a conical chamber, with taper angle between 5 and 10°.

In the electrodynamic launchers, projectile acceleration is accomplished by electromagnetic forces.

The simplest electrodynamic launcher is the contact accelerator (Figure 1.22). In this device, the current passes along the buses 1 through the projectile 2. The magnetic field is formed either by this same current or by a secondary current flowing in a special magnetization circuit. As a result of interaction of the current with the magnetic field, a ponderomotive force arises:

$$F = I \times H,$$

where I — current intensity, H — magnetic field intensity.

Two basic difficulties arise in developing contact accelerators: first, contact burning takes place and, second, a discharge arises ahead of the body because of plasma "expulsion" from the contact gap between the body and the buses.

In devices of this type, acceleration of the body takes place in a special evacuated chamber.

In the induction accelerators, the projectile is accelerated by the magnetic pressure, which is equal to:

$$p = \frac{H^2}{8\pi}.$$

The simplest induction accelerator configuration is shown in Figure 1.23. The accelerator is assembled from individual coils,

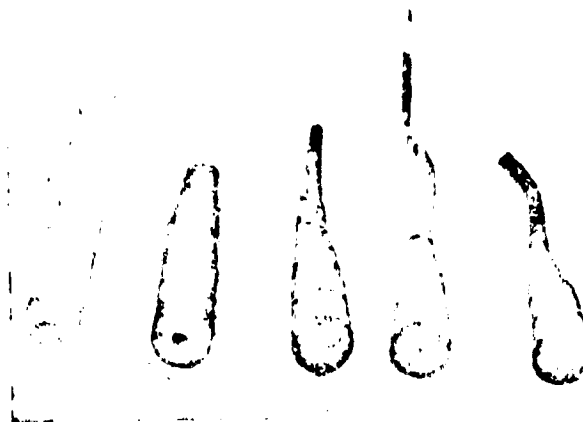


Figure 1.21. Hydrodynamic pistons before and after firing

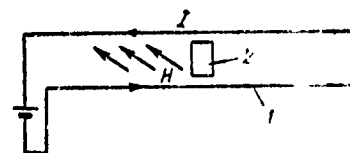


Figure 1.22. Contact accelerator

which are activated synchronously with the motion of the model, as a result of which a traveling magnetic field is created.

Figure 1.24 shows an induction accelerator in which the magnetic wave is created by explosive compression of the magnetic field. The operating principle of this accelerator is as follows.

The electrical current flowing in the solenoid 1 creates a magnetic field inside the conducting screen 2. When the explosive is initiated, the screen is compressed, and the magnetic field intensity increases in the ratio S_0/S_c , where S_0 — screen area, S_c — compression area*. As a result of the compression, very high magnetic pressure acts on the body and accelerates it.

Generally speaking, the magnetic field can be ideally likened to a light gas (in which the speed of sound is equal to the speed of light). This analogy makes it possible to create a whole series of configurations, in which the magnetic field is compressed, and then the compressed field acts on the body to impart a high velocity to the latter.

It remains to examine the combined systems in which both the gasdynamic and electrodynamic acceleration methods are used.

* In the case of rapid compression of the conducting screen, the magnetic field is not able to penetrate the screen, and therefore the relation $HS = \text{const}$ is satisfied.

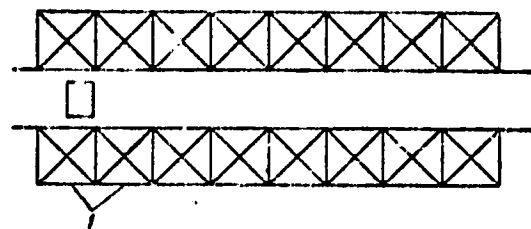


Figure 1.23. Induction accelerator:

1 — coils

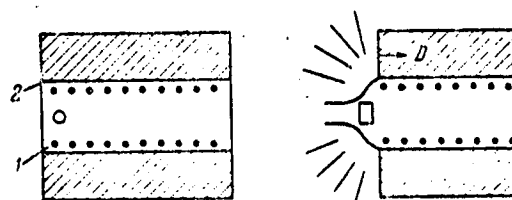


Figure 1.24. Explosive induction accelerator:

1 — solenoid; 2 — conducting screen

The simplest combined accelerator configuration is shown in Figure 1.25. In this launcher, the light gas, heated to high temperature as a result of compression or by an electrical discharge, enters the accelerating barrel. In the barrel, the crossed electromagnetic field acts on the gas (which is thermally ionized, and is therefore a conductor of electricity), and creates the accelerating force:

$$F = j \times H,$$

where j — current density, H — magnetic field intensity. The accelerated gas, in turn, accelerates the body,

since the pressure on the body increases because of the ponderomotive force.

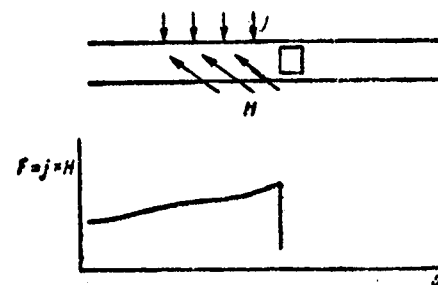


Figure 1.25. Combined-type launcher

The launcher tested in the U.S.A., in which several dischargers installed along the barrel preheat the gas behind the traveling model, is also a combined-type launcher [3].

There are launchers in which the body is first accelerated by an electropulsed device, and is then accelerated by the contact method.

Generally speaking, two-staged nature of the acceleration process is the characteristic feature of the combined-type accelerators, since it is not desirable in principle to accelerate a stationary body by the conventional gasdynamic method and then use electromagnetic forces for further acceleration.

/38

To complete the survey of the high-velocity launchers, we must dwell briefly on still another launcher type, which can be termed the jet launcher.

In all the launchers examined above (except for the induction accelerator) the body being accelerated travels in a barrel or

along rails. However, the body can also be accelerated by placing it in a high-velocity gas stream.

Two jet acceleration methods are basically used.

Explosive method. A small sphere, weighing from a few milligrams up to one gram, is accelerated by a gas flow arising as a result of detonation of a shaped cylindrical explosive charge [17]. The drawbacks of this method are: a) difficulty of its use under laboratory conditions — the explosive weight must exceed the projectile weight by at least 10,000 to 30,000 times; b) reduction of the actual projectile dimension as a result of burning in the jet (ablation); c) difficulties in separating the body from the jet stream.

Microparticle launch velocities up to 20 km/sec and higher have been achieved using the explosive method.

Plasma jet method. A gas heated by an electrical discharge issues through a nozzle, and entrains the microparticles with it. This method makes it possible to accelerate very small particles to speeds of 10 km/sec or higher and, in contrast with the explosive method, can be used under laboratory conditions; however, the drawbacks associated with burning of the body and the difficulties in separating the body from the jet remain (Figure 1.26).

Table 1.2 characterizes the capabilities of the high-velocity launch methods.

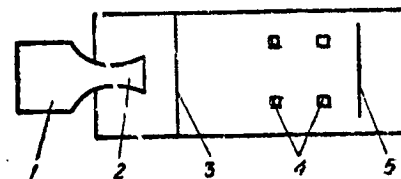


Figure 1.26. Jet launcher:

1 — chamber; 2 — nozzle;
3 — foil on which the particles being launched are placed; 4 — velocity pickups; 5 — target

/39

Practically all the high-velocity launcher schemes described above have been tried out experimentally. Extensive experimental studies have shown that the most promising launchers are: in the launch velocity range 2800 - 4000 m/sec, the launchers with heavy

TABLE 1.2. CHARACTERISTICS OF HIGH-VELOCITY LAUNCHERS

	Launch method	Velocity, m/sec	Body weight, kg
1.	Conventional cannon or rifle [$\omega/q < 0.5^*$)]	800 - 1,000	0.01 - 1,000
2.	Special cannons and antitank guns with light projectile and large charge	2,000 - 2,200**	0.001 - 10
3.	Single-stage gasdynamic launchers:		
	a) using OHM	3,000 - 4,000	0.001 - 0.1
	b) electropulsed	5,000 - 7,000	0.0001 - 0.001
4.	Light-gas launchers with heavy piston and low compression ratio	2,500 - 4,000	0.001 - 2
5.	Light-gas launchers with light piston	6,000 - 8,000	0.001 - 0.5
6.	Light-gas launchers with plastic piston	8,000 - 11,000	0.001 - 0.5
7.	Combined launchers with preheating of the gas by an electrical discharge	10,000 - 12,000	0.001 - 0.01
8.	Combined launchers with electromagnetic acceleration	12,000 - 15,000	0.0001 - 0.01
9.	Jet launchers	20,000 - 60,000	10^{-7} - 10^{-9}

* q — projectile weight; ω — charge weight.

** When firing into an evacuated space or with the barrel evacuated, the velocity achievable is about 2800 m/sec.

piston and low compression ratio; and in the launch velocity range 4000 - 8000 m/sec, the launches with plastic piston and high compression ratio.

§ 1.6. Characteristics of Some High-Velocity Launchers and Features Associated with Their Field of Application

Configurations of various launchers were described above. Now we can turn to specific data on certain typical launchers, and we can also examine the magnitudes of the overall correction coefficient ϕ , determined by comparing the experimental data with the results of calculation using the approximate engineering method presented in Chapter II. /40

Table 1.3 presents the parameters of five U.S.A. launchers, with calibers from 5.6 to 63.5 mm, used to launch bolies weighing from 0.10 to 230 grams, with velocities of 6 - 8 km/sec*.

In principle, all the launchers listed in the table can be used for both aerodynamic studies and high-velocity impact investigations. However, some general remarks should be made. /41

a) In interior ballistics, it is customary to characterize the relative projectile weight by the coefficient C_q , equal to the ratio of the projectile weight to the barrel diameter cubed:

$$C_q = \frac{q}{d^3}.$$

Figure 1.27 shows a curve of launch velocity versus C_q , obtained by correlating a large number of Soviet and foreign experiments.

As a rule, high-velocity collision studies are made using compact metal elements enclosed in sabots made from a light material. Considering that the

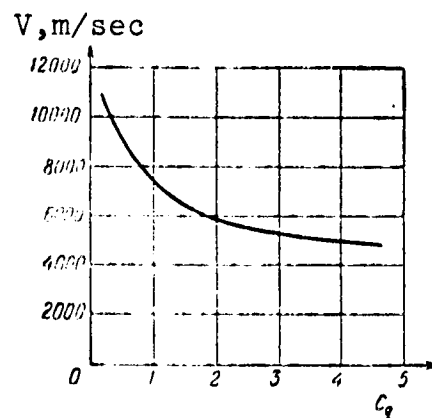


Figure 1.27. Projectile velocity as function of the coefficient C_q

* The maximal velocity was obtained on the NACA launcher, and was 11.2 km/sec for a projectile weighing 0.04 g (polyethylene pellet with $C_q = 0.22$).

TABLE 1.3. PARAMETERS OF SOME U.S.A. HIGH-VELOCITY LAUNCHERS

Parameter	Dimension	Bureau of Mines	AVCO	Arnold Center	NACA
Launcher type:					
Barrel caliber	mm	Heavy piston	Light piston	Light piston	Hydropiston
Barrel length	m	7-10	5.6	12.7	5.6
Gas chamber caliber	mm	1-1.4	0.915	3 - 4	1.2
Gas chamber length	mm	36	22	40.1	20
Charge weight	kg	1.2	1.565	6.3	4.5
Charge chamber diameter	mm	-	0.125	w. OHHM combustn.	0.110
Initial light-gas pressure	atm	-	60	69.8	-
Maximal light-gas pressure	atm	-	40,000	-	4.2
Piston weight	kg	7000	0.019	14,000	8000-10,000
Light-gas expansion ratio	-	0.9-1.8	3.2	6	0.090
Coefficient C_q	g/cm ³	-	1.7	2.6	3.0
Projectile weight	g	2	0.3	0.5	0.6
Ratio m_1/m	-	2	7.5	1.0	0.1
Launch velocity	m/sec	3000-3500	7300	22	5.4
Coefficient ϕ	-	0.8-0.85	0.8-0.85	7800	9200
Hydroeffect	m/sec	-	-	0.8-0.85	0.85
				-	2000-2500
Remarks:	<div>Hydrogen</div> <div>Fyrogen</div> <div>Maximum velocity 11.2 km/sec with $C_q = 0.22$</div>				

element specific weight varies in the range from 2.7 to 18, it is easy to understand the difficulties which arise in attempting to construct a projectile with small C_q .

With barrel caliber 8 - 12 mm, it is usually not possible to obtain a value of C_q less than 1.5 - 2, and this limits the realistically achievable launch velocity to about 6000 - 7000 m/sec.

As the caliber is increased, it becomes easier to construct a strong sabot; however, even with a caliber of about 85 mm, it is difficult to ensure $C_q < 1 - 1.5$, which in turn limits the realistically achievable launch velocity to about 8 km/sec.

In aeroballistic studies, two limiting regions immediately appear:

First, study of the aerodynamic characteristics of models of flight vehicles (airplanes, rockets, spacecraft, and so on). Such models may be fabricated from light weight materials with cavities for reducing the weight. The model dimensions are usually such that launchers of relatively large caliber (50 mm and more) can be used to launch the models. Therefore, a projectile with $C_q \sim 0.8 - 1$ can be constructed for such a study.

Second, study of the flow around bodies of simple form (cone, cylinder, sphere, etc.). In this case, the model is fired without a sabot, and is made of plastic. In such experiments, a realistically achievable value is $C_q \sim 0.2 - 0.6$, and the corresponding launch velocities are 11,000 - 10,000 km/sec.

b) Depending on where the launcher is located, it is sometimes necessary to resolve the question of what energy source to use and what light gas to use.

In the light-gas launchers, use is made of: 1) powder charge; 2) OHIM; 3) powder charge with the addition of a light gas to the chamber; 4) compressed gas (air).

It is most convenient to work with the powder charge, and it is preferred in all cases when permitted by the explosive material working rules.

The OHIM is used only when working with a light piston. Extensive experience has been accumulated in its use in operating shock tubes [38, 39].

As for the choice of the light gas, here again the safety engineering rules are of primary importance. When working in the open air, it is advisable in all cases to use hydrogen, which is less expensive than helium, and provides somewhat higher projectile velocity (on the average, 10% higher).

In enclosed areas, working with hydrogen requires the use of specialized explosion-proof equipment, the availability of gas analyzers, and strict precautionary measures. All this is particularly important when working with large launchers, where the amount of hydrogen per shot exceeds 100 - 200 g*.

In all cases, when operating in an enclosed area, it is best to conduct the first experiments on a new facility using helium, and only after the servicing personnel are familiar with the launcher should the changeover to hydrogen be made.

c) Usually, bodies accelerated by the light-gas launchers are fired into an evacuated space (vacuum range) (Figure 1.28).

The vacuum range objective is entirely different in the case of an aerodynamic experiment and when studying collision processes.

*The explosion hazard limits for a mixture of hydrogen and air are: lower, 1%; upper, 5% (by volume).

In the first case, the facility is intended for determining the aerodynamic characteristics of the model, and the vacuum range plays the primary role. The dimensions of the vacuum range may reach a length of 300 meters or more.

The gas pressure in the range corresponds to the altitude at which it is necessary to determine the model characteristics. More detailed data on the ranges and the equipment for measuring the aerodynamic characteristics are presented in Chapters III and V.

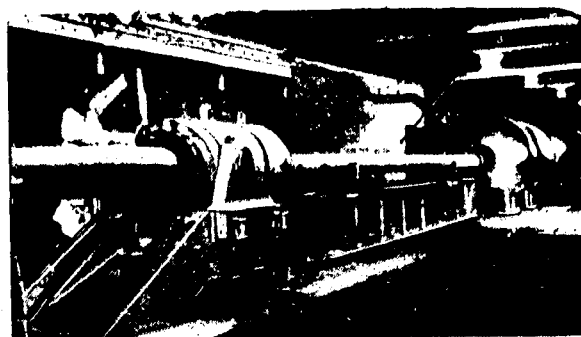


Figure 1.28. LGL with vacuum range

In the case when the launcher is used to study high-velocity impact, the range is of secondary importance, since it is necessary only in order to maintain, to the extent possible, the projectile velocity up to the instant of its encounter with the barrier. In this case, the range dimensions will be minimal, and are determined basically by the capabilities of the instrumentation, whose operation usually requires cutoff of the bases, and also by the distance at which sabot separation takes place, if one is used.

The impact experiment ranges are usually divided into three parts: 1) dump tank — a cylindrical vessel where most of the gas is trapped; 2) tube for measuring the body velocity with windows for the instrumentation; 3) space in which the target is located. In certain cases, if the article (target) being studied has large dimensions, an exit window is made in the end of the tube; this window is covered over by a film, and the article is located in the atmosphere in the immediate vicinity of the end of the range.

The necessity for use of the vacuum range and its dimensions are determined by the launcher caliber. Thus, for large-caliber launchers with projectiles weighing 30 - 100 grams, it is usually

sufficient to evacuate only the launcher barrel, covering the muzzle with a film. In this case, the velocity loss over the 5 - 10 meter distance, which the projectile flies prior to encountering the target, is of the order of hundreds of meters per second, and use of the evacuated range can be avoided.

Conversely, for launchers used to project bodies weighing about one gram, an evacuated range is absolutely necessary.

CHAPTER II

FUNDAMENTALS OF LIGHT-GAS LAUNCHER DESIGN

§ 2.1. Preliminary Remarks

We mentioned previously that light-gas launcher design is a problem of interior ballistics. However, the high velocity launchers have particular features which prevent the use of the well-developed classical ballistics method in their analysis. /44

The primary difference between the high-velocity light-gas launchers and the classical artillery systems is the fact that large launch gas charges are used in the light-gas launchers in order to obtain high velocities, and the ratio of gas charge weight to projectile weight exceeds unity considerably. In this case, wave effects, which are not considered at all in classical ballistics, arise in the barrel bore. We recall that, in the conventional artillery systems, this ratio usually does not exceed 0.1 - 0.3, and the wave effects in the system can be ignored.

The need for light-gas launcher design methods led to rapid development of gasdynamic ballistics, i.e., the branch of interior ballistics in which gasdynamic methods are used.

The gasdynamic methods were first used in ballistics by Lagrange in 1793. From that time, the problem of firing from an artillery piece under the assumption of instantaneous powder combustion has been termed the Lagrange problem.

Figure 2.1 shows a cylindrical tube with a projectile, and also the x, t coordinate plane. At the initial time, the projectile is located at the distance L_c from the breech. The gas pressure in this space is constant, and the space ahead of the body is evacuated.

Assume that projectile movement begins at $t = 0$. At this instant, a rarefaction wave begins to propagate from the base of the projectile through the gas,

and at the time t_I , this wave reaches the breech and is reflected

therefrom. In region 0, the gas is stationary. In region I, the gas travels as if there were no breechblock — this is the simple-wave region in which the gasdynamic equations have a simple solution. Complex, unsteady motion of the gas takes place in regions II, III, and so on.

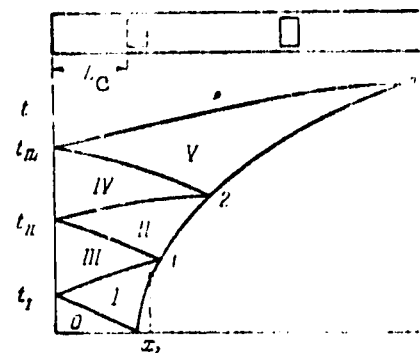


Figure 2.1. Wave system in the Lagrange problem

The gas pressure and velocity vary continuously along the space behind the projectile at each instant of time, and on the lines separating one zone from another there is a break of the pressure or velocity curve (discontinuity of the first derivatives, for example, $\partial p / \partial x$, etc.).

The highest pressure will always be at the breech, then it will decay monotonically to the base of the projectile. The gas velocity at the breech $u = 0$, and the gas velocity at the base of the projectile is always equal to the projectile velocity.

The existence of pressure and velocity variations both in time and along the x coordinate indicates that these quantities are functions of the two variables x and t , and the equations describing them are partial differential equations.

The solution of the Lagrange problem in the entire motion region is accomplished by numerical methods, and obtaining this solution has great theoretical and practical importance. Specifically, the techniques for optimal parameter selection and light-gas launcher analysis are constructed on the basis of this solution.

In fact, firing from single-stage launchers is completely described by the Lagrange problem solution for a cylindrical or "bottle-shaped" (tapered) chamber (depending on the light-gas launcher tube form).

Firing from multistage launchers is also described by the same solution, if we assume that initially (with the projectile stationary), the light gas is compressed and heated to the parameters p_{\max} and T_{\max} , and then firing takes place (with the piston stationary).

Now we can formulate briefly the fundamental difference between high-velocity launcher interior ballistics and classical interior ballistics.

In classical interior ballistics, it is assumed that the gas density is a function only of time, and is constant along the space behind the projectile. Therefore, the interior ballistics equations are ordinary differential equations. The solutions obtained on the basis of these equations cannot, in principle, take into account the wave processes which take place during firing. The classical ballistics methods are applicable when the projectile velocity is considerably less than the sound speed in the launch gas and with long barrel length, since in this case the rarefaction waves can equalize the gas parameters in the space behind the projectile.

/46

In gasdynamic ballistics, we take into account gas parameter dependence on time and position in space; therefore, partial differential equations are used. The gasdynamic methods must be used when the projectile velocity exceeds the average sound speed in the launch gas.

In the following, we shall present gasdynamic launch theory, and our primary attention will be devoted to solution of the Lagrange problem in different variants (for cylindrical or tapered chamber, with backpressure, and so on), and also to solution of questions relating directly to ballistic launchers.

The general questions of unsteady gas motion are not examined here, since they are sufficiently well illuminated in the literature (see, for example, [5, 25, 33, 39]).

§ 2.2. Equation of Gas Motion and Methods of Their Solution

Examining gas motion in a gasdynamic launcher, we must use the equations of axisymmetric gas flow*, which are known to have the form:

equations of motion:

$$\frac{\partial u}{\partial t} + u \frac{\partial u}{\partial x} + v \frac{\partial u}{\partial r} = F_x - \frac{1}{\rho} \frac{\partial p}{\partial x} + \nu \left(\frac{\partial^2 u}{\partial x^2} + \frac{\partial^2 u}{\partial r^2} + \frac{1}{r} \frac{\partial u}{\partial r} \right), \quad (2.1)$$

$$\frac{\partial v}{\partial t} + u \frac{\partial v}{\partial x} + v \frac{\partial v}{\partial r} = F_r - \frac{1}{\rho} \frac{\partial p}{\partial r} + \nu \left(\frac{\partial^2 v}{\partial x^2} + \frac{\partial^2 v}{\partial r^2} + \frac{v}{r^2} \right); \quad (2.2)$$

continuity equation

$$\frac{\partial \rho}{\partial t} + u \frac{\partial \rho}{\partial x} + v \frac{\partial \rho}{\partial r} + \rho \left(\frac{\partial u}{\partial x} + \frac{\partial v}{\partial r} \right) + \frac{\rho v}{r} = 0 \quad (2.3)$$

or:

$$\frac{1}{\rho} \frac{d\rho}{dt} = - \frac{\partial u}{\partial x} - \frac{\partial v}{\partial r} - \frac{v}{r}. \quad (2.4)$$

In these equations: u — velocity component along the x axis (along the channel); v — velocity component along the r axis (along the radius); F_x and F_r — force components along the corresponding axes; ν — kinematic viscosity.

* It is obvious that conditions in the light-gas launcher do not lead to rotational motion of the gas, and therefore only the velocity components along the channel radius and length will be nonzero.

To these equations, we must add the energy equation, which, in the general case, has the form:

$$dQ = dE + p dW,$$

where $W = 1/\rho$ — specific volume, and the equation of state, which, in the general case, may be written in the form:

$$\Psi(p, \rho, T) = 0.$$

In addition, the relation must be known:

$$E = E(\rho, p, T),$$

where E — gas internal energy. These functions must be given in explicit form.

The solution of interior ballistics problems using this system of equations requires a tremendous volume of calculations.

The system of equations presented above can be simplified somewhat.

First, the entire vast gasdynamics experience shows that the gas viscosity influences the gas flow only in a very thin boundary layer, where the gas is close to the walls. Study of gas motion in the boundary layer is best made using special methods (the flow in the boundary layer influences basically processes such as heat transfer, for example). Therefore, in order to simplify the problem formulation, it is advisable to examine the motion of an inviscid gas, i.e., take $\nu = 0$.

Second, it is found that the gas dissociation and ionization processes can be taken into account approximately by selecting an effective value of the exponent κ , and therefore the energy equation can be written in the form [5]:

$$\frac{dp}{dt} - \frac{\kappa p}{\rho} \frac{d\rho}{dt} = (\kappa - 1) p \frac{dQ}{dt}, \quad (2.5)$$

coinciding with the energy equation for an ideal gas*.

In this formula, Q characterizes the heat addition to the gas. The function $Q = Q(x, r, t)$ is specified in advance (combustion, electrical discharge), or is obtained from additional conditions — for example, when Q considers heat transfer.

In the adiabatic flow case,

$$Q \equiv 0.$$

Unfortunately, these two simplifications still require solution of a system of partial differential equations depending on three unknown variables x, t, r , which involves extremely complicated calculations.

/48

Essential for further simplification of the basic system of equations is the fact that the motion in ballistic launchers takes place in a channel of cylindrical form, but with one or more transitions from one diameter to another; however, the primary motion is that in a channel of constant diameter.

Consequently, it is best to convert to a system of equations in which there are only two variables — linear coordinate x and time t ; in the first approximation, we can neglect the variation of the quantities along the tube radius.

In this case, the equations of motion, continuity, and energy will have the form:

$$\frac{\partial u}{\partial t} + u \frac{\partial u}{\partial x} = -\frac{1}{\rho} \frac{\partial p}{\partial x}, \quad (2.6)$$

$$\frac{\partial \rho}{\partial t} + u \frac{\partial \rho}{\partial x} + \rho \frac{\partial u}{\partial x} + u \rho \frac{d \ln S}{dx} = 0, \quad (2.7)$$

$$\frac{dp}{dt} + \kappa p \left(\frac{\partial u}{\partial x} + u \frac{d \ln S}{dx} \right) = (\kappa - 1) \rho \frac{dQ}{dt}, \quad (2.8)$$

where $S(x)$ — variable channel area.

* In this case, κ is the polytropic exponent for the considered gas.

In order to clarify what assumptions are used in this system, we need only compare these equations with the equations for axisymmetric motion ($v = 0$ in both systems, and there are no external forces: $F \equiv 0$).

The equation of motion (2.6) is obtained from (2.1) and (2.2), if we assume that:

$$v^2 \ll u. \quad (2.9)$$

The continuity equation (2.7) is obtained from (2.3), when the condition (2.9) is satisfied and the quantity:

$$\frac{\partial p}{\partial r} \sim 0 \quad (2.10)$$

and, in addition,

$$p \left(\frac{\partial v}{\partial r} + \frac{v}{r} \right) \sim \rho n \frac{d \ln S}{dx}. \quad (2.11)$$

Condition (2.10) follows directly from Condition (2.9) and Equation (2.2), since in this equation, the left side and the term in parentheses are equal to zero.

Therefore,

$$\frac{\partial p}{\partial r} \sim 0,$$

and since $p \sim \rho$,

$$\frac{\partial p}{\partial r} \sim 0.$$

Now let us turn to Condition (2.11). For the tube of variable cross section:

$$S(x) = \pi r^2(x)$$

and

$$\frac{d \ln S}{dx} = \frac{1}{S} \frac{dS}{dx} = \frac{2}{r} \frac{dr}{dx},$$

consequently,

$$\frac{\partial v}{\partial r} + \frac{v}{r} \sim \frac{2u}{r} \frac{dr}{dx},$$

where

$$\frac{dr}{dx} = \operatorname{tg} \delta$$

(δ is the taper angle of the variable-section tube segment).

Assuming that:

$$\frac{\partial v}{\partial r} \sim \frac{v}{r},$$

we find that:

$$\frac{2v}{r} \approx \frac{2u}{r} \operatorname{tg} \delta,$$

hence,

$$v \approx u \operatorname{tg} \delta. \quad (2.12)$$

Condition (2.12) shows that for (2.9) to be satisfied, it is necessary that the slope of the variable section region be small.

Calculations show that the taper angle should not exceed 10 - 15°, if velocity determination accuracy of the order of 1 - 2% is required.

However, use of the one-dimensional unsteady motion equations in the light-gas launcher case is possible, even with considerably larger taper angles. The reason is that the variable-section segments occupy only very small zones (a few percent, as a rule) in the flow region; therefore, even a large error in the calculations for these segments (10 - 20%) leads to comparatively small error in the final results.

We note that in some launchers, the transition from the light-gas chamber to the barrel is very abrupt, sometimes even a step. In this case, we must formally use (2.1 - 2.4). However it will be shown later that this form of transition is not suitable*.

* Moreover, in this region, there arises a stagnant zone, creating a "liquid cone", which smooths the transition from one diameter to another.

Thus, in the following, we shall use the system of equations (2.6 - 2.8), describing one-dimensional unsteady ideal gas flow; but even in this form the gasdynamic equations are incomparably more complex than the classical interior ballistics equations. These equations must be solved with the corresponding initial and boundary conditions.

Specifically, at the stationary wall:

$$u \equiv 0.$$

At the piston, $u = V_p$ (V_p — piston velocity), and the equation of piston motion can be written in the form:

$$m_p \frac{dV_p}{dt} = S(p_l - p_r),$$

where S — section area; and p_l and p_r are the pressures to the left and right of the piston.

It is usually more convenient to introduce, in place of the sought functions u , p , ρ , the functions u , a , Φ , where a — sound speed in the gas, and Φ — entropy function.

In this case, the equation takes the form:

$$\left. \begin{aligned} \frac{\partial u}{\partial t} + u \frac{\partial u}{\partial x} + \frac{2a}{\kappa - 1} \frac{\partial a}{\partial x} &= \frac{a^2}{\kappa(\kappa - 1)} \frac{\partial \ln \Phi}{\partial x}, \\ \frac{\partial a}{\partial t} + u \frac{\partial a}{\partial x} + \frac{\kappa - 1}{2} a \left(\frac{\partial u}{\partial x} + u \frac{\partial \ln S}{\partial x} \right) &= \frac{a}{2} \frac{d \ln \Phi}{dt}, \\ \Phi &= \Phi_0 e^{\frac{\kappa(\kappa - 1)}{2} \int \frac{dQ}{x^2}}. \end{aligned} \right\} \quad (2.13)$$

Now, we can turn to a brief overview of the methods for solving these equations.

1) Exact analytic solution. The exact analytic solution of the equations of one-dimensional motion can be obtained for the simple-wave case, i.e., for the case in which one family of characteristics is rectilinear [5]. In the Lagrange problem, this

situation is realized in region I (Figure 2.1), when the gas is ideal and the tube is cylindrical with constant section.

In this case, (2.13) takes the form:

451

$$\left. \begin{aligned} \frac{\partial u}{\partial t} + u \frac{\partial u}{\partial x} + \frac{2a}{x-1} \frac{\partial a}{\partial x} &= 0, \\ \frac{\partial a}{\partial t} + u \frac{\partial a}{\partial x} + \frac{x-1}{2} a \frac{\partial u}{\partial x} &= 0, \\ \Phi &= \Phi_0 = \text{const}, \end{aligned} \right\}$$

the body velocity in the simple-wave region:

$$V = \frac{2a_0}{x-1} \left\{ 1 - \left[\frac{S p_0 t}{m a_0} \frac{x+1}{2} + 1 \right]^{-(x-1)/(x+1)} \right\},$$

the body coordinate

$$x = L_c + \frac{2a_0}{x-1} \left\{ t + \frac{m a_0}{p_0 S} \left[1 - \left(\frac{x+1}{2a_0} \frac{S p_0 t}{m} + 1 \right)^{2/(x+1)} \right] \right\}.$$

In these formulas, a_0 — initial sound speed; m — body mass; p_0 — initial pressure; S — tube area.

It is not difficult to reduce the formulas for the body velocity and coordinate to dimensionless form, introducing dimensionless time:

$$\tau = \frac{a_0 t}{L_c}$$

and launch gas mass:

$$m_1 = \rho_0 S L_c = \frac{x p_0}{a_0^2} L_c S.$$

After elementary transformations, we find:

$$\frac{V}{a_0} = \mathcal{V} = \frac{2}{x-1} \left[1 - \left(\frac{x+1}{2} \Pi \tau + 1 \right)^{-(x-1)/(x+1)} \right], \quad (2.14)$$

$$\frac{x}{L_c} = x = 1 + \frac{2}{x-1} \left\{ \tau + \frac{x}{\Pi} \left[1 - \left(\frac{x+1}{2} \Pi \tau + 1 \right)^{2/(x+1)} \right] \right\}. \quad (2.15)$$

This solution is valid only up to the point x_1 (Figure 2.1), for which:

$$\tau_1 = 2 + \frac{x+1}{2x} \Pi, \quad \Pi = \frac{m_1}{m}. \quad (2.16)$$

We once again emphasize that this solution is applicable for a cylindrical tube only in the case when there is no heat input, i.e., when $Q = 0$.

We see from these formulas that the problem solution in the simple-wave case depends only on the parameters Π and κ . It will be shown later that this is characteristic also for the complete solution of the Lagrange problem in the cylindrical tube case for $Q = 0$ and $S = \text{const}$ (in the entire motion region). /52

Tables 2.1 - 2.3 present some results of calculations made using these formulas.

We should note one characteristic feature. In the limit as $\Pi \rightarrow \infty$, the simple-wave solution is valid for the entire tube, and it follows from (2.14) that, in this case,

$$V_{\text{lim}} = \frac{2}{\kappa - 1} a_0.$$

For $\kappa = 1.4$, $V_{\text{lim}} = 5a_0$, i.e., a very light projectile can be accelerated to a velocity exceeding the sound speed by $2/(\kappa - 1)$ times.

Classical ballistics yields for the case the limiting velocity ($\eta = 1$, $\kappa = 1.4$):

$$V_{\text{lim}} = a_0 \sqrt{\frac{6}{\kappa(\kappa - 1)}} = 3.25a_0,$$

which follows directly from (1.2) for $b_1 = 1/3$.

There is still another property of the simple wave which is important for the further analysis. In the zone of motion, there is some section x_1 (Figure 2.1) with the coordinate

$$x_1 = \frac{z_1}{l_0} = 1 + \frac{2\kappa}{\kappa + 1} \frac{1}{\Pi},$$

at which the gas velocity is equal to the sound speed in the course of the entire time until the wave reflected from the wall reaches this section:

$$u_1 = a_1.$$

LAGRANGE PROBLEM SOLUTION IN THE
SIMPLE-WAVE CASE

TABLE 2.1 *

$\kappa = 1,22$

τ	$m_1/m = 0.5; \quad \tau_1 = 2,455$		$m_1/m = 1; \quad \tau_1 = 2,90984$		$m_1/m = 2; \quad \tau_1 = 3,8197$	
	$s-1$	γ	$s-1$	γ	$s-1$	γ
1	0,15	0,33	0,31	0,56	0,52	0,88
2	0,63	0,56	1,05	0,88	1,62	1,28
3	1,29	0,74	2,06	1,11	3,04	1,52
4	2,09	0,83	3,26	1,28	4,67	1,71
5	3,04	1,00	4,62	1,42	4,45	1,86
6	4,12	1,11	6,08	1,52	8,38	1,98
7	5,27	1,20	7,68	1,63	10,45	2,07
8	6,51	1,28	9,35	1,71	12,56	2,16
10	9,26	1,42	12,92	1,86	17,04	2,31
12	12,17	1,52	16,77	1,98	21,8	2,42
14	14,36	1,63	20,91	2,07		
16	18,70	1,71				
τ	$m_1/m = 4; \quad \tau_1 = 5,6331$		$m_1/m = 8; \quad \tau_1 = 9,2787$		$m_1/m = 12; \quad \tau_1 = 12,9131$	
	$s-1$	γ	$s-1$	γ	$s-1$	γ
1	0,81	1,28	1,16	1,71	1,39	1,98
2	2,33	1,71	3,13	2,16	3,63	2,42
3	4,19	1,93	5,45	2,42	6,19	2,67
4	6,28	2,16	7,95	2,60	8,95	2,84
5	8,52	2,31	10,64	2,74	11,14	2,98
6	10,90	2,42	13,42	2,84	14,92	3,09
7	13,34	2,52	16,32	2,94	18,06	3,18
8	15,91	2,60	19,32	3,02	21,28	3,26
10	21,29	2,74				

* Translator's note. Commas in numbers represent decimal points.

TABLE 2.2*
n=1,4

τ	$m_1/m = 0.5; \tau_1 = 2.1298$		$m_1/m = 1; \tau_1 = 2.857$		$m_1/m = 2; \tau_1 = 3.7142$	
	$s-1$	γ	$s-1$	γ	$s-1$	γ
1	0.14	0.28	0.27	0.49	0.45	0.76
2	0.55	0.49	0.91	0.76	1.41	1.09
3	1.11	0.64	1.78	1.95	2.61	1.30
4	1.82	0.76	2.81	1.09	3.99	1.45
5	2.65	0.86	3.96	1.21	5.51	1.56
6	3.6	0.95	5.23	1.30	7.14	1.66
7	4.55	1.03	6.58	1.38	8.85	1.73
8	5.52	1.09	7.99	1.45	10.61	1.80
9	7		9.48	1.51	12.45	1.86
10	7.93	1.21	11.05	1.56	14.33	1.91
12	10.45	1.30	14.29	1.66	18.28	2.00
14	13.16	1.38	17.69	1.73		
16	15.99	1.45				
τ	$m_1/m = 4; \tau_1 = 5.4286$		$m_1/m = 8; \tau_1 = 8.8568$		$m_1/m = 12; \tau_1 = 12.365$	
	$s-1$	γ	$s-1$	γ	$s-1$	γ
1	0.70	1.09	0.99	1.45	1.19	1.66
2	1.99	1.45	2.65	1.8	3.04	2.02
3	3.57	1.66	4.57	2.02	5.15	2.19
4	5.3	1.8	6.63	2.13	7.41	2.32
5	7.17	1.91	8.84	2.24	9.77	2.41
6	9.14	2.00	11.11	2.32	12.23	2.49
7	11.16	2.07	13.47	2.38	14.75	2.55
8	13.26	2.13	15.88	2.44	17.34	2.60
9	15.46	2.19	18.33	2.49		
10	17.68	2.21	20.86	2.53		
12	22.23	2.32				

*Translator's note.

Commas in numbers represent decimal points.

TABLE 2.3*
n=1,67

τ	$m_1/m = 0.5; \tau_1 = 2.3007$		$m_1/m = 1; \tau_1 = 2.7394$		$m_1/m = 2; \tau_1 = 3.5388$	
	$s-1$	γ	$s-1$	γ	$s-1$	γ
1	0.13	0.24	0.23	0.40	0.38	0.63
2	0.46	0.40	0.76	0.63	1.16	0.90
3	0.93	0.53	1.47	0.78	2.14	0.95
4	1.52	0.63	2.33	0.90	3.27	1.17
5	2.20	0.71	3.27	0.99	4.49	1.26
6	2.95	0.78	4.29	1.06	5.8	1.33
7	3.77	0.84	5.39	1.12	7.16	1.38
8	4.65	0.90	6.55	1.17	8.57	1.43
10	6.55	0.99	8.99	1.26	11.53	1.51
12	8.59	1.06	11.60	1.33	14.64	1.58
14	10.79	1.12	14.33	1.38	17.86	1.63
16	13.1	1.17	17.15	1.43	21.16	1.67
20	17.99	1.26				
τ	$m_1/m = 4; \tau_1 = 5.976$		$m_1/m = 8; \tau_1 = 8.3852$		$m_1/m = 12; \tau_1 = 11.5228$	
	$s-1$	γ	$s-1$	γ	$s-1$	γ
1	0.58	0.90	0.81	1.17	0.96	1.33
2	1.63	1.47	2.14	1.43	2.44	1.58
3	2.9	1.33	3.66	1.56	4.09	1.71
4	4.28	1.43	5.29	1.67	5.85	1.79
5	5.71	1.51	6.99	1.74	7.68	1.86
6	7.32	1.58	8.77	1.79	9.56	1.91
7	8.93	1.63	10.59	1.84	11.5	1.95
8	10.58	1.67	12.45	1.87	13.79	1.97
10	13.99	1.74	16.27	1.93	17.48	2.03
12	17.55	1.79	20.68	1.97		

Therefore the characteristic of the second family is directed vertically at this section.

Actually, at this section,

$$\frac{dx_I}{dt} = u_I - a_I = 0.$$

At this section:

$$a_I = \frac{2}{\kappa + 1} a_0,$$

and, consequently, the pressure and density at this section:

$$p_I = p_0 \left(\frac{2}{\kappa + 1} \right)^{\frac{2\kappa}{\kappa - 1}},$$

$$\rho_I = \rho_0 \left(\frac{2}{\kappa + 1} \right)^{\frac{2(\kappa + 1)}{\kappa - 1}}.$$

The dependence of p_I/p_0 on κ for this section is characterized by the data presented in Table 2.4. /56

TABLE 2.4

κ	1,67	1,4	1,22
p_I/p_0	0,24	0,27	0,32

It is obvious that the pressure at this section will decrease after arrival of the reflected wave. Consequently, even at a small distance from the point of projectile motion initiation, the pressure becomes lower by several times than the initial pressure in the chamber.

Since section I is stationary and the gas density, pressure, and velocity at this section are constant, the gas flowrate through this section is also constant. In this sense, this section is analogous to the nozzle throat in stationary flow. However, all this is valid only until the reflected wave reaches section I.

One important consequence follows from this analysis. In practice, the quantity Π in the light-gas launchers lies in the range 2 - 10, and consequently the value of x_I is approximately equal to $(0.1 - 0.5) L_c$. In other words, when the projectile has traveled

along the barrel only a fraction of the initial chamber length, the pressure on its base decreases by a factor of 3 - 4. This permits making the launcher barrels considerably less strong than the fore-chambers. We shall examine this situation in more detail later.

2) Numerical solutions [7, 46, 47]. The solution of an equation in partial derivatives of two independent variables is a surface in three-dimensional space (Figure 2.2). The solution of a system of such equations is several surfaces in the same space. In the case of the hyperbolic equations which describe one-dimensional unsteady gas motion, for solution of the problem, it is necessary to construct the solution (i.e., the surface) which satisfies the initial conditions (passes through the given curve) and the boundary conditions.

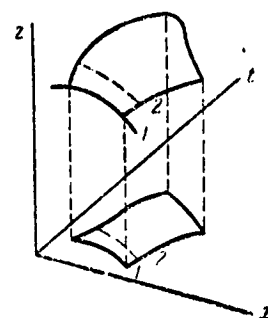


Figure 2.2. Geometric interpretation of partial differential equation solution

It is easiest to represent the numerical solution construction process as follows.

The curve 1 is specified by the initial conditions. With the aid of the differential equation, we find the derivatives of the sought function along the axes x and t : $\partial z/\partial x$ and $\partial z/\partial t$. Since these derivatives are the slopes of the tangent plane to the sought surface, it is now easy to construct the tangent plane elements, and convert from line 1 to line 2. Then we determine the slopes at the points of line 2, and so on. As the result, the sought surface is constructed from the tangent plane elements, and a grid (Figure 2.3) appears on the x, t plane.

Generally speaking, the more dense the grid, the more exactly the sought integral surface will be represented. However, this is not always so. In certain cases, the solution begins to "oscillate", and this "oscillation" may not decrease with reduction of the step size. An example of "oscillation" is shown in Figure 2.4a. We see from the figure that the velocity changes sharply from point to

point, and the amplitude of these changes increases. The scheme is unstable.

In certain cases, another difficulty arises — the numerical solution begins to deviate markedly from the true solution. This usually occurs when the formulas for determining the derivatives approximate the equation poorly (Figure 2.4b). In certain cases, it may be that the computational scheme (or initial conditions) are selected so that the slight change of the initial conditions leads to marked change of the solution (Figure 2.4c). In these cases, we speak of an incorrect scheme.

More detailed data on the numerical solutions and correct problem formulation can be found in the specialized literature [46 - 48].

a) Grid method. In solving the problem by the grid method, we select some grid — for example, a cross — in the plane of the sought variables x and t (Figure 2.5c).

Then, we write formulas which approximate with definite degree of accuracy the sought functions and their derivatives at the grid nodes, program the formulas, and make the calculation.

The primary advantage of the grid method is complete formalization of the calculation. The grid is independent of the gasdynamic

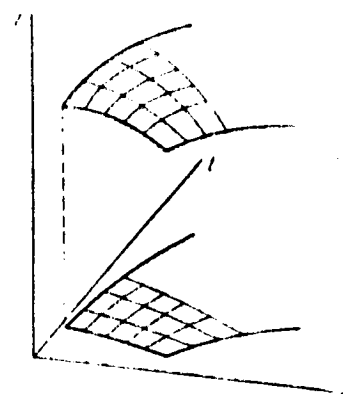


Figure 2.3. Construction of numerical solution

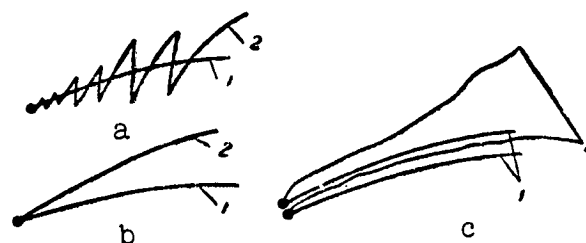


Figure 2.4. Forms of possible errors: 1 — true solution; 2 — numerical solution

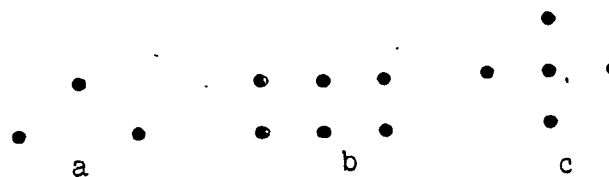


Figure 2.5. Grid types

nature of the problem. As a result, the computational program is comparatively simple.

But this advantage of the grid method is also its weakness: problems with shock waves, contact discontinuities, centered rarefaction waves, and so on, are difficult to compute using this method, since the grid is not designed to follow the subtleties of the gasdynamic solution.

In these cases, we must complicate the scheme by deforming the grid, introducing artificial viscosity, and so on, which complicates the calculation and reduces the accuracy [46].

/58

b) Method of characteristics [25, 48]. In the method of characteristics, we use for the numerical computation a special characteristic grid, formed by the intersection of two families of characteristics.

The intimate connection between the characteristic grid and the physical interpretation of the equations leads to a situation in which the method of characteristics permits following very precisely all the motion phenomena — representing those subtleties which are "smeared out" in the other methods.

The drawback of the method of characteristics is the complexity of the computational program, since it is necessary to consider all the specific features of the problem — appearance of shock waves, contact discontinuities, and so on.

A whole series of standard programs has now been developed for electronic computers of various types. These programs permit complete solution of any problem associated with gasdynamic launcher calculations, for which we need only formulate the general master program, which includes the standard program as component elements.

The master program compilation details are presented in specialized studies (see, for example, [7]).

/59

We note that use of these programs requires a highly qualified programmer and quite large volume of computational work. Because of the high cost and long time involved in the exact gasdynamic calculation, at the present stage of development such a calculation should be considered a reference, verification calculation which is performed when "feeling out" the launcher capabilities and preliminary selection of the variants have already been completed.

How should this preliminary selection be made? We can find two approach

1. We can start with the simpler classical interior ballistics equations, introducing into them certain changes and refinements which may be taken from analysis of the gasdynamic calculation data.

The drawback of this approach is the necessity for using numerical calculations, which are naturally considerably less tedious than the solution of the gasdynamic equations, but still require several days of computer time.

2. We can take as the basis of the calculation, the exact solution of the gasdynamic equations, and take the remaining factors into account by a series of coefficients.

The coefficients themselves must be determined from several comparisons of the exact complete particular problem solution with the selected solution.

In the following, we shall develop this second approach. The launch velocity from the gasdynamic ballistic launcher can be represented in the form [see (1.6)]:

$$V = V_1 + \varphi_1 \varphi_2 \varphi_3 a_0 / f(\Pi, x, x). \quad (2.17)$$

In this equation, a_0 — initial sound speed in the light launch gas, $f(\Pi, x, x)$ — complete numerical solution of the Lagrange problem for an ideal gas and tube of constant section; \bar{x} — relative piston coordinate.

This solution was obtained in 1960. Detailed data for this solution are presented in Figures 2.7 - 2.9.

The coefficients ϕ_1 take into account the chamber shape, gas real properties, thermal and friction losses, individual launcher characteristics (for example, piston displacement, and so on).

Data on these coefficients will be presented later.

In concluding this section, we should make some remarks on the complexity of the computational operations using electronic computers.

Numerical solution of complex problems on electronic computers is now termed mathematical experimentation. This term reflects quite /60 accurately the essence of the matter. Actually, the investigator must first formulate the mathematical solution scheme (algorithm), program this algorithm for calculation on the specific computer, and then debug the program.

In the debugging process, it is necessary to identify and eliminate:

- a) technical errors made in the programming process;
- b) possible systematic errors which lead to oscillation of the solution, etc;
- c) possible fundamental errors which lead to obtaining a smooth but erroneous result.

Therefore, the investigator must continually seek techniques for monitoring the solution by some method which is not associated with the solution algorithm used in the program, and must analyze the results during the computation process.

In this connection, two specialists usually participate in the program solution: a gasdynamicist, and a mathematician.

§ 2.3. Numerical Solution of the Lagrange Problem for Various Cases

Figure 2.6 shows the general scheme of single-stage and two-stage launchers.

The simplest computational variant is the calculation of the motion in the single-stage launcher in which the chamber section is equal to the barrel section:

$$S = s.$$

This problem is termed the Lagrange problem for a cylindrical tube.

More complex is the variant of the solution of the same problem when:

$$S \neq s.$$

This is the Lagrange problem for a tube of variable section.

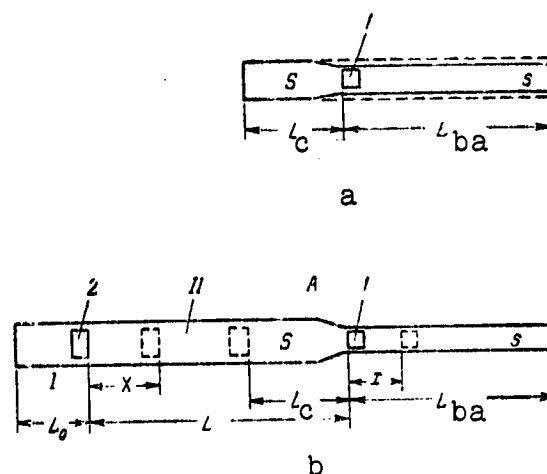


Figure 2.6. Ballistic launchers: a) single-stage; b) two-stage

It is obvious that we must resort to the solution of this same problem if we assume that the piston which compresses the light gas initially occupies its extreme position (L_c in Figure 2.6) with the projectile stationary, and then (with the piston stationary) firing takes place.

a) Numerical solution for cylindrical tube. We have mentioned previously that the solution of the Lagrange problem is of fundamental importance in gasdynamic launching theory, since it makes it possible to clarify all the physical laws governing one-dimensional unsteady gas motion.

In the cylindrical tube case, the solution of the Lagrange problem depends on the adiabatic exponent κ , and on the ratio of projectile mass m to gas mass m_1 . The complete numerical solution of this problem for three values of $\kappa = 1.4, 1.22$, and 1.67 in the range $m_1/m = 1 - 10$, was obtained in 1960, and published in [8]. The solution was made using the method of characteristics.

Considering the fact that this solution is complete, and tables have been compiled for it, it is desirable to use it as the basis for ballistic launcher analysis. Therefore, it should be examined in considerable detail.

Figures 2.7 - 2.9 show the dimensionless body velocity \bar{V} as a function of the dimensionless coordinate \bar{x} for various values of κ and $\Pi = m_1/m$.

We see from the figures that the velocity variation becomes slight, even for $\bar{x} \sim 18 - 20$.

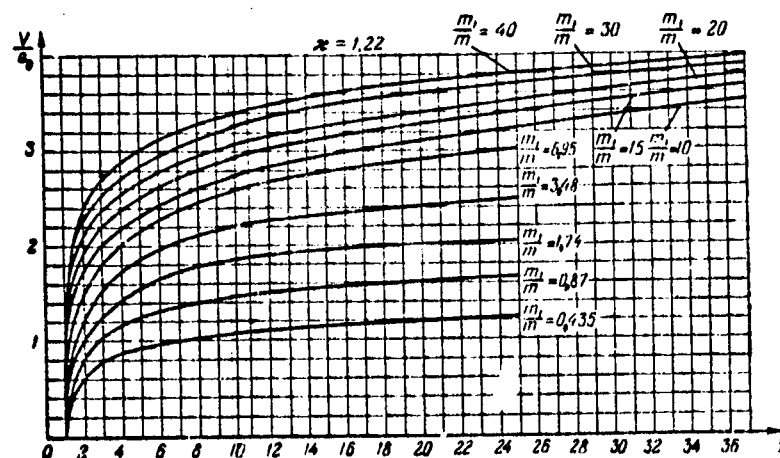


Figure 2.7. Solution of the Lagrange problem for cylindrical tube

Figure 2.10 shows the results of calculation of the gas velocity and sound velocity distribution along the chamber at various moments of time. We see that the velocity distribution is nearly linear, i.e., in the cylindrical tube case, the assumption of

interior ballistics on linear velocity distribution agrees comparatively well with reality. However, the pressure varies markedly along the chamber (in contrast with the assumptions of classical ballistics).

The weak variation of the sound speed along the chamber in spite of the marked pressure reduction is explained by the fact that the density decreases along with the pressure reduction, and the sound speed:

$$a \sim \sqrt{\frac{p}{\rho}}.$$

Figure 2.11 shows the dependence on \bar{x} of the coefficient ψ , characterizing the ratio of the projectile base pressure to the barrel breech pressure:

$$\psi = \frac{p_{pr}}{p_c}.$$

In this same figure, the dashed lines show the results obtained using the classical ballistics formula. We see from the figure that there is no agreement in this case.

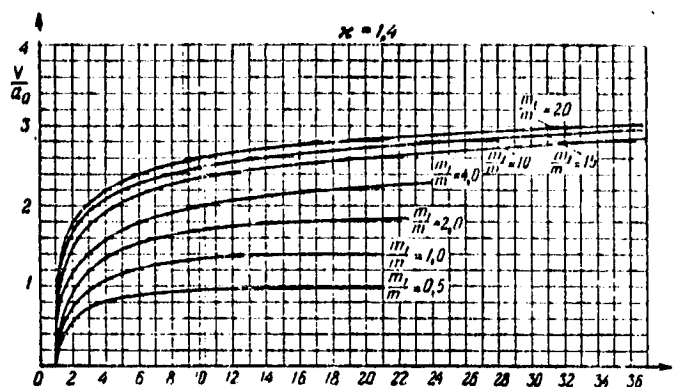


Figure 2.8. Solution of the Lagrange problem for cylindrical tube

/63

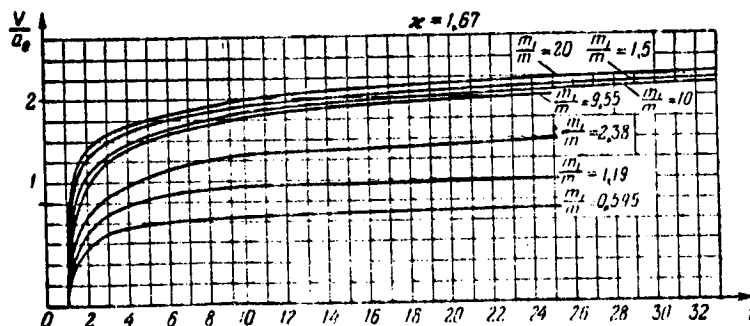


Figure 2.9. Solution of the Lagrange problem for cylindrical tube

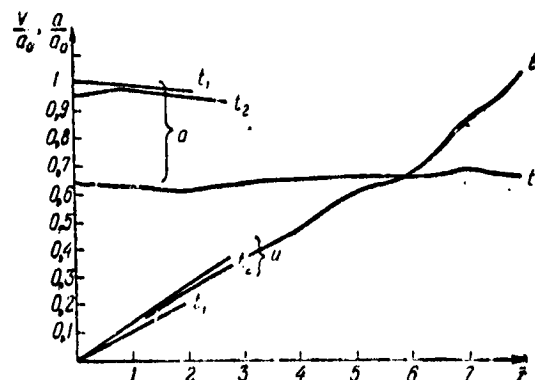


Figure 2.10. Distribution of gas parameters along chamber in the Lagrange problem

/64

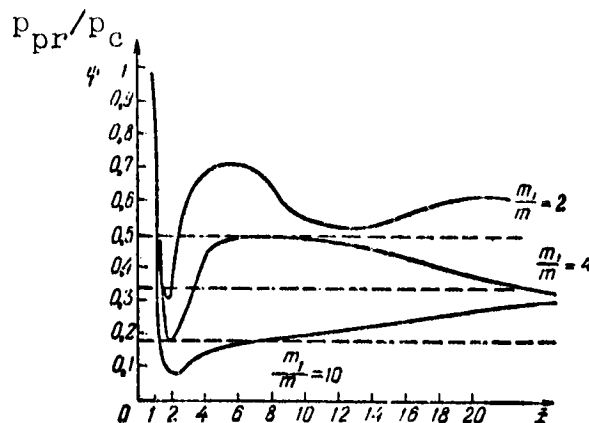


Figure 2.11 Variation of ratio of projectile base pressure to breech pressure with time

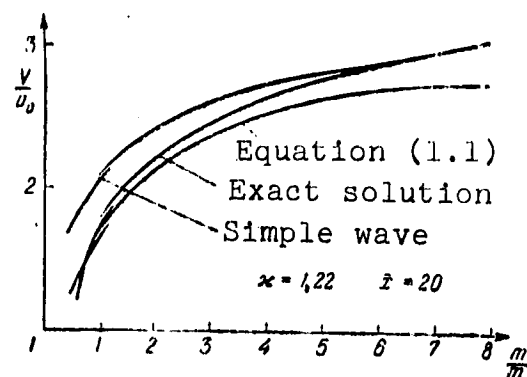


Figure 2.12. Comparison of various solutions of the Lagrange problem

Figure 2.12 compares three formulas: exact numerical solution, simple-wave formula, and approximate ballistic solution [Formula (1.1)]. The curves are plotted for $\kappa = 1.22$ and $\bar{x} = 20$.

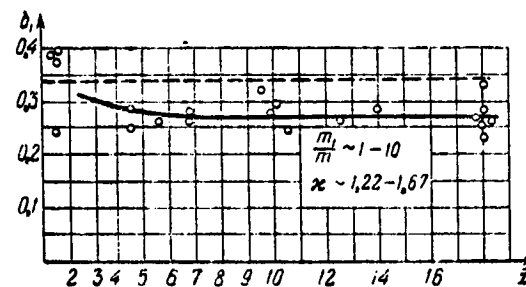


Figure 2.13. Approximation coefficient b_1

Figure 2.13 shows the coefficient b_1 , which is defined so that

the ballistic solution (1.1) will coincide with the exact gasdynamic solution. The comparatively small discrepancy between the exact solution and (1.1) makes it possible to approximate the exact solution by (1.1), with replacement of the coefficient $b_1 = 0.33^*$ by the coefficient $0.28 - 0.26$ in the range $\Pi \sim 1 - 10$ for $\bar{x} \sim 3$ and above.

The existence of this approximation permits making some analytic studies of the extremal launcher regimes.

We mentioned previously that this solution was obtained by the numerical method, and therefore it is necessary, in principle, to justify the possibility of its use.

* Which is used in classical interior ballistics — dashed line in Figure 2.13.

Analysis of the solution accuracy was made by comparing the numerical solution with the analytic simple-wave solution. This comparison showed that the numerical solution yields an error not exceeding one percent.

b) Numerical solution for tube of variable section ($Q = 0$). The system of equations (2.13) for this case has the form (see Figure 2.14):

$$\left. \begin{aligned} \frac{\partial u}{\partial t} + u \frac{\partial u}{\partial x} + \frac{2a}{x-1} \frac{\partial a}{\partial x} &= 0, \\ \frac{\partial a}{\partial t} + u \frac{\partial a}{\partial x} + a \frac{x-1}{2} \left(\frac{\partial u}{\partial x} + u \frac{d \ln S}{dx} \right) &= 0, \\ \Phi = \Phi_0 = \text{const} \end{aligned} \right\} \quad (2.18)$$

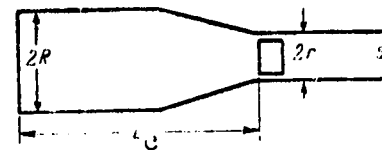


Figure 2.14. Notations adopted for tube of variable section

If we introduce the dimensionless coordinates:

$$\xi = \frac{x}{L_0}, \quad \tau = \frac{tu_0}{L_0}$$

and correspondingly represent the sought functions in dimensionless form:

$$U = \frac{u}{a_0}, \quad A = \frac{a}{a_0},$$

and also specify the chamber profile by the equation:

$$\frac{r}{L_0} = R(\xi),$$

then, (2.18) can be written as:

$$\left. \begin{aligned} \frac{\partial U}{\partial \tau} + U \frac{\partial U}{\partial \xi} + \frac{2A}{x-1} \frac{\partial A}{\partial \xi} &= 0, \\ \frac{\partial A}{\partial \tau} + U \frac{\partial A}{\partial \xi} + \frac{x-1}{2} A \left(\frac{\partial U}{\partial \xi} + 2U \frac{d \ln R(\xi)}{d \xi} \right) &= 0. \end{aligned} \right\}$$

It remains to transform the boundary condition at the piston. The equation of piston motion:

$$m \frac{dV}{dt} = sp, \quad \text{where} \quad p = \bar{p} \cdot p_0,$$

may be written as:

$$m \frac{d(Vu_0)}{d\left(\frac{\tau L_0}{a_0}\right)} = sp_0 \bar{p},$$

hence,

$$\frac{dV}{d\tau} = \frac{s p_0 L_c}{m a_0^2} = \frac{s L_c p_0 \bar{p}}{m \kappa}$$

where $a_0^2 = \frac{s p_0}{\rho_0}$.

The chamber volume can obviously be represented in the form:

$$W_c = b S L_c,$$

where b is a numerical coefficient (for a cylinder, $b = 1$); therefore, we can write:

$$s L_c p_0 = \frac{s}{S} \frac{W_c}{b} p_0 = m_1 b', \quad b' = \frac{r^2}{R^2 b}$$

or:

$$\frac{dV}{d\tau} = p \frac{m_1}{m} \frac{b'}{x} = p \Pi \frac{b'}{x},$$

where m_1 — launch gas mass.

Consequently, the boundary condition is defined by still another dimensionless parameter Π (the parameter b' is calculated uniquely if the chamber shape is given).

Thus, the solution of the Lagrange problem for given κ in the case of variable-section tube depends on two parameters: Π and the chamber profile $R(\xi)$.

In the cylindrical tube case, the chamber form parameter drops out, and the solution depends only on a single parameter. This situation has made it possible to construct the complete solution of the Lagrange problem, and obtain universal tables.

In the variable-section tube case, it is not possible to obtain such a universal solution, and it is necessary to make an individual computer calculation for each specific chamber shape.

A complete study of the problem described below was made in 1961 - 1963, and partially published in [7].

Figure 2.15 shows results of the Lagrange problem solution for a tube of variable section.

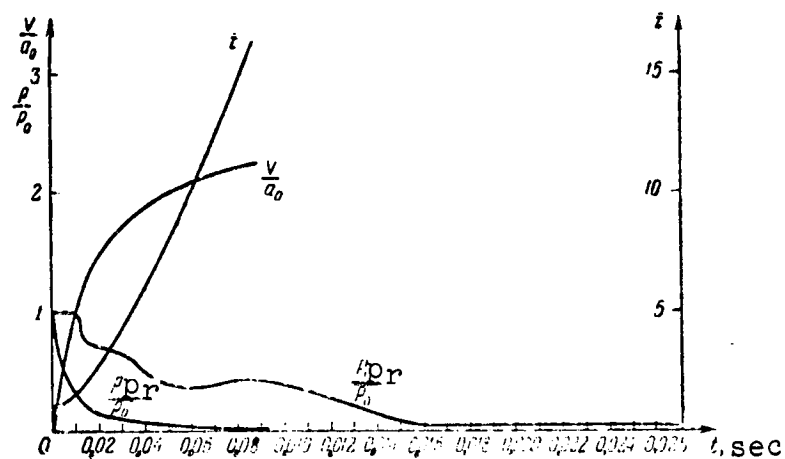


Figure 2.15. Solution of the Lagrange problem for variable-section tube

In the figure, the wall pressure (p_w), piston pressure (p_{pr}), dimensionless piston velocity, and piston coordinate are presented as functions of time.

A series of calculations was performed in which the chamber diameter ratio R/r was varied, in order to determine the flow pattern characteristics in the variable-section tube case. This diameter ratio is normally termed "chambrage" in interior ballistics. To analyze the influence of "chambrage" on muzzle velocity, we need only examine (2.17), and note that the quantity \bar{x} in this formula characterizes the gas expansion ratio in the firing process. Actually, if we denote the initial chamber volume by W_c , and its instantaneous value by W , then, obviously,

$$W = W_c + Sx,$$

where x is the distance along the barrel traveled by the piston. For the cylindrical tube:

$$\frac{W}{W_c} = \frac{Sx}{Sl_c} + 1 = x + 1,$$

and in the variable-section chamber case:

$$\frac{W}{W_c} = \frac{W_c + Sx}{W_c} = 1 + \frac{Sx}{W_c}.$$

Specifically, as the projectile departs $\frac{W}{W_c} = 1 + \frac{W_w}{W_c} = 1 + N$, where W_{ba} is the launcher barrel volume. If we now divide the variable-section barrel muzzle velocity by the cylindrical barrel muzzle velocity for the same values of $\Pi = m_1/m$, κ , and $W_w/W = N$, we can obtain the result shown in Figure 2.16. /68

We see that for the same small expansion ratios, the launch velocity from the "tapered" chamber is higher than from the cylindrical chamber by about 10 - 20%. Then, this advantage decreases and vanishes for an expansion ratio of about 10.

The favorable influence of "tapering" on the launch velocity is associated with the fact that, for the same volume of the space behind the projectile, the "tapered" chamber is shorter than the cylindrical chamber, and therefore the process of rarefaction wave reflection and pressure equalization along the chamber takes place more intensely. The wave processes are stronger in the "tapered" chamber, which is contributed to by the process of wave reflection from the chamber throat. Figure 2.17 illustrates this process, and indicates that the pressure decrease on the aft wall of the chamber takes place more slowly, the larger the "taper".

A characteristic quantity in the launch process is the overall efficiency, which is obviously equal to:

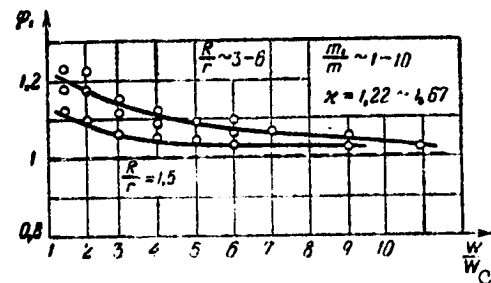


Figure 2.16. Ratio of launch velocity from tapered chamber to launch velocity from cylindrical chamber as function of expansion ratio for the same problem parameters

$$\eta = \frac{\text{body kinetic energy}}{\text{gas kinetic energy}} = \frac{E_o}{E_0},$$

where:

$$E_o = \frac{mV^2}{2}$$

and:

$$E_0 = \frac{m_1 a_0^2}{\kappa(\kappa-1)},$$

therefore,

$$\eta = \frac{mV^2 \kappa(\kappa-1)}{2m_1 a_0^2} = \frac{m}{m_1} \cdot \frac{\kappa(\kappa-1)}{2} \cdot V^2 = \frac{\kappa(\kappa-1)}{2\Omega} \cdot V^2.$$

For the "tapered" chamber:

/69

$$\frac{V}{a_0} = \mathcal{V} = \phi_1 \cdot f(\Omega, \kappa, x) = \phi_1 f, \quad V_1 = 0, \quad (2.19)$$

where ϕ_1 is a coefficient defined by the relation of Figure 2.16, and f is the dimensionless launch velocity for the cylindrical chamber case.

Consequently, we finally have the expression for the overall efficiency:

$$\eta = \frac{\kappa(\kappa-1)}{2\Omega} \phi_1^2 \cdot f^2.$$

The dependence of the quantity

$$\eta = \frac{\kappa(\kappa-1)}{2\Omega} \cdot f^2, \text{ i.e., the efficiency for}$$

the cylindrical chamber, on Ω for different κ is shown in Figure 2.18. The value of the thermal efficiency τ as $\Omega \rightarrow 0$ is calculated from the conventional ballistics formula:

$$\tau = 1 - \left(\frac{W_c}{W_c + W_{ba}} \right)^{\kappa-1},$$

since in this case the gas expansion takes place infinitely slowly.

It follows directly from (2.19) that the efficiency for the "tapered" chamber is higher than for the cylindrical chamber, since $\phi_1 > 1$ (Figure 2.16).

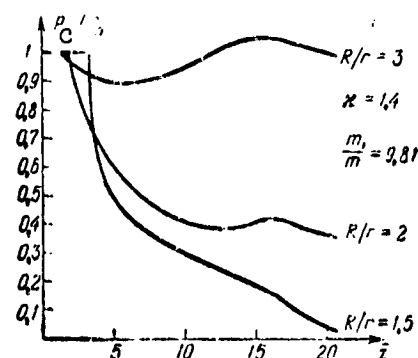


Figure 2.17. Pressure on chamber aft wall for different "chambrage"

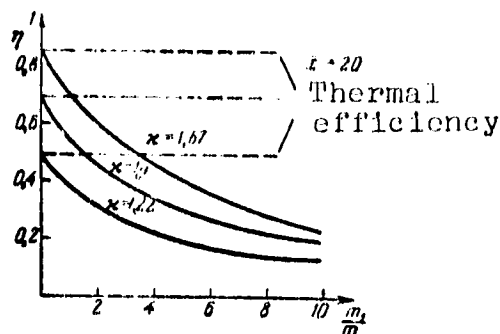


Figure 2.18. Efficiency of launch process from cylindrical chamber as function of ratio m_1/m

We see from Figure 2.18 that, for sufficient large Π , the actual efficiency is significantly lower than the thermal efficiency.

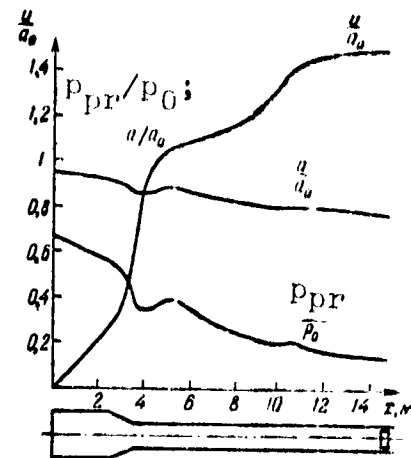


Figure 2.19. Distribution of gas parameters along variable-section tube

Concluding our examination of the numerical solution of the Lagrange problem for the variable-section tube, we need only present the data characterizing the distribution of the sought functions along the barrel bore at some fixed moment of time t (Figure 2.19). We see that, in the variable-section case, the gas velocity along the x coordinate is definitely nonlinear. The variations of the sound speed, and particularly the pressure, are quite large. /70

The data presented above complete the Lagrange problem solution; however, it is not always convenient to use the solutions obtained above in practice.

For practical calculations, it is better to generalize the results obtained as follows. If we take the launch velocity from the cylindrical tube for some expansion ratio $\bar{\kappa}$, and refer it to the velocity for the same values of Π and κ , but for $\bar{\kappa} = 20$ we obtain some function $\Psi(x)$ which is found to be practically independent of κ and Π , i.e., it is a universal function of the expansion ratio for the cylindrical tube. If we now multiply this function by the coefficient characterizing the "taper" (Figure 2.16), a universal correction

function is formed which makes it possible to obtain the launch velocity from the "tapered" chamber for a given expansion ratio N , if we know the launch velocity from the cylindrical tube for $\bar{x} = 20$.

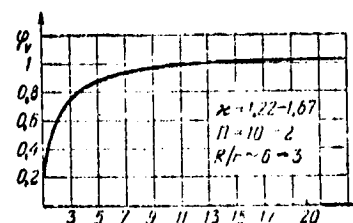
This function is denoted by ϕ_v , and is called the expansion ratio coefficient (Figure 2.20).

The launch velocity from the "tapered" chamber will now be determined by the expression:

$$v = \frac{v}{a_0} = \phi_v \cdot v / (11, \bar{x}, \bar{x} = 20), \quad (2.20)$$

and for its determination, it is sufficient to have two graphs (Figures 2.20 and 2.21).

We shall use these figures and (2.20) later in discussing the design technique and the approximate calculation method.



$$\frac{W}{W_c} = \frac{W_{ba}}{W_c} + 1 \quad /71$$

Figure 2.20. Expansion ratio coefficient

We shall later introduce into (2.20) two more coefficients: ϕ_r — coefficient accounting for the real gas properties, and ϕ_L — coefficient accounting for the losses (including the heat transfer and friction losses).

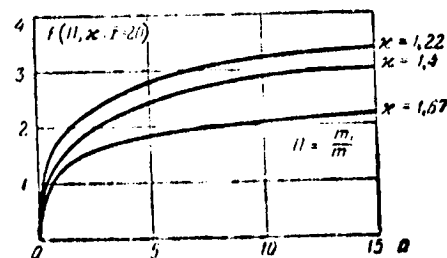


Figure 2.21. Solution of the Lagrange problem for $\bar{x} = 20$ and various κ and m_1/m

c) Numerical solution with backpressure. In the cases examined above, it was assumed that the pressure ahead of the moving projectile is equal to zero, i.e., we examined projectile launching. However, the problem of the piston motion in the light-gas chamber is no less interesting. In this case, the light gas is ahead of the piston and offers increasing resistance to the piston motion (Figure 2.22) [7, 37]. In this case, we have the Lagrange problem with backpressure.

The mathematical aspect of the problem solution is generally similar to the problem without backpressure, which was examined above. The solution is made with the aid of the same standard programs; however, the master program naturally becomes more complex.



Figure 2.22. Piston launcher

The problem solution in region I (Figure 2.1) is entirely analogous to the solution of the problem without backpressure, and there is no need to dwell on this solution. As for the problem solution in region II ahead of the piston, it must be broken down into three variants. When using a very heavy piston whose velocity is considerably below the sound speed in the compressible gas, the compression takes place without shock waves and, as the exact calculations show, practically coincides with compression along an adiabat. In the case of a light piston and quite long region ahead of the piston, a shock wave appears and, as it reflects from the wall, begins to travel between the piston and the wall. In this case, the problem solution becomes much more complex, and it is necessary to use the standard programs for a shock wave.

/72

Finally, in the case when a diaphragm is installed in place of the piston, the problem solution becomes so simple that it is easily obtained analytically [38 - 41].

It is best to begin the analysis with a short description of this very simple case.

1) Compression by a shock wave (Figure 2.23). Figure 2.24 shows the pressure variation along the coordinate, and Figure 2.25 shows the notations of the gas parameters in the incident and reflected shock waves [7].

Table 2.5 shows the gas parameters in the incident shock wave as functions of D_1/a_2 .

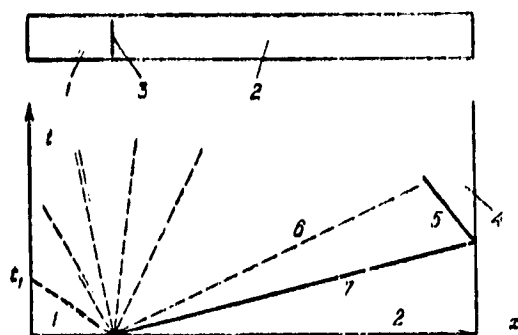


Figure 2.23. Notations adopted for gas compression by shock wave:

1 — high-pressure chamber; 2 — low-pressure chamber; 3 — diaphragm; 4 — region behind reflected shock wave (the gas parameters in this region are of greatest practical interest); 5 — reflected shock wave; 6 — contact surface; 7 — incident shock wave

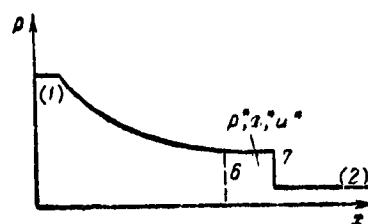


Figure 2.24. Pressure variation in arbitrary discontinuity region

Let us examine the scheme for calculating the gas motion (Figure 2.23). At the instant of diaphragm

rupture, a shock wave propagates in the gas 2 in the low-pressure chamber, and a rarefaction wave propagates in the gas 1 in the high-pressure chamber. The obvious conditions of equality of the gas pressure and velocity on both sides are satisfied on the contact surface, where the gases 1 and 2 are in contact. Writing the conditions of equality of the velocities on the contact surface, and also using the known relations from shock wave theory, we can obtain a

TABLE 2.5. GAS PARAMETERS IN SHOCK WAVE AS FUNCTIONS OF D_1/a_2 (FOR $\kappa = 1.4$)*

D_1/a_2	T_2/T_1	a_2/a_1	u_2/a_1	ρ_2/ρ_1	Φ_2/Φ_1
1.0	1.00	1.00	0	1.00	1.00
1.1	1.06	1.03	0.15	1.16	1.09
1.2	1.02	1.06	0.30	1.34	1.00
1.3	1.19	1.09	0.44	1.51	1.00
1.4	1.25	1.12	0.57	1.69	1.01
1.6	1.38	1.17	0.71	2.03	1.04
1.8	1.53	1.23	1.03	2.35	1.08
2.0	1.68	1.29	1.25	2.66	1.14
2.2	1.85	1.36	1.45	2.95	1.20
2.4	2.04	1.42	1.65	3.21	1.27
2.6	2.23	1.49	1.84	3.44	1.36
2.8	2.45	1.56	2.03	3.66	1.45
3.0	2.67	1.63	2.22	4.86	1.55
3.2	2.92	1.70	2.40	4.03	1.67
3.4	3.18	1.78	2.58	4.18	1.79
3.6	3.45	1.85	2.76	4.33	1.92
3.8	3.74	1.92	2.94	4.45	2.05
4.0	4.04	2.01	3.12	4.57	2.20

* Translator's note. Commas in numbers represent decimal points.

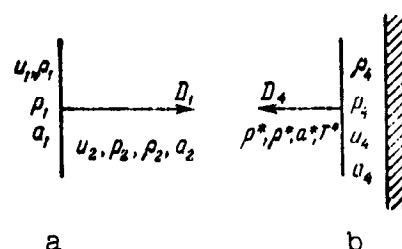


Figure 2.25. Notations adopted in incident and reflected shock wave regions

system of equations which makes it possible to calculate all the sought quantities.

The calculation is made using the formulas:

$$\frac{2}{x_1 - 1} \left[1 - \left(\frac{p^*}{p_1} \right)^{(x_1 - 1)/2x_1} \right] = \frac{a_2}{a_1} \sqrt{\frac{2 \left(\frac{p^*}{p_2} - 1 \right)}{x_2 \left[(x_2 + 1) \frac{p^*}{p_2} + (x_2 - 1) \right]}},$$

$$u^* = \frac{2a_1}{x_1 - 1} \left[1 - \left(\frac{p^*}{p_1} \right)^{(x_1 - 1)/2x_1} \right],$$

$$\frac{D_1}{u^*} = \frac{p^*}{p^* - p_1},$$

$$a^* = \sqrt{x_1 \frac{p^*}{\rho^*}}.$$

The calculation of the gas parameters in the reflected shock wave is 74 made using the formulas:

$$p_4 = p^* \frac{(3x_2 - 1)p^* - (x_2 - 1)p_2}{(x_2 - 1)p^* + (x_2 + 1)p_2},$$

$$\frac{\rho^*}{\rho_4} = \frac{x_2 - 1}{x_2} + \frac{p_2}{x_2 p^*},$$

$$\frac{T_4}{T_2} = \frac{p_4}{p^*} \cdot \frac{\rho^*}{\rho_4} \left(\frac{a^*}{a_2} \right)^2,$$

$$\frac{u_4}{a_2} = \sqrt{\frac{2x_2}{(x_2 + 1) \frac{p^*}{p} + (x_2 - 1)}} \left[(x_2 - 1) \frac{p^*}{p_2} + 1 \right].$$

Figure 2.26 shows the functional dependences of $\frac{T_4}{T_2}$, $\frac{p_4}{p_2}$, $\frac{\Phi_4}{\Phi_2}$ on $\lg \frac{p_1}{p_2}$ for the case with OHHM (optimal composition) explosion products in region 1, and hydrogen — in region 2.

The following is an example of the use of this figure.

Assume the OHHM explosion yields the pressure:

$$p_1 = 5000 \text{ atm},$$

and the initial conditions for the hydrogen:

$$p_2 = 5 \text{ atm}, T_2 = 300^\circ \text{K}, \Phi_2 = 1.$$

Consequently,

$$\lg \frac{p_1}{p_2} = 3.0$$

and we obtain from the figure:

775

$$p_4 = \frac{p_1}{p_2} p_2 = 190 \cdot 5 = 950 \text{ atm}, \quad \phi_4 = \frac{\phi_1}{\phi_2} \phi_2 = 3.3 \cdot 1 = 3.3,$$

$$T_4 = \frac{T_1}{T_2} T_2 = 10 \cdot 300 = 3000^\circ \text{K}.$$

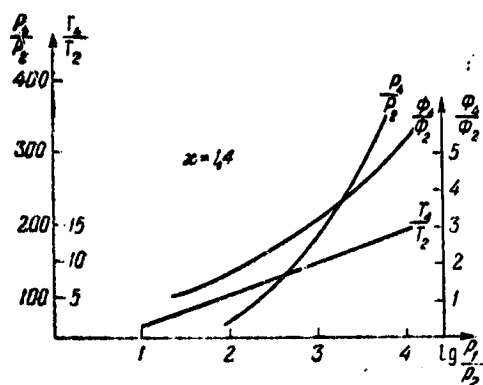


Figure 2.26. Parameters in reflected shock wave as function of initial pressure differential in launcher with OHM in region 1, and hydrogen in region 2

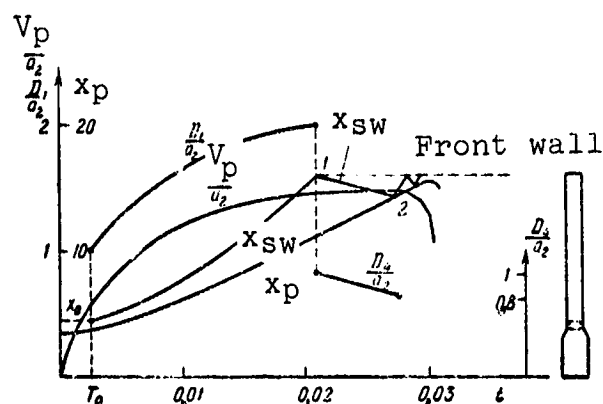


Figure 2.27. Solution of the Lagrange problem for variable-section tube with backpressure

We note that:

$$p_4 < p_1,$$

i.e., the light-gas compression pressure is lower than the OHM pressure. We can obtain $p_4 > p_1$ only if an additional charge is burned in the driver gas.

2) Compression by a light piston. We mentioned previously that in the light piston motion case, a shock wave appears ahead of the piston, and the wave formation coordinates are expressed by the formulas presented in § 1.4.

Figure 2.27 shows the results of an exact numerical calculation of the Lagrange problem with backpressure (tube closed at both ends). Here, D_1/a_2 and D_4/a_2 are the dimensionless velocities of the

incident and reflected shock waves, x_p and x_{sw} are the piston and shock wave coordinates, and V_p/a_2 is the dimensionless piston velocity. Point 1 corresponds to incident shock wave reflection from the end of the tube; point 2 corresponds to shock wave reflection from the piston. The curves of pressure variation on the walls and piston ends are not shown to avoid cluttering the figure. The magnitudes of the functions shown in the figure will vary, depending on the initial conditions — initial gas pressure on both sides, piston mass, geometric dimensions, etc.; however, the general pattern remains the same. Therefore, we can limit ourselves to this example. /76

The primary quantity characterizing the process of compression by a light piston is the entropy growth in the compression process.

The notations adopted remain the same as before: D_{max} is the maximal shock wave velocity; a_2 is the initial sound speed in the light gas; Φ^* is the entropy function behind the shock wave; Φ_2 is the initial gas entropy function, Φ_4 is the entropy function behind the reflected shock wave.

The numerical values of these quantities are shown in Table 2.6, as functions of the dimensionless maximal piston velocity.

We see from Table 2.6 that:

$$\frac{\Phi_4}{\Phi_2} \sim \sqrt{\frac{\Phi^*}{\Phi_2}}.$$

Consequently, in the first approximation, the entropy function growth in a series of shock waves can be expressed by the formula:

$$\frac{\Phi_4}{\Phi_2} = \frac{\Phi^*}{\Phi_2} \sqrt{\frac{\Phi^*}{\Phi_2}} \sqrt{\frac{\Phi^*}{\Phi_2}} \dots \quad (2.21)$$

The first three terms in this product are most significant. This can be shown by

TABLE 2.6*

V_p/a_2	1.12	1.32	1.5
$\frac{D_{max}}{a_2}$	1.87	2.06	2.3
Φ^*/Φ_2	1.11	1.16	1.22
Φ_4/Φ_2	1.17	1.25	1.36
Φ_4/Φ_2^*	1.055	1.08	1.114

* Translator's note. Commas in numbers represent decimal points.

the example of the data
for a very strong wave
(Table 2.7).

TABLE 2.7*

Reflec- tion no.	1	2	3	4	5	6	7
Φ_{i+1}/Φ_i	1,73	1,196	1,146	1,03	1,016	1,005	1
Φ_i/Φ_1	1,73	2,07	2,36	2,48	2,52	2,55	2,56

The value of Φ_1/Φ_1 ,
calculated using (2.21),
is 2.58.

*Translator's note. Commas in numbers
represent decimal points.

These numerical calculation data make it possible to evaluate
the order of magnitude of the entropy function, and indicate the
following important fact. Since the light piston velocity must be
greater than the sound speed in the light gas, it is obvious that it
will also be greater than the sound speed in the gas located behind
the piston. When using powder gases with ratio $\Pi \sim 5 - 10$, and no
backpressure, the maximal piston velocity is 2000 - 2400 m/sec. In
the backpressure case, the practically achievable piston velocity
 $V_{p \max} \sim 1500 - 2000$ m/sec, i.e., in relation to the light gas:

177

$$\frac{V_{p \max}}{a_2} \sim 1.25 - 1.8,$$

and, consequently, the shock waves are weak. Therefore, in the light
piston case, it is best to use OHHM as the driver gas, for which the
realistically achievable piston velocity with backpressure is 2500 -
3000 m/sec. This fact must be considered in designing light-gas
launchers with a light piston, in those cases when the light piston
is used to provide compression with significant entropy increase.

We note the following fact: in the shock wave reflection process,
a high entropy function gradient is created in the gas, which is
particularly clearly seen from the data of Table 2.7 and Figure 2.28:
the gas particles adjacent to the piston pass through the shock waves
2, 3, 4, 5, 6, 7, 8, and the entropy growth in the particle I (Fig-
ure 2.28) $\Phi_I = 1.196 \cdot 1,146 \cdot 1.05 \cdot 1.03 \cdot 1.016 \cdot 1.005 = 1.54$.
Conversely, the gas particles adjacent to the wall (II) pass through
all eight shock waves, and the entropy function growth:

$$\Phi_{II} = 2.56.$$

The presence of the entropy function gradient leads to the presence of a temperature gradient:

$$\frac{T_{II}}{T_I} \approx \left(\frac{\Phi_{II}}{\Phi_I} \right)^{1/4} = 1.73^{0.715} = 1.49.$$

Thus, the temperature on the piston is lower by a factor of 1.5 than on the wall. Therefore, for approximate determination of the entropy growth, it is necessary to select some averaged value.

3) Compression by heavy piston. By heavy piston, we mean one which during its motion in the light-gas chamber does not give rise to shock waves, i.e., it performs compression with constant entropy.

However, it does not follow from this that, when using a heavy piston, the process takes place in equilibrium, and therefore we can in all cases use the conventional thermodynamic relations.

Figure 2.29 shows the pressure distribution along the chamber of a piston launcher with heavy piston. We see that there is a region of reduced pressure behind the piston, and a region of elevated pressure ahead of the piston (if the piston is accelerating). The dashed line shows the pressure distribution in the uniform expansion case.

The correct magnitude of this pressure rise and the corresponding pressure reduction can be determined only with the aid of exact gasdynamic calculation.

Exact calculation of the entropy function growth in a system of shock waves is extremely complex; therefore, it is best to correlate

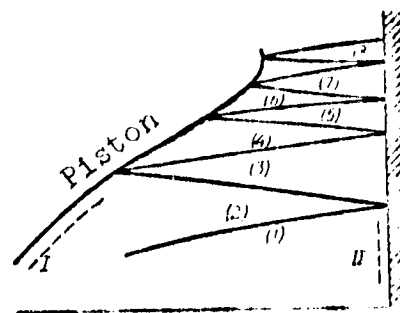


Figure 2.28. Shock wave travel ahead of the piston

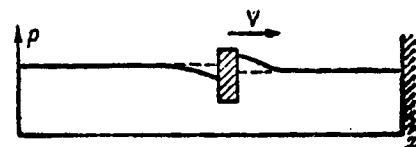


Figure 2.29. Pressure distribution ahead of and behind moving piston

the results of the calculations into a unified relation which takes into account the sound speed increase in the shock compression case, in comparison with conventional adiabatic compression to the same pressure. From (1.8) for $p_{\max}/p_0 = \text{const}$ follows:

$$\frac{L_{\text{shock}}}{a_{\text{ad}}} = \left(\frac{\Phi_{\max}}{\Phi_0} \right)^{1/2\gamma} = K_a. \quad (2.22)$$

Analysis of numerical calculations of shock compression shows that K_a in the first approximation is a function only of the ratio of the maximal piston velocity $V_{p \max}$ to the initial sound speed in the gas being compressed. The dependence of K_a on $V_{p \max}/a_2$ is shown in Figure 2.30.

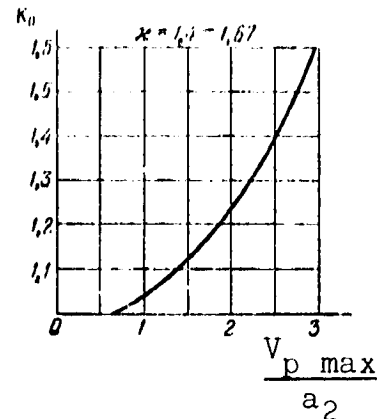


Figure 2.30. Entropy growth coefficient versus dimensionless piston velocity

§ 2.4. Corrections for Real Gas Properties, Friction, and Heat Transfer

In order to account for the real gas property influence, it is necessary to solve the gasdynamic equations in the form (2.1) - (2.5); however, this leads to tedious numerical calculations, as we mentioned previously. /79

Therefore, it is simpler to evaluate the real gas property influence indirectly, with the aid of coefficients. It is best to introduce two such coefficients: the coefficient ϕ_p , which takes into account the launch velocity variation caused by the thermodynamic processes taking place in the gas (specific heat variation with temperature, dissociation and recombination, and so on), and the coefficient ϕ_L , which takes into account the velocity reduction due to friction and heat transfer within the barrel.

Generally speaking, the coefficient ϕ_r is not a loss coefficient, since, in the ballistic range case, the barrel length is such that the dissociated molecule recombination processes can take place entirely within the launcher. This is actually a correction factor.

To determine the coefficient ϕ_r , it is necessary to solve the Lagrange problem for the case when the gas internal energy is given in the form:

$$E = E(p, T).$$

Usually, the internal energy is specified by approximation formulas constructed from the gas thermodynamic function tables. To determine ϕ_r , it is necessary to compare this solution with the solution for the cylindrical tube with an ideal gas.

The coefficient ϕ_r is always larger than one, since the recombination taking place in the barrel is equivalent to energy input in the expansion process. This result is logical if we consider that for the same p and T , the ideal gas has considerably less energy than the real dissociating gas.

As a result of the calculations made, we can recommend $\phi_r = \sim 1.05 - 1.1$ for hydrogen, and $\phi_r = 1$ for helium.

The velocity losses owing to friction and heat transfer are taken into account by the coefficient ϕ_L , which is of the order:

$$\phi_L \sim 0.85 - 0.93 \quad \left(\begin{array}{l} T_{\max} \sim 5000 - 7000^\circ \text{K}, \\ p_{\max} \sim 6000 - 10000 \text{ atm.} \end{array} \right).$$

This coefficient is conveniently broken down into two coefficients:

$$\phi_L = \phi_{L_1} \cdot \phi_{L_2},$$

where ϕ_{L_1} accounts for the losses from heat transfer and gas friction, 276
and ϕ_{L_2} accounts for losses from projectile friction.

The estimate of the coefficient ϕ_{L_1} was made by analyzing the Lagrange problem solutions for a cylindrical tube with heat removal along the barrel. Figure 2.31 shows the calculation results for three cases: 1) when there is no heat addition; 2) when an amount of heat ΔQ , equal to the initial gas energy Q_0 is added,

$$\Delta Q = Q_0; \quad \bar{Q} = \frac{Q_0 + \Delta Q}{Q_0} = 2,$$

and 3) when heat is removed ($\bar{Q} = 0.8$, i.e., $\Delta Q = -0.2 Q_0$).

The heat transfer and friction coefficients were calculated on the basis of the conventional formulas of heat transfer theory. The coefficient $\phi_{L_1} \sim 0.95 - 0.97$.

This small deviation of the coefficient ϕ_{L_1} from unity, in spite of the apparently large influence which the real gas properties should have, is explained as follows.

It was previously shown that the overall gasdynamic launcher efficiency is extremely low; therefore, the major portion of the gas energy remains in the launcher chamber, and is not utilized for launching. It is this portion of the gas energy which balances the basic heat losses due to heat transfer, which naturally has very little effect on the projectile velocity.

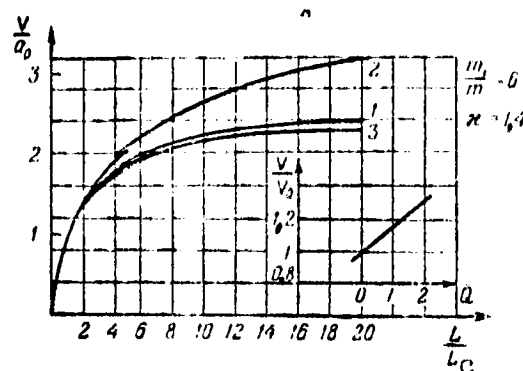


Figure 2.31. Influence of head addition on launch velocity:

1 — no heat addition; 2 — with heat addition; 3 — with heat removal

The losses from projectile friction were evaluated both computationally and experimentally.

For very highly finished new barrels, the value of the coefficient ϕ_{L_2} may reach 0.97; however, in practice, it is somewhat lower /81 ($\sim 0.93-0.95$), and the friction influence increases markedly with launch velocity increase, and decreases with launcher caliber increase (just as does the heat transfer influence).

In closing this section, it is advisable to present some data on the thermodynamic properties of hydrogen at high temperatures and pressures. For the parameter region studied, the thermodynamic properties of hydrogen can be calculated from the equation of state in virial form, which is theoretically best:

$$Z = 1 + B\rho + C\rho^2 + \dots, \quad (2.23)$$

where $Z = \frac{pW}{RT}$ — the compressibility coefficient, ρ — gas density, C and B — respectively, the second and third virial coefficients, which are functions of temperature, and R — universal gas constant.

For practical calculations, it is convenient to use the equation of state in which the right side is an expansion in powers of the pressure:

$$Z = 1 + B'p + C'p^2 + \dots, \quad (2.24)$$

where B' and C' are connected with the equation virial coefficients /84 by the relations:

$$B' = \frac{B}{RT}$$

and

$$C' = \frac{C - B^2}{RT^2}.$$

The calculation results are summarized in Tables 2.8 and 2.9.

TABLE 2.8. FOR MOLECULAR HYDROGEN*

T, °K (p = 15,000, bar)	B(T), cm ³ /mol	C(T), cm ⁶ /mol ²	T, °K (p = 15,000, bar)	B(T), cm ³ /mol	C(T), cm ⁶ /mol ²
1000	16,86	226	9000	12,39	95,57
2000	15,90	177	10000	12,15	91,05
3000	15,05	152	11000	11,92	85,90
4000	14,37	134,9	12000	11,70	79,48
5000	13,83	123,0	13000	11,50	72,60
6000	13,41	114,4	14000	11,34	67,03
7000	13,02	106,9	15000	11,15	61,51
8000	12,67	100,6			

*Translator's note. Commas in numbers represent decimal points.

TABLE 2.9. FOR ATOMIC HYDROGEN*

T, °K	4000	5000	6000	7000	8000	9000	10000	11000	12000	13000	14000	15000
B(T)	1,83	2,00	2,12	2,15	2,15	2,13	2,10	2,07	2,03	1,99	1,96	1,93

*Translator's notes. Commas in numbers represent decimal points.

The calculation of the third virial coefficient for atomic systems involves great difficulty, and is still an unresolved problem. This is explained by the absence of suitable statistical mechanics apparatus. Even for such a very simple system as hydrogen (single-electron atom), only very rough estimates have been made of the third virial coefficient. These estimates show that the contribution of the third virial coefficient to compressibility can be neglected in quite a wide interval of temperatures and pressures.

Tables 2.10 - 2.13* present the sound speed, apparent molecular weight, adiabatic exponent, and internal energy of hydrogen for temperatures 1000 - 15,000° K and pressures 1000 - 15,000 bar**.

*The calculations whose results are shown in Tables 2.8 - 2.13 were made by P. M. Kesselman and S. I. Gorykin.

**1 bar = 0.98 atm.

TABLE 2.10. SOUND SPEED, m/sec

P \ T	1000	2000	3000	4000	5000	6000	7000	8000	9000	10000	11000	12000	13000	14000	15000
1000	2820	3589	4193	4730	5208	5691									
2000	3174	3852	4407	4902	5382	5877									
3000		4088	4600		5068	5597	6214								
4000				5239	5719	6245	6801	7000	7762	8048	9591	10175	11174	11651	11968
5000				5367	5842	6331	6878	7036	7723	8345	9435	10298	11014	11557	11878
6000				5515	5985	6470	6962	7079	7717	8485	9425	10168	10887	11414	11779
7000				5695	6168	6674	7169	7293	7881	8654	9468	10194	10897	11403	11772
8000				5914	6387	6913	7419	7543	8171	8943	9705	10404	11087	11563	11871
9000					6205	6750	7283	7407	8075	8845	9599	10269	10924	11370	11717
10000				6033	6579	7134	7676	7799	8485	9258	10001	10649	11284	11711	11999
11000				6156	6702	7267	7808	7931	8637	9410	10143	10779	11394	11811	12129
12000				6254	6800	7375	7916	8039	8763	9546	10279	10904	11509	11916	12254
13000				6355	6900	7485	8026	8149	8883	9676	10409	11024	11619	12016	12374
14000				6452	6998	7593	8134	8257	9001	9804	10537	11142	11727	12114	12491
15000				6543	7090	7695	8236	8359	9111	9924	10657	11262	11837	12224	12601

TABLE 2.11. APPARENT MOLECULAR WEIGHT*

P \ T	1000	2000	3000	4000	5000	6000	7000	8000	9000	10000	11000	12000	13000	14000	15000
1000	2,0160	2,0159	2,0169	1,9855	1,8286	1,6096									
2000	2,0160	2,0160	2,0173	1,9796	1,8780	1,7010									
3000	2,0160	2,0160	2,0179	1,9817	1,9005	1,7505									
4000	2,0160	2,0160	2,0170	1,9894	1,9141	1,7795	1,6120	1,4500	1,3190	1,2240	1,1600	1,1170	1,0890	1,0670	1,0539
5000	2,0160	2,0160	2,0160	1,9920	1,9234	1,7998	1,6430	1,4860	1,3540	1,2550	1,1850	1,1370	1,1040	1,0800	1,0620
6000	2,0160	2,0160	2,0160	1,9940	1,9300	1,8149	1,6670	1,5150	1,3740	1,2820	1,2080	1,1550	1,1170	1,0900	1,0720
7000	2,0160	2,0160	2,0160	1,9950	1,9350	1,8270	1,6800	1,5300	1,4000	1,3050	1,2280	1,1720	1,1320	1,1030	1,0850
8000	2,0160	2,0160	2,0160	1,9960	1,9400	1,8370	1,7010	1,5580	1,4300	1,3340	1,2540	1,1950	1,1540	1,1240	1,1060
9000	2,0160	2,0160	2,0160	1,9970	1,9430	1,8430	1,7140	1,5750	1,4500	1,3530	1,2700	1,2090	1,1670	1,1350	1,1150
10000	2,0160	2,0160	2,0160	1,9980	1,9460	1,8470	1,7200	1,5790	1,4550	1,3580	1,2740	1,2110	1,1680	1,1350	1,1140
11000	2,0160	2,0160	2,0160	1,9980	1,9490	1,8510	1,7260	1,5830	1,4590	1,3620	1,2770	1,2130	1,1700	1,1370	1,1160
12000	2,0160	2,0160	2,0160	1,9990	1,9510	1,8550	1,7310	1,5870	1,4630	1,3660	1,2800	1,2150	1,1720	1,1390	1,1180
13000	2,0160	2,0160	2,0160	1,9990	1,9530	1,8590	1,7350	1,5910	1,5040	1,4070	1,3200	1,2550	1,2120	1,1790	1,1580
14000	2,0160	2,0160	2,0160	2,0000	1,9550	1,8610	1,7370	1,5930	1,5150	1,4180	1,3310	1,2660	1,2230	1,1900	1,1690
15000	2,0160	2,0160	2,0160	2,0000	1,9560	1,8750	1,7510	1,6070	1,5250	1,4280	1,3410	1,2760	1,2330	1,2000	1,1790

*Translator's note. Commas in numbers represent decimal points.

TABLE 2.12. ADIABATIC EXPONENT κ *

P \ T	1000	2000	3000	4000	5000	6000	7000	8000	9000	10000	11000	12000	13000	14000	15000
1000	1,40	1,32	1,28	1,20											
2000	1,40	1,32	1,28	1,25											
3000	1,40	1,32	1,28	1,30											
4000	1,40	1,32	1,28	1,40	1,28	1,16	1,07	1,03	1,03	1,08	1,15	1,21	1,24	1,28	1,30
5000	1,40	1,32	1,28	1,44	1,31	1,19	1,10	1,05	1,04	1,07	1,13	1,19	1,22	1,25	1,26
6000	1,40	1,32	1,28	1,48	1,35	1,23	1,13	1,07	1,05	1,07	1,12	1,17	1,21	1,24	1,25
7000	1,40	1,32	1,28	1,51	1,38	1,26	1,16	1,09	1,07	1,08	1,12	1,16	1,20	1,23	1,24
8000	1,40	1,32	1,28	1,54	1,41	1,28	1,18	1,11	1,08	1,08	1,11	1,15	1,19	1,22	1,23
9000	1,40	1,32	1,28	1,57	1,44	1,31	1,20	1,13	1,09	1,09	1,11	1,15	1,18	1,21	1,22
10000	1,40	1,32	1,28	1,59	1,46	1,33	1,23	1,15	1,10	1,10	1,12	1,15	1,18	1,21	1,22
11000	1,40	1,32	1,28	1,62	1,48	1,35	1,25	1,17	1,12	1,12	1,14	1,17	1,20	1,23	1,24
12000	1,40	1,32	1,28	1,65	1,50	1,38	1,27	1,19	1,14	1,14	1,16	1,19	1,22	1,25	1,26
13000	1,40	1,32	1,28	1,67	1,52	1,39	1,28	1,20	1,15	1,15	1,17	1,20	1,23	1,26	1,27
14000	1,40	1,32	1,28	1,67	1,55	1,41	1,29	1,22	1,16	1,16	1,18	1,21	1,24	1,27	1,28
15000	1,40	1,32	1,28	1,68	1,56	1,43	1,30	1,23	1,17	1,17	1,19	1,22	1,25	1,28	1,29

*Translator's note. Commas in numbers represent decimal points.

ORIGINAL PAGE IS
OF POOR QUALITY

TABLE 2.13. INTERNAL ENERGY OF HYDROGEN

$\begin{matrix} T \\ p \end{matrix}$	1000	2000	3000	4000	5000	6000	7000	8000	9000	10000	11000	12000	13000	14000	15000
1000															
2000															
3000															
4000				54 001	77 865	110 476	150 480	193 435	234 719	271 234	301 788	326 074	343 746	354 633	409 877
5000				53 880	76 530	107 943	145 714	186 840	227 632	263 624	291 812	312 070	327 631	337 549	406 069
6000				53 789	76 248	106 113	142 204	181 854	221 626	257 352	286 868	306 773	319 047	327 516	402 539
7000				53 701	75 950	104 710	139 606	177 908	216 131	251 972	280 798	300 117	310 881	318 824	399 210
8000				53 780	75 367	103 625	137 656	174 714	212 068	247 527	275 335	301 983	315 115	323 253	396 085
9000				53 780	75 070	102 740	136 829	172 956	208 655	243 661	271 438	296 734	311 652	320 233	393 166
10000				53 818	74 837	102 009	136 380	169 806	205 723	240 299	271 980	296 882	310 477	317 735	390 159
11000				53 855	74 648	101 401	135 158	167 878	203 147	237 350	268 848	297 809	312 646	319 486	387 866
12000				53 905	74 498	100 889	132 079	166 177	200 013	235 705	266 051	295 035	312 850	318 891	385 137
13000				53 961	74 376	100 445	131 170	164 718	198 928	232 335	263 490	292 442	310 349	316 483	383 134
14000				54 021	74 278	100 065	130 369	163 409	197 122	230 190	261 185	290 106	307 998	313 185	380 955
15000				54 085	74 200	99 737	129 664	162 230	195 651	228 765	259 072	287 906	305 825	310 036	378 885

§ 2.5. Influence of Forcing Pressure on Gas Flow Velocity in Barrel

We examined above the numerical solution of several problems of firing from launchers having different chamber and barrel forms, and also the solution of the auxiliary problem of gas compression by a piston or shock wave. The results obtained make it possible to calculate the light-gas launchers under the assumption that the light gas is first compressed to the maximal values p_{\max} and T_{\max} , and then the piston remains stationary and the projectile begins to move (usually practical calculations are made in this way).

However, it is also of considerable interest to make a complete analysis of the launcher with account for the fact that the projectile begins to move at a forcing pressure p_{ϕ} , where:

$$p_{\phi} < p_{\max}$$

and the piston continues to travel during the firing process.

The complete light-gas launcher analysis using the exact gas-dynamic equations requires considerable computer time, and is usually made only for a few initial condition variants.

The most important question, which must be clarified in the complete launcher analysis, is that of the forcing pressure influence.

Experiment shows that the forcing pressure has very little influence on projectile velocity; however, it has considerable influence on the maximal gas pressure in the chamber, and this is understandable, since the forcing pressure is a factor which redistributes the accumulated energy without altering the magnitude of this energy.

In order to write the equations defining the motion in the two-stage launcher in the simplest formulation, we return to Figure 2.6b.

The gas pressure in the space I behind the piston:

$$P = P_0 \left(\frac{L_0}{L_0 + X} \right)^{\kappa_1},$$

where L_0 — is the initial length of the space behind the piston, X — piston travel; κ_1 — driver gas adiabatic exponent; P_0 — initial gas pressure.

When a powder charge burns in region I, we use the equations of classical interior ballistics.

The pressure of the light gas between the piston 2 and the projectile 1 (region II) is defined by the relation:

$$p = p_0 \left(\frac{L}{L - X} \right)^{\kappa}$$

for $p \leq p_*$ (stationary projectile), and by the relation:

$$p = p_0 \left(\frac{L}{L - X + \frac{S}{S_*} x} \right)^{\kappa}$$

for $p > p_*$ (moving projectile).

Here, L is the initial length of the space behind the projectile, S is the piston barrel area, x is the projectile travel, S_* is the barrel area, κ is the light-gas adiabatic exponent.

The piston equation of motion can be written in the form:

$$m_p \frac{dv}{dt} = S(P - p),$$

and the projectile equation of motion in the form:

$$m \frac{dv}{dt} = sp.$$

It is obvious that the computational technique based on solving these equations takes into account the forcing pressure influence.

In certain cases, refinements are introduced into these very simple equations. For example, the space between the piston and projectile is broken down into two spaces: the space ahead of the piston — from the piston to the barrel entrance (section A), and the space behind the projectile — from section A to the projectile. In this case, gas flow from the space ahead of the piston into the space behind the projectile is taken into account. Usually, it is assumed here that the gas flow at section A is described by the equations of steady gas flow.

/86

Sometimes, an attempt is made to consider the pressure gradient along regions I or II, and so on.

However, in all cases, this simplified approach to solving the problem of motion within the launcher is justified only when the piston velocity does not exceed 500 - 600 m/sec, and the projectile velocity is 2000 - 2500 m/sec (when hydrogen or helium is used as the light gas), since in this case piston (projectile) motion takes place with a velocity quite close to the sound speed, and wave effects are not yet too large.

When analyzing modern light-gas launchers, this approximate method is not applicable. It leads to errors exceeding 20 - 30% in the launch velocity, and errors up to 100% in the magnitude of the maximal pressure. Therefore, we must use the exact gasdynamic calculation. The exact calculation techniques do not differ from the

technique for solving the Lagrange problem with backpressure; however, we must consider that the projectile begins to move when the pressure on it exceeds p_ϕ . As the projectile moves, a rarefaction wave develops and interacts with the shock waves coming from the piston (if the piston is light).

/87

The interaction process is also complicated because of the bore cross section change at the entrance to the barrel.

The two-stage launcher analysis with account for forcing pressure and piston motion is quite complicated.

Figure 2.32 shows the pressure p_{pr} on the projectile velocity for forcing pressures 1000 atm and 6000 atm (without account for losses) as functions of projectile travel.

We see that for a low forcing pressure, the projectile pressure curve is "fuller", the maximal pressure is lower, but the area bounded by the curve is greater (curves 1). Thus, the final projectile velocity is higher.

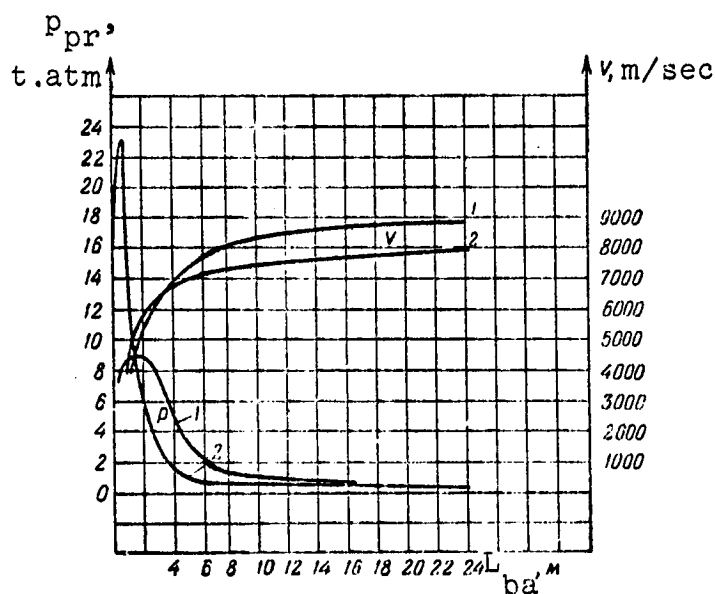


Figure 2.32. Influence of forcing pressure on ballistic launcher parameters:

1 — $p_\phi = 1000$ atm; 2 — $p_\phi = 6000$ atm

The absolute projectile velocity variation does not exceed 12%, while the maximal pressure varies by 2.5 times. These calculated values fully confirm the experimental data, in accordance with which the forcing pressure influence on the velocity is about 5 - 6%.

Figure 2.33 shows the launch velocity versus forcing pressure for one LGL. We see from this figure that the optimal value of p_ϕ is close to 300 atm.

Thus, for a very high maximal fore-chamber pressure ($p_{\max} \sim 10,000 - 20,000$ atm), proper forcing pressure selection can reduce the pressure acting on the projectile to values which are not hazardous for projectile strength (to values not exceeding $p_{\max \text{ pr}} \sim 4000 - 6000$ atm). At the same time, the motion of the piston (particularly the hydrodynamic piston) permits maintaining the pressure on the projectile base close to $p_{\max \text{ pr}}$, i.e., a full firing "indicator diagram"; it is obvious that in this case we obtain a high average pressure $p_{\text{av pr}}$ on the projectile, which in turn determines the barrel length.

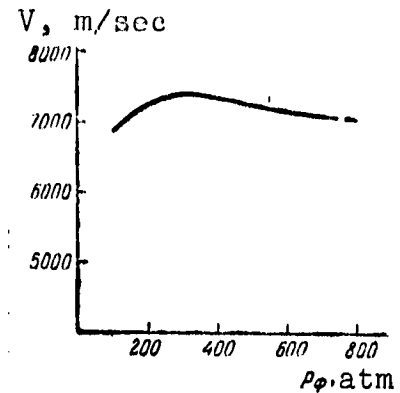


Figure 2.33. Influence of forcing pressure on launch velocity

In fact, introducing the average acceleration:

$$g_{\text{av}} = s \frac{p_{\text{av pr}}}{m},$$

and using the uniformly accelerated motion formulas, we can obtain: /88

$$L_{\text{ba}} = \frac{mV^2}{2sp_{\text{av pr}}}. \quad (2.25)$$

It is sometimes more convenient to rewrite this formula as:

$$p_{\text{av pr}} = \frac{mV^2}{2sL_{\text{ba}}}. \quad (2.26)$$

A second very characteristic quantity, which makes possible an exact calculation is the ratio of projectile base pressure to piston base pressure. The dependence of this quantity on time is shown in Figure 2.34*. We see that the ratio p_{pr}/p_p varies from 0.1 to 5.

*The calculation was made by the grid and characteristic methods.

We see from the figure that the agreement between the two calculation methods is generally good. (In the figure, we see clearly three shock wave reflections — the first is strong, the second considerably weaker, and the third quite weak).

The gas flow in the transition region from the chamber to the barrel is also very important for understanding the gasdynamic relationships in the firing process.

The reason is that "choking" of the gas flow takes place in this region, and the light gas cannot flow from the chamber into the barrel. In practice, this leads to a situation in which, under certain conditions, increase of the charge in the system increases the maximal light gas pressure in the chamber significantly, but does not change the launch velocity. Moreover, this leads to reduction of the model forcing pressure influence on its velocity.

In the gasdynamic calculation, the gas velocity in the transition region is obtained automatically. In the approximate calculations, the transition section velocity is sometimes introduced into the calculation, and in this case the calculated launch velocity depends markedly on how this velocity is specified. Under the steady flow process assumption, the gas flowrate is known to be:

$$G_{st} = s u_{cr st} \rho_{cr st} = s p_0 a_0 \left(\frac{2}{\gamma + 1} \right)^{\frac{\gamma + 1}{2(\gamma - 1)}},$$

while, under the unsteady flow process assumption, the flowrate may be represented in the form:

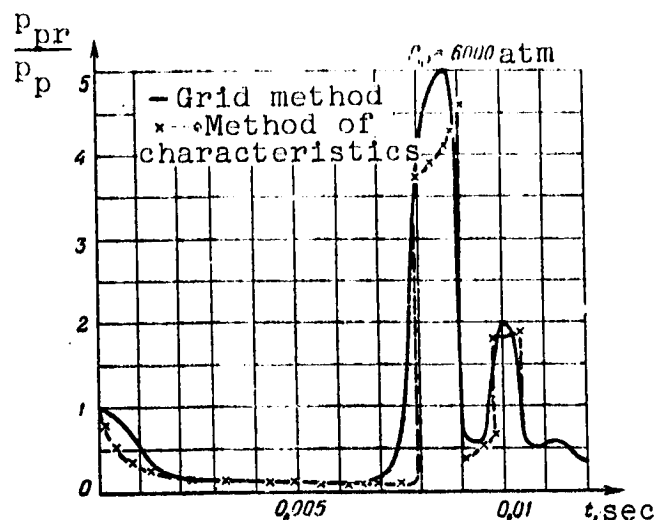


Figure 2.34. Ratio of projectile base pressure to piston base pressure

$$G_{un} = s u_{cr.un} \rho_{cr.un} = s \rho_0 a_0 \left(\frac{2}{\kappa + 1} \right)^{\frac{\kappa + 1}{\kappa - 1}},$$

hence,

$$\frac{G_{st}}{G_{un}} = \left(\frac{\kappa + 1}{2} \right)^{\frac{\kappa + 1}{2(\kappa - 1)}}. \quad (2.27)$$

Data on G_{st}/G_{un} as a function of κ are presented in Table 2.14.

Thus, the gas flowrate through the barrel entrance section is actually limited, and depends markedly on the process scheme adopted. In the ballistic launchers, the flow process does not fit into either of the classical (steady or unsteady) schemes; however, it is evident that the process is closer to the classical unsteady scheme.

TABLE 2.14*

κ	1,22	1,4	1,67
$\frac{G_{st}}{G_{un}}$	1,69	1,72	1,77

*Translator's note. Commas in numbers represent decimal points.

These data explain why some approximate techniques (based on specifying the critical steady-state flowrate at the barrel throat) lead to a situation in which the launch velocity is too high, and the pressure in the gas chamber is too low by nearly a factor of two.

In order to refine such calculation methods, it is necessary to introduce an experimental adjustment factor (flow coefficient), whose value will be about 0.5 - 0.7. /90

Data on the gas flowrate through the barrel entrance section, obtained by exact gasdynamic calculation with account for piston motion, are shown in Figure 2.35. Also shown is the flowrate obtained under the unsteady flow assumption. We see that the true curve is close to the unsteady model. Results of two calculations (curves 1 and 2) are presented, which differ only in the initial conditions.

§ 2.6. Light-Gas Launcher Optimal Parameter Selection

In the preceding sections, we examined various light-gas launcher configurations, described their calculation methods, and obtained an approximate formula for the velocity imparted to the projectile:

$$V = V_1 + \phi_V \phi_r \phi_L f(\Pi, \alpha, \alpha = 20). \quad (2.28)$$

Here, we shall present some launcher design methods (selecting optimal launcher parameters and its dimensions).

When creating a new light-gas launcher, we must usually solve two types of problems: first, the gasdynamic problems (charge selection, optimal powder weight selection, light-gas pressure selection, and so on) and, second, the purely structural problems (associated with failure or faulty operation of the components of the launcher itself). It is obvious that the solutions of these problems should be separated from one another, and the solution of the first problem should be made on a launcher of the smallest possible dimensions, i.e., on a scale-model launcher.

By scale-model, we usually mean a launcher which is geometrically similar to the full-size launcher, but of considerably smaller dimensions. However, all the characteristic pressures and temperatures (p_0 , T_0 , p_{\max} , T_{\max} , p_d , α , a_0 , etc.) are the same in the scale-model and full-size launchers, and the same gases (helium, hydrogen) are used. (Generally speaking, we can also use a broader meaning of modeling: for example, without using the condition that T_{\max} and p_{\max} are the same.)

It is well known that the equations of motion are easily reduced to dimensionless form, and in these equations there appear only the

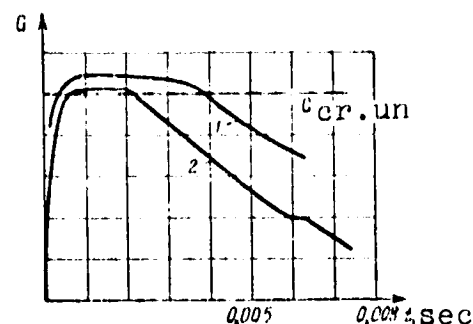


Figure 2.35. Gas flowrate at barrel entrance section as a function of time

exponent κ , which is the same on the scale-model and full-size units by assumption.

The boundary condition in general form is written as:

$$\frac{dv}{dt} = \frac{SL\rho_0}{m} (p_L - p_R),$$

where L — characteristic dimension. In this case, there appears the dimensionless parameter:

/91

$$\frac{SL\rho_0}{m},$$

which can be treated in two ways:

a) the quantity $SL\rho_0$ is proportional to the gas mass m_1 and, consequently, similarity requires that the quantities $m_1/m = \Pi$ be the same in the scale-model and full-scale launchers;

b) the quantity m/SL is proportional to the projectile density, i.e., the ratios of the gas and projectile densities in the scale-model and full-scale launchers must be the same.

These two requirements are evidently equivalent and, consequently, for similarity, it is sufficient that the pistons (projectiles) be geometrically similar and made from the same material. These conditions are sufficient for similarity of the scale-model and full-size launchers, if the gas is considered ideal.

The situation changes somewhat if we consider gas viscosity and thermal conductivity.

With account for viscosity, similarity requires equality of the Reynolds numbers in the full-scale and scale-model launchers:

$$Re = \frac{uL}{\nu}.$$

Since the gas viscosity and characteristic velocity are the same in the scale-model and full-scale launchers, the Reynolds number is always larger in the full-scale launcher than in the scale-model launcher.

Increase of the Reynolds number leads to reduction of the friction coefficient and increase of the heat transfer coefficient in the first approximation, in direct proportion to the square root of the Reynolds number. Consequently, the friction and heat transfer coefficients in the full-scale launcher will be, respectively, smaller and larger than in the scale-model launcher by:

$$\sim \sqrt{Re} \sim \sqrt{\frac{L_{act}}{L_{mod}}} \text{ times.}$$

However, in accounting for the relative influence of friction and heat transfer, we must consider that the friction force and thermal losses are proportional to the surface area, i.e., L^2 , while the inertial forces and the total amount of heat are proportional to the volume, i.e., L^3 , and therefore the influence of friction and heat transfer in the scale-model launcher will be greater by:

$$\frac{L_{act}}{L_{mod}} \text{ times,}$$

than in the full-scale launcher.

If we consider the dependence of the friction and heat transfer coefficients on the dimensions, we find that, roughly speaking, in the scale-model launcher the influence of friction and heat transfer is greater than in the full-scale launcher by at least:

/92

$$\sqrt{\frac{L_{act}}{L_{mod}}} \text{ times.}$$

Therefore, if a certain velocity is achieved in the scale-model launcher, then from the gasdynamic viewpoint, this same velocity can be achieved in the full-scale launcher, and this is confirmed experimentally.

This very important conclusion makes it possible to limit ourselves to study of scale-model launchers when selecting optimal gas-dynamic launcher configurations.

All the above discussion relates to the case when the powder charge has burned completely prior to piston movement initiation.

If the powder charge continues to burn, it is necessary to require that the physical and chemical characteristics of the powder in the full-scale and scale-model experiments be the same, and that the web thickness of the powder used in the scale-model experiment be L_{act}/L_{mod} times less than in the full-scale experiment.

Failure to satisfy these conditions leads to a situation in which the curves of piston base pressure in the scale-model and full-scale launchers will be somewhat different, although generally speaking this is not too important, since in practice the primary importance lies not in p itself, but rather in the quantity $\int p dx$, i.e., the piston base pressure work.

It is obviously quite simple to select conditions under which these areas will be related as the cube of the linear dimensions.

After these general remarks, we can turn to selecting the optimal launcher parameters.

It is well known from classical ballistics that two problems arise in designing any artillery system:

1. The direct problem, when from the given system geometric dimensions and the charging conditions we must determine the firing parameters (velocities, pressures, and so on).
2. The inverse problem, when from the given firing parameters (projectile velocity and weight, maximal gas chamber pressure, etc.) we must select the launcher geometric parameters (configuration) and the charging conditions.

The solution of the direct problem is carried out either by numerical methods or with the aid of (2.28), using the technique discussed in § 9 of the present chapter. Let us now examine the solution of the inverse problem. The launch velocity from the ballistic launcher, obtained as a result of the numerical solution, can be approximated by (1.1): /93

$$V = \varphi a_{\max} \sqrt{\frac{2\eta}{\kappa(\kappa-1)\left(\frac{1}{\Pi} + b_1\right)}}, \quad (2.29)$$

where $\eta = 1 - \left(\frac{W_c}{W_c + W_{ba}}\right)^{\kappa-1}$, W_c — chamber volume prior to initiation of model movement, W_{ba} — barrel volume, ϕ — overall correction coefficient, a_{\max} — maximal sound speed.

The coefficient b_1 is obtained from the exact gasdynamic calculations and for an expansion ratio exceeding 3 - 5 is practically constant, equal to 0.25 - 0.27.

Writing the sound speed at the end of compression in the form:

$$a_{\max} = a_0 \left(\frac{p_{\max}}{p_0}\right)^{(\kappa-1)/2\kappa} \cdot K_a$$

(K_a is a coefficient accounting for the increase of a_{\max} , resulting from the entropy increase during shock compression; see Figure 2.30), and the light-gas mass in the form:

$$m_1 = W_0 \rho_0 = W_0 \frac{p_0}{RT_0},$$

where the subscripts 0 refer to values of the quantities prior to compression, we can write (2.29) as:

$$V = K_a \cdot \varphi a_0 p_{\max}^{(\kappa-1)/2\kappa} \sqrt{\frac{2\eta}{\kappa(\kappa-1)}} \sqrt{\frac{p_0^{1/\kappa}}{\frac{mRT_0}{W_0} + b_1 p_0}}.$$

Under the assumption that b_1 and η remain constant, differentiating V with respect to p_0 , and equating the derivative to zero, we can obtain:

$$(p_0)_{\text{opt}} = \frac{mRT_0}{(\kappa-1)b_1 W_0}.$$

Recalling that

$$\frac{p_0 W_0}{m R T_0} = \frac{m_1}{m} = \Pi,$$

we can conclude that there is an optimal ratio $m_1/m = \Pi_{\text{opt}}$, which depends only on κ and the approximation coefficient b_1 (Table 2.15):

$$\Pi_{\text{opt}} = \frac{1}{(\kappa - 1) b_1}. \quad (2.30)$$

In practice, we can take Π somewhat smaller than Π_{opt} , since the dependence of the velocity on Π is quite weak.

We emphasize that (2.30) is valid only for the case when the volume increase during firing exceeds 3 - 4 ($b_1 = \text{const}$), or when we can neglect $\frac{\partial b_1}{\partial p_0}$. If it is necessary to take the variation of b_1 into account precisely, all the arguments become more complex, and it is more convenient to seek the optimal value of Π by varying numerically the calculation initial conditions.

The existence of an optimal value of Π yields a firm basis for rational design of the optimal system. If the projectile mass is given, the system caliber is essentially known (see Table 2.16), since the projectile weight coefficient is usually specified:

$$C_r = \frac{q}{d^3} \sim 1 - 3.$$

TABLE 2.15*

κ	Π_{opt}	
1,22	17,5	$b_1 = 0,26$
1,4	9,6	
1,67	5,7	

/94

*Translator's note. Commas in numbers represent decimal points

TABLE 2.16*

Caliber, mm	5,3	7,8	12,5	16	23	34	50	85
Body weight, grams	0,2-0,4	1,0-2,0	4-6	7-12	18-28	55-120	200-400	1000-2000

*Translator's note. Commas in numbers represent decimal points.

The barrel length is expressed in calibers: $L_{ba} = \lambda d$. The barrel volume is easily found from the formula:

$$W_{ba} = \lambda d^3 \frac{\pi}{4},$$

where λ — barrel length in calibers.

It was shown above that the gas expansion ratio N in the barrel has a large influence on the projectile velocity. Usually, N has a value of 3 - 10. Specifying the value of N , we can immediately determine the minimal volume at the end of compression:

$$W_{min} = \frac{W_{ba}}{N},$$

where $N = \frac{W_{ba}}{W_{min}}$ — expansion ratio in the barrel.

The light-gas mass is found from the formula:

$$m_1 = W_{min} \rho_{max} = W_{min} \frac{p_{max}}{RT_{max}}.$$

Using the existence of an optimal value of Π , we can write:

/95

$$m_1 = \Pi m,$$

or, expressing m through the coefficient C_q ,

$$m = C_q d^3.$$

Substituting, in place of m_1 , its value, we obtain:

$$\Pi C_q d^3 = W_{min} \frac{p_{max}}{RT_{max}} = \frac{W_{ba} p_{max}}{N R T_{max}}.$$

Usually, during design, maximal pressure is selected from structural consideration; therefore, we can write:

$$T_{max} = \frac{\pi d^2 L_{st} p_{max}}{4 R C_q d^3 \Pi N} = \frac{\pi \lambda p_{max}}{4 N R C_q \Pi}. \quad (2.31)$$

This formula makes it possible to construct a directive diagram which gives a complete picture of the multistage launcher capabilities.

Formula (2.31) can be written in the form:

$$\frac{T_{\max}}{p_{\max}} = \frac{(\pi\lambda)}{4NRC_q\Pi}. \quad (2.32)$$

In this formula, Π and R^* are known. The quantity p_{\max} characterizes launcher strength, and is also usually known in advance. Consequently, (2.32) connects T_{\max} with the light-gas launcher constructive parameters N , λ , C_q .

The quantity T_{\max} can be easily transformed into projectile velocity. In fact,

$$V = \varphi f(\Pi, \kappa, N) \cdot a_{\max},$$

where Π and κ are given, $a_{\max} \sim \sqrt{T_{\max}}$, and therefore (2.32) takes the form:

$$\frac{V}{p_{\max}} \sim \psi(\lambda, N, C_q). \quad (2.33)$$

Thus, the launch velocity referred to p_{\max} is a function of three constructive parameters: barrel length, expansion ratio, and projectile weight coefficient. The existence of the functional relation (2.33) makes it possible to analyze any multistage launcher with the aid of the directive diagrams.

The launcher directive diagram relates four quantities: p_{\max} , T_{\max} , V , C_q — for given values of the gas constant, dimensionless barrel length, and correction coefficient $\phi = \phi_r \cdot \phi_L$. The diagram is constructed for several values of the expansion ratio N , in the following sequence:

1. Using (2.32), we calculate a table of $\frac{T_{\max}}{p_{\max}} = \psi(C_q)$ for the given λ , N , R , Π .

*The gas constant for helium is 212 m/deg, for hydrogen — 424 m/deg.

2. In the coordinates p_{\max} , C_q , we construct the field of the T_{\max} values and points with the same values are joined by straight lines.

3. The launch velocity:

$$V = a_{\max} \cdot f(\Pi, \kappa, \tau = 20) \cdot \varphi_r \cdot \varphi_L.$$

The quantity a_{\max} is known, since the temperature is known: $f(\Pi, \kappa, \tau = 20)$ is taken from the exact solution for the cylindrical tube. The coefficient $\varphi_r(N)$ accounts for the relative expansion correction (from Figure 2.20); ϕ_L and ϕ_r account for the friction and heat transfer correction and the real gas property correction.

We present, as an example, three diagrams (Figure 2.36). The diagrams are constructed for helium ($R = 212$), with $\lambda = 350$ and $\Pi = 5$ for three values of $N = 10, 5$, and 2.5 , which correspond to the values of $(W_{\min} + W_{ba})/W_{\min}$ equal to 11, 6, and 3.5, respectively. In the diagrams, the abscissa axis is C_q , i.e., the projectile weight referred to the caliber cubed (g/cm^3), and the ordinate axis is the maximal pressure at the end of compression. The straight lines on the diagrams are lines of constant velocities V and temperatures T_{\max} . Consequently, each straight line on the diagram, corresponding to a constant temperature, is at the same time a constant velocity line.

We see from the diagrams that, with reduction of N for the same C_q and p_{\max} , the launch velocity and maximal gas temperature increase simultaneously. For example, for $N = 10$ and $C_q = 3$, a launch velocity of 7500 m/sec can be obtained only for $p_{\max} = 18,000$ atm and $T_{\max} = 6500^\circ \text{K}$; for $N = 5$, $p_{\max} = 11,000$ atm and $T_{\max} = 7200^\circ \text{K}$; for $N = 2.5$, $p_{\max} = 7500$ atm and $T_{\max} = 10,300^\circ \text{K}$.

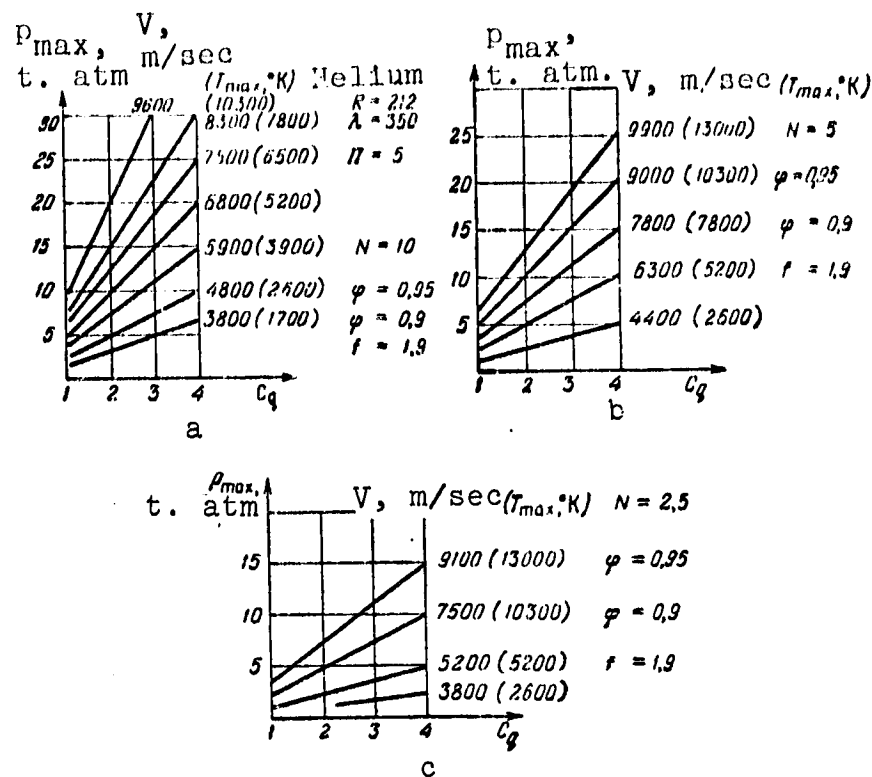


Figure 2.36. Launcher directive diagrams.

The dependence of p_{\max} and T_{\max} on N for a given velocity is shown in Figure 2.37. We see that, by varying N , which is proportional to the degree of volume increase during firing, we can, while retaining a given velocity, alter the maximal temperature and pressure in the launcher chamber in quite wide limits. This is quite natural, since the quantity N is connected with launcher efficiency.

In this way, we find the relationship between N , \bar{T}_{\max} , and p_{\max} for the optimal light-gas launcher. Knowing the maximal allowable pressure (strength parameter), we can relate the constructive parameter N with the maximal gas temperature (or velocity). We emphasize that the relations obtained are valid for any multistage LGL, since no limitations were imposed on the light-gas compression process.

Now we can examine the laws governing the compression process, i.e., we can seek the charging parameters p_0 and T_0 , and the initial system volume W_0 . Obviously,

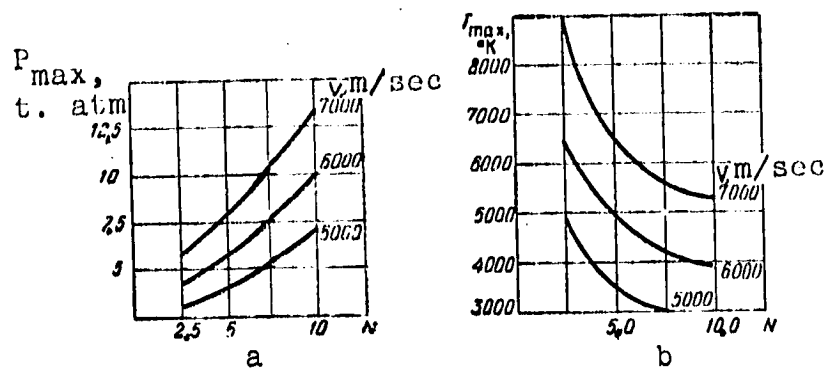


Figure 2.37. Dependence of p_{\max} and T_{\max} on gas expansion ratio N in the barrel for given launch velocity

$$m_1 = V_0 \frac{p_0}{RT_0} = W_{\min} \frac{p_{\max}}{RT_{\max}},$$

hence,

$$\frac{W_0}{W_{\min}} = \frac{p_{\max} T_0}{p_0 T_{\max}}.$$

For the compression process taking place with entropy change,

$$pW^s = \Phi,$$

from which we can easily obtain the expression for the geometric compression ratio: /98

$$\frac{W_0}{W_{\min}} = \left(\frac{\Phi_0 T_{\max}}{\Phi_{\max} T_0} \right)^{1/(s-1)}. \quad (2.34)$$

Assuming that the chamber temperature must not exceed 8000°K , we conclude from this same figure that N must not be less than 3.0. We finally take $N = 3$, $T_{\max} = 8000^\circ \text{K}$, $p_{\max} = 6200 \text{ atm}$, $V = 7000 \text{ m/sec}$.

Now we can analyze the compression process. Assume that a light piston, whose maximal velocity can reach 2000 m/sec , is used in the launcher, and the entropy function growth in the shock waves $\Phi_{\max}/\Phi_0 \sim 2.0 - 2.5$ (see § 2.2). Preheating of the gas in the launcher is not provided; therefore $T_0 = 290^\circ \text{K}$; consequently, $T_{\max}/T_0 = 27.5$.

TABLE 2.17. RESULTS OF CALCULATION OF ENTROPY
FUNCTION INFLUENCE ON INITIAL SYSTEM VOLUME*

Φ_{\max}/Φ_0	1	1,5	2,0	3,0	Φ_{\max}/Φ_0	1	1,5	2,0	3,0
$T_{\max}\Phi_0/T_0\Phi_{\max}$	27,5	18,4	14,7	9,2	p_0	1,5	4,4	8,7	24
W_0/W_{\min}	144	78	51	28	W_0/W_{ba}	48	26	17	9,3
p_{\max}/p_0	4000	1110	710	260	W_0	1670	880	580	320

*Translator's note. Commas in numbers represent decimal points.

Table 2.17 presents the values of W_0/W_{\min} , p_{\max}/p_0 , W_0/W_{ba} , W_0 for the caliber 50 mm ($W_{ba} = 34$ liters) for $\Phi_{\max}/\Phi_0 = 1, 1.5, 2.0$, and 3.0, for the case when the launch velocity is 7000 m/sec. The calculation was made using (2.34) and (2.35).

/99

The launcher parameter selection made above is naturally not the only possible choice. For example, we could increase the pressure to 10,000 atm. In this case, N will be about seven (Figure 2.37a). Then the maximal gas temperature decreases to 6000° K. It is obvious that the dimensions of this launcher will be smaller; however, a stronger forechamber is required*. Using (2.34), we can find the initial chamber volume, since $W_{\min} = W_{ba}/N$.

For a system with heavy piston, $\Phi_{\max}/\Phi_0 = 1$. For light piston systems or systems with entropy increase owing to throttling, the values of Φ_{\max}/Φ_0 are taken in accordance with the data presented previously.

The quantity p_0 is easily found from (1.7), which can be written as:

$$\frac{p_{\max}}{p_0} = \frac{\Phi_0}{\Phi_{\max}} \left(\frac{W_0}{W_{\min}} \right)^{\epsilon}. \quad (2.35)$$

* In light-gas launcher design practice, the compression chamber segment adjacent to the barrel in which the highest pressure is reached is termed the forechamber.

These formulas can be used to analyze the influence of ϕ_{\max}/ϕ_0 and T_0 on the chamber geometric dimension W_0 and the compression ratio p_{\max}/p_0 of the optimal system.

We shall now present a specific example of system optimal parameter selection for a launcher, for example, with a light piston.

We specify the quantities:

launch caliber $d = 50$ mm, $C_q = 2.5$ g/cm³;
barrel length in calibers $\lambda = 350$;
parameter $\Pi = 5$;
the light gas is helium ($R = 212$ kgm/kg deg);
velocity 7000 m/sec.

Using the directive diagram, we plot p_{\max} and T_{\max} versus N for $V = 5000, 6000, 7000$ m/sec (see Figure 2.37).

Assuming that the maximal chamber pressure cannot exceed $p_{\max} \sim 7000$ atm, we see from Figure 2.37 that a launch velocity of 7000 m/sec is obtained for $N > 4$.

We see from Table 2.20 that the initial optimal light-gas launcher chamber volume, as a function of entropy increase in the shock wave, lies in the range from 1670 to 184 liters. If the light piston is accelerated by powder gases, then in practice $\phi_{\max}/\phi_0 \sim 1.4 - 1.5$, and the chamber volume is best taken to be about 1000 liters. In launchers in which the light gas is accelerated by OHHM, $\phi_{\max}/\phi_0 \sim 2.5 - 3.0$, and in these launchers the initial volume may be taken considerably smaller. /100

It is interesting that increase of the initial gas temperature is equivalent to increase of the entropy growth [which follows directly from (2.34)]. Consequently, while maintaining the barrel

dimensions and projectile weight and velocity constant, in order to optimize the system it is necessary to reduce the gas chamber dimensions (reduce W_0 , since in this case the required compression ratio decreases) as the gas entropy (or the initial preheat) increases.

We discussed above the technique for solving the inverse problem — selecting the optimal launcher dimensions for given projectile weight and velocity. If the light-gas launcher were intended for launching a projectile of the same weight and with the same velocity, the problem would be completely solved. However, in practice, the situation is different: as a rule, it is necessary to launch from the same system projectiles of different masses with different velocities.

Therefore, we shall examine the direct problem: given the launcher, i.e., W_0 , W_{ba} , d , we wish to find the connection between the launch velocity and the charging parameters.

This problem can be formulated in two ways:

a) For given charging parameters, determine the velocity of a projectile of given weight. In this case, we simply carry out the system calculation. In the exact formulation, this problem is solved by the gasdynamic calculation presented in the first part of the book, or in the approximate formulation with the aid of the engineering method, which will be presented in § 2.9.

b) We wish to select the charging parameters so that, for given launcher geometric dimensions and projectile weight, the launch velocity will be maximal (the projectile weight and velocity are different from the design value for which the system parameters were selected).

Let us examine briefly this second formulation of the problem, for which we again use (2.29).

We determined previously the extremum of the function V under the assumption that η is constant, since we examined launchers with constant adiabatic efficiency. This approach was justified, since the launcher geometric dimensions were not specified, and they could be varied (for example, elongate the barrel, and so on). Now, in the solution of the direct problem, we cannot change the system geometric dimensions, and this must be considered in determining the extremum.

The quantity:

$$\frac{W_{\min}}{W_{\min} + W_{ba}} = \psi\left(\frac{W_{ba}}{W_0}, \frac{p_{\max}}{p_0}, \frac{\Phi_{\max}}{\Phi_0}\right)$$

is a function of p_0 and p_{\max} , the energy increase, and the ratio W_{ba}/W_0 , i.e., the launcher geometric parameters. /101

Differentiating with account for the dependence of W_{\min} on p_0 , and equating the derivative to zero, leads to an expression of the form:

$$\psi\left(a_0, p_{\max}, p_0, x, \frac{W_{ba}}{W_0}, \frac{\Phi_{\max}}{\Phi_0}\right) = 0,$$

and p_0 will appear in this expression to a fractional power.

It is not possible to obtain the solution of this equation for p_0 in explicit form, and therefore $(p_0)_{\text{opt}}$ must be found numerically or graphically. Here, it is very important that the optimal value $(p_0)_{\text{opt}}$ and, consequently, Π_{opt} will depend on all the quantities appearing in the expression for ψ . At a single point (for given η), p_0 and, consequently, Π_{opt} are found to be the same when determined by the two techniques.

Usually, it is not rational to carry out this calculation, since the question of light-gas launcher operating economy (charge weight economy) is not posed in practice.

Thus, for given projectile velocity and weight, we can select the optimal multistage light-gas launcher parameters, using the method described above.

However, when changing the projectile velocity and weight, it is necessary to change the launcher dimensions, in order to obtain the optimal conditions, and this is obviously undesirable.

When it is necessary to use a given light-gas launcher in an off-design regime, we can take other approaches; for example,

1. reduce the barrel length (reduce N);
2. reduce the charge weight ω (reduce p_{\max});
3. simultaneously reduce p_0 and ω (alter the ratio m_1/m);
4. change the light gas composition (add air), etc.

In this case, we need only make a ballistic calculation of the system, using the approximate method, in order to determine launch velocity.

In the general case, the selected regime which provides the specified projectile velocity will not be the extremal regime; however, this is not particularly important, since the launcher parameters will obviously be lower than the optimal values.

In concluding this section, we shall make some general remarks on selection of the quantities N , p_{\max} , T_{\max} , barrel length, chamber shape, etc.

a) Expansion ratio. It is best to select $N = W_{ba}/W_{\min}$ in the range 2 - 6, and with reduction of the "taper" the expansion ratio should be increased. For cylindrical chambers (which are not used in practice) $N \sim 10 - 14$.

b) Maximal pressure. We must always remember the connection which exists between the maximal pressure and C_q of the projectile.

/102

The lighter the projectile, the lower the required p_{\max} for the same velocity and the same chamber geometric dimensions.

Selection of a rational value of p_{\max} is very important in designing ballistic ranges. In modern barrel-type artillery, the maximal pressures are 4000 - 6000 atm. In the light-gas systems, this value can undoubtedly be increased, since in the light-gas launchers the time of high pressure action on the chamber material is an order of magnitude shorter than in artillery systems of the same caliber. Moreover, the length of the segment on which the high pressure is developed usually does not exceed 0.1 - 0.05 of the gas chamber length, which permits the use of special multilayer forechambers.

However, a pressure of 8000 - 10,000 atm, achieved in practice in many launchers, is by no means the limit. There are data in the literature on obtaining pressures of 20 - 30 thousand atmospheres in light-gas launchers [3, 19]. In this case, multilayer chambers (up to five layers), in which there are no internal threaded connections, are used. All attachments are made using flanges clamped together by external bolts.

c) Maximal temperature. We showed previously that T_{\max} , along with p_{\max} , is the parameter which determines the launch velocity. Unfortunately, it is not possible to obtain very high light-gas temperatures in the LGL because of the high heat transfer at the high gas pressures and velocities which are realized in the launchers.

In practice, the limiting temperature in the ballistic ranges without electrical discharge can be considered to be 7000 - 8000° K. When using an electrical discharge, the gas temperature can reach approximately 10,000° K for a very short time period. However, we note that high gas temperature reduces barrel service life markedly.

d) Piston weight. The next essential LGL constructive parameter is the piston weight. We mentioned above that selection of

the projectile weight, and also the value of T_{\max} , essentially specifies the light-gas energy, and since this energy in the first approximation is equal to the piston kinetic energy, the piston energy is thereby specified.

Using (1.12), we can determine the piston weight in the first approximation. Here, we must bear in mind that, when using powder gases to accelerate the piston, its maximal velocity is about 2000 m/sec; when using OHHM, or if there are two light pistons in the launcher, the maximal velocity is about 3000 m/sec. If the designer has selected a launcher with plastic piston, the question of selecting its weight becomes somewhat more complex because of the fact that the piston must have the kinetic energy required not only for compression of the light gas, but also for deformation of the polyethylene. Therefore, the hydropiston is usually made quite heavy, and its constructive parameters are worked out experimentally. /103

e) Chamber shape. The gasdynamic calculation in the one-dimensional formulation is formally applicable only if the transition from the gas chamber to the barrel is sufficiently smooth. Unfortunately, such smooth transition is not provided in all launchers; therefore, it is very important to know the influence of the forechamber transition shape on the launch velocity.

This can only be found experimentally.

As a result of the experiments conducted, it has been found that change of the transition angle from 0 to 90° leads to about 5% change of the velocity (Figure 2.38) This result is logical, since in the steep transition case a stagnant zone ("liquid cone") develops in the chamber and smooths out the irregularity. Experiments studying the influence of transition shape are important in two regards: first, they confirm the recommendation to the designers on the need for making the transition from the forechamber to the barrel sufficiently smooth; second, they confirm the possibility of using the one-dimensional model for the gasdynamic calculation. At the same time, the

comparatively weak influence of transition shape gives a basis for the designer to select this shape on the basis of constructive and technological considerations. However, if system fabrication conditions permit, we should make the transition from the gas chamber to the barrel comparatively smooth, with average taper angle $< 30^\circ$.

f) Barrel length. This question is very essential. We have shown that it is not the barrel length, but rather the quantity $W_{ba}/W_{min} = N$, i.e., the ratio of the volume at the end of expansion to the initial volume, which is of primary importance. We see from Figure 2.20 that in all cases use of $N > 10$ is ineffective.

In practice, if we take into account barrel friction and the influence of joints, this quantity will be still smaller. In order to clarify this question, we fabricated an experimental launcher, in which the expansion ratio was varied from 1 to 10 by elongating the barrel or changing the chamber volume. The experimental results are shown in Figure 2.39.

We see that it is advisable to take an expansion ratio not exceeding 6 - 7, since with further increase of the expansion ratio, the friction will have a larger effect that the projectile base pressure.

However, it does not follow from these data that the barrel length can be arbitrarily long. The reason is that industry has

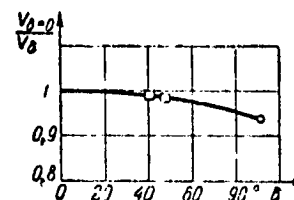


Figure 2.38. Influence of gas chamber taper on launch velocity

/104

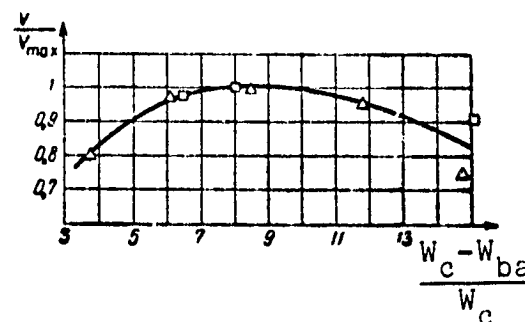


Figure 2.39. Influence of expansion ratio on launch velocity with account for friction:

Δ — $L_{ba} = 60 - 325$ calibers
($d = 7.5$ mm); \circ — $L_{ba} = 220$
calibers ($d = 16$ mm)

available equipment adapted for drilling bores whose length does not exceed 80 - 120 calibers. Therefore, in practice, the light-gas launcher barrels must be made from several pieces joined with one another. The presence of joints between the barrels, no matter how perfectly they are fitted, causes projectile impact on the joints, and sometimes leads to projectile destruction within the barrel.

Studies made, in which the ratio W_{ba}/W_{min} was held constant but the barrel length was varied, showed that it is not advisable to use barrels whose length exceeds 200 - 300 calibers.

In view of the fact that the optimal barrel length depends markedly on such individual launcher qualities as inner surface smoothness, curvature, conditions of the joints, and so on, the optimal length must be determined experimentally.

g) Contamination of the light gas. The presence of impurities in the light gas has a marked influence on the molecular weight, and consequently on the sound speed.

Table 2.18 shows the sound speed in helium as a function of the volumetric percentage content of an impurity (with molecular weight $\mu = 28$), and also the molecular weight of the mixture. /105

We see from the table that the sound speed decreases, even for comparatively small impurity content.

We shall say a few words about the reasons for the appearance of impurities.

1. Light-gas quality.

Depending on bottle filling level, the helium content lies in the range 99.97 - 99.91%, i.e., the gas is quite pure.

TABLE 2.18. SOUND SPEED IN HELIUM AS FUNCTION OF VOLUMETRIC PERCENTAGE IMPURITY CONTENT*

%	0	1	2	5	10	20
a/a_0	1	0,97	0,93	0,85	0,76	0,64
μ	4	4,3	4,6	5,5	6,9	9,8

* Translator's note. Commas in numbers represent decimal points.

2. Filling the system.

When filling the system, some amount of air always remains in the system. The air content by volume is

$$\epsilon_1 = \frac{p_{00}}{p_0} \cdot 100\%.$$

where p_{00} is the chamber pressure prior to filling, p_0 is the pressure after filling. When using evacuation, p_{00} is about 0.05 - 0.01 atm, $p_0 \sim 5 - 10$ atm. Consequently, with proper filling:

$$\epsilon_1 = \frac{0.05 - 0.01}{5 - 10} \cdot 100\% = 1 - 0.1\%.$$

The coefficient of launch velocity reduction, owing to light-gas contamination, may vary over quite wide limits, depending on launcher construction.

For well constructed launchers, this coefficient may be taken equal to 0.95 - 0.98. Usually, this coefficient is taken into account in the calculation by corresponding reduction of the coefficient ϕ_L .

§ 2.7. Remarks on Charge Selection

In contrast with the conventional artillery systems, where the powder charge is of decisive importance, in the light-gas launchers, the powder charge plays a secondary role. The powder charge must provide in the compressed light gas those values of p_{\max} and T_{\max} which were determined in the ballistic calculation of the gas part of the launcher.

Normally no particular limitations are imposed on powder charge and charge cost is small in comparison with the overall firing cost. This makes charge design still easier.

However, familiarity with the basic charge design techniques is necessary when designing the light-gas launcher [2].

A powder charge consisting of the following three basic parts is normally used in light-gas launchers:

/106

q 1) an igniter cap of percussion or electrical type; normally, primer sleeves PS or EPS* are used, and are threaded into the breech-block or a sabot, which seals the launcher chamber;

2) igniter — a small amount of black powder located around the primer cap, either compactly or, if the charge is elongated, in the form of a tube along the entire charge (primer weight is 1 - 3% of the charge weight);

3) the charge proper, consisting of pyroxylin or nitroglycerin powder.

If the charge is not required to have particularly high characteristics, the use of pyroxylin powders is preferable, since they are less toxic.

Table 2.19 shows the characteristics of the conventional artillery and firearm powders used in launchers [2].

In addition to the powder characteristics listed in the table, there is still another characteristic which depends on the charge shape. This is the total pressure impulse I_c , which is determined by the initial burning grain web thickness and by the burning rate coefficient u_1 in the burning rate law:

$$\frac{de}{dt} = u_1 p,$$

where e — web half thickness.

* PS — standard primer sleeves; EPS — electrical primer sleeves.

TABLE 2.19*

Powder	Specific energy, kcal/kg	Combustion temp, °K	Density kg/liter	Burning rate u_1 , dm ³ /sec·kg	Powder force f , kg·dm/kg
Pyroxylyene	900—800	2800—2500	1,62—1,56	$0,6—0,9 \cdot 10^{-5}$	770 000—950 000
Nitroglycerine	1100—1200	3000—3500	1,62—1,56	$0,7—1,5 \cdot 10^{-5}$	900 000—1 200 000
Smoking					280 000—300 000

*Translator's note. Commas in numbers represent decimal points.

By definition,

$$I_c = \int_0^{t_c} p dt = p_{av} \Delta t = \frac{e_1}{u_1}, \quad (2.36)$$

where e_1 — initial web half thickness.

We see from (2.36) that the powder charge burnup time depends on three quantities: u_1 — burning rate at atmospheric pressure; e_1 — initial web thickness; p_{av} — average pressure during the burning process*. From (2.36), it follows:

$$\Delta t = t_{com} = \frac{I_c}{p_{av}}.$$

It is obvious that, from the viewpoint of best powder energy utilization, Δt should be less than the time of gas compression by the piston, and the powder gases which form should have three- - five-fold expansion (by volume).

Finally, the charging conditions are characterized by the charging density:

*We assume that the burning rate dependence on pressure is linear.

$$\Delta = \frac{\omega}{W_c}, \quad (2.37)$$

where ω — charge weight in kg, W_c — powder chamber volume in dm³.

In designing the LGL with both heavy and light piston, the design of the powder part of the launcher can be made using the well-developed techniques of interior ballistics.

Usually, when designing a launcher, it is necessary to determine the charging density Δ and the powder grade (i.e., e_1). The piston velocity V_p and its weight are determined so that the piston kinetic energy will be adequate for light-gas compression, to ensure obtaining the specified values of P_{\max} , T_{\max} . The maximal powder gas pressure is usually also specified in advance from strength considerations. Use of ballistic tables is advisable for the preliminary calculations. Normally, the tables are calculated for various values of the charging density Δ .

The table entry numbers are the maximal powder stage pressure P_{\max} and the relative piston travel (relative expansion of the volume behind the piston) $\lambda = \frac{l}{l_0}$, where l is the piston travel, $l_0 = \frac{W_c}{S}$ is the reduced charge chamber length, S is the piston barrel bore section area. The tables present the piston velocity V_{tab} for the relative distance traveled λ and given P_{\max} , calculated under the condition that $\sqrt{\frac{\omega}{\varphi G_p}} = 1$, where G_p is the piston weight, $\varphi = 1 + 0.33 \frac{\omega}{G_p}$.

In spite of the fact that the tables are compiled without account for backpressure and, generally, $p \sim 300$ kg/cm², LGL operating experience shows that the tabular calculation yields satisfactory agreement with the experimental results, and can be used for light-gas launcher preliminary design.

/108

When developing a ballistic range, the first experiment is usually made with charge size equal to half the design size (by weight).

100

Then, the charge size is gradually increased, with account for the pressures which are obtained in the powder and gas chambers. Therefore, pressure measurement during charge development in the ballistic system is absolutely necessary.

In launchers having comparatively small dimensions and high pressures, we sometimes limit ourselves to estimation, using the formula:

$$P_{\max} = \frac{\Delta f}{1 - \alpha \Delta} \quad (\text{where } f \text{ — powder force, } \alpha \sim 1 \text{ covolume})$$

which yields the maximal possible powder chamber pressure for instantaneous charge burnup, and the maximal gas chamber pressure is estimated from the permanent deformation of the forechamber or the initial segment of the ballistic barrel.

In designing and developing the light-gas launcher charge, we must always remember that the powder charge must have adequate strength to withstand the piston pressure. When filling the gas chamber with the light gas, the pressure p_0 acts on the piston, and the compressive force $F = p_0 S$, where S is the piston area, acts on the charge. If crushing of the charge takes place under the action of this force, the charge density increases, which may lead to failure of the breech part of the launcher or wedging of the breechblock.

The following piston locating techniques are normally used:

1. A strong cylindrical metal sleeve in which a large number of holes of diameter 5 - 10 mm are made, so that the powder gases act on the sleeve from all sides (this prevents bulging and wedging of the sleeve). The powder charge is located inside the sleeve.

2. A cruciform metal, plastic, or wooden retainer — in this case the powder charge, is located in four viscose bags, and is packed along the retainer slots.

3. A strong cardboard sleeve (for small-caliber launchers with low initial pressure).

In certain cases, in order to facilitate retainer operation, longitudinal or spiral grooves of small section are made on the piston surface, and the light gas passes through these grooves into the charge chamber and equalizes the load acting on the retainer. It is /109 obvious that in this case the chamber filling must take place quite slowly (the gas pressure in the charge chamber and in the gas chamber is monitored by pressure gauges during filling). This method is used only for large light-gas launchers.

§ 2.8. Sabots, Projectiles, and Diaphragms

In developing methods for increasing projectile velocity, the researcher encounters three limitations:

1. The "limiting" projectile velocity, associated with the launch gas internal energy and the limiting temperature which the materials used will allow.

2. The launcher forechamber material strength, which limits the maximal pressure p_{\max} in the launcher chamber.

3. The projectile strength, which limits the maximal pressure in the launcher barrel.

Let us examine the third limitation in more detail.

When launching a solid body (projectile) from a barrel system, the projectile velocity is connected with the gas pressure acting on the projectile base by the obvious relation:

$$\frac{mV^2}{2} = s \int_0^{L_{ba}} p(L) dL = s p_{av} L_{ba}, \quad (2.38)$$

where m and V are the projectile mass and velocity, s and L_{ba} are

the barrel cross section area and length, $p(L)$ is the pressure acting on the projectile.

Let us see how we can characterize the function $p(L)$. First, there is a limiting pressure $p_{\max \text{ pr}}$, which is determined from projectile strength considerations. The maximal acceleration acting on the projectile:

$$g_{\max} = \frac{s p_{\max \text{ pr}}}{m}.$$

Let us examine a projectile (Figure 2.40) consisting of the element 1 and the driving sabot 2. It is obvious that the inertial force acting from the element (mass m_e) on the sabot:

$$f_1 = m_e g_{\max} = \frac{m_e p_{\max \text{ pr}} s}{m}$$

and the specific pressure:

$$\sigma = \frac{F_1}{s_1} = \frac{m_e s}{m s_1} p_{\max \text{ pr}},$$

where s_1 — contact surface area. Since the quantity σ is limited by the sabot material strength, the quantity $p_{\max \text{ pr}}$ is also naturally limited, and is equal to:

$$p_{\max \text{ pr}} = \frac{\sigma s_1 m}{m_e s}.$$

Second, there is an average pressure p_{av} , which was introduced by (2.38). It is obvious that this pressure is uniquely associated with the projectile and barrel parameters by the relation:

$$p_{av} = \frac{mV^2}{2sL_{ba}}. \quad (2.39)$$

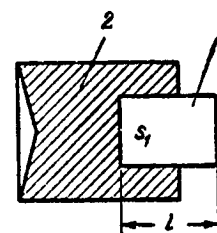


Figure 2.40.
Sabot and
projectile

If we define the pressure efficiency η_1 by the relation:

$$\eta_1 = \frac{p_{av}}{p_{max} pr}$$

and replace in (2.39) p_{av} through η_1 and $p_{max} pr$, we obtain the equality:

$$\eta_1 p_{max} pr = \eta_1 \frac{\sigma s_1 m}{m_e s} = \frac{m V^2}{2 s L_{ba}},$$

hence,

$$V^2 = \eta_1 \frac{2 s_1 \sigma L_{ba}}{m_e} \quad (2.40)$$

We take a cylindrical element of diameter d and length l . Then,

$$m_e = s_1 l \rho_e, \quad \frac{s_1}{m_e} = \frac{1}{\rho_e l},$$

where ρ_e — element density.

Formula (2.40) for this particular case takes the form:

$$V^2 = \eta_1 \frac{2 \sigma L_{ba}}{l \rho_e}$$

Consequently, the launch velocity will be higher, the larger the coefficient η_1 , the stronger the sabot σ , the longer the barrel L_{ba} , and the shorter the element length l , and the lower its density.

The magnitude of the coefficient η_1 is determined by the gas-dynamic characteristic of the firing process.

1. η_1 will be larger, the smaller the ratio V/a , i.e., the less the wave effect influence (a — sound speed in the launch gas). This is achieved by using low-molecular gases and increasing the gas temperature.

2. η_1 can be increased by utilizing the hydroeffect, heat addition, and so on (Figure 2.41), which is accomplished by selecting the launcher configuration.

/111

The next parameter which the designer can vary is the barrel length. We see from (2.40) that for given projectile dimensions it is advantageous to use longer barrels. However, we must take into consideration that in the actual launcher there is considerable friction of the gas and the sabot itself with the barrel; therefore, in practice, it is not advisable to take a barrel length exceeding 150 - 200 calibers. Thus, elongation of the barrel must take place along with increase of the caliber, and this means that it is easier to launch a given projectile from launchers of larger caliber.

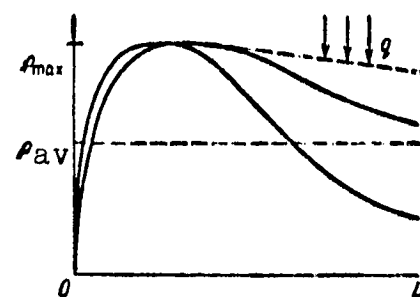
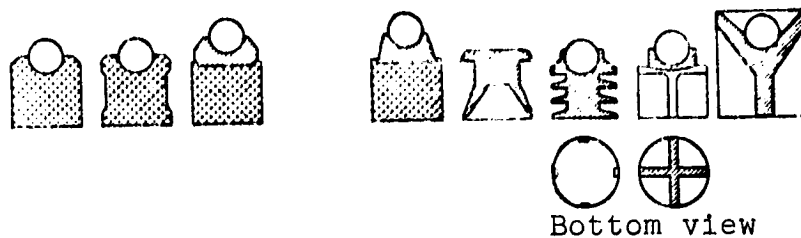


Figure 2.41. Variation of pressure on projectile along the barrel

Now, let us turn to the maximal pressure which the projectile can withstand.

Figure 2.42 shows various 8 mm-diameter sabots made from duraluminum, titanium, textolite, and polyethylene, and intended for launching a 5 mm-diameter sphere with specific weight 17 (weight 0.46 grams). The first line of the table in Figure 2.42 shows the projectile coefficient C_q , the second line is the projectile weight, the third line is the sabot weight, and the fourth line is the maximal pressure which the projectile can withstand without failure. We see that the projectiles have high strength, but, at the same time, the limiting pressure which the projectile can withstand is considerably lower than the pressure which the barrel can withstand (up to 112 8000 kg/cm² for two-layer construction). Using the similarity criteria, on the basis of these data we can design sabots for other barrel diameters. Here, we must always keep in mind that reduction of the absolute dimensions of the projectile (sphere, for example) reduces the loads experienced by the sabot.

In practice, it is not sufficient to ensure integrity of the projectile in the barrel. Usually, it is also necessary to



	Tex	Tex	$\frac{D16T}{Pol}$	$\frac{D16T}{Tex}$	$\frac{D16T}{Tex}$	$\frac{D16T}{Tex}$	$\frac{D16T}{Tex}$	$\frac{D16T}{Tex}$	$\frac{D16T}{Tex}$
C_g	1,8	1,6	2,1	2,4	2,3	2,0	1,9	1,6	1,7
q	0,92	0,81	1,06	1,21	1,19	1,02	0,85	0,83	0,89
q_n	0,46	0,35	0,60	0,75	0,73	0,56	0,48	0,37	0,43
P_m	1800	<1700	5400	6300	>6300	2600	<5200	<4500	>5800

Figure 2.42*. Different projectile forms:

Tex — textolite; Pol — polyethylene

*Translator's note. Commas in numbers represent decimal points.

separate the sabot from the element when the projectile leaves the barrel. As a rule, this is achieved either by fabricating a split sabot, i.e., a sabot assembled from two or three component parts, or by breaking the sabot up as it collides with a special thin barrier (cardboard, or plywood, for example) whose influence on the element is slight. Special splitters of different form are also used.

Usually, provision for sabot separation is particularly difficult when working with a small-caliber launcher used to study the impact process, since in this case the distance at which sabot separation takes place is usually restricted. Development of the sabot separation procedure requires conducting a large number of experiments and, unfortunately, with change of the projectile shape and weight, the development work must be repeated.

The sabot separation question is resolved more simply when conducting aerodynamic studies, since the aerodynamic characteristics of the model and of the sabot fragments are usually different, and the latter fall behind the model.

In concluding this section, we shall make some remarks on the methods used to force the projectile in the barrel bore.

Usually, three forcing techniques are used: by deformation of a sabot extruded through the conical entrance segment of the barrel, by special diaphragms, and by shearable collars on the projectile.

Use of a conical sabot is the simplest technique; however, it makes it possible to obtain only comparatively low forcing pressures, and leads to the necessity for a quite heavy sabot, since its strength must be maintained even after contraction.

Use of diaphragms permits considerable reduction of the projectile weight, and at the same time permits increasing the forcing pressure to 1000 - 1500 atm, or even higher.

Figure 2.43 shows a diaphragm before and after rupture.

Figure 2.44 shows a drawing of the diaphragm assembly.

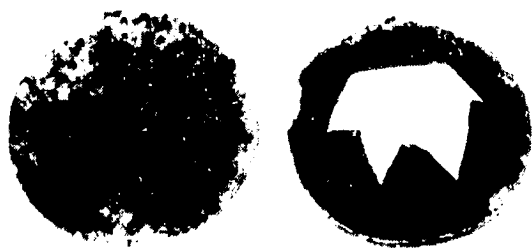


Figure 2.43. Diaphragm before and after rupture

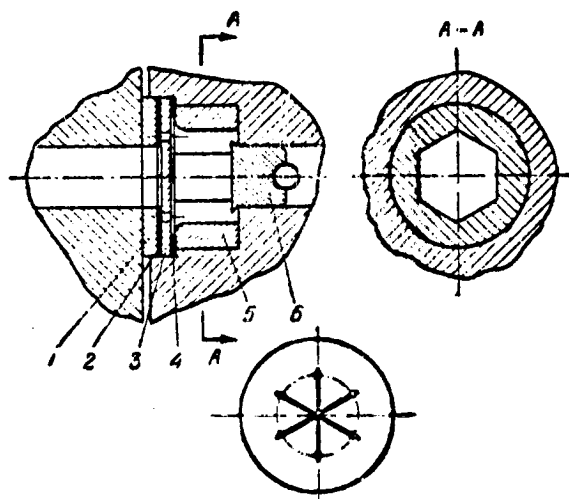


Figure 2.44. Schematic of diaphragm assembly:

1 — ring; 2 — foil; 3 — diaphragm; 4 — seal 5 — polyhedron; 6 — projectile

Usually, the diaphragms are developed experimentally using special powder bombs, and not only is the burst pressure determined but, most of all, integrity

of the diaphragm lobes after opening is ensured. In order to ensure /113
opening of the diaphragm into the required number of lobes, the diaphragm is first scribed into 3 - 6 lobes (the scribing depth extends to half the thickness). Holes are sometimes drilled at the ends of the scribe lines, in order to relieve the stresses. The diaphragm dimensions are selected with account for the fact that, after complete opening, the aperture must be no less than the barrel cross section. Behind the diaphragm there is located a polyhedron (with number of sides equal to the number of diaphragm lobes), on which the lobes rest after opening. The diaphragm material is soft steel, copper, /114
or brass. Sealing of the membrane assembly is ensured by proper tensioning of the joint.

When holes are drilled at the ends of the diaphragm scribe lines (Figure 2.44), a special foil diaphragm is installed, in addition to the primary diaphragm, to provide sealing.

§ 2.9. Approximate Light-Gas Launcher Analysis Method

The calculation of launchers of all types is made by integrating the gasdynamic equations on electronic computers, using standard programs.

However, all the available techniques for such calculations require considerable computer time, which makes them tedious and not always convenient. Therefore, we need a short, approximate technique for calculating launcher muzzle velocities which does not require the use of computers.

In the following, we describe a short, approximate calculation technique. This technique is based on results obtained by numerical solution of the gasdynamic equations.

The technique for approximate calculation of the launcher muzzle velocity is based on the assumption that the firing process can be broken down into two stages:

1. the process of obtaining the light gas with parameters

$$a_{\max}, p_{\max}, T_{\max}.$$

2. the firing process.

All the remaining factors — piston motion, real gas properties, and so on — are accounted for by coefficients. This approach makes it possible to calculate any gasdynamic system (with heavy, light, and hydrodynamic pistons, diaphragm-type, electro-pulsed, and so on).

The techniques for calculating both stages and determining the auxiliary coefficients are based on numerical solution of the gasdynamic equations.

The primary launcher parameter is the projectile muzzle velocity:

$$V = V_1 + a_{\max} \cdot \phi_V \cdot \phi_r \cdot \phi_L \cdot f\left(\frac{m_1}{m}, \kappa, \frac{W}{W_{\min}} = 20\right), \quad (2.41)$$

where V_1 is the transport velocity (m/sec), a_{\max} is the maximal sound speed in the light gas (m/sec), ϕ_V is the expansion ratio coefficient (Figure 2.20), ϕ_L is the coefficient of friction and heat transfer losses, ϕ_r is a coefficient accounting for the real gas properties, $f\left(\frac{m_1}{m}, \kappa, \frac{W}{W_{\min}} = 20\right)$ is the solution of the problem of launching a projectile of mass m from a cylindrical tube (Figure 2.21) with expansion ratio equal to 20, W_{\min} is the chamber volume at the end of compression, W is the chamber volume at the end of compression plus the barrel volume, $W = W_{\min} + W_{ba}$, κ is the adiabatic exponent, m_1 is the launch gas mass.

/115

The following quantities are usually given in launcher design:

- 1) light-gas type (exponent κ and a_0);
- 2) maximal light gas pressure p_{\max} ;
- 3) projectile weight q ;
- 4) barrel volume and dimensions W_{ba} , L_{ba} , s ;

- 5) gas chamber volume and dimensions W_0, L_0, S ;
- 6) maximal powder-gas pressure p_{\max} ;
- 7) powder chamber volume and dimensions W_c, L_c ;
- 8) piston weight G_p ;
- 9) powder charge weight ω ;
- 10) initial light-gas pressure p_0 ;
- 11) powder-gas adiabatic exponent κ_p .

I. Launch velocity calculation scheme
(case of instantaneous charge burnup)

1. Knowing the piston weight G_p and the powder charge weight ω , using Figure 2.7, we can determine the dimensionless piston velocity \bar{V}_p for the given $W_0/W_p, \kappa, \omega/G_p$.

2. Knowing the dimensionless velocity, we can determine the true maximal piston velocity without account for backpressure:

$$V_p = \bar{V}_p \cdot a_p = \phi f a_p, \quad a_p = \sqrt{\kappa_p R_p T_p},$$

where R_p, T_p — are the powder-gas constant and powder burning temperature, ϕ is the loss coefficient ($\phi \sim 0.97 - 0.95$ for the piston*).

If we consider backpressure, the true maximal velocity will be 5 - 20% lower (Figure 2.45).

From the known maximal piston velocity, using Figure 2.30, we determine the entropy increase during the compression process (correction to the sound speed).

* Calculation using the ballistic tables yields a more accurate result, and is to be preferred when the charge does not burn up instantaneously.

3. Knowing p_{\max} , p_0 , and the entropy increase correction K_a , we determine the sound speed in the compressed light gas:

$$a_{\max} = a_0 \left(\frac{p_{\max}}{p_0} \right)^{(1-\gamma)/2} \cdot K_a.$$

4. Then, we calculate the light-gas mass*:

/116

$$m_1 = \gamma_0 p_0 W_0 \cdot \frac{1}{g}$$

(where γ_0 is the gas specific weight at $p = 1$ atm), and using this mass and the projectile mass m with the aid of graphs similar to those shown in Figure 2.27, we find the theoretical launch velocity without correction for "taper", friction, and heat transfer (here, we take $W/W_{\min} = 20$);

$$V_{\max} = a_{\max} \cdot f(\Pi, x, x=20).$$

Now, we must determine the magnitude of the correction coefficients.

5. Determination of correction for expansion ratio. The gas volume at the end of compression is easily found from (2.35):

$$W_{\min} = W_0 \left(\frac{p_0 \Phi_{av}}{p_{\max} \Phi_0} \right)^{1/\gamma}$$

where Φ_{av} is the average gas entropy (we use the average entropy, since the difference between the values of the entropy function at the wall and at the piston cannot reach 50%).

That part of the gas in which the entropy increase is maximal is the primary part participating in the launch; therefore, we use the value Φ_{\max} when calculating the sound speed in the launch gas. However, when it is necessary to examine all the gas as a whole, the entropy function should be averaged:

$$\frac{\Phi_{av}}{\Phi_0} = \left(\frac{\Phi_{\max}}{\Phi_0} + 1 \right) \cdot 0.55. \quad (2.42)$$

* Usually, the ratio $m_1/m = \Pi$ is given, and therefore the quantity m_1 is known. In this case, p_0 is found from (2.44).

From the known W_{\min} and the barrel volume W_{ba} , we find the expansion ratio:

$$\frac{W}{W_{\min}} = 1 + \frac{W_{ba}}{W_{\min}}$$

and with the aid of Figure 2.20, we find the correction ϕ_V . We emphasize that the primary importance in calculating this coefficient lies not in the barrel length itself, but rather in the ratio of the volume at the end of expansion to the initial volume. We see from Figure 2.20 that, in all cases, it is advisable to take this ratio no larger than 10; however, in practice, if we consider friction in the barrel and the influence of barrel joints, this quantity will be still smaller (no more than 5 - 6). /117

6. Correction for real gas properties. The influence of the real gas properties is of considerable interest.

We assume a launcher with given gas chamber volume and maximal allowable pressure p_{\max} . Assume this chamber is filled with hydrogen. The energy of the given hydrogen charge:

$$E_{hy} = \frac{m_{hy} a_{hy}^2}{\kappa_{hy} (\kappa_{hy} - 1)}.$$

If we fill the chamber under the same initial pressure with helium, the gas energy will be:

$$E_{he} = \frac{m_{he} a_{he}^2}{\kappa_{he} (\kappa_{he} - 1)}.$$

Consequently,

$$\frac{E_{hy}}{E_{he}} = \frac{a_{hy}^2 \kappa_{hy} (\kappa_{hy} - 1)}{2 \cdot a_{he}^2 \kappa_{he} (\kappa_{he} - 1)} = \frac{a_{hy0}^2 \kappa_{hy} (\kappa_{hy} - 1)}{2 \cdot a_{he0}^2 \kappa_{he} (\kappa_{he} - 1)} \left(\frac{p_{\max}}{p_0} \right)^{\frac{\kappa_{hy}-1}{\kappa_{hy}} - \frac{\kappa_{he}-1}{\kappa_{he}}},$$

since $m_{he} = 2m_{hy}$.

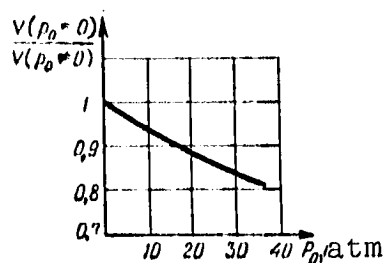


Figure 2.45. Correction for backpressure

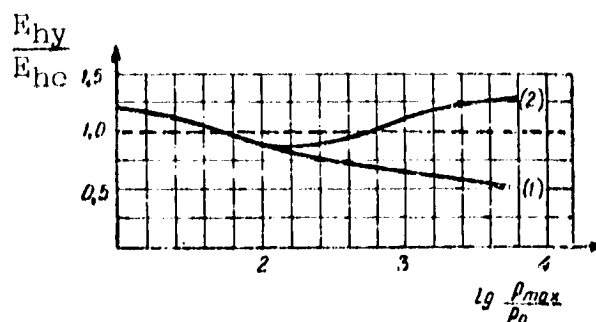


Figure 2.46. Ratio of charge energy required for compression of hydrogen and helium versus compression ratio (1 — helium; 2 — hydrogen)

Figure 2.46 shows the ratio E_{hy}/E_{he} versus the compression ratio. Curve 1 corresponds to the assumption that the gases are ideal. Curve 2 is calculated with account for hydrogen dissociation, and corresponds to the initial gas temperature $T_0 = 300^\circ \text{ K}$. The resulting E_{hy}/E_{he} relation is very interesting. In the region of compression ratios of the order of 80 - 150, the helium charge energy is greater than the energy of the equivalent hydrogen charge. In other words, when converting from helium to hydrogen, the powder charge must be reduced in order to obtain the same final parameters.

This conclusion is confirmed by direct experiment. The powder charge when operating with helium is actually larger than when working with hydrogen. Conversely, at high compression ratios, the equivalent hydrogen charge requires considerably larger powder charge for its compression, because of energy expenditure on dissociation.

If gas preheating is used in the launcher, all these effects become considerably stronger, since marked hydrogen dissociation begins at temperatures exceeding 4000° K .

The hydrogen dissociation process can be utilized quite successfully in the light-gas launcher. For maximal light-gas temperature at the end of compression, exceeding $5000 - 6000^\circ \text{ K}$, the internal energy of hydrogen is 40 - 60% higher because of dissociation than for an ideal gas, even at a pressure of 10,000 atm. This means that a more powerful charge is needed to compress the real gas to the

same p_{\max} and T_{\max} . But then, when firing takes place, the gas be- /118
gins to expand, its temperature decreases, and recombination of the
molecules starts, in the process of which the energy previously ex-
pended on ionization begins to be released in the barrel. Calcula-
tions show that the energy released during recombination is quite
significant, as a result of which the projectile velocity will in-
crease markedly. For example, at the maximal temperature 7000°K ,
because of dissociation (in comparison with the calculations made for
an ideal gas), the powder charge energy may be nearly doubled, and
the velocity increase because of recombination in the barrel reaches
15 - 20% in the case when the expansion ratio is equal to 4. This
means that the coefficient ϕ_r reaches $\phi_r = 1.15 = 1.2$.

In practice, we take $\phi_r \sim 1.05 - 1.1$ for hydrogen, and $\phi_r = 1$
for helium.

The coefficient ϕ_r is introduced into consideration when it is
assumed that the gas is ideal (κ and a are taken for the ideal gas).

If the characteristics of the real gas (for example, hydrogen)
are known, the quantity κ can be taken from Table 2.15, averaging it
in the operating range, and the sound speed is taken from Table 2.13,
also averaging it. In this case the coefficient ϕ_r is not introduced.

7. The loss (friction, heat transfer) correction coefficient for:

small-caliber launchers (6 - 16 mm): $\phi_L = 0.8$;

large-caliber launchers (23 - 85 mm): $\phi_L = 0.9$.

8. Correction for piston motion. Analysis of the exact gas-
dynamic calculations shows that the forward movement of the piston
has some influence on the initial segment of the projectile motion,
increasing the projectile velocity by 0.6 - 0.7 of the piston velo-
city. Conversely, piston rebound leads to some decrease of the
velocity. Therefore, for the piston of conventional construction,

we can take, in the first approximation:

$$V_1 = 0,5 V_{p \text{ max}}.$$

In the hydropiston case, i.e., when the piston forward wall motion is specifically used to increase the projectile velocity $V_1 \sim$ 1000 - 1200 m/sec, and depends on the piston characteristics. /119

9. Account for heat addition in the launcher barrel is usually made with the aid of exact numerical calculation on a computer. The influence of heat addition (removal) in the process of projectile motion can be evaluated approximately with the aid of Figure 2.31, which shows the results of several exact calculations.

II. Calculation of maximal light-gas chamber pressure

The light gas energy prior to compression initiation is:

$$E_0 = \frac{m_1 a_0^2}{x(x-1)}.$$

The piston energy upon reaching maximal velocity (without account for backpressure):

$$E_p = \frac{m_p V_{p \text{ max}}^2}{2}.$$

The light gas energy when all the piston energy is transferred to the gas (compression energy when the projectile is restrained):

$$E_{\text{gas}} = E_0 + E_p = \frac{m_1 a_{\text{max}}^2}{x(x-1)}.$$

Consequently, we can write:

$$\frac{a_{\text{max}}^2}{a_0^2} = 1 + \frac{m_p (x-1)}{2m_1} \frac{V_{p \text{ max}}^2}{a_0^2}.$$

Since:

$$\frac{a_{\max}^2}{a_0^2} = \left(\frac{p_{\max}}{p_0} \right)^{(x-1)/x} \left(\frac{\Phi_{av}}{\Phi_0} \right)^{1/x},$$

we obtain the formula for the maximum light-gas pressure and the end of compression:

$$\frac{p_{\max}}{p_0} = \left(1 + \frac{m_0^x (x-1)}{2m_1} \frac{V_{\max}^2}{a_0^2} \right)^{x/(x-1)} \left(\frac{\Phi_0}{\Phi_{av}} \right)^{1/(x-1)}. \quad (2.43)$$

The quantity Φ_0/Φ_{av} is found with the aid of (2.42) and Figure 2.30, if we consider that:

$$\frac{\Phi_{\max}}{\Phi_0} = (K_a)^{2x},$$

where K_a — correction for increase of the sound speed.

If we take the launcher operating scheme in which the forcing pressure is equal to $p_\phi = p_{\max}$, the calculation terminates at this point, and (2.43) serves only for verification of charge and piston weight selection correctness. (These quantities are determined when selecting the basic launcher parameters.) In practice, the forcing pressure is always less than the maximal pressure p_{\max} ; therefore, the true maximal pressure in the launcher is always less than the value obtained from (2.43). /120

In the first approximation, the condition $p_{\max} > p_\phi$ has no effect on projectile velocity (if the barrel length is greater than 100 - 150 calibers). The primary influence of p_ϕ is on the maximal pressure acting on the projectile in the barrel bore. With forcing pressure of the order of 500 - 1000 atm, it is possible to reduce the pressure on the base of the projectile to $(0.25 - 0.33)p_{\max}$, i.e., for $p_{\max} \sim 15,000 - 20,000$ atm, the maximal pressure acting on the projectile does not exceed 4000 - 6000 atm.

There are several techniques for approximate calculation of the maximal pressure in the case when $p_\phi < p_{\max}$. These techniques are based on account for leakage of part of the gas from the fore-chamber into the barrel. Unfortunately, all these techniques are unreliable; therefore, it is best to limit ourselves in the calculation to determining p_{\max} , using the technique outlined above, which serves as the starting point for launcher development.

In developing the launcher, the maximal pressure must be measured, and then we correct the charging conditions (ω , p_0 , G_p , etc.), so as to gradually approach the maximal light-gas pressure specified on the basis of strength.

The initial pressure p_0 can be found from the known light-gas weight:

$$p_0 = \frac{m_1 a_0^2}{W_0 \pi g}, \quad (2.44)$$

where g — gravity force acceleration; a_0 — initial sound speed in the light gas.

The sound speed in the light gas:

$$a_0 = \sqrt{\pi g R T_0},$$

where

$$R = \frac{848}{\mu}.$$

Here, μ — molecular weight; T_0 — initial gas temperature.

For helium at $T_0 = 290^\circ \text{ K}$, $a_0 = 1000 \text{ m/sec}$, and for hydrogen at $T_0 = 290^\circ \text{ K}$, $a_0 = 1250 \text{ m/sec}$.

10. The light-gas energy is found from the formula:

$$E_{\text{he}} = \frac{m_1 a_{\max}^2}{\pi (n-1)}.$$

This energy must be imparted to the light gas either by an electrical discharge (ignition of fuel) or by compression by a piston shock wave. /121

11. The light-gas utilization efficiency:

$$\eta = \frac{mV^2}{2E_{he}}$$

We assumed above that the piston and powder charge weights are known in advance.

However, this is not always so. Frequently the values of G_p and ω must be assumed, and therefore the maximal pressure given by (2.43) may be either lower than the assumed p_{max} or, conversely, much higher. Then, it is necessary to assume a new charge weight (and, if necessary, a new piston weight), and make a new calculation.

In practice, the charge and piston weight must be selected so that the maximal pressure found from (2.43) exceeds the pressure allowable on the basis of launcher strength by no more than 15 - 30%. The further selection of the launcher parameters is accomplished experimentally.

After selecting the final value of ω , it is necessary to verify the maximal possible powder pressure (with instantaneous burn-up):

$$P_{max} = \frac{\Delta f}{1 - \alpha \Delta},$$

where F — powder force, Δ — charging density, α — co-volume ($\alpha - 1$).

It is obvious that P_{max} should not exceed significantly the pressure allowable on the basis of strength. (The values of P_{max} can be calculated more exactly using ballistic tables.)

In the case of compression by a shock wave (diaphragm-type launchers), we can consider for preliminary estimates that the correction owing to entropy increase is 1.8 - 2.0 (for the powder-gas case).

The charge weight may be taken as $m \sim (10-20)m_1$. It can be calculated more exactly using ballistic tables.

This technique takes into account the basic launcher characteristics: maximal light-gas pressure p_{\max} , projectile weight q , barrel length, chamber geometric form — and makes it possible, in practice, to obtain the launch velocity approximately for any launcher configuration.

This approximate technique for calculating piston-type launchers, which is based on the exact gas dynamic calculation, provides calculation with $\pm 5\%$ accuracy, and has been verified for launch velocities up to 7000 m/sec. Use of the technique does not require the application of numerical integration, since all the required solutions have already been obtained in dimensionless form and represented graphically. /122

The fundamental advantage of the proposed calculation technique, in comparison with the techniques based on the approximate formulas of classical ballistics (in addition to the fact that numerical integration of the equations is not required), lies in the fact that this technique takes into account the wave processes, both in the powder chamber and in the barrel.

In addition to the scheme examined above for calculation of the two-stage launcher, this technique can be used to calculate other launcher configurations.

1. Calculation of single-stage launchers (using OHM, electro-pulsed) is made exactly, since this corresponds to the Lagrange problem for a variable-section tube, which was solved in Chapter I.

2. Launchers with electrical preheat in the projectile movement process — combined launchers — are calculated just as the piston launchers, but a correction depending on the energy supplied is introduced into the launch velocity (see Figure 2.31).

3. Launchers with preheating are calculated using the same technique, since preheating is considered in the value of a_0 (a_0 is the initial sound speed in the light gas). This applies to all launchers with preheating (multistage launchers).

Thus, all the existing launcher types can be calculated using the proposed technique.

The information presented in the first two chapters gives a quite complete picture of both the principles involved in selecting the launcher configuration and the methods for ballistic calculation of the launchers, although there is obviously no claim that this is a complete exposition of the entire store of knowledge which has been accumulated in the high-velocity launching field.

The bibliography devoted to problems of high-velocity launching is very extensive. We shall cite only certain studies which we believe to be of particular interest. Particular note should be taken of [19], which is a survey paper and includes an extensive bibliography.

In summarizing the first two chapters, we shall dwell briefly on the prospects for developing launchers intended for conducting scientific studies.

Stationary launchers which impart velocities of up to 8 km/sec to large models (caliber 50 - 70 mm) are widely used at the present time in the field of aeroballistics. It appears that in the near future the muzzle velocity of these launchers will be increased only slightly, since further increase of the model velocity (to 10 km/sec or higher) leads to the necessity for replacing certain launcher components after each firing.

/123

In the field of impact physics (where the caliber of the launchers used in the studies is usually smaller), with projectile weight

of the order of one gram, we can expect extension of the launch velocity range up to 15 km/sec in the near future.

Here, there will be further development of launchers having individual components which can be replaced after each experiment (explosive light-gas compression, counterflow launch with the use of shaped charges, and so on). It appears that launch velocities up to 30 - 40 km/sec will be reached with microparticles weighing 10^{-4} - 10^{-10} g by using electrodynamic methods, laser beams, high-velocity jets obtained with the aid of discharges, etc.

CHAPTER III

MEASUREMENT APPARATUS AND TECHNIQUES

§ 3.1. Preliminary Remarks

A body accelerated by a powder or light-gas launcher can be used /124 to conduct gasdynamic studies, and also to study collision processes. No matter what type of experiment is conducted with fast-flying bodies, knowledge is always required of characteristics such as body velocity, shape, and orientation in space.

In order to determine these and several other characteristics, the ballistic range is equipped with various recording and measuring apparatus, constructed using electronic components, pulse technology, high-voltage technology, optics, radiography, and so on.

In the present chapter, we shall describe and systematize the basic forms of equipment used in ballistic range experiments.

The methods for recording the times at which the models pass given range sections are examined in § 3.2.

Coincidence of the exposure times with model location in the photographic field is accomplished using electronic synchronizing systems of automatic and discrete types, and also radar synchronizing systems; these are described in § 3.3.

The various techniques for measuring flying model velocity and the equipment used for this purpose are described in § 3.4.

Photography of the model position at several points of the trajectory, with simultaneous measurement of the time between exposures, provides recording of the motion space-time relationships which are necessary for determining the model trajectory parameters from which the aerodynamic characteristics are calculated. The combined operation of the series of camera stations and the technique for measuring the negatives are examined in § 3.5.

Section 3.6 describes the optical and electronic chronographs used in ballistic studies, and indicates the time measurement accuracy which they provide. /125

The principles used in constructing the systems for photographing and visualizing the flow around flying bodies are presented in § 3.7.

Photography of high-speed processes requires the use of special equipment: short-duration light sources and high-speed shutters. The description of pulsed light sources and fast-acting electrical shutters is presented in § 3.8 and § 3.9, respectively.

The basic method for studying the impact and destruction processes during the collision of bodies with barriers is the pulsed radiography technique, which is examined in § 3.10.

The capabilities and some examples of telemetry use under laboratory ballistic experiment conditions are presented in § 3.11*.

The present study is the first attempt to correlate the scattered literature material. Because of the broad range of questions

* Section 3.11 was written together with B. F. Padtochly.

examined, the presentation is of necessity somewhat compressed, and therefore the associated literature is cited at the end of the book for more detailed acquaintance with the original investigations.

§ 3.2. Passage Time Recording

Mechanical contact systems of the target-frame type have long served as sensors to record the time at which the model passes definite sections of the range. Photoelectric, magnetic, and radar barriers appeared much later.

The target-frames are the simplest and most reliable recording technique, which has led to wide use of this method. Target-frames have been used basically in working with powder guns; however, they are also used in ranges with light-gas launchers.

The characteristic features of target-frame use when conducting experiments with light-gas launchers are discussed in [1]. In that study, sphere drag coefficient measurements were made, i.e., experiments requiring not only measurement of the velocity, but also recording of the velocity variation along the range, for which target-frames mounted at six equally spaced sections were used.

Reference [1] describes two target-frame systems operating on the circuit-breaking principle.

The target frames are grids made from fine wire, stretched on insulators or bonded to a substrate of nonconducting material (paper, film). Metal foil can be used in place of the wire. /126

The simplest target-frame wiring scheme is shown in Figure 3.1.

When any target frame wire breaks, a signal recording the time the model passes the particular range section appears at the output leading to the chronograph amplifier. This target-frame wiring scheme is suitable for operation with an electronic chronograph.

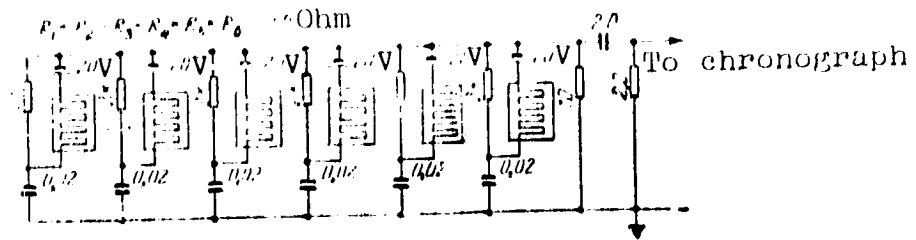


Figure 3.1. Wiring scheme of target-frames with output to electronic chronograph

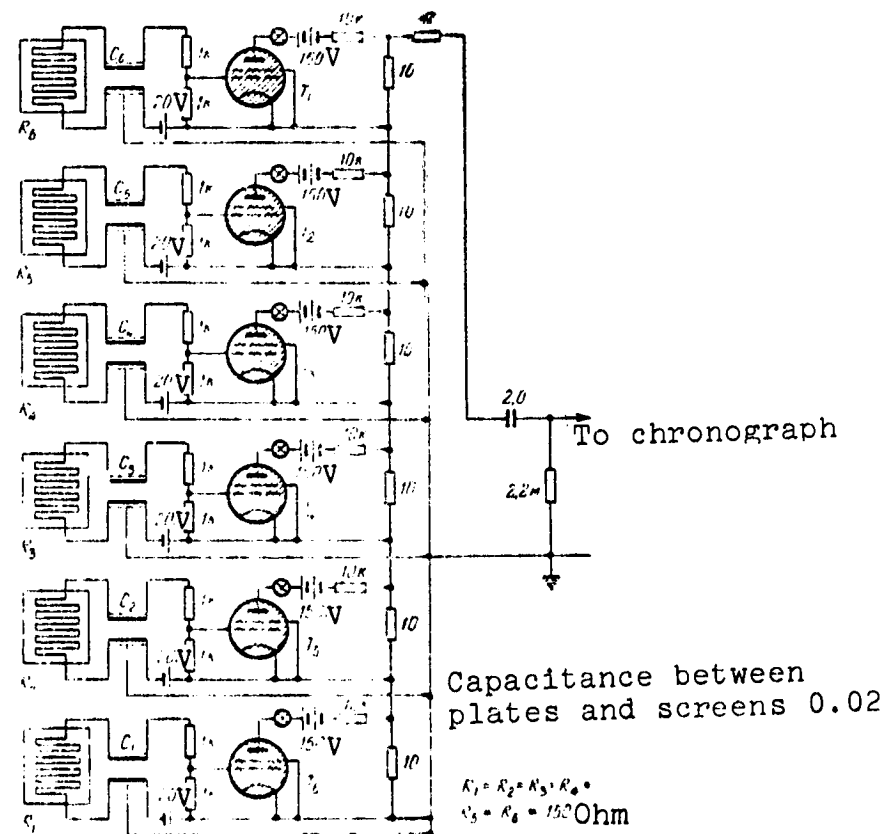


Figure 3.2. Wiring scheme of target-frames with output to optical chronograph

Figure 3.2 shows the wiring diagram of target-frames operating with chronographs utilizing the rotation of drum-type cameras. When the wire stretched on the target-frame breaks, first, a pulse arises (as a consequence of discharge of the capacitance between one of the capacitor plates and the grounded screen); second, the blanking voltage is removed and the thyatron fires. Since the time constant of

the circuit output to the chronograph amplifier is relatively long (4.5 sec), thyatron firing leads to the appearance of a practically constant voltage, which shifts the trajectory of the writing beam on the drum by a small step. This makes it possible to avoid repeated beam passage along the same path, as a result of which errors in determining the time interval duration are eliminated.

Target-frame designs operating on both circuit breaking and circuit making are simple, and therefore there is no need for their detailed description.

The convenience of target-frame application lies in the fact that they are insensitive to both electrical and mechanical interference, and large areas can be easily covered. In addition, they are applicable for both luminous and nonluminous models.

A drawback of these recording systems is the uncertainty in the time of circuit breaking (or making), which can be accomplished by either the nose or tail of the model, and also the uncertainty because of possible stretching of the wire (or foil). If the model is metallic, the circuit may close through the model, even after the wire breaks. The target-frame cannot be located along the trajectory with high absolute accuracy with respect to distance. After each experiment, the broken wires must be replaced. Further, the model surface may be damaged upon impact with the target-frame. Model retardation caused by the target-frames affects aerodynamic coefficient determination accuracy.

Noncontact sensors are primarily used at the present time to record model passage time. Such sensors have no influence on model motion and are not destroyed by model passage, which, in the case of a large number of recording stations, facilitates and speeds up the experiments considerably.

The construction principle of the light-beam or, as they are sometimes called, photoelectric recording systems is based on using the modulation of a light beam incident on an element which is

/128

sensitive to illumination. Many variants of the light barriers operating with radiation lying in the visible (for example, [2 - 6]) and, less frequently, the infrared spectrum regions [7, 8] have been described in the literature. Use of IR has the advantage that the recording section can be located in the immediate vicinity of the camera stations without any fear of exposing the photofilms.

The recording systems used (Figure 3.3) consist of a light source (S) supplied by direct current, collimators K_1 and K_2 , and the photorecorder (Φ). Since the collimated light beam depends on the light source dimensions, it is advisable to use lamps (SG-2, for example) with "point" filaments.

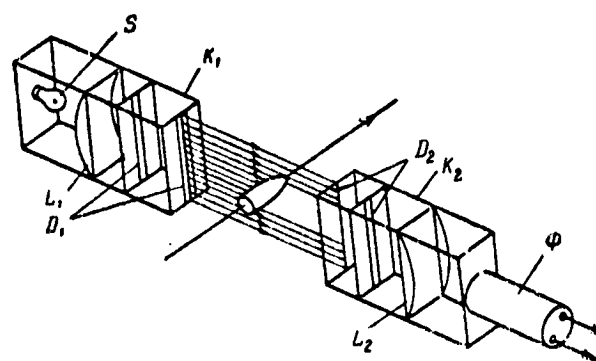


Figure 3.3. Photoelectric recording system

The collimator K_1 consists of a spherical or cylindrical condenser lens L_1 and a system of slotted diaphragms D_1 , which form a narrow light beam and reduce light scattering. In the collimator K_2 with the aid of the narrower slots D_2 , a central zone whose dimensions (height and width) determine the projectile passage recording region is cut from the narrow light beam. The light is focused on the photosensitive element by the second condenser lens L_2 .

Photodiodes, photoresistors, and photoelectronic multipliers (PEM) can be used as the photosensitive element. When conducting experiments with short models, the PEM are most suitable and provide high output signal rate of rise. Of the various PEM types, the most suitable for this purpose are PEM-11 and PEM-12, which have low noise levels in the regime with constant photocathode illumination and quite rigid dynode mounting, which determines the resistance to detonation noise arising from the firings.

/129

Since proportional signal amplification is not required of the PEM, we can use high-resistance dividers, which simplifies the problem of power supply for a large number of PEM.

The optimal PEM supply voltage, which provides adequate gain with low noise level, is about 1 kV.

Systems like that shown in Figure 3.4 are used when there is need for a tall photoelectric barrier while maintaining a high light beam modulation coefficient.

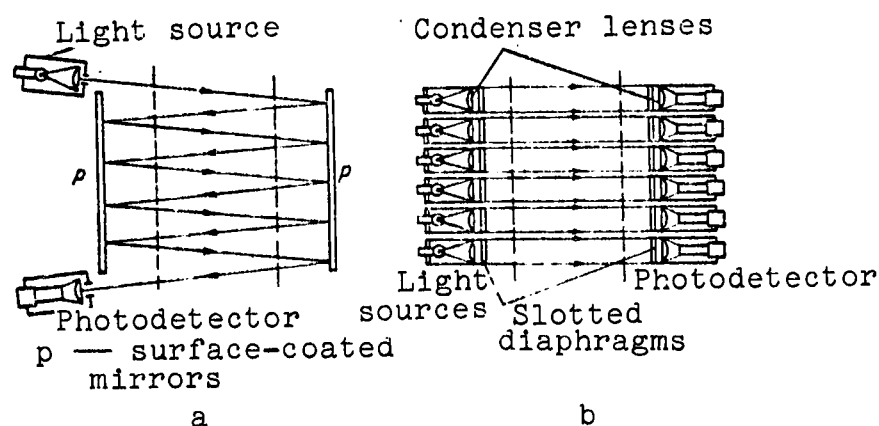


Figure 3.4. Systems for constructing photoelectric barriers of considerable height: a) system with multiple beam reflection; b) system consisting of a set of illuminators and photodetectors

In system a), the passing body blocks completely or partially a light beam which is reflected repeatedly from surface-coated mirrors [9].

In system b) [3, 8], height increase is achieved by using several illuminators and a corresponding number of photodetectors. From the viewpoint of operating reliability, preference should be given to type b), since system a) is sensitive to vibration.

Flight of bodies at hypersonic speeds is accompanied by intense luminescence of the gas [7]; therefore, there is no need to use

illuminators to record passage time, since the gas self-luminescence can be directed with the aid of similar collimators to the PEM cathodes.

The difference in the operation of the electronic circuits is not significant, and is associated with the fact that a signal of negative polarity appears on the PEM collector, and it is possible to use large loading resistors in the PEM collector circuit.

A detailed description of such a system is presented in [7]. The light-sensitive detector, located on one side of the range, is directed toward a dark field which is created with the aid of an optical cavity located on the opposite side. The detector field of view is limited to the optical cavity by a system of screens. The cavity is formed between two metallic sheets which are curved exponentially; the sheets butt together and are covered at the sides. The inner surfaces of the sheets are coated with matte paint which does not reflect light. The cavity shape is such that a beam which enters the cavity cannot emerge. Upon entry of the luminous model into the wedge-shaped field of view of the detector, a phototransistor in this case, a recording signal is generated.

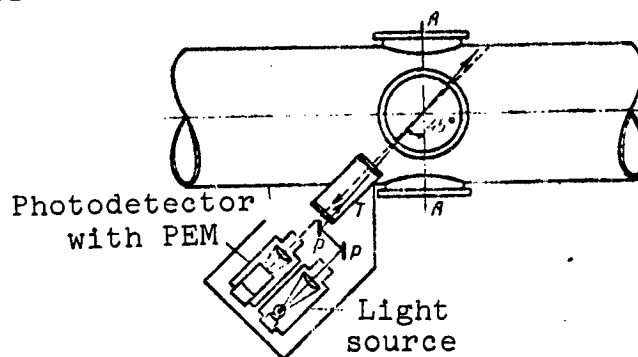


Figure 3.5. Universal photorecording system

The photoelectric systems which are capable of recording both luminous and nonluminous objects are most convenient because of their universality [10, 11]. A typical universal system, consisting of a photodetector and associated light source, is shown in Figure 3.5.

In front of the PEM, which is the light-sensitive element, there is a lens which focuses the central part of the range onto the PEM photocathode. The light "trap" (T) is a slotted collimator which selects a narrow zone (with vertical dimension 8.4 cm and horizontal

— 2.4 cm) that cuts horizontally across the range. The point-type light source and two flat mirrors send a narrow light beam in the direction of the zone scanned by the PEM, and the angle between the light beam and the PEM scan region is made as small as possible. When the model crosses the PEM scan region, both the reflected illumination and the self-illumination (if present) strike the PEM photocathode, triggering the recorder.

The use of spectral systems for reducing the noise level is also possible for recording model passage under conditions of strong luminosity, created either by the model itself or by the gases issuing from the gun barrel (which can propagate to considerable distances along the range). However, the spectral systems require expensive equipment [7], and therefore are rarely used.

In addition to the photoelectric barriers, noncontact recording /131 can be accomplished with the aid of electromagnetic, electrostatic [12], ionization [13], high-frequency, and radar detectors.

The electromagnetic method is based on the appearance at the ends of a solenoid (a thin coil with magnetization created either by direct current or by an annular magnetized core) of an emf as the metallic model enters and leaves the coil. The solenoid detector, just as the target-frame, is a detector with low internal resistance, as a result of which it is easily matched with the supply cable resistance.

A drawback of the solenoid detectors is the relatively low slope of the generated pulse fronts, which makes it difficult to form signals with high temporal resolution.

A capacitor with holes in the plates through which the model flies (in the direction perpendicular to the plates) can play the role of an electrostatic detector, since in this case a corresponding recording signal will be generated on the capacitor plates.

A passage time detector can be created using interaction of high-frequency radiation with the model material. To this end, high-frequency radiation is transmitted in the direction perpendicular to the range axis, and this radiation is sensed by the detector. When the model enters the UHF field, the detector will record a weakening of the signal.

These detectors are not widely used because of poor reliability and limitations in selection of the model material.

§ 3.3. Synchronizing Equipment

After amplification in amplitude and power, the signals generated by the projectile passage recording detectors can be used to trigger the measuring and photographing apparatus.

/132

Vacuum-tube photoelectric detector signal amplifier circuits can be found in [5, 10, 14].

The amplifier (Figure 3.6) described in [6], thanks to the input phase-inverting stage (pentode part of T_1), makes it possible to amplify both the positive signals arising during light beam modulation by the flying model and the negative signals caused by self-luminous objects. The stages utilizing T_2 perform limiting of the signals (left half) and "clipping" of the PEM noise (right half). The presence of the second phase-inverting component (right half of T_3) with input differentiating loop makes it possible to discriminate, when desired, either the leading or trailing edge of the amplified signals. A cathode follower (pentode part of T_4) and a thyatron (T_5) serve as the final stages.

A similar circuit based on transistors was used in [8]. The equipment was tested on 4.6-mm diameter models at speeds from 3 to 6.3 km/sec.

In the case of widely spaced recording and photographing fields, time delay components must be introduced into the circuit in order to synchronize the photographic device triggering time with the model appearance in the field of observation (and also when studying the wake downstream of the model or investigation collision processes).

Reactively triggered circuits of the monovibrator type [5, 15], single tube reactively triggered circuits of the phantastron type based on use of linearly varying voltage [14, 16], and delay lines are usually used as delay elements.

The drawback of the delay lines is the necessity for using artificial lines constructed from discrete elements in order to obtain large time delay magnitudes. As a result of this, smooth variation of the delay magnitudes and their automatic regulation become impossible. /134

The drawback of the monovibrator circuits is the instability of the generated delays, amounting to 2 - 5%, which is due to the fact that the output pulse duration is determined by the exponentially varying coupling capacitor discharge voltage. In addition, linear variation of the delay duration as a function of the controlling voltage magnitude cannot be provided when using monovibrators.

Taking this into consideration, preference is given to the phantastron circuits, which have high operating stability over a long time period and linear relationship between the controlling voltage and the delay magnitude. The phantastron relative timing error can be reduced to $\pm 0.5\%$, and the nonlinearity between the controlling voltage and the delay magnitude can be reduced to 0.1%.

Figure 3.8 shows the complete synchronizing apparatus circuit [16], consisting of a PEM signal amplifier, shaping stage, phantastron delay block, output stages, and blocking circuit.

The T₁6N1P two-stage amplifier with integrating loop amplifies the positive signals (with minimal amplitude 0.1 V) appearing across

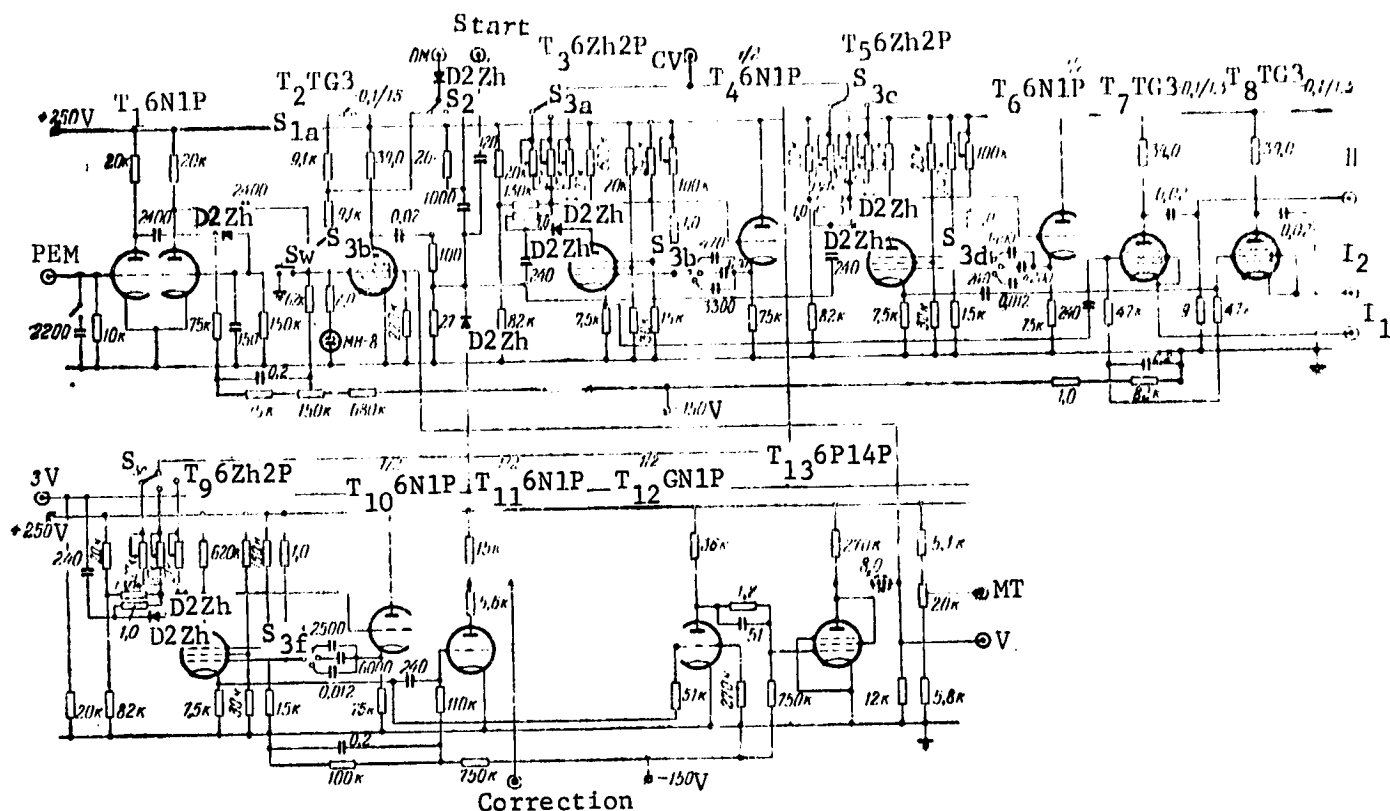


Figure 3.8. Schematic of PEM signal shaping amplifier, phantatron type delay units, blocking stage, and output amplifiers

the PEM load with partial modulation of the light beam to a sufficient voltage to trigger the shaping stage. The T_2 TG3-0.1/1.3 pulse shaping stage also performs the functions of a power amplifier, PEM noise amplitude discriminator, and circuit sensitivity regulator.

The pulse delay block T_3 uses a phantatron circuit with a 6Zh2P pentode. Reduction of the charging time of the capacitor in the anode grid circuit is achieved by the T_4 6N1P cathode follower.

The thyatron T_7 TG3-0.1/1.3 with 200 ohm cathode load remoted to the spark source serves as the power amplifier.

/136

Stages T_5 and T_8 are a phantastron and the corresponding power amplifier, arranged in a similar scheme, which make it possible to trigger the system for photographing the model at another section.

The entire phantastron operating interval is broken down into three ranges, established by the selector switch S_3 , in order to realize the required accuracy in the magnitudes of the delays obtained.

The purpose and operation of the blocking circuit, consisting of tubes $T_9 - T_{13}$, will be examined in § 3.5.

The controlling voltage, which determines the durations of the delays generated by the phantastrons T_3 and T_5 , is applied to the terminal CV. The required controlling voltage magnitude can be established manually by means of a calibrated potentiometer of the "range" type.

Because of several factors relating to the field of interior ballistics, exact specification of the projectile velocity is not possible. Therefore, in order to obtain delays corresponding to the model velocity, it is advisable to use apparatus in which the magnitude of the controlling voltage is not established in advance, but rather is generated in the circuit itself on the basis of actual model flight velocity.

The block diagram of an electronic unit for converting model velocity into controlling voltage (automatic control station — AC) is shown in Figure 3.13, and the functional diagram and forms of the voltage variation at different points of the circuit are shown in Figures 3.9 and 3.10, respectively.

The signal I , arising at the instant the model crosses the photoelectric registration field of the AC station, triggers the phantastron T_3 6Zh2P, which generates a delay whose magnitude T_1 is constant for each of the bands. The magnitude of the delay T_1 is

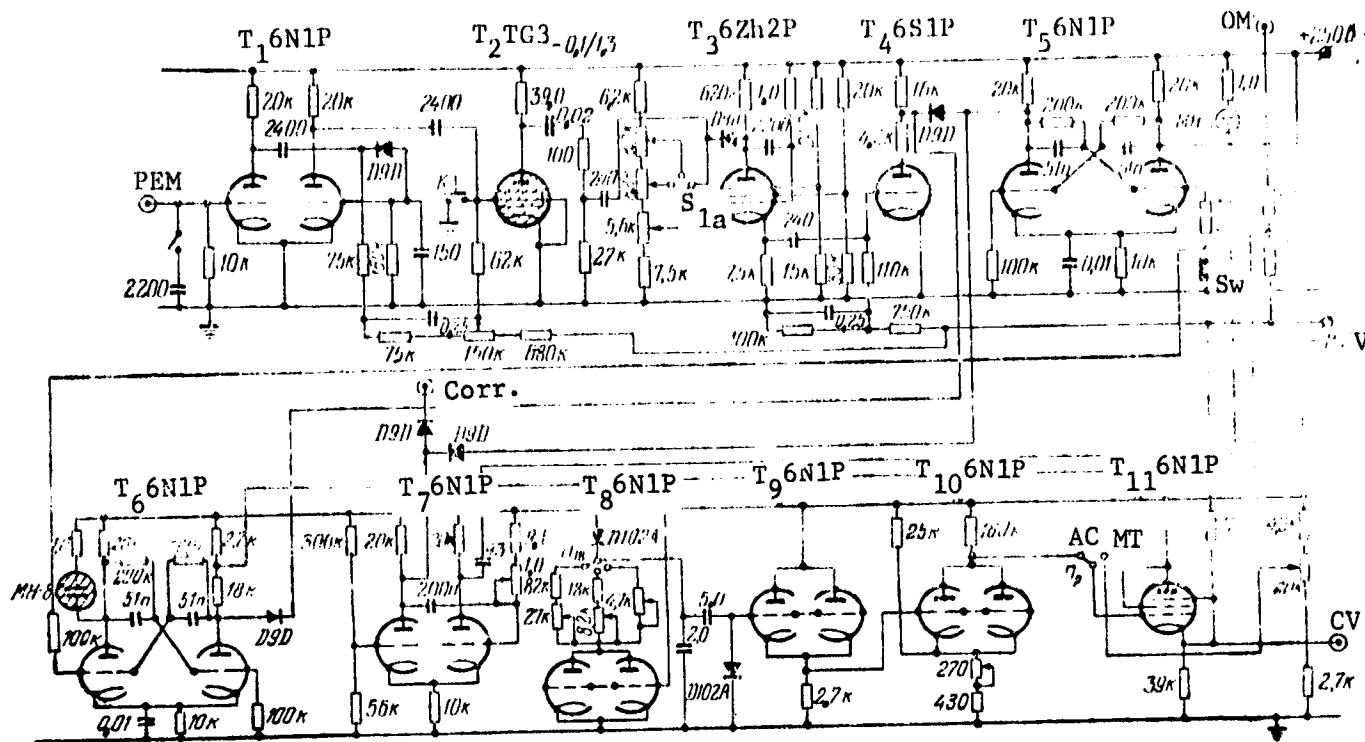


Figure 3.9. Automatic delay duration control

equal to the time for the model to travel the distance between the AC station and the first station with maximal velocity for the given band. Satisfaction of this condition ensures linear dependence of the controlling voltage magnitude on the flight time.

The delayed pulse, amplified and phase-inverted with the aid of T_4 6S1P, activates the triggers T_5 6N1P and T_6 6N1P. When the trigger T_5 is activated by the triode T_8 ,

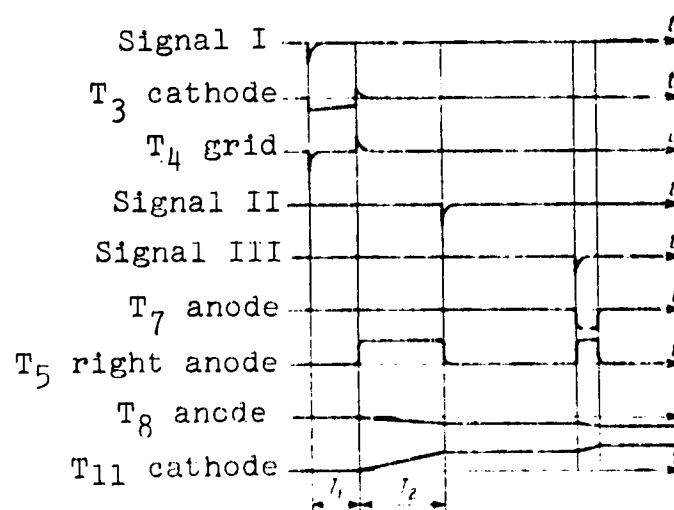


Figure 3.10. Voltage variation at primary points of automatic delay duration control circuit

which is a linearly decreasing voltage generator, fires and activation of the trigger T_6 leads to increase of the generator capacitor (2.0 μ F) charging time constant. The voltage drop across T_8 is first converted into a linearly increasing voltage by the triode T_{10} , and is then amplified in power by the cathode follower T_{11} 6P14P.

After arrival of the signal II from the terminal OM of the first station (see Figure 3.8) at the corresponding terminal of the AC station, the trigger T_5 returns to the initial position, and therefore increase of the controlling voltage on the cathode T_{11} (CV output) terminates. Thus, a common controlling voltage, whose magnitude is proportional to the time for the model to travel the distance between the AC station and the first station, is applied to all the phantastrons. /138

The functions of the correction monovibrator T_7 are examined in § 3.5. Because of component parameter scatter, it is necessary to match the maximal and minimal delays of the phantastrons located both at a single station and at different stations. The maximal delay is established at the highest controlling voltage + 200 V, by selecting the capacitance, and the minimal value at the lowest controlling voltage +40V is established by varying the 27-kOhm variable resistor. This tuning method makes possible practically independent regulation of the upper and lower delay limits.

With the parameters indicated in Figure 3.8, automatic synchronization system operation is provided in three delay bands, each of which provides six-fold overlap (in μ sec): I — from 594 to 3560, II — from 214 to 1286, III — from 52 to 312.

When conducting ballistic experiments, we also run into several problems requiring the use of equipment which makes it possible to obtain series of synchronizing signals [17, 18]. The need for such instruments arises in those cases when it is necessary to photograph the flying body at severally spatially separated and sequentially /319

triggered pulsed recording systems. In addition, such equipment is necessary in order to obtain a series of photographs at a single section — for example, when studying the wake or sequential phases of the destruction process.

Figure 3.11 shows the block diagram of a multichannel synchronizer which generates series of pulses with precisely known time intervals [17]. The signal arising in the recording system when the model crosses the light beam activates the trigger controlling the impact excitation generator.

After the trigger flips, the generator begins to operate with the same initial phase and with constant frequency and amplitude. In the next stage, the sinusoidal voltage is converted into short, nearly rectangular pulses. These pulses then pass to a frequency divider with division ratio 32, from which they enter the monovibrator, which forms broad pulses, equal in duration to the master generator period.

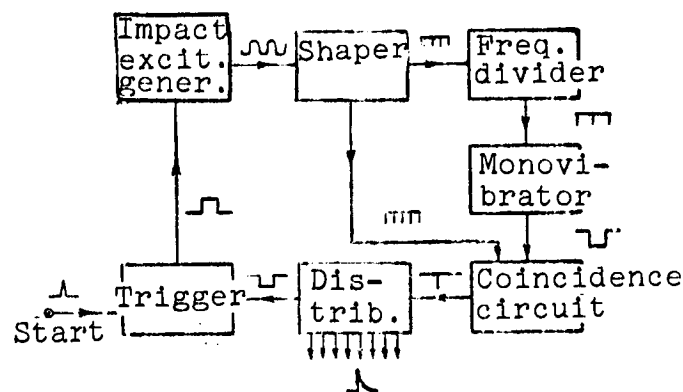


Figure 3.11. Block diagram of multichannel synchronizer for ballistic studies

In the coincidence circuit, the pulse coming from the monovibrator singles out one of the pulses coming directly from the shaping stage. This eliminates output signal "drifting" in time, which occurs as a consequence of use of the binary-type frequency divider with high division ratio. From the coincidence circuit, the calibrated pulses pass to the distributor, equipped with output signal amplifiers. After activation of the final distributor stage, the trigger returns to the original position, and the generator signals stop.

/140

The main advantage of the radar synchronization method is elimination of the need for locating a large number of passage detectors along the range. Instead, we use only a single transceiver system, which provides precise synchronization of the spark light source triggering times at the moments the model is located in the corresponding fields for practically any number of recording stations [19, 20].

Figure 3.12 shows the functioning of a radar synchronization system (b), and the construction of the transceiving metering head (a), consisting of a klystron generator (wavelength 3.16 cm), radiator, parabolic antenna, mixing system, and detector channel.

The transceiving head is located at the end of the range (see diagram b), and the beam from the SHF radiator is directed toward the flying model with the aid of a metallic mirror having an opening for passage of the model and positioned at a 45° angle to the flight trajectory and to the optical axis of the parabolic antenna.

Part of the electromagnetic radiation is reflected by the model and returns to the measuring head, where it is mixed with the primary SHF radiation. Since reflection takes place from a moving body, the reflected signal changes radiation frequency in accordance with the Doppler effect. As is well known, when combining signals with close frequencies, beats arise whose frequency is equal to the difference of the interfering signal frequencies; in this case, the Doppler frequency:

$$f_D = 2 \frac{V}{\lambda}, \quad (3.1)$$

where V — model velocity; λ — primary SHF radiation wavelength. The Doppler frequency can be expressed in terms of the number n of beats appearing in the course of the time interval ΔT :

$$f_D = \frac{n}{\Delta T}. \quad (3.2)$$

Hence, using (3.1), we obtain:

$$V \Delta T = n \frac{\lambda}{2}. \quad (3.3)$$

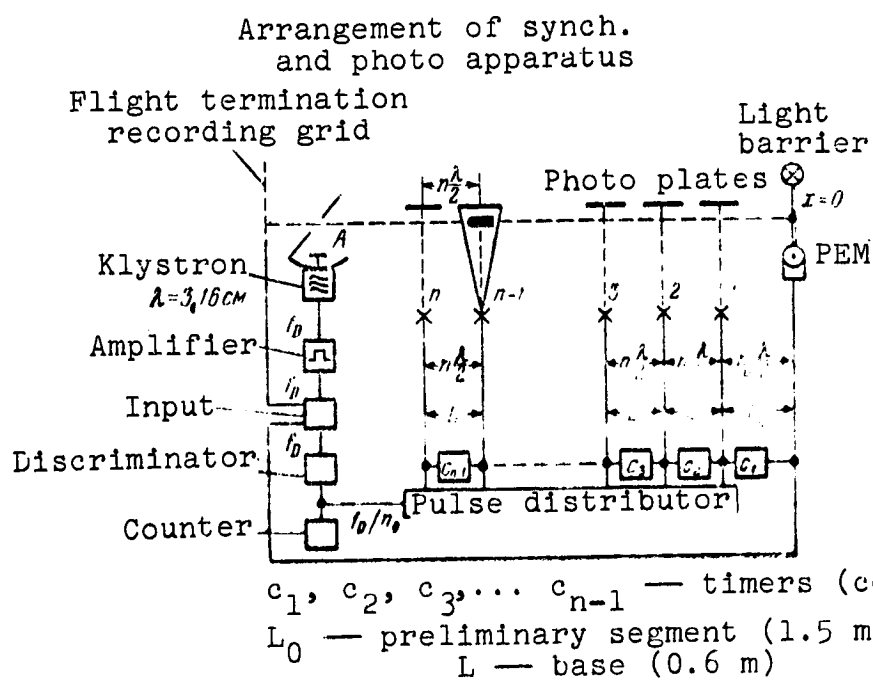
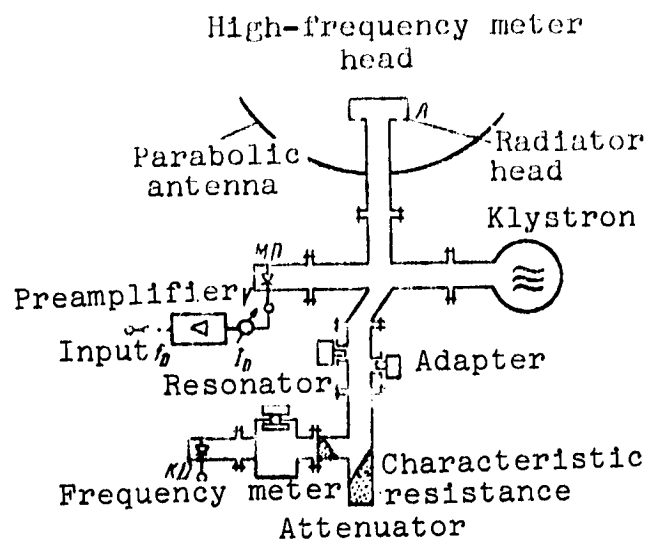


Figure 3.12. Block diagram of equipment and transceiver head for radar synchronization method

Examination of (3.3) shows that, if the camera stations are equally spaced along the range at a distance $n(\lambda/2)$ from one another, each n th beat pulse will appear at the time the model is located in the center of the camera field, regardless of the model velocity.

To this end, the detected, amplified, and shaped beat signals enter a distributor, where each n^{th} pulse is directed sequentially to the corresponding camera activation channel.

System activation is accomplished by a photoelectric passage detector. The use of a 20-mW power klystron generator is adequate for servicing a range 15 m long, when using a 3 cm-diameter model. Use of higher power generators is necessary for smaller model diameters, and also when using very highly pointed models.

We note that the microwave diagnostic methods are used successfully for measuring electron concentrations and wake dimensions behind bodies traveling at hypersonic speeds [59].

§ 3.4. Measuring Flying Body Velocity

The velocity measuring methods can be divided into two categories: direct and indirect.

The direct methods for measuring the average velocity are based on measuring the time during which the body travels a known distance (between two neighboring range sections) and, less frequently, by measuring the distance traveled in a known time [17].

The indirect measurement methods are based on recording effects whose manifestation depends directly on the body velocity, and therefore can be used for determining the velocity. As an example of the indirect methods, we shall discuss the velocity measurement method described in [12]. The model travels parallel to a plate with 1.5 mm-diameter holes forming a chain with 6.4 mm spacing along the direction of the trajectory. As the model bow shock wave impinges on the holes, each of them becomes, in sequence, a source of spherical waves. In accordance with the Huygens principle, the envelope of the secondary waves will indicate the wave front position. Since the wave envelope slope is approximately equal to the Mach angle, after measuring this slope from shadow photographs and introducing

some corrections for diffraction, we can calculate the model velocity to within a few percent.

The direct methods have found wide application in conducting aerodynamic experiments and studying collision of bodies, since they provide velocity measurement with high accuracy. /143

A system which does not require complex electronic apparatus and exact equipment synchronization was used in [13, 21, 22] for measuring velocity. The basis of the instrument is a camera with continuous image scanning (obtained with the aid of a mirror rotating at constant speed) and a pulsed xenon lamp which flashes as the model approaches the instrumented section of the range.

The two flat light beams of this lamp, formed by narrow slots perpendicular to the direction of flight, cross the test range at two sections located at a verified distance from one another. These beams are brought out to different film tracks with the aid of mirror-prism systems. At the same time, timing marks are applied to the edge of the film by a stroboscopic pulsed lamp. At the instant the model passes the first slot, it crosses the light beam and creates a shadow on the corresponding film track. Then, the model crosses the second beam, and its shadow is recorded on the track on which the image of the second slot is projected. Lamp illumination is cut off before the slot image begins to re-expose the film. By measuring the distance on the film between the model shadows and knowing the mirror rotational speed and the distance between the slots, we can calculate the model velocity with satisfactory accuracy.

The relative velocity measurement error is made up from the sum of the relative baseline and time determination errors; therefore, in order to reduce the velocity measurement error, we must use recording systems with high spatial resolution and increase the baseline length in the case of not very large values of the delay parameter $C_{xp} S/2m$.

If the photoelectric systems with narrow collimator slots described above (§ 3.3) are used as the passage time detectors, and if we measure the baseline with suitable accuracy, we can, generally speaking, achieve good measurement accuracy, even on a short baseline 100 - 300 mm long [6]. Photoelectric detectors with amplifiers of the type shown in Figure 3.6 or Figure 3.7, with baseline measurement error of a few tenths of a millimeter and time measurement error amounting to tenths of a microsecond, make it possible to determine body velocity with relative accuracy to within tenths of a percent.

In this case, the measurement errors are due to nonidentity of the recording channels with respect to individual channel sensitivity and with respect to height of the recording field, presence of possible recording field nonorthogonality to the trajectory, appearance of model angle of attack, and other factors. /144

However, such accuracy is not adequate for many aerodynamic investigations — for example, when conducting experiments in the transonic velocity region (where there is rapid change of the flow parameters along the body) and when studying the drag coefficient.

In order to realize the required velocity determination accuracy, we attempt to minimize the distance and time measurement errors. The first is achieved by photographing (with short exposure time) the flying models on the background of a reference system, with subsequent measurement of the coordinates on the resulting photographs. The second is achieved by using precision electronic chronographs which record the durations of the time intervals between the exposures. In this case, the synchronization apparatus role reduces to recording the passage times, forming the signals for activating the camera stations, and controlling the timers [4]. In order to reduce the coordinate measurement errors, the measurement techniques ensure reliable determination of the body velocity to within hundredths and even thousandths of a percent.

§ 3.5. Determining Flying Model Trajectory Parameters

Under the influence of the resistance exerted by the medium, the model motion takes on a complex nature, and determination of the longitudinal center-of-gravity coordinate dependence on the time of flight is necessary in order to calculate the drag coefficient. Correspondingly, the variation of the transverse center-of-gravity coordinate as the model travels along the range makes it possible to find the lift coefficient. Recording of the model angular motion is necessary for determining the aerodynamic moment coefficient. In this connection, one basic problem of the ballistic experiment is to determine the space-time relationships, i.e., the variation in time of the flying model linear and angular coordinates.

The accuracy of the aerodynamic characteristic calculation is the higher, the smaller the errors of the measurement of the time between exposures, the smaller the errors of the measurement of the linear and angular coordinates at each section, and the more recording sections there are located along the range.

We noted in the preceding section that maximal accuracy of the model center-of-gravity spatial coordinate determination is provided by measurement from "instantaneous" photographs of the model position relative to a reference system which is tied in to the laboratory coordinate system. If, in this case, photography is accomplished in two mutually perpendicular directions, the measurements from the photographs make it possible to determine the angles of attack and sideslip. Moreover, in the case of photography using optical systems for visualizing the flow, study of the photographs makes it possible to simultaneously obtain useful information on the flow around the bodies.

/145

The passage time recording and photography systems are combined into station blocks, which are usually spaced uniformly along the range.

Figure 3.13 shows the block diagram of the location of the stations and timing equipment [4], which illustrates the nature of the combined operation of the series of stations.

The initiating signal which triggers the instrumentation operating in the standby regime (chronographs, for example) in this variant is taken from the first station shaping stage output.

Depending on the chronograph construction, the signals which control the time measurement systems are taken either from the output stages, the station power amplifiers, or directly from the spark source circuits [10, 23]. For direct use of the chronograph indications in calculations using the least squares method, it is advisable to trigger all the measurement channels simultaneously, rather than accomplish sequential measurement of the time intervals between neighboring stations.

If spark or any other high-voltage light sources are used on the range, their triggering is accomplished by large electromagnetic and optical surges, which are capable of causing the appearance of signals on the detector inputs of the neighboring stations. A blocking system $T_9 - T_{13}$, located at station I (see Figure 3.8), is provided in order to prevent station triggering from false signals. The blocking system circuit is activated by a pulse coming from the shaping stage signal of the station past which the model is traveling at the given instant. The negative polarity pulse which arises across the 12-kOhm resistor is applied to the second grids of all the shaper thyratrons, blanking them for a time somewhat longer than the photographic channel delay duration, but shorter than the time for the model to travel the distance to the next station. Thus the surges arising during triggering of each given station cannot activate any other station.

During both manual tuning (MT) and automatic application of the controlling voltage, the blocking pulse duration exceeds the magnitude of the delay resulting from the large values of the time delay capacitors in the blocking phantatron.

/147

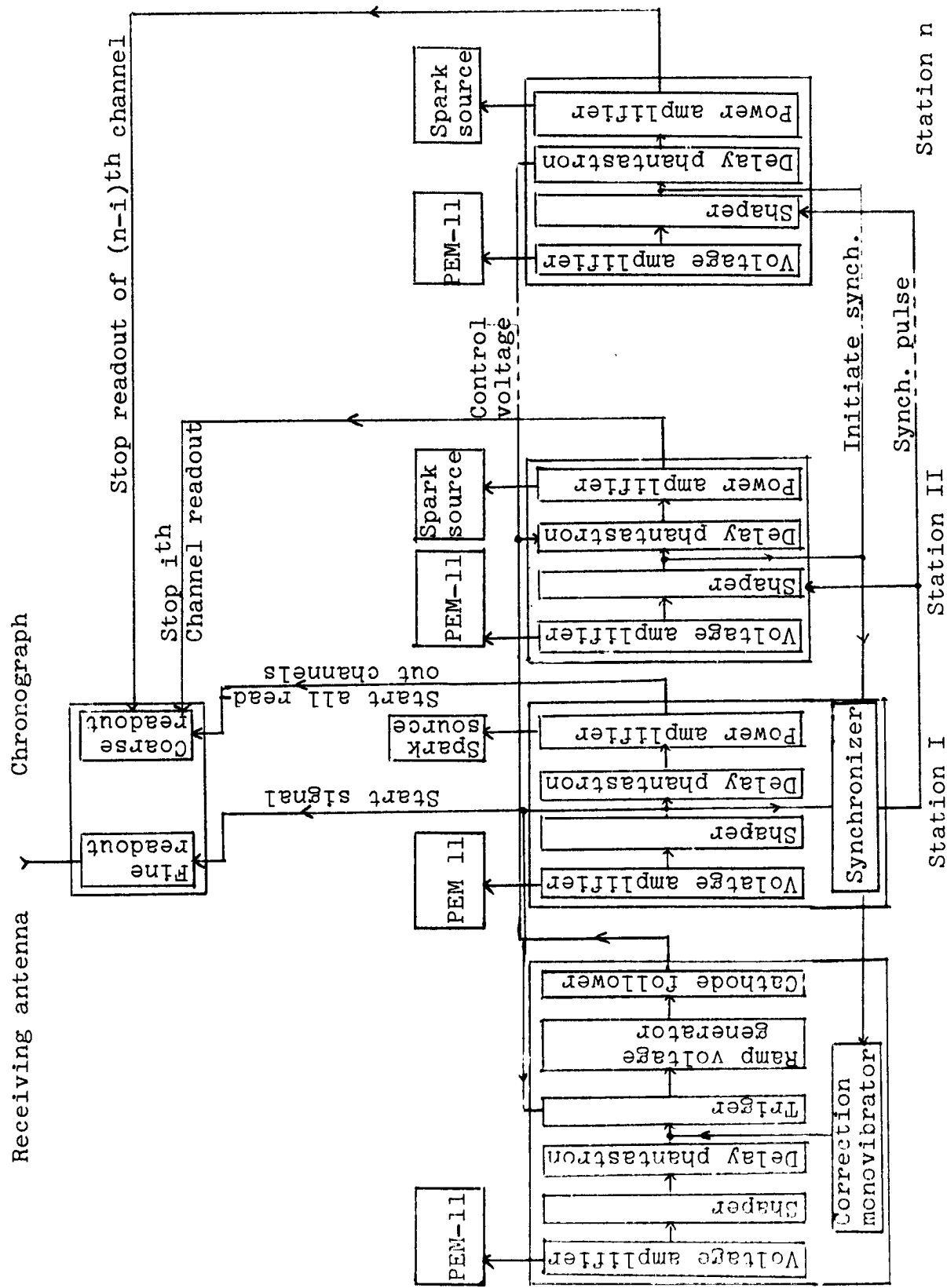


Figure 3.13. Block diagram of recording and photography station location along ballistic range

Along with the described method, use is also made of sequential removal from station to station of a previous applied blocking voltage [24, 25]. In this case, in the initial condition, all the stations other than the first are blocked by a constant blocking voltage, which is removed upon triggering of the previous station. Thus, after recording of the model by the first station, the second is prepared; the second station, in turn, prepares the third, etc.

In comparison with the first technique, the method of sequential blocking voltage removal has the drawback that, in the case of random failure of any station to trigger, all the remaining stations cannot record model passage, while in the first method, failure of any of the stations has no effect on operability of the remaining stations, which results in increased range functioning effectiveness.

If the range is equipped with automatic delay generator apparatus, then in experiments with light-weight models it is necessary to use a correction system, because of the considerable decrease of their velocity along the range (see Figure 3.9). The corrector increases the delays generated by the phantatron of each succeeding station by means of gradual increase of the controlling voltage.

The pulses which activate the blocking stage (signal III in Figure 3.10) lead to triggering of the monovibrator T_{76N1P} and the associated trigger T_5 , which provides additional activation of the linearly rising voltage generator. The time of monovibrator stay in the unstable equilibrium state, which determines correction depth, is established by means of a 1.0-MOhm variable resistor.

We note that a technique based on determining the model position at predetermined time intervals whose magnitude is known with high accuracy is used in some ballistic ranges for recording the space-time relationship [17]. In this case, actuation of several sequentially positioned camera stations can be accomplished from a single common detector.

The requirements imposed on the time recording precision and the time measurement technique will be examined later; in the present section, we shall examine only the technique for determining the model linear coordinates and angles of attack.

The discrete positions of the body in space are found by measuring on the photographs (see, for example, Figure 3.14) the coordinates of the characteristic points of the body and the angles formed by the model generators with the reference system axes, with subsequent calculation of the center-of-gravity coordinates and angles of attack. Instruments of the MIR-12, IZA-2A, UIM-21, UIM-23, UIM-24, and other types can be used for the measurements.

Comparators of the MIR-12 and IZA-2A types must be equipped with additional vertical displacement carriages. The drawbacks of instruments of this type are, first, that they can provide measurement of only a single coordinate and repositioning of the negatives is required for determining the other coordinate, and, second, that the instruments are not suitable for measuring angles.

The UIM-21 universal measuring microscope is a more convenient instrument, and makes it possible to measure with a single setup both the x and y coordinates and also the angles of the model generators to the coordinate axes. The maximal linear quantity readout accuracy is $1 \cdot 10^{-4}$ mm, and angular quantities can be read to within 30".

The UIM-23 and UIM-24 universal measuring microscopes have coordinate and angle measurement accuracy identical with that of the



Figure 3.14. Photograph of model in flight on background of coordinate scale

UIM-21 instrument, but are more convenient in operation. The UIM-23 and UIM-24 instruments are equipped with screens, on one of which an enlarged image of the model and coordinate grid is projected; enlarged images of the x and y coordinate readout system scales are projected on two other screens, and the images for measurement of angular quantities are projected on the fourth screen. The screens have green lighting to prevent vision fatigue. Since in this case it is not necessary to use eyepieces in order to align the model image with the instrument coordinate system or to take the readings from the measuring microscopes, the operator's work is facilitated considerably, and therefore the operator's productivity improves significantly. /149

At the present time, considerable attention is being devoted to automating the process of analyzing the pictures obtained in ballistic tests and cinetheodolite observations [26]. In the specialized analyzers, the analysis results are printed out directly or transferred to punched cards with subsequent calculation of the center-of-gravity spatial coordinates on electronic computers.

The conduct of precision aerodynamic experiments is impossible without careful adjustment of the range optical equipment and tie-in of the station reference systems to the laboratory coordinate system. A description of adjustment techniques which do not require the use of specialized instruments is presented in [27, 2].

§ 3.6. Time Interval Measurement Methods

We shall examine briefly the requirements which are imposed on the apparatus intended for measuring time intervals when conducting ballistic experiments.

The coordinate determination error when using precision photographic systems amounts to about 0.1 mm, and further reduction of this error encounters severe difficulties. For a flight velocity of about 5000 m/sec, the exposure time recording error corresponding

to this coordinate error is $2 \cdot 10^{-8}$. If we consider still higher velocities, it is necessary to measure time in the chronograph to within $1 \cdot 10^{-8}$ sec. Correspondingly, in experiments with flight speeds less than 1000 m/sec, it is sufficient to use chronographs with time resolution of about $1 \cdot 10^{-7}$ sec.

The use of chronographs of higher accuracy than required in each specific case has no significant effect on the space-time relation recording errors, which are made up from the coordinate and time recording errors, since the coordinate determination error will limit the accuracy improvement.

In addition, the conduct of aerodynamic studies by the ballistic method involves the measurement of several time intervals (on the order of ten or more).

Even relatively small ranges have an "effective" length of about ten meters; thus, the time measuring equipment must be capable of recording time intervals with total duration of a few milliseconds.

We can see that the relative and absolute time measurement errors play a dissimilar role, since the former influences acceleration calculation accuracy, while the latter changes the time "scale" and, therefore, affects only the velocity determination error.

/150

The general questions of time measurement technique are discussed in [28, 29].

We shall examine the fundamentals of the construction of the circuits and specific examples of chronographs which can be used in conducting ballistic tests.

The optical chronographs were the first to provide a combination of high resolution with the possibility of measuring long time intervals.

The typical construction of the optical chronograph was described in [2, 46]. The timer is a "streak" camera utilizing 450 cm-long light-sensitive film positioned on the inside of a circular drum, at the center of which there is a mirror mounted at a 45° angle which rotates at high speed. Marks with 20 μ sec repetition period are made on the film with the aid of a pulsed mercury lamp (simultaneously with the signals defining the time intervals), in order to monitor mirror rotational speed and film shrinkage. A different mark repetition frequency can be specified if desired.

At the instant of activation of the light source which photographs the model, part of the light is directed by a system of lenses and mirrors onto the film, causing localized darkening of the film corresponding to the signal appearance times. By counting the number of whole 20 μ sec marks located between these signals and adding the "durations" of the segments from the nearest mark to the signal, found by interpolation, for each of the signals, we can determine to within about 0.2 μ sec the durations of the time intervals between flashes.

High absolute measurement accuracy is ensured by using a quartz generator to establish the mark repetition frequency.

A laser can also be used in the place of the pulsed lamp to apply the marks to the film [30].

The drawbacks of chronographs of this type are their large dimensions, sensitivity to mechanical interference, and the necessity for using comparators or measuring microscopes for the interpolative readouts.

The use of electronic timers is very promising from the viewpoint of providing accuracy and operating convenience.

We shall note several chronograph designs in which spiral-scan cathode ray tubes are used as indicators.

/111

The chronographs of the IV-13 and IV-13M types [31] have temporal resolution of 0.1 μ sec, and permit measuring a single time interval of duration no longer than 300 μ sec. The IV-13MA chronograph can be used to record with the same accuracy several intervals; however, the total time recording duration is only 180 μ sec.

The instruments described in [32, 33] are used to measure a single millisecond time interval to within 0.2 μ sec.

The IV-22 chronograph provides high time recording accuracy, equal to 0.02 μ sec, but permits measuring only a single interval with duration less than 300 μ sec.

Instruments which permit measuring long time intervals with high accuracy are also constructed using the principle of converting the time interval into a number of pulses which is proportional to the given interval. This number is recorded by a counter equipped with an indication system.

The time measurement error, when using counters, depends primarily on the stability of the generator pulse repetition frequency and the counter resolving time, which determines the discreteness error.

The pulse generators are usually constructed using a circuit with quartz frequency stabilization. The day-to-day stability of such generators is 10^{-5} - 10^{-7} . Thermostating further reduces the instability by several orders of magnitude.

Several variants of counter and commutator circuits with time resolution equal to or better than 0.1 μ sec are known (see, for example [34 - 37]). The Ch3-9 and Ch3-35 frequency-meter counters have a discreteness error equal to 0.1 μ sec.

Time measurement accuracy is often improved by using an electronic vernier.

Specifically, a time interval of duration up to 256 μsec can be measured to within 0.1 μsec , using a chronograph [38] which is a combination of a counter-generator with resolution 1 μsec and a precision readout system with resolution 0.1 μsec , which serves to reduce the discreteness error. The vernier system uses a delay line segment, and is equipped with a type MTKh-90 indicator, so that the total time is determined visually.

The need to measure a large number of nonperiodic time intervals has led to the creation of multichannel timers.

The chronograph described in [39] permits recording six millisecond time intervals to within 0.1 μsec . The chronograph consists of six identical counters, six commutators, and a common 10-MHz-frequency master generator.

/152

The chronograph described in [40] uses four counters with 0.625 sec resolution, operating together with a vernier unit using a circular-scan CRT to measure four time intervals. The time for a single scan is 2.5 μsec . The signal appearance times are marked by short (less than a full circle) illumination pulses with stepwise varying scan radii prior to recording of the signal from each succeeding station. Measurements from the oscillogram make it possible to obtain a "vernier" readout with an error not exceeding 0.025 μsec , and thus make it possible to refine the measured time interval durations.

Since the problem of measuring a large number of time intervals cannot be solved by simple increase of the number of counting channels, special chronographs have been developed. These instruments are based on using either several cathode ray tubes, or one or two counters, in combination with a system for storing the intermediate indications corresponding to the successively measured time interval durations.

A chronograph is described in [41] which makes it possible to measure several time intervals of overall duration seven milliseconds to within 0.1 μsec by using two cathode ray tubes.

The first tube, with spiral scan period equal to 200 μ sec and marks denoting 10- μ sec intervals, increases the total recording time but does not permit precise readout. On the second CRT with 20 times faster scan, and consequently 20 times smaller step, only the spiral segments corresponding to the ends of the measured time intervals are illuminated in order to avoid merging of the sweeps. These "fast" spiral segments, with timing markers every 0.5 μ sec, serve for precision readout.

The chronograph of [42], consisting of two identical counters and two systems for readout of the intermediate indications of the counter triggers, a dual-beam CRT memory, and a commutator, makes it possible to measure about a hundred time intervals of duration up to 13,000 μ sec to within ± 1.2 μ sec. The instrument operating principle is as follows: when measuring time by one of the counters, the indications of the other counter, corresponding to the previously measured interval, are output to the CRT by means of a special interrogate system. /153

Figure 3.15 shows the block diagram of an electric chronograph [43] for measuring approximately 40 time intervals with accuracy 0.02 μ sec, constructed using a single counting channel with resolution 1 μ sec, a block for transferring the intermediate counter indications into the memory system, and the vernier unit. The memory system is constructed similarly to the preceding instrument, except that the linear-scan-type vernier indication is output to the second beam of the CRT. Thus, the oscillogram presents the time intervals in binary code and the corresponding series of vernier scans.

Prior to arrival of the signals defining the time intervals, the counter continuously counts the pulses of the 1-MHz-frequency quartz oscillator. The first signal arriving at the instrument input triggers scan I and the strobing pulse generator, which generates a positive pulse of duration 1.5 μ sec. The strobing pulse enters the coincidence circuit, which passes a single counting pulse. The amplified coincidence pulse passes through the 0.5 μ sec delay line and triggers the disconnect monovibrator, which blanks the amplifier

II for 3 μ sec, i.e., it disconnects the counter for three counting pulses. In the course of this time, the counter is interrogated and its indications are recorded.

The interrogate blocking generator is triggered by the front of the disconnect pulse, with 1 μ sec delay. The pulse from the blocking generator enters the interrogate circuit and triggers scan II. From the output of the interrogate circuit, the counter indication, in the form of a sequential series of pulses, passes through the amplifier III to the tube vertical deflection plates, and is recorded in scan II.

The input pulse is applied to scan I with 0.5 μ sec delay, and the 1-MHz timing marks and the interrogate pulse pass through the mixer. The interrogate pulse must be input to scan I in order to eliminate the ambiguity of ± 1 period of the quartz generator signals; it serves to correlate scan I of the input pulses to the first and last counting pulses of the corresponding time interval.

The chronograph described in [44] makes it possible to record 14 sequential time intervals of duration from 64 μ sec to 16,448 μ sec, each to within 0.02 μ sec. The instrument is based on the principle of counting the number of microsecond pulses during the measured time intervals with simultaneous oscillographic recording of the time of arrival of the pulses defining the time intervals on a type 23L051 circular-scan CRT.

Counting of pulses with 1- μ sec repetition period in this chronograph is also accomplished by the single binary counter from which the information is taken sequentially to the corresponding columns of a matrix consisting of cold cathode thyratron memory elements [45]. /155

The coupling and interaction of the chronograph elements are easily followed in the block diagram of Figure 3.16.

After arrival of the initiating signal, the monovibrator I activates, opening the selector I, and thus energizing the instrument

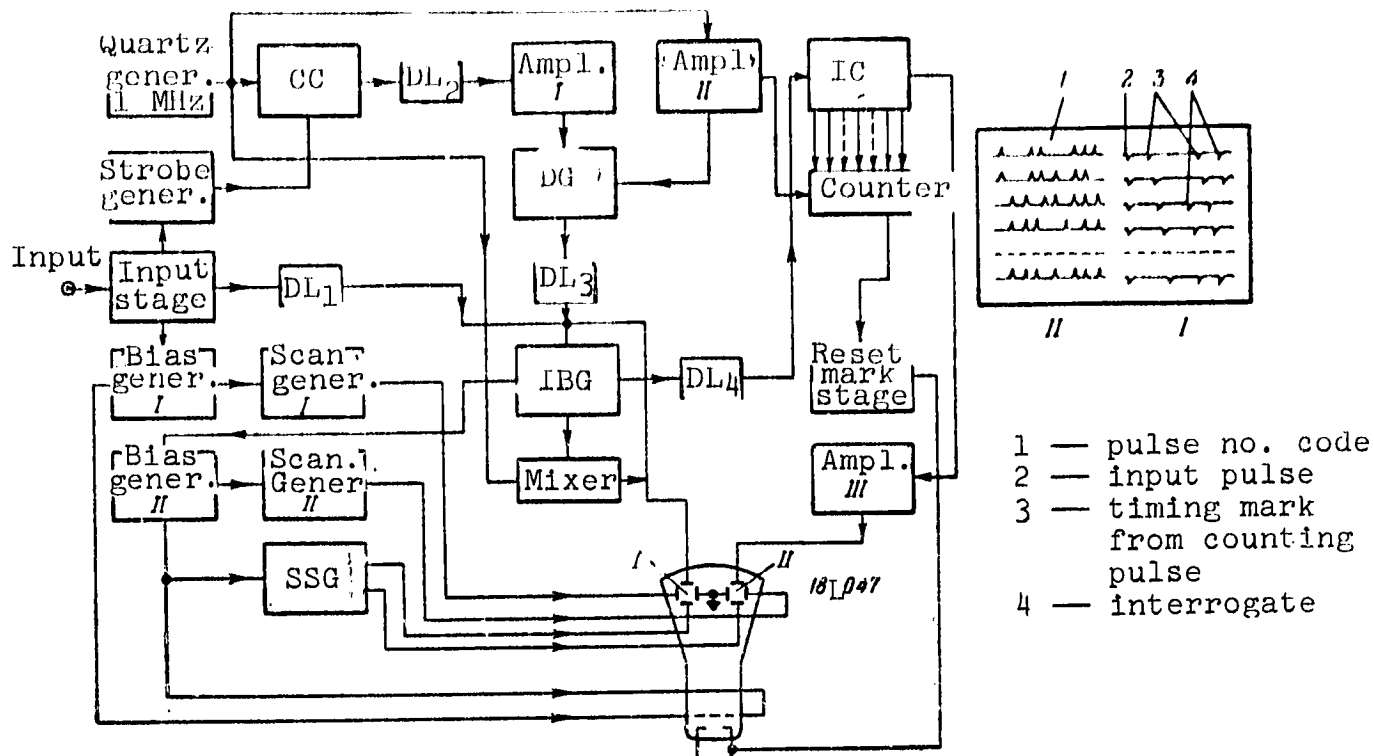


Figure 3.15. Block diagram of electronic chronograph with CRT recording of the measured time intervals:

CC — coincidence circuit; IBG — interrogate blocking generator; DG — deflection generator; IC — interrogate circuit; SSG — sinusoidal scan generator

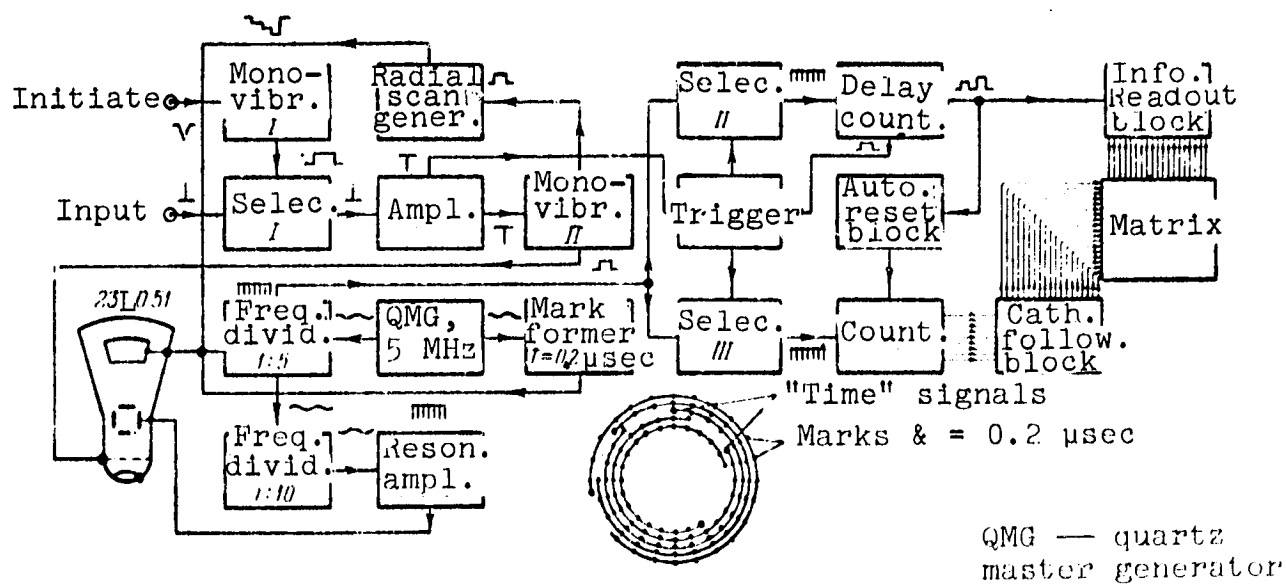


Figure 3.16. Block diagram of electronic chronograph with matrix memory using cold cathode thyatrons

for a time established in accordance with the expected experiment duration. After passing through the selector and amplifier, the signals defining the time interval flip the trigger controlling selectors II and III into the position in which selector II is open and selector III is closed. At this point, the counter stops, and counting begins in the delay counter.

In the course of the delay time, equal to 64 μsec , information is taken from the primary counter and transferred into the memory matrix; then, with the aid of the automatic reset block, the counter is set to the original position. After completing the operating cycle, the delay counter puts out a pulse which flips the trigger, as a result of which selector II is blocked and selector III is opened, and the primary counter again begins to count off the next time interval.

In addition, the pulses from the input signal amplifier are input to the monovibrator II, which generates bias pulses 8.5 μsec long and controls the radial scan generator, which provides stepwise compression of the circular scan to prevent overlapping of the sweeps.

Analysis of the oscillogram (see Figure 3.16), consisting of parts of coaxial circles of no less than 140 mm diameter, which are broken down into segments 0.2 μsec long, makes it possible to count the number of microseconds and fractions of a microsecond to within 0.02 microsecond. This time is a correction of the total time read-out, taken from the indications of the corresponding matrix column.

The standby operating regime is quite convenient, since it permits identify the group of signals between which the time intervals are measured from the series of pulses arriving at the instrument input. This makes it impossible for the chronograph to trigger from random signals prior to and after conduct of the experiment.

A single 5 MHz quartz-stabilized master oscillator is used in the chronograph. All the other signal frequencies required for

instrument operation are obtained by direct division of the master oscillator frequency, which eliminates the "racing" phenomenon.

Since the measured time interval durations are determined to within ± 1 μ sec directly from the indicator matrix, it is possible to obtain fast estimates and monitor the experiments being conducted without the need to develop, dry, and analyze the oscillograms. /157

The time measurement problem cannot be considered separately from operation of the detectors and the circuits for forming the "time" signals, and also transfer of these signals from the detectors to the chronograph. Serious attention must be devoted to determining the operating point on the detector signal diagram, relative to which the "time" measurement is made. The operating point should be selected so that the stability of its temporal coordinate will be maximal.

Realization of time measurement with accuracy on the order of hundredths of a microsecond requires careful specification of the program in each individual case and control of the process of detector signal conversion into electrical pulses.

The degree of detector standardization should be subjected to periodic verification.

Analysis of the phenomena taking place in communication lines indicates the necessity for matching detector output resistance, line characteristic resistance, and chronograph input resistance.

Another significant factor influencing time measurement accuracy is the presence of electromagnetic and frequently detonation interference, accompanying the conduct of the experiments. General procedures relating to the methods for eliminating these interferences or reducing their influence cannot be defined, and in most cases individually approved techniques are used.

§ 3.7. Visualization Methods and Photographic Systems

High-speed photography is the primary source of information when conducting aerodynamic studies, and also experiments involving the study of collision and destruction processes.

When photographing flying bodies with the use of any flow visualization system, we can obtain various data on the flow around the bodies. At the same time, we can determine from these photographs the "instantaneous" values of the model center-of-gravity coordinates and angles of attack.

The shadow method, the schlieren or Toepler method, and interference methods can be used to visualize compressible gas flow. These methods are based on the fact that the local refractive variations index caused by density variations influence light ray propagation, and this results in screen illumination variation. /158

The optical visualization methods make it possible to study flows without causing any disturbance in the stream and obtain information on the entire region being observed simultaneously.

Moreover, since the "detector" is the medium itself, the lag phenomena associated with inertia of the recording instruments are naturally absent.

Figure 3.17 shows the path of a light ray in the case when an optical nonhomogeneity — schlieren — is encountered along the ray path. The disturbed ray A' strikes the screen at point B' at the instant of time t' . Correspondingly, the undisturbed ray A would arrive at point B of the screen at the instant of time t . With the aid of special optical apparatus, we can record on the screen either the ray linear displacement $B' - B$ (shadow method), the angular deflection ϵ (schlieren method), or the phase lag $t' - t$ (interferometer method).

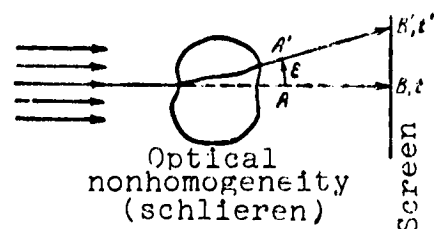


Figure 3.17 Ray path in optical nonhomogeneity

The recording of combinations of these effects is also possible. Along with the visualization methods mentioned above, wide use is also made of various modifications of these techniques.

The optical flow visualization methods are described in detail in numerous original studies and monographs [14, 47 - 55]; in the present section, we shall examine some features of their application in ballistic studies.

The shadow visualization method ("luminous point method") is extremely simple and, specifically, when photographing in diverging rays does not require any optical equipment. Since a large number of photographic stations are used when conducting ballistic experiments, the shadow method has found very wide application because of its simplicity. Since during photography in diverging light rays there is distortion of the image of three-dimensional objects, and determination of the model coordinates and angles of attack definitely require the introduction of corrections, preference is given to photography in parallel rays in two orthogonal projections.

Figure 3.18 shows two versions of shadow photography systems in parallel rays with external location of the photographic equipment. Figure 3.19 shows a system with internal location of the equipment [5]. In the latter case, the parallel light beams are created by the silvered parabolic reflectors 6 and 7 and point light sources 5. The model is photographed in the mutually perpendicular light beams 1 and 2, yielding on the films 3 and 4 horizontal and vertical shadow projections of the flow pattern around the body. A similar system was also used in [8].

/159

The light sources used in the shadow instruments ("luminous point method") must have small luminous zone linear dimensions, since otherwise it is impossible to obtain adequate spatial resolution. The magnitude of the blurring d , owing to the finite light source diameter D , can be estimated from the formula:

$$d = D \frac{t}{T},$$

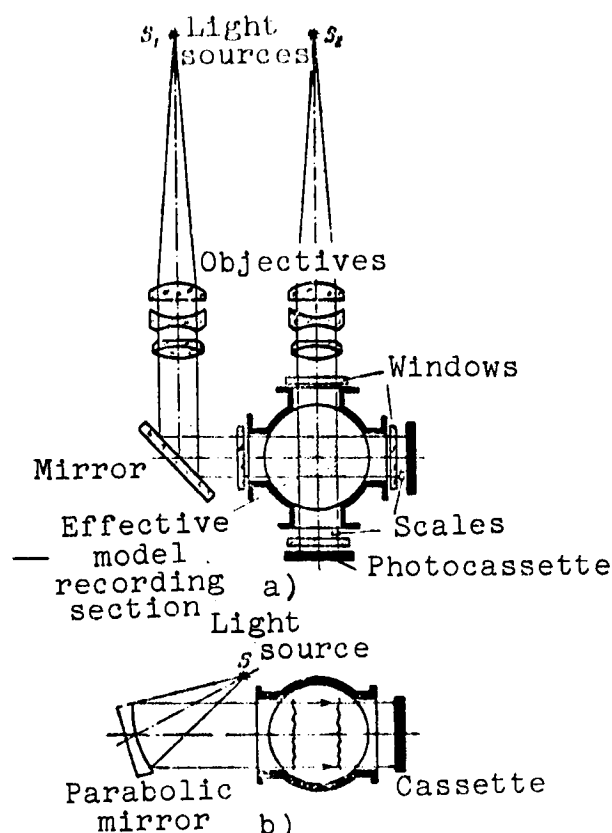


Figure 3.18. Shadow photography in parallel rays: a) system using point light source and objectives; b) system with parabolic reflector

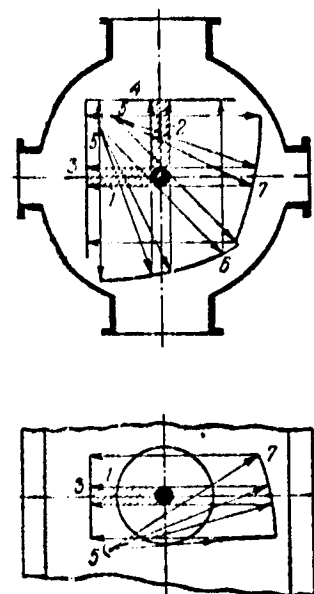


Figure 3.19. Shadow photography in parallel rays with internal location of the apparatus

where l is the distance from the object to the cassette, and f is the objective focal length.

/160

As is well known, the shadow method records the second derivative of the density, which makes

it possible to use this method for recording shock waves, tangential discontinuities, turbulent phenomena, and other gasdynamic processes which are accompanied by rapid variations of the refractive index gradient.

With account for diffractive phenomena [55, 56], the shadow method provides simple and reliable determination of data, such as shock wave location and shape, separation point location, flow detachment angles, boundary layer regime and thickness, and wake geometric patterns [57, 58, 61].

The basic drawbacks of the shadow method are its comparatively low sensitivity and, since this method is based on recording ray displacement, the appearance of geometric distortions of the model contours. Diffractional phenomena, which show up more strongly the greater the sensitivity of the method, lead in turn to image sharpness deterioration.

Other significant drawbacks of the shadow method are the difficulties in analysis of the results and the limitations in obtaining quantitative information, which reduce to determination of the density at the apex of the axisymmetric shock wave [62, 63].

A schematic of the shadow method, with diaphragming of the beam in the receiving part of the optical system (schlieren method) is shown in Figure 3.20.

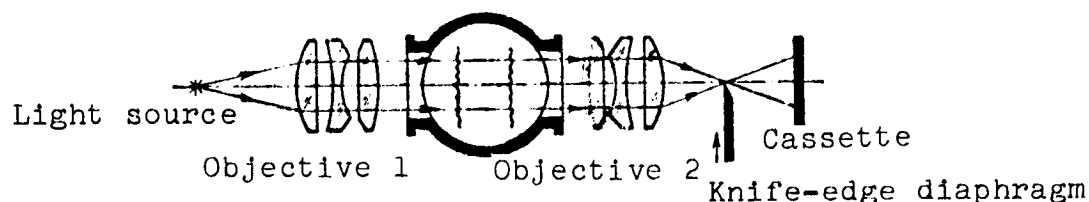


Figure 3.20. Schematic of shadow method with diaphragming of the light beam in the receiving part of the optical system

As an example of a schlieren photograph obtained with horizontal knife-edge alignment, Figure 3.21 shows model flying in air, with $P = 1$ atm, $M = 2.74$, and $Re = 9 \cdot 10^6$.

There are many different schlieren system variants, but in practice preference is given to the scheme with parallel ray passage through the region under study [10].

A parallel light beam is created by the objective 1 (see Figure 3.20), while the objective 2 focuses the range central plane on the cassette. A Foucault knife edge or diaphragm of some other type is located at the focus of the objective 2. In the presence of

schlieren in the ray path, part of the deflected rays is blocked by the diaphragm, which leads to change of the screen illumination in the region where the schlieren are focussed.

In place of the diaphragm, we can also use a grid, which is located either in the focal plane of the objective 2, or is shifted out of the focal plane along the optical axis (defocused diaphragm method).

Severe requirements in regard to absence of nonhomogeneities and spherical and chromatic aberrations are imposed on the optics used in the schlieren system. Most suitable are the long-focus objectives, and large diameter reflector-meniscus objectives are used in schlieren instruments.

The schlieren method makes it possible to detect refractive index gradients and permits quantitative determination of the magnitude of the first derivative of the density [49, 52, 53, 55]. Even relatively small, but sharp, density variations are clearly recorded on the schlieren photographs.

The addition of a pair of parallel semitransparent mirrors mounted at the edges of the region under study permits significant schlieren system sensitivity increase [64]. A schlieren system with double ray passage through the optical nonhomogeneity is described in [59, 60].

Since the schlieren and the cassette are located in conjugate planes of the objective 2 in the schlieren instrument, the image of the flying model is undistorted.



Figure 3.21. Schlieren photograph of model flying in air
($M = 2.74$, $Re = 9 \cdot 10^6$, $P = 1$ atm)

/161

In those cases when it is desirable to obtain photographs on a 1 : 1 scale — for example, when recording the space-time dependence of flying bodies, the objective 2 is positioned so that the schlieren and the cassette are located in the principal conjugate planes of the objective, i.e., at twice the focal distance from the objective. We note that optical systems analogous to Figure 3.20, but not equipped with knife-edges or diaphragms, have found application in photographing the silhouettes of models with minimal recording of the optical nonhomogeneities of the medium [25, 58]. /162

Both point-type and line-type light sources are used in the schlieren instruments. The line-type sources have the advantage that they are more effective in relation to light output.

The interference method [49, 50] has the greatest potential capabilities in relation to obtaining quantitative data. With the aid of the interferometer, we can record the refractive index variation and, consequently, we can determine the corresponding distribution of the density of the medium.

In ballistic studies, we normally use the Mach-Zehnder interferometer, whose schematic can be seen in Figure 3.22. The interferometer operating principle is as follows. The light ray from the source arriving at the first semitransparent mirror is split into two coherent rays, one of which passes through the range region under study, while the other passes through a compensator which regulates

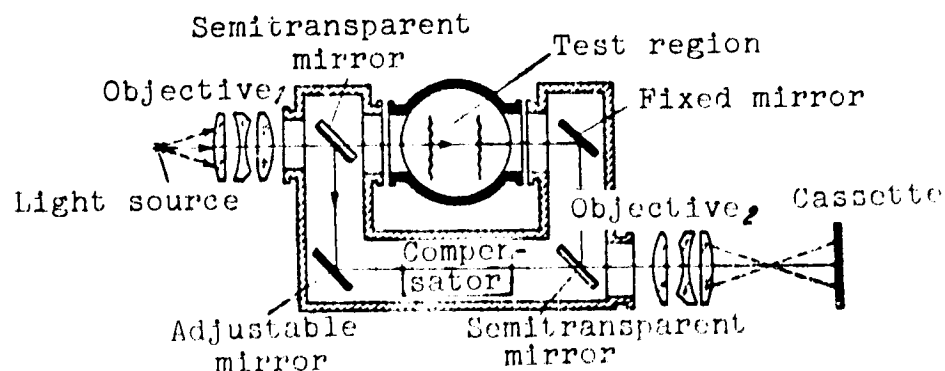


Figure 3.22. Mach-Zehnder interferometer

the ray path difference. The rays are recombined by the second semitransparent mirror, and the interference pattern is projected onto the cassette. By varying the adjustable mirror angle, we can establish the spacing and slope of the interference fringes.

Variation of the "working" ray optical length (the optical length is the product of the refractive index by the ray path length) is accompanied by proportional shift of the interference fringes.

Measurements of the fringe shift make it possible to determine the refractive index change, and therefore the change of the density of the medium (since the density is linearly related with the refractive index). /163

The theory and application technique of the Mach-Zehnder interferometer with single-mirror regulation are presented in detail in [49, 66, 67]. An original interferometer design with parabolic mirrors is described in [68].

The direct use of interferometers in ballistic experiments is described in [12, 65, 66, 69 - 72]. As an illustration, Figure 3.23 shows an interferogram of the flow past a cone in air, with $P = 1$ atm and $M = 2.35$.

At the present time (along with quantitative studies of plane and axisymmetric density fields), studies of three-dimensional flows [73 - 75] have been initiated as a consequence of the fact that suitable interferometer measurement techniques have been developed. Consequently, the capabilities of the optical methods for studying gasdynamic flows have expanded significantly.

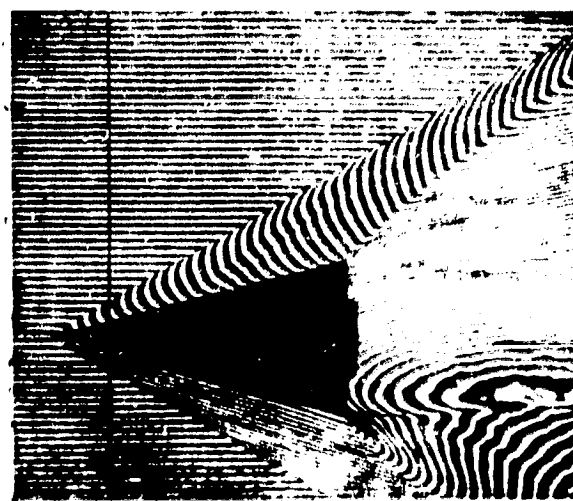


Figure 3.23. Interferogram of flow past a cone in air ($M = 2.35$, $P = 1$ atm)

The sensitivity of the various flow visualization methods is examined in [49, 52, 55, 76].

The density measurement methods based on absorption of various sorts of radiation [49, 54] are effective only at low gas pressures and, therefore, are not used in practice in ballistic studies.

§ 3.8. Pulsed Light Sources

One of the most important requirements imposed on the photographic systems used in ballistic studies is short exposure duration. An exposure duration of 0.1 μ sec is required, in order that blurring owing to body displacement not exceed 0.1 mm, even at a velocity of 1000 m/sec. /164

In addition, the photographic system must make it possible to obtain images of high clarity (resolution) which permit studying the details of the flow pattern and permit measurement of the model spatial coordinates with adequate accuracy.

Another important requirement is photographic system constructional simplicity and operational reliability, since a large number of photographic stations are normally used in ballistic ranges.

The process of blur spot formation, associated with rapid movement of the object being photographed, is studied in [77].

Analysis of the various high-speed recording and cinematography methods, from the viewpoint of obtaining space-time information, is made in the detailed survey [78].

The techniques and capabilities of high-speed photography using optical-mechanical systems are examined in detail in [51].

The need to ensure high temporal and spatial resolution and photography of the model at sections spread out along the range has led to relatively rare application of high-speed cameras for

conducting aerodynamic experiments in laboratory ballistic ranges. Examples of the use of cameras in ballistic studies can be found in [7].

High-speed cameras (usually together with systems for generating series of sequential light flashes) are used primarily for studying essentially unsteady processes [83], such as wake development behind bodies [59, 80], shock wave propagation, collision phenomena, etc.

The high-speed camera version termed the "time magnifier", in which image separation is achieved optically (by selecting the mutual positioning of the pulsed light sources, the object being photographed, and the film cassette) is a simple design, and makes it possible to obtain series of high quality photographs of high-speed processes.

Spark "time magnifiers" of various types are described in [18, 79, 83 - 89]. /165

The high-speed photography method most widely used in ballistic ranges is photography with the aid of pulsed light sources of short duration.

The primary light sources used are gas discharge lamps and spark generators, in which the illumination source is gas heated to high temperature by current passing through the gas. These sources and their power supply circuits and control circuits are exceptionally simple, and they consist of a small number of component parts.

The systematization and description of various gas-discharge lamps are presented in [52, 90, 91]. The gas-discharge lamps are highly economical, permit variation of the radiation intensity and flash frequency in wide limits, have long operating life, and are stable in operation. Inert gases or mercury vapors are used in the gas-discharge lamps in order to increase the luminous efficiency.

However, because of gas afterglow — which is particularly long in the inert gases, the minimal gas-discharge lamp light flash duration amounts to about 1 μ sec, which permits their use only for the solution of particular ballistic experiment problems. Another disadvantage of the gas-discharge lamps is the relatively large luminous region dimension.

Spark generators using discharge in air are the pulsed light sources most widely used in ballistic ranges. This is explained by the fact that the light flashes generated by the spark sources can have a duration of the order of 0.1 μ sec, and brightness adequate for operation of the schlieren instruments. The spark source radiator luminous region (luminous body) dimensions may be small; consequently, the spark light generators are used with success in shadow photographic systems to provide the required spatial resolution.

Many spark generator designs are described in the literature. They are all based on the same principle, and consist of a capacitor (or coax line segment) which is charged from a high-voltage source and discharges at the required instant of time through the spark gap [7, 10, 92, 93].

In such light sources, initiation is accomplished by a discharge between an auxiliary (third) electrode and one of the primary (working) electrodes.

Pulsed light sources are characterized by the following three basic parameters: brightness of the luminous body, duration of the generated light flash, and the spectral composition of the radiation. /166

The results of studies of the discharge processes in pulsed light sources, presented in [90 - 103], have made it possible to identify the factors which influence the brightness and duration of generated light flashes.

Since the maximal current in the spark circuit is defined by the expression:

$$t_{\max} \approx U \sqrt{\frac{C}{L}}, \quad (3.4)$$

and the discharge time constant is:

$$\tau \approx \frac{2\pi}{\sqrt{\frac{1}{LC} - \left(\frac{R}{2L}\right)^2}}, \quad (3.5)$$

where U — breakdown voltage; C — condenser capacitance; L — inductance; R — resistance; we see that reduction of the inductance leads to increased energy release rate in the discharge gap, and consequently, other conditions being the same, increased flash brightness and reduced flash duration.

The use of short coaxial cable segments with low characteristic impedance, which is achieved by using as the dielectric barium titanate, whose dielectric constant is of the order of 1000, as capacitors has been proposed in order to reduce the discharge loop inductance as much as possible [104]. A coaxial cable segment only 16.5 cm long and having about 0.01 μF is sufficient for forming a current pulse of duration $3 \cdot 10^{-8}$ sec. Mounting the discharger directly on the capacitor makes it possible to eliminate lead inductance completely. The duration of the resulting light flashes is 0.1 μsec .

A similar principle was used in constructing a spark light pulse of duration 0.25 μsec and maximal brightness $4 \cdot 10^7$ candles/cm² (corresponding to brightness temperature $\sim 40,000^\circ \text{K}$) [93].

The discharges in inert gases have well known advantages in relation to luminous efficiency; nevertheless, in those cases when it is necessary to obtain short duration spark flashes, preference is given to gases with lower molecular weight, particularly nitrogen or air, at atmospheric or elevated pressure, since the afterglow is less in these gases.

In order to avoid the afterglow caused by metal vapors, the electrodes are made from tungsten, which has high melting and

vaporization temperatures. In addition, increase of the distance between the electrodes is accomplished by shortening of the light pulse duration. /167

It was shown in [97] that there is a minimal light pulse duration for each discharge energy. Without analyzing the reasons for this phenomenon, we simply note that for discharge energy equal to 1 Joule, the minimal light pulse duration at the 0.35 level is about 0.14 μ sec; for discharge energy equal to 0.7 Joule, the corresponding duration is about 0.1 μ sec; and for discharge energy 0.15 Joule, the duration is about 30 - 40 nsec.

The description of several light source variants having light pulse durations of 20 - 60 nsec can be found in [96, 105 - 108]. A pulsed light source of still shorter duration (~ 2 nsec) is described, for example, in [109].

The drawbacks of the three-electrode sources include the difficulty of ensuring high luminous body position stability and the inevitable initiating spark influence on the light pulse parameters.

Figure 3.24 shows a spark generator [81], in which capacitor discharging is accomplished through two gaps in series, which eliminates both of these drawbacks. The source operating principle can be seen if we turn to Figure 3.25, which shows a modification of the subject light source which makes it possible to obtain a series of sparks in the same radiating gap l_2 by using a corresponding number of discharge loops having their own control gaps l_1 .

In order to use the source in the shadow photography scheme using the "luminous point" method, the light from the radiating discharge channel is emitted through a hole of about 0.5 mm diameter, drilled in one of the electrodes.

When using the source in schlieren photographic systems, pointed tungsten electrodes are used in the radiating gap, and are positioned in a slot cut in a ceramic. The presence of a substrate ensures

high luminous body position stability, and at the same time makes it possible to increase the length of the gap, thus increasing the luminous efficiency.

With condenser capacity equal to $0.047 \mu\text{F}$ (condensers of the KOB-4 or K-15-4 type), charged to 15 kV, the light pulse duration at the 0.5 level is about 35 nsec, and at the 0.35 level — about 50 nsec. With working voltage 9 kV, the light pulse durations at the 0.5 and 0.35 levels are about 25 and 40 nsec, respectively.

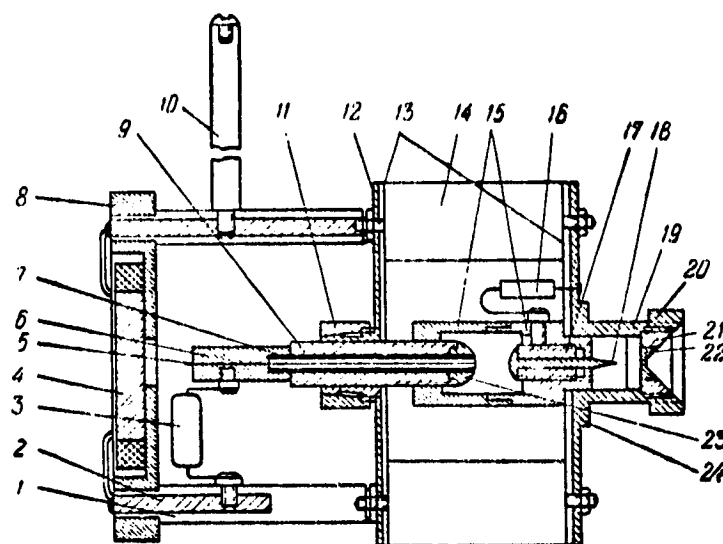
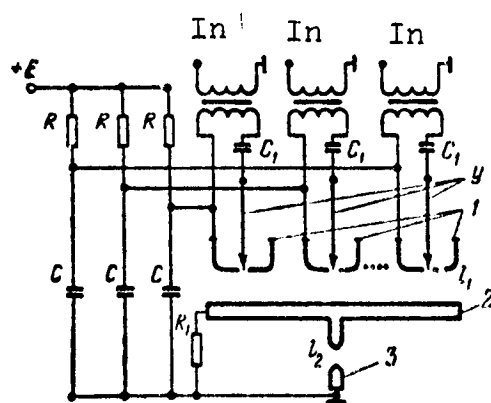


Figure 3.24. Spark light source:

1 — plexiglass posts; 2 — brass rod; 3 — condenser; 4 — transformer; 5 — tungsten needle; 6 — needle holder; 7 — porcelain tube; 8 — transformer mounting cup; 9 — high voltage electrode; 10 — high-voltage resistor; 11 — nut; 12 — brass disk; 13 — plexiglass disk; 14 — condenser; 15 — housing for mounting electrodes; 16 — resistor; 17 — intermediate electrode; 18 — molybdenum needle; 19 — insulator cup; 20 — nut; 21 — washer; 22 — molybdenum insert; 23 — molybdenum cap



1, 2, 3 — electrodes
y — controlling (initiating) electrodes
C — capacitors
R — charging resistor
C₁ — isolating capacitors
R₁ — potential equalizing resistor
l₁ — control gap
l₂ — radiating gap

Figure 3.25. Spark light source for obtaining series of sparks in a single gap

The light source intensity is adequate for use in photography using the schlieren method (with the IAB-451 instrument), and in the Mach-Zehnder interferometer of the TE-42 type when using a light filter with 20 Å passband. /169

Figure 3.26 shows spark source circuits with a single gap and initiating devices. Also shown is the typical geometry and positioning of the primary and initiating electrodes, which form a thyratron

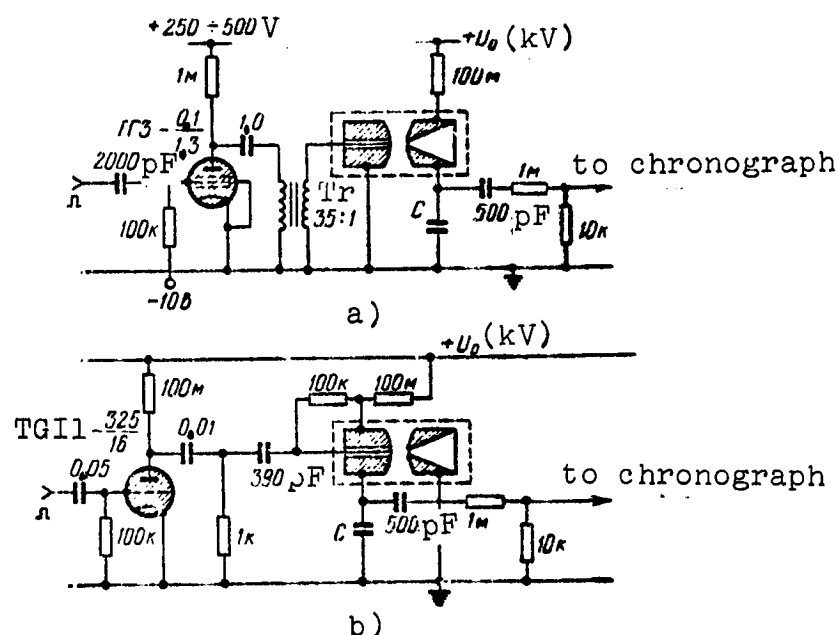


Figure 3.26. Spark generator control scheme:
a) initiation with aid of pulsed transformer;
b) initiation with aid of pulsed thyratron

system. Initiation of the light sources with two gaps is accomplished by means of similar devices (see, for example, Figure 3.25).

In scheme a), source initiation is accomplished by a low-voltage thyratron and pulsed step-up transformer. In scheme b), initiation is accomplished by a type TG11-326/16 high-voltage hydrogen-filled thyratron. The initiating pulses can be applied either to the grounded electrode (scheme a), or to the high-voltage electrode (scheme b). In the latter case, it is necessary to introduce an isolating high-voltage capacitor ($\sim 390 \text{ pF}$) and a potential equalizing resistor ($\sim 100 \text{ k}\Omega$).

These schemes make it possible to ignite sources with a delay of about 1 μ sec, and scatter — about 0.1 μ sec [95, 111, 112]. We note that the thyatron triggering time and its scatter decrease if the initiating pulse has polarity opposite that of the ungrounded electrode, and if the initiating pulse front slope is increased. /170

A thyatron which triggers with nanosecond accuracy is described in [112]. A short delay time is ensured by placing the thyatron in a freon atmosphere and increasing the operating voltage to 50 kV.

Methods for synchronizing two spark sources, necessary when photographing in two planes, are shown in Figure 3.27. Scheme a), which is the simplest synchronization variant, initiates the second source (with operating voltage 25 kV) with a delay of about 80 nsec,

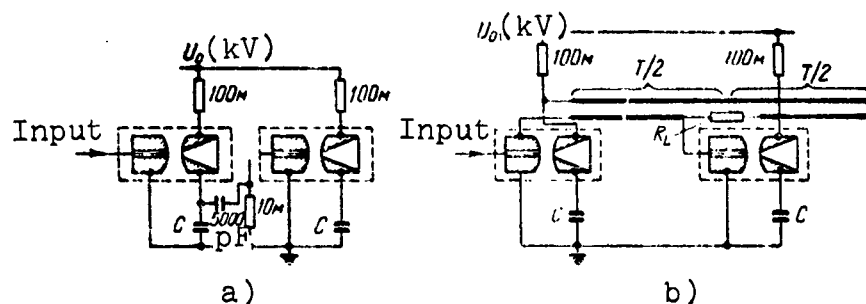


Figure 3.27. Scheme for controlling two spark sources: a) sequential activation; b) initiation with short delay time

and 10 nsec scatter of the instant of initiation. In those cases when more precise synchronization is required, it is advisable to use scheme b), which as a result of using a two-conductor line ensures the appearance of spark flashes with 50 nsec time difference and second source triggering time scatter about 2 nsec.

The signals denoting the instants at which the pulsed light sources trigger, which are required for timer operation, can be obtained either by recording the excitation pulses in antenna loops [4, 10], or with the aid of voltage dividers [7, 112], as shown in Figure 3.26, or by means of photodetectors and a lightguide system.

Since in the latter version the "time" signals are formed directly from the light signals, this provides maximal time recording accuracy.

A pulsed source of exceptionally short light pulses, of about 2 nsec duration, whose operating principle is based on illumination of a CdS target under the influence of a high-density electron stream, is described in [82].

The source provides essentially monochromatic radiation with wavelength 5300 Å. The wavelength can be altered by suitable target material selection. As a consequence of target heating during electron bombardment, the radiation band has a width amounting to 1% of the wavelength. Thanks to the monochromaticity of the radiation, the use of light filters is permissible if it is necessary to eliminate self-luminosity of the objects being photographed. /171

The energy of the light pulse emitted by a source with target diameter 14 mm is equal to 0.025 J. When using diaphragms, the source can be utilized, specifically, for photography using the "luminous point" method in ballistic studies.

The use of lasers as light sources for high-speed photography has been initiated relatively recently. The pulsed light source, based on the laser, has exceptionally high radiation intensity and is monochromatic (line width less than 0.5 Å), and has space-time coherence and high directivity. In addition, photography with exposure times on the order of a few nanoseconds is possible with operation of the laser in the pulsed Q modulation regime.

The high brightness of the laser light sources [113] makes it possible to use them for photography with external illumination of strongly luminescing objects, and also for high-speed microphotography. For example, results are presented in [115] of photography of an exploding tungsten wire on the background of a diffusion screen illuminated by a Q-modulated ruby laser having several megawatts radiation power. A description is given in [113 - 122] of laser use for shadow, schlieren, and interferometric plasma studies.

The combination of lasers with high-speed cameras or electron-optic converters opens up possibilities for cineradiography with nanosecond exposure durations and picture frequency of about $15 \cdot 10^6$ frames per second [123 - 127].

A unique "time magnifier" with exceptionally high time resolution (exposure duration 5 nsec, time between frames 10 nsec) is described in [128]. In this instrument, the flashes of a laser operating in the giant pulse mode are separated optically by a system of semitransparent mirrors, located so as to ensure different light beam path length. As a result, there are formed from a single laser pulse four signals, shifted in time by magnitudes corresponding to the optical path lengths. In order to reduce graininess, a diffusing screen is introduced, and the self-luminosity of the process being studied is reduced by an interference filter. This "time magnifier" makes it possible to study phenomena taking place with velocities up to 10^4 m/sec. /172

The high intensity and short duration of the flashes created by the laser light sources have led to their use for ballistic studies [129 - 138].

In [133], a laser in which Q modulation was accomplished by a Kerr cell served as the source of light pulses of duration ~ 30 nsec for photographing models of various form, flying at speeds up to 7 km/sec. A schematic of the photography system is shown in Figure 3.28. A similar technique was used in [138].

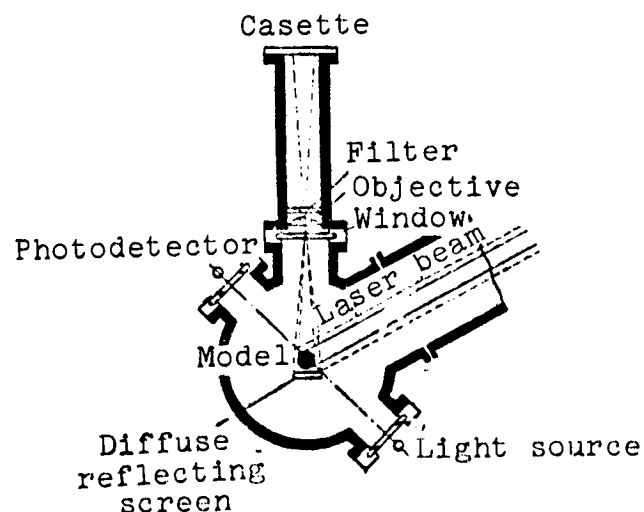


Figure 3.28. Schematic of setup for photography in reflected laser light

Shadow photography in parallel light rays of bodies in free flight with the aid of a pulse-modulated laser was performed in [129, 130, 136], with the exposure duration reaching 5 - 15 nsec. The photographic system optical channels did not differ in principle from those shown in Figure 3.20.

Thanks to the use of a laser light source with 5 nsec duration, photographs were obtained in [130] of a model flying at 6000 m/sec, which permitted obtaining information on the model geometric characteristics with accuracy better than 0.05 mm.

Analysis of the cited studies shows that the use of pulsed lasers as sources of short light flashes is advisable, particularly when studying model material ablation.

The appearance of lasers, whose radiation has high space-time coherence, has stimulated development of the holographic investigation method [134 - 163].

The basic principles and possible applications of laser holography are presented in [141, 142, 148].

/173

Several dual-beam holography system variants are known. In this case, the hologram is a photographic record of the interference pattern which arises on the photofilm during interaction of the wave coming through the nonhomogeneity being studied and a reference wave (see, for example, [135, 162]).

Reconstruction of the image is achieved by placing the hologram in the path of a coherent light beam with the same wavelength, if certain geometric relations are satisfied.

The use of lasers, which generate nanosecond band light pulses, makes it possible to obtain "instantaneous" holograms of definite moments of gasdynamic and other high-speed processes, and thus permits us to essentially "freeze" the wave fronts corresponding to these moments of time. After reconstruction, the wave front re-

corded on the hologram can be studied in detail by various optical methods (shadow, schlieren, interferometric).

The description of the technique for forming pulsed laser radiation with monochromaticity and spatial coherence (mode selection) necessary for holography by a laser operating in the giant pulse generation regime can be found in [136, 162].

In order to illustrate the specifics of holography application in ballistic studies, we cite [134 - 136, 161]. The diagram in Figure 3.26 [134] shows the basic elements of a pulsed ruby laser, controlled by a Kerr cell (or Pockels cell), the laser beam expander, and the holographic part of the apparatus, which consists of a beam splitter and three surface coated mirrors. The instant of laser

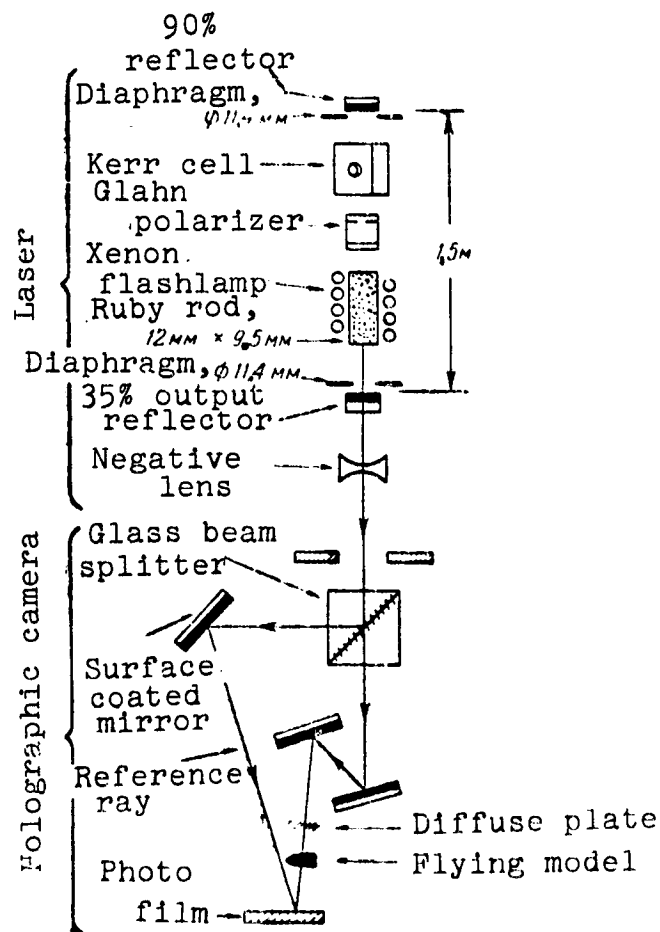


Figure 3.29. Pulsed holographic setup

triggering is synchronized by the passing model and "pumping" of the ruby crystal is accomplished about 1 msec earlier.

The authors of [161] used a ruby laser to obtain holograms of a model flying at 2 km/sec.

In [135, 137], two holograms were photographed on the same photo-film (with approximately equal exposures), without the flying projectile, and then at the instant of projectile passage. A two-dimensional interference pattern, analogous to that obtained using the conventional interferometer, was observed upon reconstructing the wave front of this dual hologram.

Several advantages of holographic interferometry have been noted, primarily the absence of the need to make precise adjustments and use precision optical elements.

An important advantage of holographic interferometry — in comparison with the Mach-Zehnder interferometer, for example — is the possibility of obtaining holograms with broad angle of continuous scan of the fields being studied, which is necessary for studying three-dimensional flows and, specifically, the influence of shock waves created by a discharge on the flow around flying bodies [110] and density fluctuations in wakes [115]. /174

We can mention other possibilities for laser use in ballistic studies — for example, for recording the passage time [136] and for measuring projectile velocity in the gasdynamic gun barrel [164].

§ 3.9. Electrical Fast-Acting Shutters

Model movement in air at hypersonic speed is accompanied by intense luminescence of the surrounding gas, and collision of a body with a barrier causes the appearance of a bright light flash; therefore, fast-acting shutters must be used in order to photograph the radiation of such processes. Since the shutters open for only a /175

very short time, the photographic materials are protected against long-term action of the luminous object radiation.

Fast-acting shutters are based on the Faraday [94, 165, 166], Kerr [6, 94, 167 - 174], and Pockels [180, 181] effects. In addition, electron-optical converters [182 - 189], television [175 - 177], and photoelectronic [178] systems can act as high-speed shutters. An important advantage of the electrical shutters is the possibility of their synchronization with definite moments of the process being recorded.

The phenomenon of light wave polarization plane rotation by a magnetic field is called the Faraday effect. A schematic of a magneto-optic shutter is shown in Figure 3.30. The optically active element is a glass cylinder F with polished ends, usually made from heavy flint glass. At the two ends of the cylinder, there are the polarization filters P and A, crossed at a 90° angle; therefore, in the initial state, light cannot pass through the shutter.

In order to open the shutter, it is necessary to rotate the light polarization plane through $\pi/2$ along its path from the polarizer P to the analyzer A.

With the light directed parallel to the magnetic field, the magnitude of the polarization plane rotation angle α is determined by the magnitude of the magnetic field intensity H and the length l of the path traveled by the light:

$$\alpha = WHl,$$

(3.6)

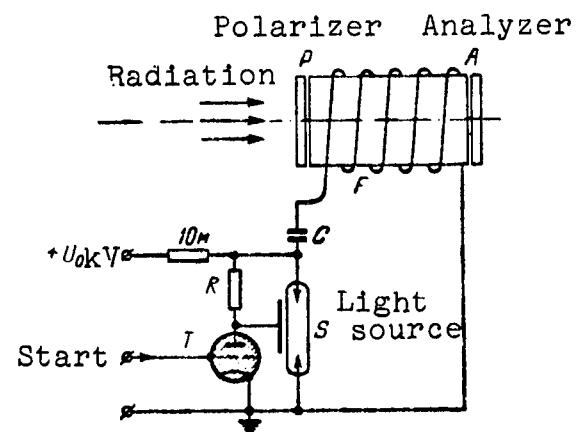


Figure 3.30. Schematic of light shutter utilizing the Faraday effect

where W — coefficient of proportionality (Verdet constant), which depends on the nature of the material, temperature, and wavelength of the light.

The magnetic field of intensity H required for short-term opening of the shutter is created in a solenoid by discharge of the capacitor C , and the light source — if external illumination is used — is the pulsed lamp S , controlled by the thyatron T . Sequential activation of the pulsed lamp and the solenoid ensures synchronization of the moments of illumination pulse appearance and shutter opening with the corresponding phase of the phenomenon under study.

The relations which make it possible to evaluate the required voltage U_0 and capacitance C , which ensure pulsed opening of the shutter, are presented in [96, 165, 166]. The operating voltage is usually 10 - 20 kV, and the condenser capacitance varies from one to several microfarads. /176

The minimal exposures obtained using magneto-optic shutters are relatively long — of the order of one or two microseconds.

Considerably shorter exposures are provided by the shutters using birefringence in an electrical field (Kerr effect).

The limit corresponding to the minimal exposure duration of such a shutter is determined by two factors: the presence of parasitic interelectrode capacitance and the relaxation time τ of the Kerr effect itself. It was shown in [78] that the time interval associated with the existence of parasitic capacitance and inductance can be determined roughly as the time for light to travel a distance of the order of 1 cm, i.e., $3 \cdot 10^{-11}$ sec. As for the Kerr effect relaxation time, it can be evaluated from the formula, due to Debye:

$$\tau = \frac{4\pi\eta r^3}{kT}, \quad (3.7)$$

where η — internal friction; r — average molecular radius; k — Boltzmann constant, T — absolute temperature. Calculations made

for nitrobenzene yield $\approx 10^{-11}$ sec. Thus, we can state that, for the Kerr cell, operating as a fast-acting shutter, the limiting exposure time is about 10^{-11} sec.

The construction of the Kerr cell and the shutter control circuit are shown in Figure 3.31, a and b. The cuvette, filled with an optically active substance, usually nitrobenzene, is located between two

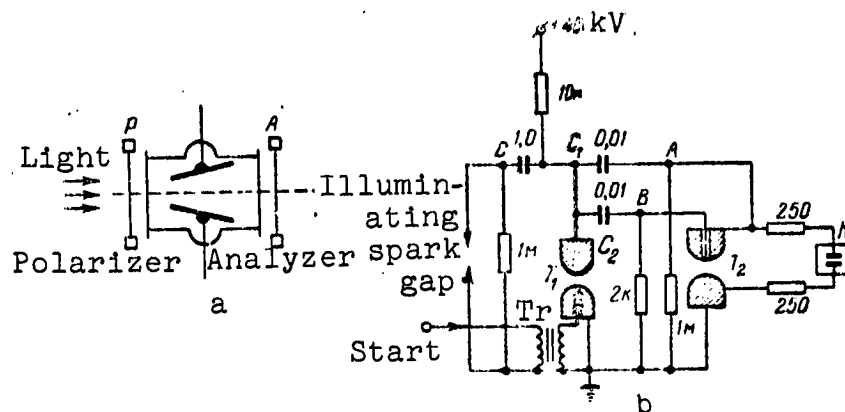


Figure 3.31. Kerr cell control scheme:
a — Kerr shutter; b — circuit for applying opening voltage to the Kerr shutter

crossed polarizers P and A, where the first acts as the polarizer and the second is the analyzer. A voltage pulse, whose duration determines the time during which the shutter stays open, is applied to the plates of a condenser immersed in the nitrobenzene.

Under the influence of the voltage applied perpendicular to the light propagation direction, the nitrobenzene becomes capable of birefringence. In this case, the polarized light components with electrical vectors directed along and across the external field will propagate in the same direction, but with different velocities, and the amplitudes of both beams will be the same if the entering light polarization plane form a 45° angle with the direction of the electrical field. The difference in the beam propagation velocities

/177

leads to a phase shift, and consequently, with addition of the components, to rotation of the polarization plane through the corresponding angle. The magnitude of the phase shift ϕ is proportional to the square of the electrical field intensity E , the path length l traveled by the light in the field, and the Kerr constant B , which depends on the birefringent fluid type and condition, and on the wavelength of the light:

$$\varphi = B l E^2. \quad (3.8)$$

If we ignore the losses associated with light absorption, the intensity I of the light passed by the shutter is related with the incident light intensity I_0 and the magnitude of the phase shift by the relation:

$$I = \frac{I_0}{2} \sin^2(\pi\varphi) = \frac{I_0}{2} \sin^2(\pi B l E^2). \quad (3.9)$$

We see from Formula (3.9) that the maximal light intensity which can be obtained at the Kerr cell output is $I_0/2$, with phase difference $\phi = 1/2$. /178

Using (3.8), and denoting the distance between the electrodes by h , we obtain the expression for the voltage at which maximal shutter opening takes place:

$$U = \frac{3 \cdot 10^2 \cdot h}{\sqrt{2B l}}. \quad (3.10)$$

We should point out the nonlinear dependence of light transmission by the Kerr cell on the applied voltage. According to the data of [94], 50% of the maximal flux passed by the cell flows with a voltage amounting to only 70% of that corresponding to complete opening. This phenomenon is useful when modulating the cell by short voltage pulses of trapezoidal or triangular form.

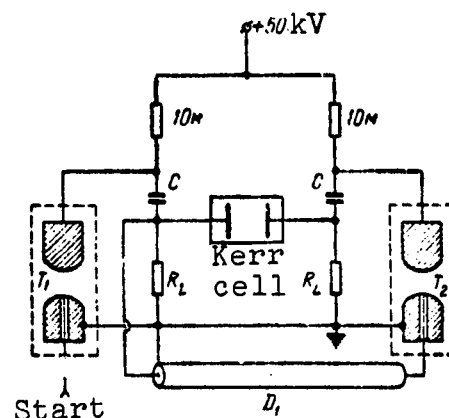
One version of a control circuit for the Kerr cell, which opens with the appearance of an external illumination pulse, is shown in Figure 3.31b. The initiating pulse, amplified in voltage by the transformer Tr , triggers the thyatron T_1 , as a consequence of which

negative voltage pulses of approximately 40 kV arise at the circuit points A, B, and C, and breakdown of the illumination gap (or ignition of a light bulb) takes place. At the same time, the Kerr cell opens.

Since the time constant for discharge of the capacitance C_2 is considerably shorter than that of the capacitance C_1 , after some time the thyatron T_2 triggers, and this removes the voltage from the Kerr cell and closes the shutter.

The drawbacks of this circuit are: impossibility of obtaining small shutter opening durations with the aid of this circuit, instability of the shutter stay time in the open state, and relatively low shutter triggering time accuracy.

Figure 3.32 shows a circuit intended for generating pulses to open the Kerr shutter for microsecond time intervals. The activating voltage is applied to the left-hand electrode of the Kerr cell when the thyatron T_1 triggers, and is removed by applying to the right-hand electrode a voltage of the same magnitude after activation of the thyatron T_2 . The time between the moments of triggering of the thyatrons is determined by the length of the delay cable D_1 , and can be reduced to 3 μ sec.



/179

Figure 3.32. Circuit for applying long opening pulses to the Kerr shutter

A Kerr cell is described in [168] which has large aperture (2 x 4 cm at the entrance, and 3 x 4 cm at the exit), and duration of the shutter stay in the open position equal to 5 nsec, which makes it possible to photograph fast-flying bodies at speeds up to 20,000 m/sec.

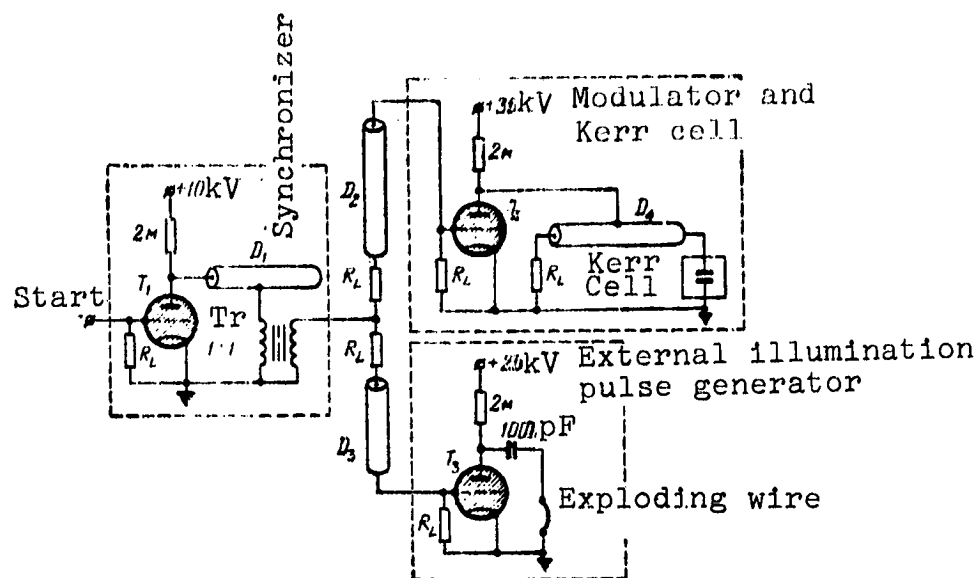


Figure 3.33. Circuit for pulsed Kerr cell control which provides short exposure times

A schematic of the synchronizer, modulator, Kerr cell, and external illumination pulse generator is shown in Figure 3.33. Formation of short-duration and high-intensity pulses is accomplished using coax cable segments D_1 and D_4 , and thyatrons T_1 and T_2 , which play the role of switches.

When the thyatron T_2 fires, a negative voltage pulse with amplitude equal to half the charging voltage and effective duration about 5 nsec, determined by the length of the cable segment D_4 , appears at the end of the cable D_4 , which is connected with the Kerr cell. /180

By varying the length of the delay cables D_2 and D_3 , we can specify the required time intervals between arrival of the initiating signal and the moments of triggering of the illumination pulse generator and the modulator which opens the Kerr cell. If the generator based on the thyatron T_3 is used for synchronization of some phenomenon (exploding wire, for example), then we can photograph various stages of the process by varying the delay magnitude. If the generator based on T_3 is used as an external light source, then by selecting the lengths of the cables D_2 and D_3 , we can achieve

coincidence of the moment of cell opening with the moment when the illumination source brightness reaches its maximum. The synchronization accuracy achievable by this circuit is on the order of a nanosecond.

An analogous system using a Kerr cell with aperture 1×0.6 cm, and duration of the open condition about 30 nsec, is presented in [6].

Since when using thyratrons the Kerr shutter aperture is limited by the maximal anode voltage on the thyratrons, a Kerr cell modulation scheme (Figure 3.34) was proposed in [112, 170], in which commutation is accomplished by a thyatron immersed in Freon-12 (the thyatron is enclosed by a dashed line) and, consequently, the supply voltage can be increased to 50 - 60 kV.

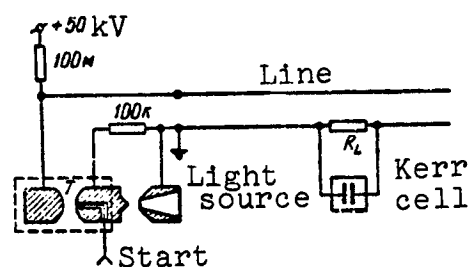


Figure 3.34. Circuit using thyratrons for pulsed Kerr cell opening

Suitable connection of a long line segment made it possible to form shutter activating pulses 50 nsec long, and synchronize the moments of opening with the light flash peak.

A drawback of the Kerr shutters is the large light loss in the polaroids and in the nitrobenzene, which absorbs the blue part of the spectrum, amounting to 55 - 70% of the total light flux entering the shutter.

At the present time, the Kerr shutters are being systematically improved, and new electro-optically active fluids are being sought [179].

In those cases, when it is necessary to use shutters with higher light transmission coefficient, we turn to the crystalline Pockels cells, in which the optically active elements are, for example, potassium dihydrophosphate crystals KH_2PO_4 [180, 209, 210]. The electrical field is applied parallel to the crystal optical axis and

the direction of light propagation. The optical effect depends linearly on the electrical field intensity and the optical path length of the light in the crystal.

We note that the durations of the light pulses generated by pulsed lasers are determined by the opening time of the Kerr or Pockels electro-optical shutters used in the lasers.

A shutter with exposure time less than 1 nsec, whose basic element is a Pockels cell located between two Glahn polarizers, was reported in [181]. The shutter makes it possible to obtain laser radiated pulses with 0.6-nsec risetime, with small synchronization scatter time.

Electron-optic converters (EOC) [182 - 189] have also found wide application for high-speed photography of fast processes, particularly low-brightness processes. A schematic of a photographic camera with EOC is shown in Figure 3.35.

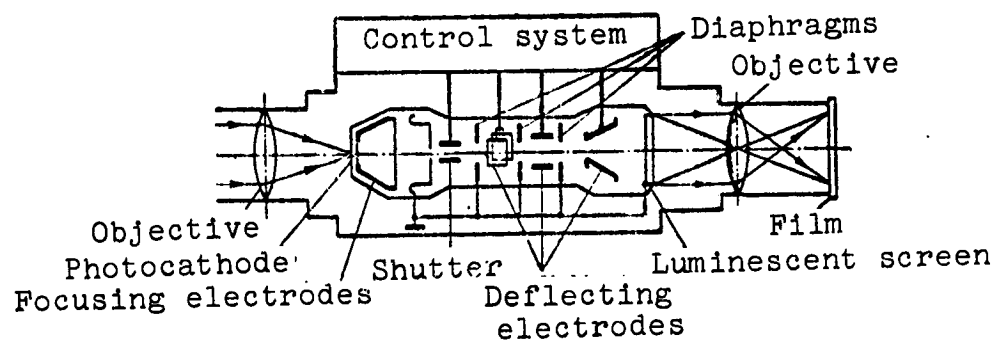


Figure 3.35. Camera with EOC

The EOC is a high vacuum instrument, consisting of a semitransparent photocathode, a system for accelerating and focusing the emerging electrons, and a luminescent screen. The instrument operating principle is based on the fact that the light image projected onto the photocathode is converted into an electronic image, which in turn is transferred with retention of its clarity to the luminescent screen, where it is reconverted into an optical image. Here,

the energy of the accelerating electrical field makes it possible for even the simplest EOC to increase the image brightness by one or two orders of magnitude, and by thousands of times in the cascade-type EOC.

The cameras which have now been developed using EOC as fast-acting shutters [183 - 185] make possible photography with exposures shorter than 1 nsec. The time resolutions achievable using EOC are exceptionally short $\sim 10^{-12} - 10^{-14}$ sec [182].

/182

In addition, an important EOC advantage is the relatively easy possibility of obtaining, with the aid of electronic deflecting systems, series of frames positioned on different parts of the screen [183].

The OEC's can be used in conjunction with various high-speed photographic systems and pulsed light sources, including lasers.

If we introduce a delay between the moment of transmission of the light "packet" generated by a pulsed laser and the moment of EOC opening, then, depending on the magnitude of the delay, segments of space positioned at various distances from the recording system will be photographed. The depth of the examined segments will be equal to the distance travelled by the light during the exposure time.

Since only certain segments are scanned, and objects located in the foreground and background remain in darkness, such a recording system is a sort of "photographic radar" [186, 187].

Reference [188] describes EOC application for photographing phenomena taking place during hypersonic (6 - 9 km/sec) body impact on a barrier, and [211, 212] report on EOC application for photographing flying models.

The limitations in EOC use are associated with the presence of geometric image distortions and the small dimensions of the photocathodes and screens.

§ 3.10. Pulsed Radiography

The penetrating ability of x-rays is the factor which determines the application of pulsed radiography.

Photography in x-rays makes it possible (when using light-protective screens) to record processes which are accompanied by strong luminescence in the visible part of the spectrum. Such processes include flying body collision with barriers, behavior of models and sabots in the immediate vicinity of the barrel muzzle [7], and explosive phenomena (explosives, fine wires under the action of large currents [190], and so on).

Pulsed radiography makes it possible to observe the form and position of the projectile in the launcher barrel bore, and also to study unsteady processes (for example, fracture phenomena and shock and detonation wave propagation) in media which are opaque in the optical wavelength band. /183

Obtaining a series of sequential x-ray photographs with simultaneous chronometry of the moments of photography makes it possible to determine the velocity and acceleration, and also to study the variation in time of different phases of the observed process.

Simultaneous use of two x-ray tubes makes it possible to conduct stereoscopic and orthogonal photography [191].

When conducting studies using pulsed radiography, we take into account three criteria: the size of the x-ray radiation source, exposure duration, and thickness of the material through which the x-radiation passes.

Pulsed radiographic studies of high-speed processes are made either with the aid of a single, multiply-radiating x-ray tube or with the aid of several x-ray tubes operating sequentially at given time intervals.

In the first case, it is necessary to use a high-speed cine camera. In the second case, it is necessary to use a number of cassettes equal to the number of tubes, and spatial separation of the images is achieved by suitable geometric positioning of the cassettes [192], similar to the situation in the spark "time magnifiers" (see § 3.8).

The block diagram of a pulsed radiography setup for studying high-speed processes using a single x-ray tube is shown in Figure 3.36.

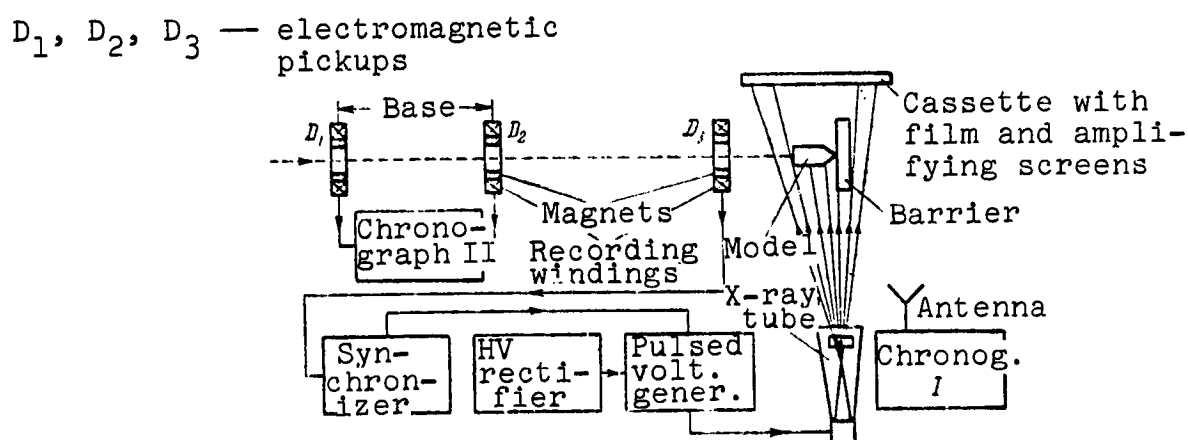


Figure 3.36. Block diagram of pulsed radiography setup

The system consists of the x-ray tube, cassettes with film and intensifying screens, pulsed voltage generator, synchronizing block, and recording and measuring equipment.

The x-ray tube is a high-voltage vacuum (pressure in the envelope less than 10^{-4} mm Hg) diode or triode capable of generating x-ray pulses of short duration and high radiation intensity, which makes it possible to obtain the required darkening of the film in spite of the short exposure time [213]. For this purpose, short current pulses reaching several thousand amperes, with voltage from a few tens of kilovolts [193] ("soft" radiation) to several million volts ("hard" radiation) are passed through the tube. The high electrical current density in the tube is provided by using autoelec-

/184

The construction of a demountable x-ray tube of the diode type [192], operating at about 1000 kV, is shown in Figure 3.37.

The plexiglass tube envelope 1 is mounted on the metal base 2, to which a diffusion pump is connected in order to create a high vacuum in the envelope, since the demountable tube requires continuous evacuation. The tungsten anode 4, mounted in the holder 5, is a needle with $4 - 5^\circ$ angle at the tip and 3 mm diameter. The cathode 3 is a steel ring, with its sharp edge facing the anode. The anode holder 5 is attached to a rubber diaphragm or bellows 6, as a result of which the anode can be aligned with the tube axis by adjusting screws. The required distance between the anode and cathode is established by the regulator 7.

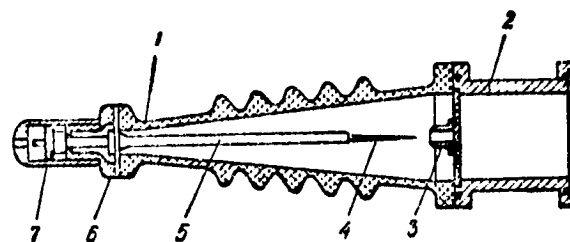


Figure 3.37. Demountable x-ray tube

1 — tube envelope; 2 — metal base; 3 — cathode; 4 — anode; 5 — anode holder; 6 — diaphragm; 7 — regulator

The tube generates x-radiation pulses which can penetrate 10 - 15 mm of steel, and has quite sharp focus (diameter about 3 mm).

Sealed type pulsed x-ray tubes, which do not require continuous evacuation, consist of similar basic elements.

Along with the drawback of requiring continuous evacuation, the demountable x-ray tube has certain advantages: the possibility of periodic cleaning and sharpening of the electrodes.

Impact type generators or pulsed transformers are used to obtain the high pulsed voltages which are applied to the tube.

In order to study the operation of the impact type pulsed voltage generator, we turn to Figure 3.38, which shows a schematic of the GIN-500 generator, specially designed for pulsed radiography.

/185

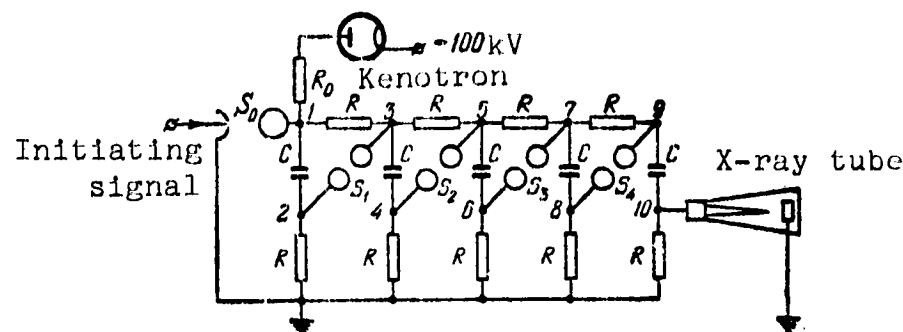


Figure 3.38. Pulsed voltage generator

In the initial position, all the capacitors C ($0.01 \mu\text{F}$), connected in parallel, are charged from a high-voltage rectifier through the kenotron and resistors R_0 and R . Upon triggering of the thyatron S_0 , point 1 is at ground potential, and the voltage between points 2 and 3 doubles, which leads to breakdown of the discharger S_1 and, consequently, of S_2, S_3 , and S_4 . As a result of this, capacitors C are connected in series, and a pulsed voltage exceeding the supply source voltage by five times is applied to the tube. The pulse duration is determined by the effective capacitance and inductance ($\sim 25 \mu\text{H}$) of the discharge loop.

Firing of the thyatron S_0 is accomplished by a pulse formed in the synchronizer. The synchronizer (see § 3.3) also provides the required delay of the signal coming from the model passage detector /186 D_3 (detectors of the electromagnetic type are shown in the schematic). One of the circuits shown in Figure 3.26 can serve as the sync output signal amplifier.

In those cases when it is necessary to synchronize the operation of several tubes or transmit a series of signals to a single tube, we use multichannel synchronizers, similar to those described in [17, 18], or artificial delay lines with different number of elements.

When using synchronizers which generate pulses with uncalibrated time intervals between pulses, it is necessary to measure the time

intervals between tube triggering times in order to determine the rate of development of the process being studied.

Since high-voltage discharges are accompanied by strong electromagnetic surges, on the one hand, we must take measures to prevent random equipment triggering and, on the other hand, we can use a chronograph with antenna input for measuring the time (chronograph I in Figure 3.36).

The detectors D_1 and D_2 (the detector D_3 can also play the role of D_2), located at a known distance from one another, and chronograph II make it possible to measure the projectile velocity prior to impact with the barrier.

Considerable success has recently been achieved in creating radiography systems generating pulses of duration less than 100 nsec [194 - 199]. Specifically, [199] describes systems capable of generating 20 nsec duration x-ray pulses using a diode type tube (length 40 cm, diameter 10 cm) with conical tungsten anode, which provides an effective radiation source diameter of 5 mm. The x-ray radiation pulse intensity scatter is about 1%.

The impact generator used in the system is capable of generating 2-MW pulses, with current intensity 5000 A. Compactness of the pulsed voltage generator and reduction of the interference caused by the generator are achieved by installing the generator in a hermetically sealed metal container. Freon-12 (pressure 2 atm) is used as the insulator between the fiberglass generator case and the container. The generator case is filled with nitrogen at 5 atm pressure in order to reduce the spark gap inductance.

This system permits radiography of moving objects through 9 cm-thick steel and 28 cm-thick aluminum shields, with a distance of one meter between the radiator and the object.

The minimal exposure time provided by modern pulsed radiography units is 3 nsec [195, 196]. /187

The characteristics of radiography units in which a single tube is used to obtain a series of pulses are presented in [193, 195, 200, 201].

When using tubes which generate dense electron beams, it becomes possible to photograph fast-flying bodies and collision processes in electron beams (betagraphy) [194, 196].

Reference [196] reports obtaining high-contrast images (20-micron diameter particles are recorded with the aid of dense electron beams, 4000 A/cm^2 , accelerated to an energy of 600 keV). The exposure time is 3 nsec.

High speed phenomena can also be studied by photographing the luminescence which arises when bombarding the object of observation with fast electrons. Since the radiated light properties depend on the object material, such photography can yield additional information.

Of considerable interest is simultaneous photography in x-ray, electronic, and visible light beams [196].

The use of combined pulsed x-ray and television systems is very promising for studying the collisions of bodies with barriers [214].

§ 3.11. Telemetry Methods

External observations of the trajectories of bodies make it possible to identify only their integral aerodynamic characteristics (drag coefficient, lift coefficient, moment coefficient, etc.). The use of quantitative optical methods for determining the gasdynamic parameters on the surface and near models, in the general case (large angles of attack, nonaxisymmetric three-dimensional bodies), runs into major difficulties.

Because of this, telemetry methods are used to measure the pressure and temperature distribution over the model surface. Telemetry systems can also be used to measure the axial and angular accelerations and, consequently, the forces and moments acting on the bodies. Still another important advantage of certain radiotelemetry methods, in comparison with the optical study methods, should be noted: the possibility of continuous parameter recording during flight.

Effective use of telemetry encounters at least three obstacles: high load factors, which lead to destruction of the telemetry equipment during acceleration in the launchers; small calibers (about 10 mm) of the high-speed firing systems, which require miniaturization of the telemetry components and impede transmitting antenna installation; and the limited ballistic range flight time, amounting to several milliseconds for ranges of "average" length, in connection with which it is necessary to develop fast-response detectors and use equipment which provides fast data collection. /188

The telemetric research methods are now widely used, and we can consider that the ways to overcome the basic difficulties in their realization have been found. The conduct of telemetry measurements is becoming an inseparable part of the total ballistic research program, the absence of which would lead to loss of an important fraction of the information obtained.

The following telemetry utilization fields are particularly useful.

Of considerable interest are telemetric pressure measurements [7, 202] — specifically, base pressure [203] and pressure near the flow separation points, study of which in wind tunnels is complicated by interference between the model and its support.

The telemetry measurement methods are called on to play an important role in studying unsteady aerodynamic phenomena, study of which requires continuous parameter recording.

The use of telemetry measurement methods is also advisable when studying transonic flow around bodies, since in this case the load factors during model acceleration are low and the problem of recovering and protecting the models is easily solved, which makes it possible to use multielement radioelectronics.

Telemetry can also yield extremely useful information on rate-of-rotation model vibration frequency and amplitude [202, 204], and consequently on dynamic stability over a wide velocity range.

Telemetry measurements of the model surface temperature make it possible to obtain thermal flux and boundary layer data, which are particularly valuable in the hypersonic speed range. The most important study areas are the stagnation point region [11, 202, 204 - 207] and the model base region [203].

Using suitable detectors (for example, phototransistors or lead-sulfide radiation receivers), with the aid of telemetry systems we can record the intensity of the radiation reaching the model and, using detectors analogous to the dual probe, we can measure the ionization at the model surface [204, 206].

/189

Modern telemetry systems can be arbitrarily divided into radiotelemetry (multielement systems) and single-channel systems.

Analysis and systemization of the ballistic telemetry system construction principles are presented in [208].

Radiotelemetry systems can provide for information transmission over long distances, practically regardless of model spatial orientation relative to the receiving antenna, and in the general case permit simultaneous measurement of several parameters.

The large load factors experienced in the acceleration process, reaching several thousand g, have required radio component selection and ruggedization, and the use of printed circuits. The technology for transistor ruggedization is presented in [7], and reduces

basically to first potting the elements with acrylic resin (to prevent deterioration of the frequency characteristics), and then with epoxy resin with various fillers, which are capable of providing plasticity and hardness. Procedures for silicon coating of transistors are discussed in [205].

Measurement result transmission is accomplished basically by frequency modulation, since in this case variation of the received signal magnitude does not affect the measurement accuracy. Frequency modulation is accomplished by varying the capacitance or inductance of the transmitter circuit. Pickups of "capacitive" or "inductive" types can serve (completely or partially) as the transmitter.

The transmitter carrier frequency is selected in the range from 50 MHz to several hundred MHz. Increase of the frequency is useful from the viewpoint of increasing the radiating antenna efficiency.

Figure 3.39 shows a schematic of a transducer-transmitter [7, 203], consisting of a Hartley oscillator and a capacitive pressure transducer connected directly into the carrier frequency circuit.

The inadequate stability of such signal generators, due to the influence of load factors on the assembly and the electronic components, has led to the use of more complex measuring and transmitting device configurations. The use of two oscillators was proposed in [204, 205]: carrier and subcarrier frequency oscillators. The first serves as the radio transmitter, and the second serves as a frequency-modulated transducer, which controls the carrier-frequency oscillator.

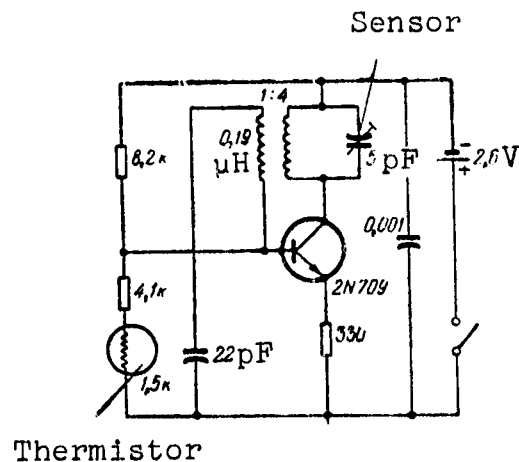


Figure 3.39. Schematic of radiotelemetry transmitter

Alternating transmission of a reference signal and the measured signal has been suggested [204, 205] for monitoring drift of the subcarrier frequency. Such a system, in which periodic calibration is performed, can improve measurement accuracy significantly. /190

The capacitive transducers used to measure pressure at the stagnation point [7] and in the base region [203] are miniature condensers, one plate of which is a thin elastic membrane which deflects under the action of the pressure and thus alters the condenser capacitance.

Most of the transducers used for measuring temperature [203 - 206] are based on variation of the active resistance under the influence of the temperature. Transducers operating on the thermocouple principle are also encountered [203].

The difficulty in creating temperature transducers lies in the necessity for simultaneous satisfaction of such requirements as low inertia and strength. "Resistance" transducers are made by applying to glass very thin (about 0.1 micron [205]) platinum films, which are subsequently peeled off to form flat 2 - 4 k Ω resistors. The quite high transducer output impedance makes them suitable for use in semiconductor circuits.

Wires stretched along the ballistic range, or a series of other antenna devices — for example, of the quarter-wave dipole type installed sequentially, can serve as the receiving antennas.

An example of successful radiotelemetry application is the study [7], in which stagnation point pressure measurement accuracy of 4 - 15% was achieved on 40 mm-diameter models at 400 - 500 m/sec flight speeds.

The radiotelemetry system, consisting of an accelerometer, high input impedance amplifier, and a radio transmitter, and also angle-of-attack telemetry measurement results are presented in [204]. The experiments were conducted with three 25.4-mm-diameter models at

atmospheric pressure and speeds to 1580 m/sec. Comparison of the telemetry measurement data and yaw diagram measurements showed that they agree satisfactorily with one another, even with low magnitude of the received signal. /191

The desire to locate telemetry on small-caliber models capable of withstanding the high load factors developed during model acceleration in gasdynamic guns has led to the development of miniaturized telemetry systems [11, 202, 207]. Other important advantages of these systems are the extreme simplicity of construction and low cost.

Several principles can be used as the basis for constructing miniaturized telemetry systems (Figure 3.40, a and b).

Figure 3.40b shows the schematic of a model [207] with built-in LC loop (8 MHz) and temperature sensor in the form of an active resistance R, which determines the circuit attenuation. The circuit is excited by a short resonant-frequency pulse at the moment the coil passes an antenna. The oscillations taking place in the circuit are recorded by the receiving antenna located "downstream". Measurement of the signal decay with time makes it possible to determine the sensor resistance and, consequently, the surface temperature. Direct coupling between the circuit and the receiving antenna is eliminated by shielding and suitable positioning of their coils. Depending on the number of points at which it is necessary to measure the temperature, the required number of excitation and recording antennas are positioned along the ballistic range.

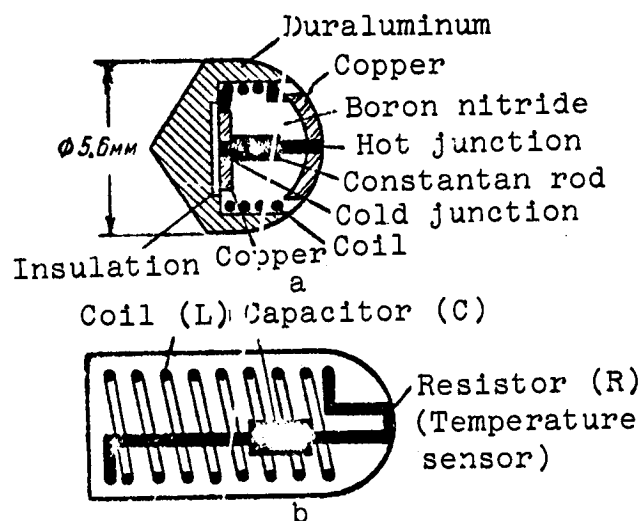


Figure 3.40. Constructions of miniaturized telemetry systems: a) system using thermoelectric current; b) system with impact excitation loop

In addition to simplicity, another advantage of this telemetry system is the absence of need for a power supply. /192

The drawbacks of this telemetry system lie in the discrete nature of the information received; the low radiated signal power, which is limited by the time during which the transmitting circuit is excited; and measurement accuracy dependence on model spatial orientation in flight.

Reference [202] proposes that the mutual induction effect between two circuits tuned to the same frequency, one of which is located in the model while the other is the loading circuit of the receiving-recording system, be used for measurement of velocity, angle of attack, pressure, and temperature.

As the model travels inside the receiving-recording system circuit coil, inductive coupling leads to considerable recording circuit impedance increase. Using the scheme shown in Figure 3.41, the impedance change can be recorded on an oscillograph which records the envelope of the RF signals.

The resonant frequency of the circuits is selected in the 1 - 5 MHz range, since in this case, on the one hand, it is easy to create the long receiving-recording system circuit coils and, on the other hand, it is possible to fabricate circuits of quite small dimensions which can be installed in the 12.7 mm diameter models.

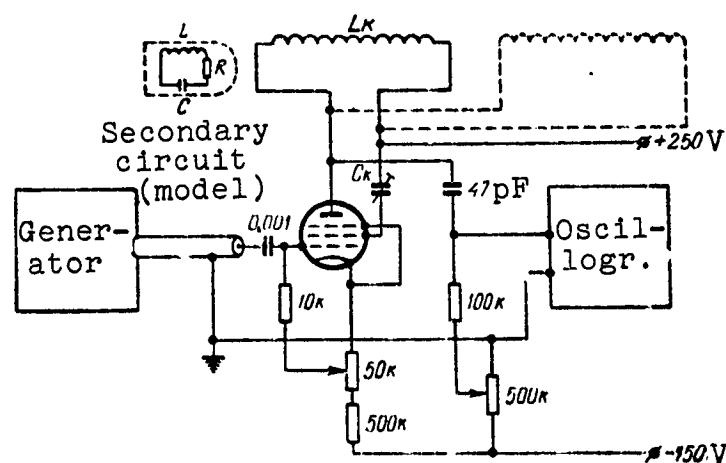


Figure 3.41. Miniaturized telemetry system utilizing the mutual induction effect

The marked change of the signal amplitude in the receiving-recording circuit coil at the moment the model enters and leaves the coil can be used to calculate the velocity. The magnitude of the signal recorded while the model is in the coil is determined only by the angular orientation of the model, and is independent of the model velocity and location relative to the coil. /193

This technique was tested on 12.7 mm-diameter models weighing 2.5 grams at accelerations exceeding $2 \cdot 10^5$ g, and maximal flight speeds of 2250 m/sec.

Reference [11] described a miniaturized telemetry system which was used to measure thermal fluxes during flight of models with hemispherical noses in air and CO_2 at velocities to 5500 m/sec. The shape, construction, and dimensions of the models used are shown in Figure 3.40a.

The system operating principle is as follows. As a result of heating of the copper layer at the stagnation point, a current appears in the thermocouple circuit, and as this current flows in the four-turn solenoid, it creates a magnetic field. Since the temperature of the cold layer located within the model can be considered constant because of thermal inertia, the resulting magnetic field intensity is proportional to the stagnation point temperature.

The model magnetic field is recorded oscillographically by means of a series of pickup coils through which the model travels, and in general form we can consider that the maximal induced emf appearing in the coil is proportional to the product of the model velocity by the stagnation point temperature. Thus, using the velocity values from the measured emf values, we can calculate the temperature change and, consequently, the thermal fluxes (see § 5.8). Measurement accuracy close to 20% is achieved.

200

--	--	--	--	--	--	--	--	--	--

A drawback of this telemetry system is the received signal dependence on model orientation and velocity, which leads to additional errors.

The general drawbacks, characteristic of miniaturized telemetry systems, lie in the discrete nature of the information obtained, the single-channel nature of the system, and the influence of the plasma surrounding the model on the interaction between the magnetic fields of the model and of the receiving and recording system coils.

CHAPTER IV

DYNAMICS OF SOLID MEDIA

§ 4.1. Preliminary Remarks

The successes in the development of methods for imparting high velocities to solid bodies of given form and the successes in developing methods and apparatus intended for studying impulsive and high-speed processes have led to obtaining significant new results in various fields of experimental physics. Specifically, the application of these methods and apparatus have made it possible to obtain in the course of the last 15 - 20 years results of fundamental importance in numerous studies devoted to the solution of several questions of solid media dynamics. The basic trends in studies in this field include, first, study of the compressibility of solid substances under pressures on the order of hundreds of thousands and millions of atmospheres [1 - 27], second, study of the nature of the shaped charge effect — primarily in application to profiling lined charges [27 - 36], and, third, study of the mechanism of the collision of solid bodies, particularly at high encounter speeds [37 - 92]. /194

While the results of studies in the first two of these directions have already been well systematized [24 - 29], the correlation of the results of studies in the third direction reduces to date to surveys of a fragmentary nature [41, 53, 59, 64, 66]. The reason

for this situation apparently lies in the fact that the numerous studies in the third direction have generally been performed in application to limited and specific impact condition variation intervals. Depending on the specific objectives of the individual studies, the object of study in each investigation was some particular material, frequently even of different physical nature.

In this connection, in the present chapter we have made an attempt to present systematically the results of only those investigations devoted to the physical aspects of the collision of deformable (primarily metallic) bodies.

The three research directions noted above naturally have not developed and are not developing in isolation from one another. They are intimately related and supplement and nourish one another. Therefore, in presenting and discussing the basic results of deformable body impact studies, we must inevitably turn to some results from the other two directions, as we shall do in the following. /195

The problem of deformable body collision, just as any other physical problem, has relatively simple solution in certain asymptotic cases. One such case is that of nondeformable body penetration into a massive ("semi-infinite") deformable target. A very large number of studies [37 - 41, 53] have been made of this solid body collision case. However, physically precise results have been obtained only in comparatively recent studies [42]*.

Another asymptotic case of the subject problem is that of high-velocity penetration of a long deformable rod into a massive deformable target. Some results in application to this asymptotic case are presented in § 4.3, in discussing the current model of the high-velocity deformable body interaction process.

* A discussion of these results is presented in § 4.2, which was written together with one of the authors of [42], V. A. Stepanov.

Section 4.4 is devoted to analysis of the dynamic interaction of deformable bodies in the most general formulation possible at the present time. The analysis rests on the dimensional analysis, and makes it possible to conclude that the deformable body collision process is well modeled. This means that the result of the collision of two bodies with high encounter velocities can be reproduced experimentally with another properly selected pair of bodies colliding at significantly lower velocity. A description and discussion of experimental data confirming this theoretical conclusion are presented in sections 4.5 and 4.6.

Later, in § 4.7, we examine the thermal phenomena which arise during the collision of solid bodies. Starting from the essential difference in the processes of dynamic interaction of bodies in the steady and unsteady state regimes, we refine the definition of the so-called "threshold" encounter velocities, i.e., those velocities upon exceeding which the collision process is complicated by melting and vaporization of the materials of the interacting bodies. Theoretical and experimental estimates are made of the influence of the thermal effects on the final result of high-speed interaction of metallic bodies.

Finally, § 4.8 is devoted to the destruction of massive bodies and bodies of limited dimensions under the action of a short-term pulse ("short" impact). The discussion of the experimental data rests on a physical model, which explains the observed effects by wave phenomena. The exposition terminates with examination of the problem of target protection (significant reduction of the damage parameters) with the aid of a thin shield which the impacting body encounters prior to striking the target. /196

§ 4.2. Nondeformable Body Penetration Into Plastic (Metal) Halfspace

In any dynamic problem, the basic question is that of the forces which determine the motion. In the subject asymptotic deformable

body collision case, the question of the forces of resistance to penetration is basic.

The process of penetration of a nondeformable axisymmetric body of given shape and mass into a metal target has been studied in order to solve this problem for impact velocities $V_0 = 10^2 - 10^3$ m/sec [42]. Body encounter took place under conditions of impact along the normal. In order to exclude the influence of edge effects on the measurement results, massive blocks were used as the targets. These blocks were made from technically pure (ARMCO) iron, duraluminum, copper, aluminum, and lead. The impacting bodies ("strikers"), with cylindrical part diameter $d_0 \approx 8$ mm, were made from high carbon steel, heat treated to Rockwell (C scale) hardness 60 - 62. The striker noses were made in the form of cones with different apex angles α . The strikers were accelerated by a powder-driven launcher.

The kinematic method was used to determine the forces of resistance to striker penetration. Specifically, the position of the striker trailing edge, relative to a stationary reference at various moments of time, was determined from high-speed photography data (Figure 4.1), and a curve of "striker travel L in the target versus time t " was plotted. Double differentiation of the curve made it possible to obtain the dependence of the penetration resistance

force $P = m \frac{d^2L}{dt^2}$ (where

m — striker mass), or the average pressure

$p = \frac{P}{S_0}$ (where $S_0 = \frac{\pi d_0^2}{4}$ —

cross section area of cylindrical part of the striker, coinciding with the base area of the striker conical nose) on the time t

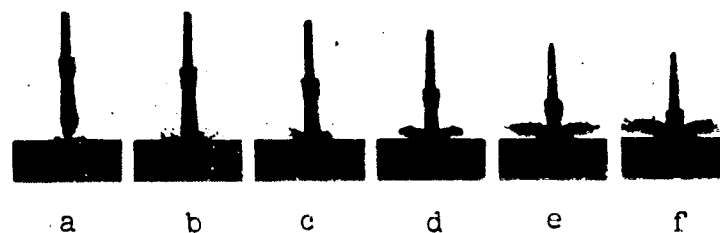


Figure 4.1. Time-sequential photographs of rigid striker ($m = 13$ g) with conical nose ($\alpha = 90^\circ$) penetrating a massive copper target with encounter velocity $V_0 = 740$ m/sec: a) 7 μ sec before encounter; b) moment of encounter; c) 7; d) 13; e) 20; and f) 27 μ sec after encounter of the bodies [42]

(or the distance L or the instantaneous velocity $V = \frac{dL}{dt}$).

The experimental relations established in the studies are shown schematically in Figure 4.2, and reduce to the following.

(a) The resistance to striker penetration into the surface ($L \lesssim d_0$) layers of the semi-infinite metal target (curves 1, Figure 4.2) for any velocities V in the range covered by the experiments, and into the deep ($L > 2d_0$) layers (curves 2, Figure 4.2) for velocities $V \geq V_{cr}$, is defined by the relation:

$$p = H_1 + \kappa_0 \rho_{01} V^2, \quad (4.1)$$

where H_1 — target metal dynamic hardness, which is measured for penetration velocities of order of 10 - 100 m/sec [42 - 46], and the value of which depends weakly on the conical indenter apex angle [42]; ρ_{01} — target metal density; and κ_0 — drag coefficient (form coefficient) of the striker nose, calculated following Newton, i.e., assuming that the target particles do not interact with one another, and therefore their velocity change takes place right at the striker nose surface [42, 47, 48]. As is well known [38, 47], for a cone in axial flow and having the apex angle α , the Newtonian drag coefficient can be calculated from the formula:

$$\kappa_0 = \sin^2 \frac{\alpha}{2}. \quad (4.2)$$

As for the resistance to penetration into the deep ($L > 2d_0$) layers of the massive metal target for velocities $V \leq V_{cr}$, this

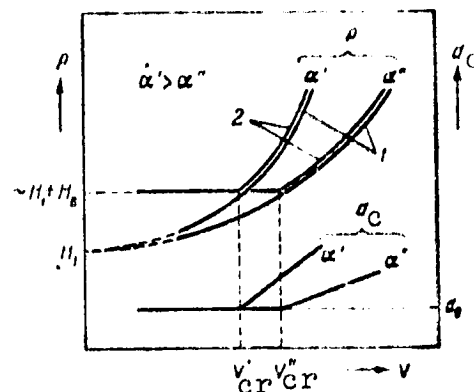


Figure 4.2. Schematic curves of penetration resistance p of rigid strikers with different conical nose apex angles α into surface (1) and deep (2) layers of massive metal target, and curves of final diameter d_c of the cavity created in the target by these strikers versus encounter velocity V

resistance in the first approximation is independent of the striker conical nose apex angle, and also of the penetration velocity, and is defined by the equality:

$$p \approx H_1 + H_B, \quad (4.3)$$

where H_B — "static" hardness of the target metal, measured using the Brinnell method.

(b) The work b of unit target metal volume displacement, defined by the ratio of the striker initial energy $mV_0^2/2$ to the final cavity volume W_c , for $L > 2d_0$ is independent of the impact velocity V_0 , and also of the striker nose shape, and obeys the relation:

$$b \approx H_1 + H_B. \quad (4.4)$$

(c) In the deep ($L > 2d_0$) layers of the metal target for penetration velocities $V \geq V_{cr}$, the final diameter d_c of that cavity cross section which the striker passes with the velocity V is defined by the expression:

$$d_c = d_0 \left(\frac{p}{b} \right)^{1/4}, \quad (4.5)$$

where p and b are given by (4.1) and (4.4).

For velocities $V \leq V_{cr}$, the cavity diameter d_c is independent of the striker conical nose apex angle, and also of the penetration velocity, and is equal to the striker diameter d_0 .

(d) The critical velocity V_{cr} is found from the relation:

$$V_{cr} \approx \left(\frac{H_B}{\kappa_0 \rho_0 l} \right)^{1/4}. \quad (4.6)$$

Table 4.1 presents some basic characteristics of the metals used in the experiments, and also compares the resistance coefficients κ_0 , critical velocities V_{cr} , and specific works b of volume

200

TABLE 4.1. SOME PHYSICAL AND MECHANICAL CHARACTERISTICS OF TARGET METALS AND COMPARISON OF CALCULATED AND EXPERIMENTAL IMPACT PROCESS PARAMETER VALUES*

Target metal		Techn. pure iron	Duralu- minum	Copper	Alu- minum	Lead	
Target metal density ρ_{01} , g/cm ³		7,85	2,80	8,90	2,70	11,34	
Target metal Brinnell hardness, H_B , kg/mm ²		90	110	45	30	~5	
Target metal dynamic hardness, H_1 , kg/mm ²		200	140	72	56	~8	
Striker nose conical apex angle α_0		90	90	90	180	180	
		60		60	90	90	
						60	
				37		37	
Resistance coefficient κ_0	Calculation using (4.2)		0,50	0,50	0,50	1,00	1,00
			0,25		0,25	0,50	0,50
					0,10		0,25
	Experiment		0,50	0,47	0,49	0,85	1,00
			0,23		0,24	0,52	0,49
					0,12		0,26
Critical velocity, V_{cr} , m/sec	Calculation using (4.6)		475	880	315	330	65
			670		445	465	95
					705		130
	Experiment		460	830	320	350	—
			620		440	470	100
					—		—
Specific work of volume displac- ment b , kg/mm ²	Calculation using (4.4)		290	250	117	86	~13
	Experiment		260	220	120	83	~10

*Translator's note. Commas in numbers represent decimal points.

displacement obtained under various impact conditions with the results of calculation of these parameters using (4.2), (4.4), and (4.6).

As an example, Figures 4.3 - 4.6 show some typical experimental curves and an axial section of a typical cavity.

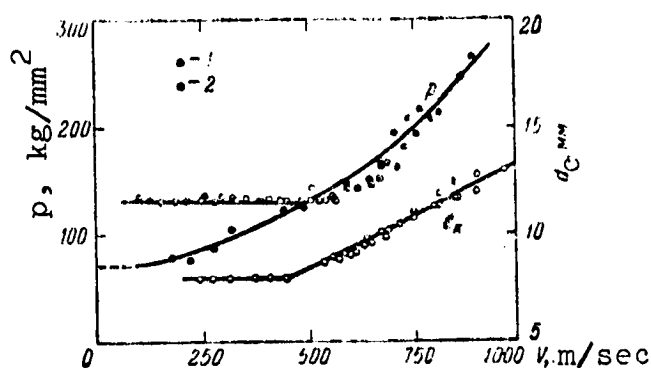


Figure 4.3. Penetration resistance p of rigid striker with conical nose ($\alpha = 60^\circ$) into surface (1) and deep (2) layers of massive copper target, and final diameter d_c of the cavity created by the striker in the target versus penetration velocity V .

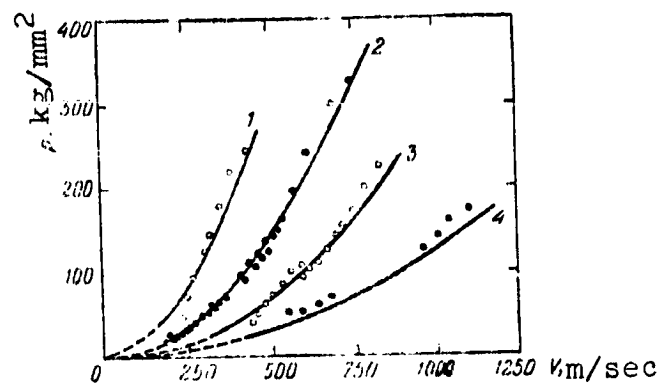


Figure 4.4. Penetration resistance p of rigid strikers with different conical nose apex angles α entering massive lead target versus penetration velocity V : 1 — $\alpha = 180^\circ$; 2 — $\alpha = 90^\circ$; 3 — $\alpha = 60^\circ$; 4 — $\alpha = 37^\circ$ [42].

Turning to analysis of these experimental results, we note that previously, starting from general consideration on the possible nature of deformable medium resistance to penetration into it of a rigid body, various forms of penetration resistance dependence on the velocity were proposed — specifically, relations of the form $A + BV$, $A + CV^2$ and $A + BV + CV^2$, where A , B , and C are constants [38]. The

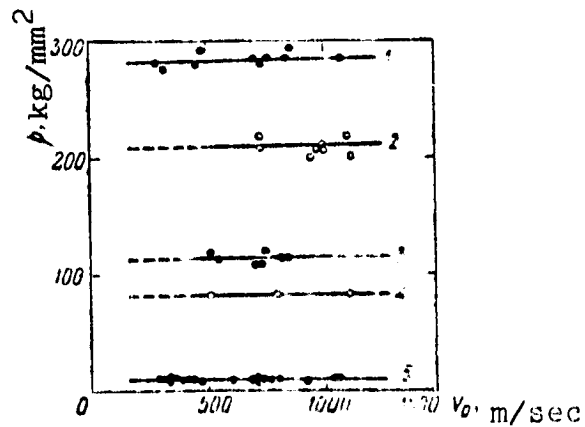


Figure 4.5. Specific work b of volume displacement for different impact velocities V_0 for technically pure iron (1), duraluminum (2), copper (3), aluminum (4), and lead (5).

fundamental results of the cited studies are: first, experimental proof that this dependence has the form $A + CV^2$ and, second, revelation of the physical meaning of the constants A and C .

It follows from (4.1) that the change of the deformable medium resistance to motion of a rigid body in the medium, at least for velocities above the critical value, is proportional to the product $\rho_0 V^2$, i.e., it is determined by forces of hydrodynamic origin. But, in contrast with the fluid media, which — if we neglect the viscous forces — exhibit only inertial resistance, the overall deformable solid media resistance is made up from the intrinsic resistance to deformation (H_1), reflecting the forces of the bonds in the body, and from the inertial resistance ($\rho_0 V^2$).

Generally speaking, the intrinsic resistance of a solid medium to penetration, expressed by the dynamic hardness H_1 , should not be constant. However, at temperatures close to room temperature for most metals and alloys (iron and iron-base alloys, aluminum and aluminum-base alloys, copper, and many others), this resistance varies with the velocity as $v^{0.02-0.04}$ [43 - 45, 49]. It is obvious that, in the velocity range covered by the experiments (and, particularly for velocities above the critical value), this weak variation with velocity of the first term of the binomial (4.1) can be neglected in comparison with the variation of the second term, and we can consider the first term constant and equal to the hardness measured for impact velocities of the order of 10 - 100 m/sec [42 - 46].

The experimental studies of solid body motion in liquid and gaseous media indicate that for subsonic velocities, the drag coefficients differ significantly from their theoretical Newtonian



Figure 4.6. Section of cavity created in massive copper target by rigid striker ($m = 11$ g) with conical nose ($\alpha = 90^\circ$) for impact velocity $V_0 = 710$ m/sec

values [47, 48]. Therefore, the good agreement of the experimental values of the drag coefficients found in the cited studies with their calculated Newtonian values is at first glance unexpected and seems to contradict the known facts. /202

However, this contradiction is only apparent. The reason is that the flow around the rear portions of the rigid bodies, which is not taken into consideration in the Newton theoretical scheme, plays a major role during solid body motion in liquid and gaseous media [47]. However, during motion of rigid bodies in a metallic medium, in complete agreement with the Newton scheme, the shape of the aft portions of the moving bodies cannot play any role, since open cavities are formed in the metal.

The Newton scheme also assumes that the particles of the medium alter their velocity right at the surface of the immersed body. For supersonic velocities, this assumption for liquid and gaseous media is very far from the actual velocity distribution in the flow [47, 48]. However, in a metallic medium, large deformations are localized near the point of loading [26, 40, 50, 51]. Therefore, the flow in a metallic medium will approach the requirements of the Newton computational scheme.

These characteristics of the metallic media, and also the important circumstance that the process of rigid striker penetration into a deformable medium over the major part of the striker travel in the medium can be assumed to be close to steady state, have apparently led to the quite good agreement of the experimentally determined resistance coefficients with their Newtonian values. It is obvious that the degree of agreement, generally speaking, will depend on the degree to which the form of the surface bounding the zone of large target metal deformations reproduces the striker nose shape. From this viewpoint, we would expect that the agreement between the experimental and calculated values of the resistance coefficient κ_0 would be best for "moderate" ($60^\circ - 90^\circ$) striker conical nose apex angles, while for "blunt" strikers, the experimental values of κ_0

would be less than the calculated values, and, conversely, higher for "sharp" strikers. The experimental data in Table 4.1 do indeed exhibit this tendency.

This is the interpretation of the primary result of the conducted studies, expressed by the Relation (4.1).

/203

The interpretation of the results expressed in (4.3) and (4.4) is more complex. Physically clear and simple models which can be used to interpret these relations have not yet been obtained.

As for (4.5), this formula can be obtained if the striker energy loss along the distance ΔL (i.e., the work performed by the striker along this path element) is equated to the energy required to create the corresponding cavity volume element:

$$\rho \frac{\pi d_0^2}{4} \Delta L = b \frac{\pi d_c^2}{4} \Delta L. \quad (4.7)$$

In spite of the difficulty in interpreting (4.3) and (4.4), it is possible to give a comparatively simple explanation of the meaning of critical velocity, if we make use of the deformation criterion, rather than the force criterion for this purpose.

In accordance with the schematic relations of Figure 4.2, the critical velocity is that value upon exceeding which the final cavity diameter d_c will be greater than the diameter d_0 of the cylindrical part of the striker (or, what is the same, greater than the striker conical nose base diameter). But, broadening of the cavity in a given section perpendicular to its axis is possible only through that kinetic energy which the corresponding target metal volumes acquire as the striker passes this section. It is obvious that the maximal pressure developed with realization of this kinetic energy will be equal to the inertial component of the penetration resistance $\rho_0 c_{ul} V^2$. It is also obvious that the final cavity diameter d_c can be greater than the striker diameter d_0 if, and only if, the pressure $\rho_0 c_{ul} V^2$ exceeds the characteristic value of the target metal resistance

to deformation. Since cavity broadening must take place with decay of the deformation velocity to zero, considering the nature of the stress state around the cavity, it is logical to take as this characteristic value of target metal resistance to deformation the "static" hardness — for example, the Brinnell hardness H_B . It is easy to see that (4.6) is a direct consequence of the approximate equality:

$$\rho_0 V_{cr}^2 \approx H_B \quad (4.8)$$

These relations governing nondeformable solid body penetration into a massive metal target make it possible to calculate from the basic experimental parameters the final cavity dimensions and, specifically, its final depth L_c .

The equation of motion of a nondeformable striker in a metallic medium can be written in the form: /204

$$m \frac{dV}{dt} = -S \cdot p, \quad (4.9)$$

where S — projection of contact surface of the interacting bodies on the plane perpendicular to the striker axis, and p — pressure on the striker nose, defined by (4.1).

If we write (4.9) in the form:

$$m V \frac{dV}{dL} = -S \cdot p, \quad (4.10)$$

the variables are easily separated.

In the general case, the integration with respect to the velocity V should be broken down into three intervals:

(a) the interval corresponding to striker penetration with velocities $V_0 \geq V \geq V_n$, where V_n is the striker penetration velocity at the instant of its immersion into the target to the height of the nose;

(b) the interval corresponding to striker penetration with velocities $V_n \geq V \geq V_{cr}$, and, finally,

(c) the interval corresponding to striker penetration with velocities $V_{cr} \geq V \geq 0$.

Integration leads to the formula:

$$L_c = \frac{d_0}{3} \left(\frac{1 - \alpha_0}{\alpha_0} \right)^{1/2} + \frac{2m}{\pi \alpha_0 \rho_{01} d_0^2} \left(1 - \frac{H_1}{b} + \ln \frac{H_1 + \alpha_0 \rho_{01} V_0^2}{b} \right). \quad (4.11)$$

In the simplest case, when a striker made from a material with density ρ_{02} has the form of a circular cylinder, and when the impact velocity V_0 is considerably greater than V_{cr} , which makes it possible to consider the distance traveled by the striker with $V \leq V_{cr}$ small in comparison with the final cavity depth L_c , integration of (4.10) yields the approximate formula:

$$L_c \approx l_0 \frac{1}{2\alpha_0} \frac{\rho_{02}}{\rho_{01}} \ln \left(1 + \alpha_0 \frac{\rho_{01} V_0^2}{H_1} \right), \quad (4.12)$$

where l_0 — striker length.

Figure 4.7 gives the calculated values of L_c compared with the values of the same parameter obtained in experiments encompassing a wide range of changes in the collision velocity, the physico-mechanical characteristics of the target metals, the masses and angles of the striker points. The data in Figure 4.7 point to the good agreement between the quantities compared and consequently, confirm the validity of the relations obtained.

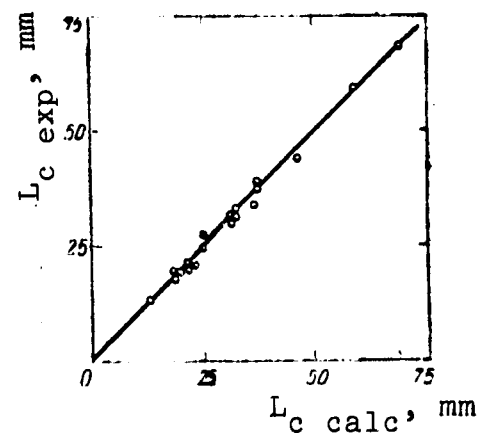


Figure 4.7. Comparison of experimental and calculated values of cavity depths, created in various massive metal targets by rigid strikers whose geometric parameters, mass, and velocity varied in wide limits

Formulas (4.11) and (4.12) were derived for strikers with conical nose. The position of the line of separation of the target material from the surface of such a striker is independent of the penetration velocity, and always coincides with the base contour of the conical striker nose. However, if the undeformable striker nose has a convex curvilinear generator — for example, if the nose is hemispherical, then the calculation of the final cavity depth inevitably becomes more complex. In order to obtain formulas analogous to (4.11) and (4.12) for this body collision case, it is necessary to establish the law of displacement of the forementioned line of separation with variation of the penetration velocity. Unfortunately, this law has not yet been established for solid media, and the problem is usually solved empirically for the specific collision conditions (see, for example, [52]).

Thus, in the studies examined in the present section, some physical and mechanical relations, which the undeformable body motion process in a metallic medium obeys, are revealed. With the aid of these relations, we can calculate the final depth of the cavity formed in a massive metal target during impact on the target of an undeformable axisymmetric body with conical nose. The good agreement of the calculations results with the experimental data makes it possible to state that the parameters defining the process of massive target metal deformation during undeformable body impact on the target are the strength and density of the target metal, the impact velocity of the colliding bodies, the rigid striker nose shape and mass, which in turn can be expressed in term of striker density and characteristic dimensions.

§ 4.3. Qualitative Analysis of the Cavity Formation Process during High-Velocity Impact of Deformable Bodies

The preceding section was devoted to questions associated with motion in a solid plastic medium of a rigid body, i.e., a body whose deformations in the process of interaction with the medium are

negligibly small in comparison with its initial dimensions. Since the resistance of the medium to a body traveling in it is directly proportional to the square of the velocity, such a process can be realized only for comparatively low subsonic velocities. When the velocity of encounter of the bodies exceeds some value which is characteristic for each given pair of bodies, both interacting bodies will deform. Unfortunately, an analytic solution which permits making the required estimates of the process parameters has not yet been obtained for the problem in this most general formulation. Only for high impact velocities — those for which the material strength of the interacting bodies is negligibly small in comparison with the inertial component of the resistance to penetration — has a qualitative model of cavity formation in a massive ("semi-infinite") target been proposed, on the basis of the latest theoretical and experimental study [66]. In accordance with this model, the cavity formation process can be divided into four stages (Figure 4.8).

/206

The first stage — interaction of the bodies in the unsteady regime — covers some small time interval t_1 . In this stage, there will act in the striker and target contact zone pressures p , corresponding to collision of bodies without their flow [24, 25]:

$$p = \rho_{01} D_1 U_1 \quad (4.13)$$

where ρ_{01} — density of target material at normal pressure, and D_1 and U_1 — wave and mass velocities, characterizing the shock wave which arises in the target as the bodies meet.

With striker and target interaction in the unsteady regime, the body contact surface displacement velocity V_1 coincides with the

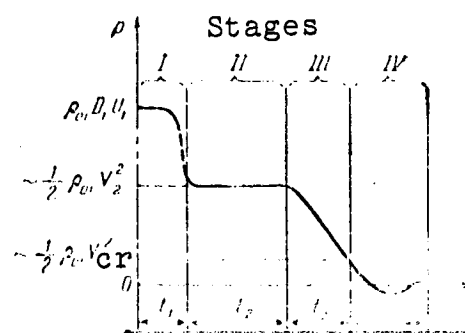


Figure 4.8. Model cavity formation in massive deformable target with high velocity impact of deformable striker

mass velocity U_1 [24]. Considering this, and using the known relations of shock wave theory [25], from the condition of equality of the pressures in the colliding bodies on both sides of the contact surface, we can obtain [27, 70, 71]:

$$\frac{V_1}{V_0} = \frac{1}{1 + \left(\frac{\rho_1 (1 - \frac{\rho_{02}}{\rho_2})}{\rho_2 (1 - \frac{\rho_{02}}{\rho_1})} \right)^{1/2}} \quad (4.14)$$

where V_0 — impact velocity, ρ_1 — target material density behind the shock wave front, and ρ_{02} and ρ_2 — densities of the striker material in the undisturbed state and behind the front of the shock wave which arises in the striker as the bodies meet. /207

Formulas (4.13) and (4.14) make it possible to evaluate both the pressure p and the penetration velocity V_1 , characterizing the first stage of the interaction process. For this, it is necessary to know the impact velocity V_0 and have the shock adiabats of the materials of the colliding bodies.

Shock wave propagation in the striker and target is accompanied by propagation of unloading waves, which arise on the free surfaces of the interacting bodies. Therefore, transverse flow will take place over the entire contact surface in both bodies after a time interval of the order of:

$$t_1 \approx \frac{d_0}{2a}, \quad (4.15)$$

where d_0 — initial striker diameter, and a — smaller of the sound speeds in the target and striker materials. As a result, the pressures in the contact zone of the interacting bodies will decrease to the level corresponding to hydrodynamic flow of the two media in the steady state regime. The first stage terminates at this point.

It is obvious that the distance L_1 traveled by the striker in the target in the course of the first stage is determined by the product $V_1 t_1$.

This analysis makes it possible to conclude that the target deformation (depth of striker penetration into the target) in the first stage is determined by the impact velocity, initial striker diameter, densities, and compressibility characteristics (i.e., shock adiabat parameters) of the materials of the interacting bodies.

The second stage — interaction of the bodies in the steady state regime — covers the time interval t_2 from beginning of interaction of the bodies in the steady state regime until the moment of complete "depletion" of the striker. In this stage, pressures of the order of:

$$p \approx \frac{1}{2} \rho_0 V_2^2 \quad (4.16)$$

will act in the contact zone of the bodies, where V_2 — velocity of the contact surface of the bodies in the steady state flow regime*.

The velocity V_2 (and consequently the pressure p), time t_2 , and distance L_2 which the striker travels in the target during the second stage can be estimated on the basis of the following considerations [72].

If striker penetration into the target takes place in the steady state regime with supersonic velocity, the penetration velocity V_2 will coincide with the head wave velocity D_1 in the target. Considering this and also assuming that the pressure is nearly constant [69, 71] along the striker axis between the bow waves in the striker and the target, with the aid of shock wave theory relations we can obtain:

* Strictly speaking, high-velocity interaction of compressible bodies in the steady state regime should be characterized by somewhat higher pressures than those given by (4.16); the corresponding estimates can be found, for example, in [69].

$$\frac{V_2}{V_0} = \frac{1}{1 + \left(\frac{\rho_{01} (1 - \rho_{01}/\rho_1)}{\rho_{02} (1 - \rho_{02}/\rho_2)} \right)^{1/3}}, \quad (4.17)$$

where the notations are the same as in (4.14)

In the first approximation, (4.17) can also be extended to the case of interaction of compressible bodies in the subsonic flow regime, if, naturally, the encounter velocities are sufficiently close in the sense mentioned above. The basis for this is the fact that the isentrope and the shock adiabat of a solid body practically coincide in a wide range of pressure variation [24, 25], and also the fact that in the subsonic flow regime the distribution of pressures, densities, and velocities near the contact surface of the bodies can be approximated by a jump similar to a shock front, since these parameters will decrease very rapidly with increasing distance from the contact surface of the bodies [26, 40 50, 51]. This is indicated, specifically, by the agreement established above (§ 4.2) between the experimental coefficients of resistance of rigid bodies to penetration into a deformable target and their theoretical Newtonian values.

For a given velocity V_0 and known shock adiabats of the striker and target materials, (4.16) and (4.17) yield the possibility of estimating the pressure p and penetration velocity V_2 , which are characteristic for the second stage. As for the parameters t_2 and L_2 , they can be evaluated with the aid of the obvious equalities:

$$t_2 = \frac{l_0}{V_0 - V_2} \quad (4.18)$$

and

$$L_2 = V_2 t_2, \quad (4.19)$$

where l_0 — initial striker length.

Consequently, the target deformation in the second stage, in the most general case, is determined by the impact velocity, striker length, and the densities and compressibility characteristics of the materials of the colliding bodies.

It is essential to note that for metals the formulas (4.14) and (4.17) can be reduced to a single formula, and rewritten without loss of accuracy in the form:

$$\frac{V}{V_0} \approx \frac{1}{1 + (\rho_{01}/\rho_{02})^{1/2}}, \quad (4.20)$$

which coincides with the known solution of the basic problem of shaped-charge theory [28, 29]. This possibility is a result of the fact that, for a known fixed value of the pressure p , the ratios ρ/ρ_0 for the different metals differ comparatively little, and for many pairs of metals the parameter $\left(\frac{1 - \rho_{01}/\rho_1}{1 - \rho_{02}/\rho_2}\right)^{1/2}$ in (4.14) and (4.17) is close to one [24, 70].

/209

The third stage — afterflow — begins from the moment of complete "depletion" of the striker, and its exclusion from the process as an effective factor. In this stage, there is expansion ("afterflow") of the cavity as a result of the kinetic energy stored by those target columns which were entrained into motion by the time of striker "depletion". The cavity expansion velocity, equal in the beginning of the stage to the striker penetration velocity V_2 in the second stage, must obviously decay with time. The rate of decay will clearly be determined by the target material strength and compressibility characteristics. In accordance with the data presented above (§ 4.2), cavity expansion and deepening will terminate when its surface velocity decreases to the value V_{cr} ; unfortunately, no reliable methods have been developed for evaluating the parameters of the third stage. However, the system of parameters determining target deformation in the third state can be defined. This system includes the impact velocity, density and compressibility characteristics of the colliding body materials, and the target material strength.

Finally, the fourth stage — elastic (possibly elastoplastic) reduction of the cavity dimensions — completes the cavity formation process. It is clear that in this stage, the cavity dimension change will be of the rapidly decaying oscillation type.

Methods for evaluating the parameters of the last cavity formation stage have not yet been developed, although what we have said makes it possible to state that the target deformation under these conditions will be determined by the elastic characteristics, strength, and density of the target material.

Examples of experimental data confirming the above model, and the applicability of the proposed interaction process parameter estimates are shown in Figures 4.9 - 4.11.

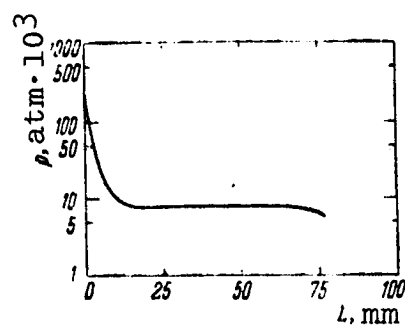


Figure 4.9. Pressure p in contact zone of a soft steel cylinder ($l_0/d_0 = 10$) with methyl methacrylate target versus cylinder penetration depth L from experimental data of [66]; encounter velocity $V_0 = 3.7$ km/sec

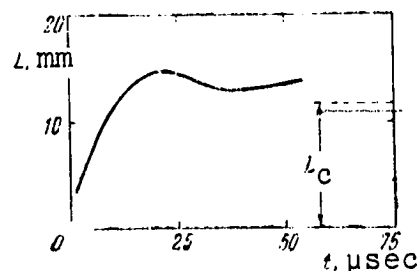


Figure 4.10. Experimental variation with time of the depth of the cavity formed in a massive aluminum target upon impact of a soft steel sphere ($m = 0.18$ g, $d_0 \approx 3.5$ mm) with velocity $V_0 \approx 5.01$ km/sec [64]

Figure 4.9 shows the pressure acting during penetration of a cylindrical soft steel striker ($l_0/d_0 = 10$) into a methyl methacrylate target in their zone of contact; in this experiment, the encounter velocity was 3700 m/sec [66]. The described relationship determines precisely the first and second stages, and also the beginning of the third stage of the subject model.

Figure 4.10 characterizes the variation with time of the depth of the cavity formed in a massive aluminum target during impact of a soft steel sphere with velocity ~ 5000 m/sec. This figure illustrates clearly the fourth stage of the subject model.

7219

Finally, Figure 4.11 compares the measured penetration velocities V of a cylindrical metal striker into a massive metal target in the first (unsteady regime) and second (steady regime) interaction stages with the same velocities calculated using (4.14) (line 1), (4.17) (line 2), and (4.20) (line 3) [72]. We see that the experimental data agree quite well with the calculation results. At the same time, we see that the kinematic parameters of the metal body interaction process for both unsteady and steady flow regimes can actually be estimated with good accuracy using (4.20), which results from the ideal incompressible fluid model.

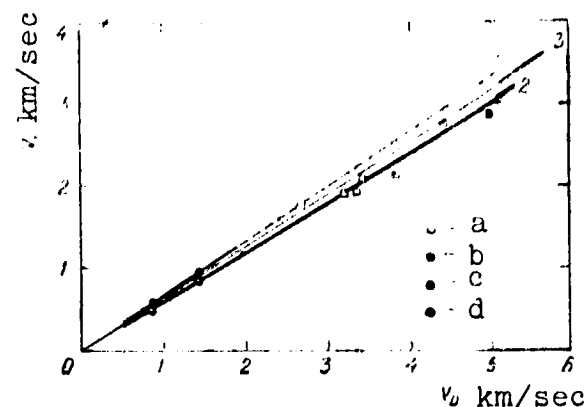


Figure 4.11. Comparison of calculation using (4.14) (line 1), (4.17) (line 2), and (4.20) (line 3) with experimental data obtained during interaction of colliding bodies under steady-state (a, b, c) and unsteady-state (d) conditions: a — soft steel striker ($\frac{l_0}{d_0} = 10$), aluminum target [66]; b — soft steel striker ($\frac{l_0}{d_0} = 10$), duraluminum target [66]; c — copper striker ($\frac{l_0}{d_0} = 7$), aluminum target [72]; d — copper striker ($\frac{l_0}{d_0} = 0.5$), aluminum target [72]

This division of the cavity formation process into four stages is obviously to some degree arbitrary. Actually, the phenomena characterizing the neighboring stages overlap one another in certain stages of the process and, under certain specific experimental conditions, the individual stages may not play any role at all in determining the final cavity depth. Thus, in the case of high-speed impact of a short striker ($\frac{l_0}{d_0} \ll 1$) on a massive target, the second stage of the process — interaction of the bodies in the steady state regime — will be entirely missing. Conversely, under conditions of high-speed impact of a long rod ($\frac{l_0}{d_0} \gg 1$) on a massive target, the roles of the first, third, and fourth stages of the process are negligibly small. If the rod and the target are metallic, the final cavity

depth can be determined, in this case, with satisfactory accuracy from the formula:

$$L_c = l_0 \left(\frac{\rho_{02}}{\rho_{01}} \right)^{1/2}, \quad (4.21)$$

which follows directly from (4.18), (4.19), and (4.20). We have noted previously that the solution of the problem for this collision condition case constitutes the basic content of the hydrodynamic theory of shaped-charge action [28, 29].

Thus, in spite of being somewhat arbitrary, the described model is very useful for analysis of the subject process. In the general case, it does not yet permit making a complete quantitative calculation of the process, but with its aid we can quite confidently construct the system of parameters which determine the characteristic dimensions of the cavity created in a massive deformable target as a result of high-velocity impact of a deformable body on the target. In accord with the above discussion, this system of parameters will include the target strength, striker characteristic dimensions, encounter velocity of the bodies, densities and compressibility characteristics of the materials of the interacting bodies. The elastic characteristics of the target material may obviously be left out of the system, since they are uniquely connected with the density and compressibility characteristics. /212

§ 4.4. Formulation and Analysis of the Problem of Modeling the Deformable Body Encounter Process

We see from the above discussion that the possibilities of calculating the parameters of the deformable body collision process in a wide range of encounter velocity variation are very limited at the present time. The existing computational methods are suitable only for the two asymptotic body collision cases. Therefore, until an analytic solution of the problem in the most general formulation is available, the only way to obtain the required information on the laws governing deformable body collision in a wide range of encounter velocity variation is to analyze the problem by the methods of

dimensional theory, and then verify the analytic results experimentally [73]. Since the possibilities of conducting experiments at high body encounter velocities are also still very limited, this approach is also attractive, in that it permits examining the problem in the model formulation. The problem can be formulated as follows (Figure 4.12) [74, 75, 85].

We wish to know the final depth L_c of the cavity created in a massive ("semi-infinite") target 1, as a result of impact on the target of a body 2 of given geometric parameters, having prior to impact a high velocity V_0' , which cannot be reproduced under laboratory conditions. Let the target and impacting body be made from the materials A' and B' , respectively.

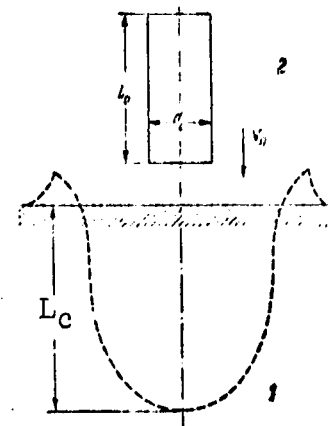


Figure 4.12. Problem schematic

We ask whether we can select target and impacting body materials A and B such that, for some experimentally achievable velocity $V_0 < V_0'$, the result of the collision of this pair will coincide with the results of the collision of the first pair? What criteria must the velocities V_0' and V_0 satisfy in this case, and also what are the geometric parameters and physical characteristics of the two pairs of bodies?

The solution of the problem in this formulation is facilitated by the fact that the data from the known studies of the question, as was shown above, permit quite reliable validation of the selection of the system of parameters which determine the process.

In accordance with the above discussion, we can state that, in a wide range of impact velocity variation, the final cavity depth L_c (dimension L) will be determined by: the impact velocity V_0 (L/T), the densities of the colliding body materials under normal conditions ρ_{01} and ρ_{02} (M/L^3), the characteristic dimensions of the impacting body l_0 and d_0 (L), the initial value of the impacting body nose

form factor κ_0 (dimensionless quantity), and the strength and compressibility characteristics of the colliding body materials.

It was shown above (§ 4.2) that the strength characteristic which determines halfspace deformation under impact conditions is the dynamic hardness of the halfspace material. Therefore, the dynamic hardnesses of the materials H_1 and H_2 ($ML^{-1}T^{-2}$) of bodies 1 and 2 are included as the strength characteristics of these bodies.

It is natural to take into account the compressibility of the material of each colliding body with the aid of the shock adiabat parameters, assuming in accordance with the experimental results [4, 24] that the shock wave velocity D and the mass velocity U of the particles behind the wave front are connected linearly with one another. Under this assumption, the pressure p and density ρ behind the shock wave front for different materials in the pressure ranges where polymorphic changes are absent can be determined with adequate accuracy by the relations [24, 25]:

$$p = p_0(a + \lambda U)U \quad (4.22)$$

and

$$\rho = \rho_0 \frac{a + \lambda U}{a + (\lambda - 1)U}, \quad (4.23)$$

where a — sound speed in the material; ρ_0 — material density under normal conditions; and λ — a constant of the material.

Consequently, the shape of the material shock adiabat is completely defined by specifying the sound speed a and the constant λ for known initial density ρ_0 . Therefore, we can take as the compressibility characteristics of the materials of bodies 1 and 2 the sound speeds in these materials a_1 and a_2 (LT^{-1}) and the values of the constants λ_1 and λ_2 (dimensionless quantities).

In accordance with the basic theorem (Π theorem) of dimensional analysis [73], from the 13 listed process parameters ($L_0, V_0, \rho_{01}, \rho_{02}, l_0, d_0$

$\alpha_0, H_1, H_2, a_1, a_2, \lambda_1, \lambda_2$) we can form ten independent dimensionless combinations, the functional connection between which will give an implicit form of the equation describing the subject process in a wide range of encounter velocities; the equation may be written in the form:

$$\frac{L_C}{l_0} = f\left(\frac{\rho_{01} V_0^2}{H_1}, \frac{H_2}{H_1}, \frac{\rho_{02}}{\rho_{01}}, \alpha_0, \frac{l_0}{d_0}, \frac{a_2}{a_1}, \frac{\rho_{01}^{1/2} a_1}{H_1^{1/2}}, \lambda_1, \lambda_2\right). \quad (4.24)$$

From this there follows directly the criterion for modeling the subject process: the relative cavity depths in two experiments will have the same value if in these experiments the corresponding dimensionless parameters appearing under the function symbol have the same value.

Equation (4.24) and the associated modeling criteria can be simplified considerably if we are interested only in such a large group of deformable bodies as the metals. In accordance with experimental data [4, 24, 42], we can take for the metals $\frac{\rho_{01}^{1/2} a_1}{H_1^{1/2}} \approx \text{const}$ and $\lambda_1 \approx \lambda_2 \approx \text{const}$. Under this assumption, (4.24) takes the form:

$$\frac{L_C}{l_0} \approx F\left(\frac{\rho_{01} V_0^2}{H_1}, \frac{H_2}{H_1}, \frac{\rho_{02}}{\rho_{01}}, \alpha_0, \frac{l_0}{d_0}, \frac{a_2}{a_1}\right). \quad (4.25)$$

For analysis of this equation, it is best to turn to a somewhat altered system of dimensionless parameters appearing under the function symbol; namely, we rewrite the equation in the form:

$$\frac{L_C}{l_0} \approx \Phi\left(\frac{\rho_{01} V_0^2}{H_1}, \frac{H_2}{H_1}, \frac{\rho_{02}}{\rho_{01}}, \alpha_0, \frac{l_0}{d_0}, \frac{\rho_{02} a_2}{\rho_{01} a_1}\right). \quad (4.26)$$

It is interesting to see how (4.26) transforms in application to some particular collision condition cases. In so doing, the modeling conditions will obviously undergo corresponding simplifications.

1) In the interval of relatively low subsonic impact velocities V_0 , we can take for body 2 a material whose hardness satisfies the inequality $H_2 \gg H_1 + \alpha_0 \rho_{01} V_0^2$. For these low velocities, such a body 2 can with adequate accuracy be considered nondeformable (rigid)

and body 1 can be considered incompressible, which makes it possible to exclude the parameters $\frac{H_2}{H_1}$, $\frac{l_0}{d_0}$ and $\frac{\rho_{02} d_2^2}{\rho_{01} d_1^2}$ from (4.26). Therefore, (4.26) will take the form for this case:

$$\frac{L_C}{l_0} \approx \varphi_1 \left(\frac{\rho_{01} V_0^2}{H_1}, \frac{\rho_{02}}{\rho_{01}}, \kappa_0 \right). \quad (4.27)$$

It is not difficult to see that this equation is expressed in explicit form by (4.12), which agrees well with the experimental data. /215

2) In the interval of relatively high velocities V_0 , the inequalities $H_1 \ll \rho_{01} V_0^2$ and $H_2 \ll \rho_{02} V_0^2$ will be satisfied. If in this case $l_0 \gg d_0$, the body interaction process can, with adequate accuracy, be considered to be steady state. We can also consider that, with satisfaction of these conditions, the contact surface of the colliding bodies will rapidly take a form which is nearly hemispherical and remain such throughout the entire process [28]. In other words, we can consider that the form factor κ_0 of the nose of body 2 remains constant throughout the entire process, and close to 0.5 [42, 47, 48]. Finally, as was shown above (§4.3), when these conditions are satisfied, we can exclude from consideration the compressibility characteristics of the colliding body metals. Consequently, (4.26), describing the collision process of metal bodies, will contain under the function symbol in this particular case only a single dimensionless argument:

$$\frac{L_C}{l_0} \approx \varphi_2 \left(\frac{\rho_{02}}{\rho_{01}} \right). \quad (4.28)$$

This equation is expressed in explicit form by the well-known formula (4.21), which is in good agreement with the experimental data [28, 29].

3) Equation (4.26) also simplifies considerably in the particular case when the colliding bodies are made from the same metal.

In this case, the dimensionless parameters $\frac{H_2}{H_1}$, $\frac{\rho_{02}}{\rho_{01}}$ and $\frac{\rho_{02} d_2^2}{\rho_{01} d_1^2}$ become

unity, and the equation describing the process will contain only three dimensionless arguments under the function symbol:

$$\frac{I_C}{I_0} \approx \varphi_3 \left(\frac{\rho_{01} V_0^2}{H_1}, \kappa_0, \frac{l_0}{d_0} \right). \quad (4.29)$$

4) Equation (4.26) will also simplify when the shock adiabats of the colliding body metals are similar to one another in the coordinates "pressure p versus mass velocity U ". For example, according to the experimental data [4, 7, 9, 10, 12], the shock adiabats of iron, copper, and lead practically coincide in this coordinate system. It follows from (4.22) that, in this case, the approximate equality $\rho_{01} a_1 \approx \rho_{02} a_2$ will be satisfied. Therefore, under the subject conditions, we can exclude from (4.26) the parameter $\frac{\rho_{02} a_2}{\rho_{01} a_1}$, i.e., we can write the equation in the form:

$$\frac{I_C}{I_0} \approx \varphi_4 \left(\frac{\rho_{01} V_0^2}{H_1}, \frac{H_2}{H_1}, \frac{\rho_{02}}{\rho_{01}}, \kappa_0, \frac{l_0}{d_0} \right). \quad (4.30)$$

Finally, if in this particular case the impact velocities are /216 so high that the deformation process can be considered to satisfy the model described in §4.3, and if in this case the striker dimensions and shape are such that the impact process cannot become steady state, the body contact surface velocity throughout the entire time of impacting body action on the target will be equal to approximately half the impact velocity for any values of the ratios $\frac{H_2}{H_1}$ and $\frac{\rho_{02}}{\rho_{01}}$. Consequently, for these impact conditions, (4.30) can be reduced to the form:

$$\frac{I_C}{I_0} \approx \varphi_5 \left(\frac{\rho_{01} V_0^2}{H_1}, \kappa_0, \frac{l_0}{d_0} \right), \quad (4.31)$$

which coincides with (4.29).

Thus, analysis of the deformable body collision problem, using the methods of dimensional theory, makes it possible to obtain in implicit form the equation describing the impact process in a wide range of encounter velocity variations, and also makes it possible to derive the criteria for modeling this process.

§ 4.5. Comparison of "Original" and "Model" Process Parameters

We have shown that the problem solution obtained using dimensionless analysis coincides with the known theoretical and experimental solutions in two particular asymptotic collision condition cases. Therefore, the experimental verification of (4.26) and the modeling criteria which follow from this equation should be accomplished, first of all, for impact conditions differing significantly from those of these two cases.

The natural first step in this verification was comparison of the results of two experiments, in each of which the interaction body metals and impact velocities were selected so that in both experiments the dimensionless ratios appearing under the function symbol (4.26) had the same value. Consequently, one of these experiments ("high-velocity") can be considered to be the "original", and the other ("low-velocity") can be considered to be the "model". We would expect that, in these experiments, not only the final cavity depths would be similar, but at the corresponding moments of time the instantaneous values of the force and deformational characteristics of the process would be the same.

Collision of the bodies was studied using the pulsed radiography method. In accordance with the capabilities of the method, heavy metal striker penetration into light metal targets was studied [76]. Specifically, strikers having the form of cylinders of diameter $d_0 \approx 8$ mm and length $l_0 \approx 20$ mm were made from soft steel (density $\rho_{02} = 7.85$ g/cm³), heat treated to dynamic hardness $H_2 = 167$ kg/mm², and from annealed copper ($\rho_{02} \approx 8.90$ g/cm³) with dynamic hardness 65 kg/mm². As for the blocks acting as "semi-infinite" targets, they had the form of 60 mm-diameter cylinders, and were made from duraluminum ($\rho_{01} = 2.80$ g/cm³), heat treated to dynamic hardness $H_1 = 67$ kg/mm², and from annealed aluminum ($\rho_{01} = 2.70$ g/cm³) with dynamic hardness $H_1 = 20$ kg/mm². In one experiment series ("original" process), penetration

of the steel cylinder into the duraluminum target with encounter velocity $V_0 = 1380$ m/sec was studied, and in the other experiment series ("model" process), penetration of the copper cylinder into the aluminum target with velocity $V_0 = 870$ m/sec was studied.

It is easy to see that the dimensionless ratios appearing under the function symbol in (4.26) ("modeling criteria") had essentially the same values in both experiment series. Specifically, in both series:

$$\left. \begin{aligned} \frac{\rho_0 V_0^2}{H_1} &= 8.1; \frac{H_2}{H_1} = 2.5; \frac{\rho_0}{\rho_1} \approx 3; \\ \kappa_0 &= 1; \frac{l_0}{d_0} \approx 2.5; \frac{\rho_0 a_0}{\rho_1 a_1} \approx 2.3. \end{aligned} \right\} \quad (4.32)$$

As we would expect, in both experiment series, the final cavity depths L_c had the same value, equal to 35.5 ± 0.5 mm. The total process time t_c in the first experiment series (soft steel and duraluminum) was 68 μ sec, and in the second series (copper and aluminum) the time was 100 μ sec. Figures 4.13 and 4.14 show some characteristic radiograms of the cylindrical steel striker penetrating the duraluminum target, and of the copper striker penetrating the aluminum target. Simple comparison of the radiograms of Figures 4.13 and 4.14 shows that qualitatively the two processes develop similarly in time, and analysis of the radiograms leads to the conclusion that the two processes are quantitatively similar. The latter is to be understood in the sense that the instantaneous values of a particular parameter, referred to a parameter of the same dimension which is characteristic for the given process, will be the same in the "original" and "model" processes at corresponding moments of time.

It is not difficult to see that the radiograms make it possible to obtain for both series of experiments the variations in time of all the collision process parameters of interest: penetration depth L , striker length l , diameter d of the line of separation, and striker nose form factor κ , which, if we approximate the contact surface of the interaction bodies by part of a sphere of radius r ,

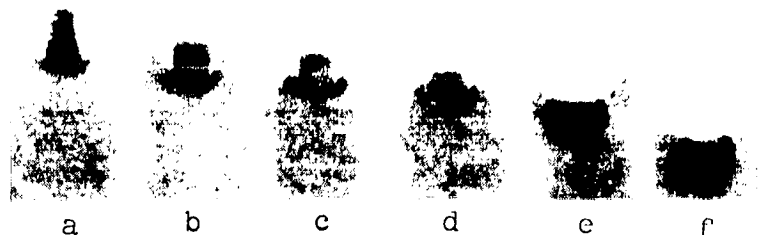


Figure 4.13. Sequential radiograms of steel cylinder penetrating duraluminum "halfspace" with encounter velocity $V_0 = 1380$ m/sec

("original" process): a) 10, b) 16, c) 19, d) 26, e) 34, and f) 68 μ sec after body encounter [76]

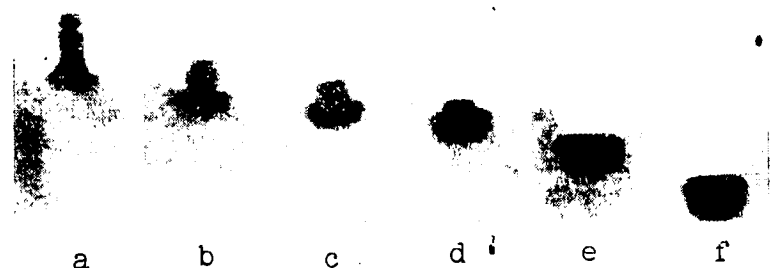


Figure 4.14. Sequential radiograms of copper cylinder penetrating aluminum "halfspace" with encounter velocity $V_0 = 870$ m/sec

("model" process): a) 9, b) 21, c) 27, d) 34, e) 50, and f) 100 μ sec after body encounter [76]

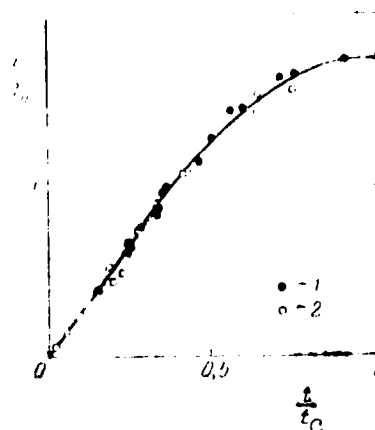


Figure 4.15. Relative penetration depth L/L_0 of cylindrical strikers into massive target in the "original" (1) and "model" (2) processes at corresponding moments of time t/t_c [76]

can be calculated from the formula [38]:

$$\alpha = 1 - \frac{1}{8} \left(\frac{d}{r} \right)^2. \quad (4.33)$$

As an example, Figure 4.15 shows, in the dimensionless coordinates $(\frac{t}{t_c}, \frac{L}{L_0})$, measurement results concerning the penetration depth variation in both processes. We see that in the selected dimensionless coordinates, the relations obtained for the two processes agree quite well. The same situation holds for all the other parameters listed above in suitably selected dimensionless coordinates.

It should be emphasized that this agreement of the relations for the "original" and "model" processes indicates similarity in the two processes of both the deformational and force characteristics. Actually, the force characteristics of the studied process are

[76]

determined by the coefficient κ and the striker penetration velocity V , and also by the target metal density and strength and compressibility characteristics. But similarity of the form factors was established by the measurements made, while similarity of the densities and compressibility characteristics is specified by the conditions (4.32). As for the penetration velocity $V = \frac{dL}{dt}$, according to Figure 4.15, such dimensionless functions as:

$$\frac{V}{l_0/t_0} = \frac{d(L/l_0)}{d(t/t_0)}, \quad (4.34)$$

coincide in the "original" and "model" processes. Consequently, the penetration velocities and, along with them, the force characteristics will be the same in the two processes at corresponding moments of time.

Thus, the very first experiments conducted to verify experimentally the dimensional analysis of the deformable body collision problem show that when the modeling criteria (4.32) are satisfied, the deformable body collision process is modeled both in terms of the final result and in terms of the instantaneous deformational and force characteristics.

§ 4.6. Modeling Curve

A broader experimental verification of the analysis of the deformable body collision problem was conducted in [77], for which both the targets and strikers were soft steel (density $\rho_0 = 7.85 \text{ g/cm}^3$, Brinnell hardness $H_B = 116 \text{ kg/mm}^2$, dynamic hardness $H = 167 \text{ kg/mm}^2$), copper ($\rho_0 = 8.90 \text{ g/cm}^3$, $H_B = 42 \text{ kg/mm}^2$, $H = 65 \text{ kg/mm}^2$), aluminum ($\rho_0 = 2.70 \text{ g/cm}^3$, $H_B = 22 \text{ kg/mm}^2$, $H = 26 \text{ kg/mm}^2$), and lead ($\rho_0 = 11.34 \text{ g/cm}^3$, $H_B \approx 5 \text{ kg/mm}^2$, $H \approx 8 \text{ kg/mm}^2$). The shock adiabats of these metals are shown in Figure 4.16. We see that this choice of the metals provided a quite broad range of variation of the density and resistance-to-deformation (dynamic hardness) characteristics of the colliding bodies, and also made it possible to obtain an

experimental solution for the case when the shock adiabats of the interacting body metals are similar to one another in the coordinate system "pressure p versus mass velocity U ".

For the experiments, the targets were made in the form of blocks, whose dimensions in the direction of impact and in the transverse direction exceeded by approximately an order of magnitude the corresponding dimensions of the cavities created in the blocks, and the strikers were made in the form of $d_0 \approx 9.4$ mm diameter spheres. The strikers were given velocities V_0 from 150 to about 2500 m/sec, using a powder launcher.

It follows from (4.29), obtained for the case when the striker and target are made from the same metal, that if the strikers are geometrically similar ($x_0 = \text{const}$, $\frac{l_0}{d_0} = \text{const}$), the experimental results will satisfy the same curve:

$$\frac{L_C}{l_0} \approx \psi \left(\frac{\rho_0 V_0^2}{H_1} \right). \quad (4.35)$$

regardless of the metal used.

Figure 4.17 shows the results of experiments conducted to verify this conclusion. In constructing the graph, it is assumed that the characteristic length l_0 of the sphere penetrating the target is equal to the sphere diameter d_0 . We see that the experimental points, in complete agreement with (4.35), in the dimensionless coordinates $\left(\frac{\rho_0 V_0^2}{H_1}, \frac{L_C}{d_0} \right)$ lie on the same curve with good accuracy, which is new direct proof of the possibility of modeling the subject deformable body collision process.

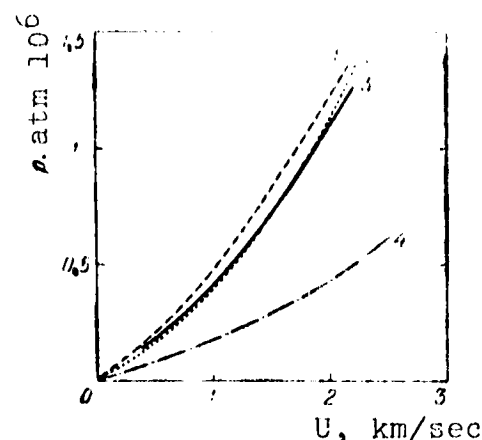


Figure 4.16. Shock adiabats of copper (1), lead (2), iron (3), and aluminum (4) from data of [4, 7, 9, 10, 12]

Since the lead sphere cannot be accelerated to more than 1000 - 1200 m/sec without changing its shape, in the subject series of experiments, the relative cavity depth L_c/d_0 measurements were

made only up to values of the dimensionless parameter $\frac{\rho_0 V_0^2}{H_1} \approx 220$. Therefore, the modeling curve in the form in which it is represented in Figure

4.17 makes it possible to predict the result of collision of a sphere made from iron, aluminum, or alloys based on these metals with a massive target of the same metal as the sphere, only for encounter velocities up to 7 - 8 km/sec. Actually, for example, for a target steel with dynamic hardness $H_1 = 250 \text{ kgf/mm}^2$, on which impact takes place with the velocity $V_0 = 8 \text{ km/sec}$, $\frac{\rho_0 V_0^2}{H_1} \approx 200$, and for a duraluminum target with dynamic hardness $H_1 = 80 \text{ kgf/mm}^2$ with the same impact velocity $\frac{\rho_0 V_0^2}{H_1} \approx 220$.

It would obviously be interesting to investigate the behavior of the modeling curve of Figure 4.17 in the region of higher values of the dimensionless argument $\frac{\rho_0 V_0^2}{H_1}$. For the solution of this problem, it was natural to turn to study of the collision of bodies whose densities and resistance-to-deformation characteristics were different, but whose shock adiabats were similar in the "pressure p versus mass velocity U " coordinate system. We showed above (§ 4.4) that, in this case, the equation describing the collision process will coincide with (4.29) if the colliding body encounter velocities and the process of striker interaction with the target takes place in

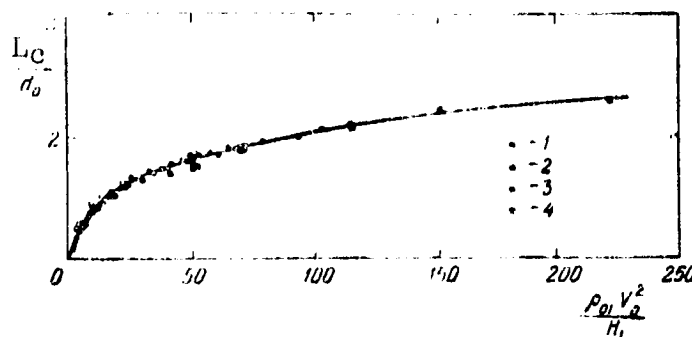


Figure 4.17. Dependence of final depth of cavity created in a massive target with impact of a sphere made from the same metal as the target on the encounter velocity: 1 — soft steel; 2 — copper; 3 — aluminum; 4 — lead [77]

the unsteady regime. Strictly speaking, the colliding body interaction process will take place in the unsteady regime when the striker longitudinal dimension is much less than its transverse dimension ($l_0 \ll d_0$). However, sphere penetration into a target can also be considered in the first approximation to be a process taking place in the unsteady regime, since in this case the dimensions of that striker section at which the particles entrained into motion at each given instant are located vary continuously. Therefore, in accordance with the data of Figure 4.16, we can extend the modeling curve of Figure 4.17, in the first approximation, into the region of high values of the argument $\frac{\rho_0 l_0^3}{H_1}$, when studying, for example, impact of iron and copper spheres on a massive lead target. /222

The results of these experiments are shown in Figure 4.18. Also shown here by the dashed line is the relation from Figure 4.17. We see from Figure 4.18 that the data obtained make it possible to extend the modeling curve to values of the dimensionless argument $\frac{\rho_0 l_0^3}{H_1} \approx 800$, i.e., they make it possible to broaden the interval of variation of this argument covered by direct measurements by nearly a factor of four. Formally speaking, the modeling curve of Figure 4.18 makes it possible to predict the result of steel and duraluminum spherical striker collision with massive targets of the same material as the striker for encounter velocities up to 14 - 15 km/sec.

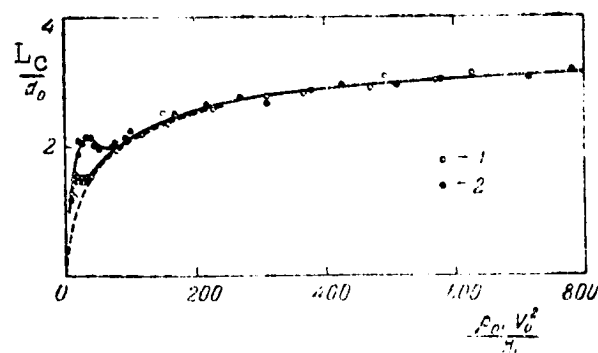


Figure 4.18. Depth of cavity formed in massive lead target with impact of copper (1) and iron (2) spheres versus encounter velocity; dashed line reproduces the relation of Figure 4.17 [77]

At the same time, the data of Figure 4.18 make it possible to estimate those values of the parameter $\frac{\rho_0 l_0^3}{H_1}$, upon exceeding which striker material strength can actually be neglected. These values

of this parameter in the subject case of impact on a lead halfspace are equal to about 80 for iron strikers ($\frac{H_2}{H_1} \approx 21$), and about 40 for copper strikers ($\frac{H_2}{H_1} \approx 8$). For smaller values of the parameter $\frac{\rho_0 V_0^2}{H_1}$, /223
striker material strength plays a quite obvious role: the nature of the corresponding segments of the curves in Figure 4.18 depends markedly on the level of the H_2/H_1 values. In this region of relatively low impact velocities, the iron and copper spherical strikers, when penetrating the lead target, either do not deform at all (left-hand rising branches of the solid curves in Figure 4.18) or deform partially, but with significant increase of the transverse section, which in some interval of variation of the parameter $\frac{\rho_0 V_0^2}{H_1}$ leads even to reduction of the relative cavity depth L_c/d_0 with increase of the parameter (descending segments of the solid curves of Figure 4.18).

The modeling curve of Figure 4.18 can be extended to the region of still larger values of the dimensionless argument $\frac{\rho_0 V_0^2}{H_1}$, if we use the experimental results of [59], in which ($d_0 \approx 3.2$ mm) steel sphere impact on a massive lead target was studied for encounter velocities up to about 6 km/sec. The results of these experiments are presented in Figure 4.19. The dashed line reproduces the relation of Figure 4.18.

As we would expect, the results of these experiments, although they relate to spheres whose diameter is smaller by a factor of three than the diameter of the spheres used in the experiments described above, agree well with the relation of Figure 4.18. The results of these experiments extend the modeling curve to values of the dimensionless argument $\frac{\rho_0 V_0^2}{H_1} \approx 5000$, which makes it possible to formally /224
predict the result of steel sphere interaction with a massive steel target, or duraluminum sphere interaction with a massive duraluminum target for impact velocities of 30 - 50 km/sec.

It is remarkable that all the experimental data corresponding to the subject problem conditions known at the present time agree well with this modeling curve. As an illustration of this statement, Figure 4.20 shows the modeling curve (solid line) and the experimental points obtained for impact velocities $\sim 3 - 10.5$ km/sec [59, 78 - 80].

Thus, the cited experimental data again confirmed the validity of the problem analysis presented above. They make it possible to construct a modeling curve which is confirmed well by direct experimental data obtained at impact velocities to about 10.5 km/sec. The modeling curve was extended to large values of the basic modeling parameter $\frac{\rho_0 V_0^2}{H_1}$, which, generally speaking, make it possible to predict the results of the collision of spherical bodies made from iron, aluminum, or alloys based on these metals with a massive target of the same material as the sphere for encounter velocities of 30 - 50 km/sec, which are inaccessible for direct experiment. However, we must

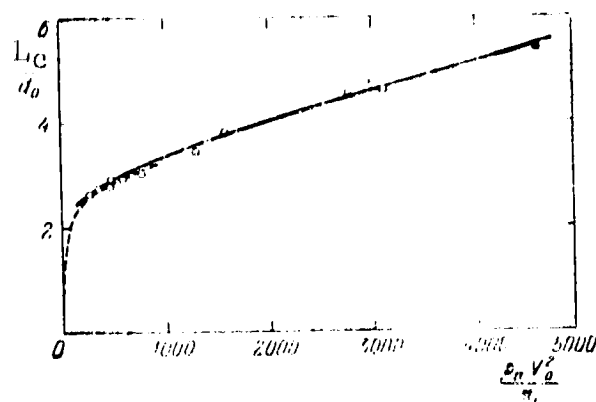


Figure 4.19. Depth of cavity formed in massive lead target with iron sphere impact versus encounter velocity from data of [59]; dashed line reproduces the relation of Figure 4.18

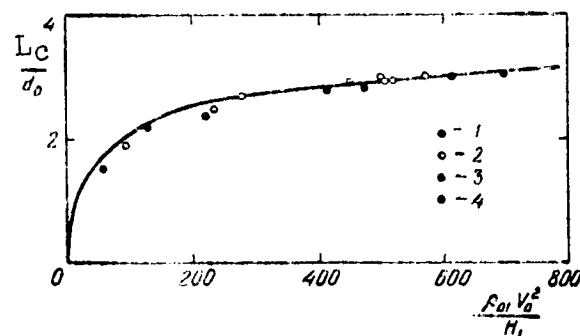


Figure 4.20. Modeling curve of Figure 4.18 (solid line) and experimental data (points) obtained at high collision velocities of spherical strikers with massive targets: 1 — duraluminum striker and target, $V_0 = 3.2 - 10.7$ km/sec [79]; 2 — aluminum striker and target, $V_0 = 3.1 - 7.5$ km/sec [78]; 3 — steel striker and copper target, $V_0 = 5.6$ km/sec [59]; 4 — steel striker and target, $V_0 = 6.7$ km/sec [80]

emphasize that until the question of the limits of applicability of the model representation is resolved, this prediction is of a purely formal nature.

§ 4.7. Evaluation of Thermal Phenomena Role in Metallic Body Interaction

In light of the above, a question naturally arises: what is the upper limit of that velocity interval in which the estimate of the final cavity depth from the modeling curve will not differ markedly from the true collision result?

The formulation of this question is a result of the fact that the cavity depth dependence on impact velocity must have a singularity near a value of the velocity which is unique for each pair of colliding bodies [25, 67, 68, 81, 83]. The "thermal explosion", i.e., evaporation in the unloading wave of the colliding body metals in the volumes adjacent to their contact surface, is usually cited as the physical reason for this singularity.

The impact velocities which can lead to the onset of this phenomenon are very high. According to the theoretical estimates [25], for the various metals they lie in the range of 10 - 20 km/sec, where study of the solid body collision process is not yet accessible in practice to direct experiment.

However, we must bear in mind that, regardless of whether or not target metal vaporization in the unloading wave takes place, those target volumes which, as a result of shock loading, are in the molten condition will be ejected from the cavity upon unloading. In other words, we can state that the magnitude of the target volume ejected from the cavity will be determined in the final analysis not by the vaporization conditions, but rather by the target metal melting conditions. This means that the cavity depth dependence on impact velocity will have a singularity not at the cited high velocities, but rather at considerably lower body encounter velocities. These are termed the threshold velocities; these are the impact velocities

upon exceeding which the unloaded target metal in some volume of the impact zone will be heated to a temperature close to its melting point. To the threshold impact velocities, there will naturally correspond threshold values of the mass velocities, pressures, and other thermodynamic parameters at the disturbance front, which arises in the colliding bodies during their encounter. From estimates based on theoretical data [4], for various metals, the threshold impact velocities $V_t \approx (0.7 - 1)a$, where a — sound speed in the metal, i.e., they lie in the range of about 1.5 - 6 km/sec, which at the present time is covered by the velocity range accessible for experiments.

However, in spite of the expectations, the experimental curves of cavity depth versus impact velocity, as we see from the above discussion and also from numerous other studies of this question (see, for example, [56 - 59, 78 - 80]), do not show any singularities at the threshold velocities. /226

This experimental fact can be explained as follows.

The cited estimated threshold impact velocities V_t were calculated for those body encounter conditions in which the body interaction process takes place in the unsteady regime, and is not accompanied by hydrodynamic flow of the bodies. However, in the experiments examined above, and also in other cited studies [58, 59, 78 - 80], the collision process was accompanied by flow of the two interacting bodies and, in this sense, approached the steady state regime, since either equiaxed bodies or bodies which were elongated in the direction of impact were used as the strikers. We noted previously (§ 4.3) that the difference between the body interaction processes in the unsteady and steady regimes is very significant. In the first case, the impact velocity V_0 determines the mass velocity U on the shock wave front arising in the interacting bodies during their encounter; in the case of collision of two bodies made of the same metal, $U = V_0/2$. In the second case, the impact velocity V_0 determines the shock (head) wave velocity D ; in the case of interaction

of bodies made from the same metal, $D = V_0/2$. Since $D \approx a + 1.5U$ [4, 7], in the nearly-steady-state interacting body hydrodynamic flow processes, the threshold shock wave velocity D_t will be reached only for encounter velocities $V_0 \geq 2a + 1.5V_t$. If we consider that for the metals $V_t \approx (0.7 - 1)a$, we can state that, in processes which transition into hydrodynamic flow of the colliding bodies, the thermal effects will not influence the final cavity depth when the body encounter velocity $V_0 \lesssim (3 - 3.5)a$.

Naturally, for encounter velocities V_0 satisfying the condition $V_t < V_0 < (3 - 3.5)a$, the threshold values of the thermodynamic parameters will be reached in certain volumes of the colliding bodies in the initial stage of body interaction taking place in the unsteady regime. However, this circumstance cannot influence in any way the final cavity depth or the further behavior of the process, since these volumes will spread out into a film on the surface of the forming cavity, regardless of the state in which these volumes are found.

Thus, provided the theoretical threshold velocity estimates are correct, the predictions resulting from the model concepts will be close to the true collision result in application to sphere impact on a massive target of the same metal, at least up to encounter velocities $V_0 \approx (3 - 3.5)a$. Consequently, when the sphere and the massive target are made from iron, aluminum, or alloys based on these metals, the predictions resulting from the modeling curve will be reliable, at least up to encounter velocities of 15 - 18 km/sec*.

/227

* It also follows from this discussion that, in the processes which transition into hydrodynamic flow of the colliding bodies, vaporization in the unloading wave ("thermal explosion") can occur during interaction of bodies made from the same metal only for encounter velocities $V_0 \gtrsim 2a + 1.5V_{\text{vap}}$. Consequently, when the sphere and massive target are made from iron, aluminum, or alloys based on these metals, these velocities, with account for the estimates of [25], will be 30 - 40 km/sec.

In this connection, experimental determination of the threshold velocities becomes very important. To this end, experiments were conducted in which the phenomena arising in a massive target in the case of a flat-wise "short" impact, when the collision process takes place in a definitely unsteady regime [25, 84]. The strikers for the experiments were made from aluminum, and had the form of thin plane-parallel disks (diameter $d_0 = 15$ mm, thickness $l_0 = 4$). The disks were imparted a velocity of about 2.4 km/sec. The targets were blocks made from lead, tin, and cadmium, for which the theoretical threshold velocities lie in the indicated interval. It is important to note that this choice of the colliding body metals ensured the most complete unloading of the target after passage of the loading and unloading waves through the impacting disk. This conclusion follows directly from the mutual positioning of the aluminum and target-metal shock adiabats in the coordinate system "pressure p versus mass velocity U " (see, for example [4, 7, 9, 10, 12], and also Figure 4.16).

As an example of the data obtained, we need only examine the results of the experiments with lead targets.

Figure 4.21 shows photographs of axial sections of two characteristic cavities. The cavity profile in Figure 4.21a is typical for relatively low ($\lesssim 1$ km/sec) impact velocities, while the cavity profile in Figure 4.21b is typical for velocities above 1.7 - 1.8 km/sec. We see that the cavity profiles are not similar. The cavity of Figure 4.21b is essentially "composed" of two parts: an upper part which is similar to the cavity of Figure 4.21a, and a lower part, which is nearly conical in form. The entire surface of the "conical" part of the cavity of Figure 4.21b has definite traces of melting.

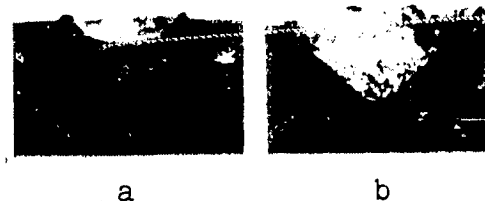


Figure 4.21. Sections of typical cavities obtained during impact of an aluminum disk on a lead target: a) for low ($\lesssim 1$ km/sec) and b) for high ($\gtrsim 1.7 - 1.8$ km/sec) impact velocities [84, 85]

It is significant that a shock wave with mass velocity approximately 650 m/sec [4, 24] arises in the target for the aluminum disk and lead target encounter velocity 1.7 - 1.8 km/sec. This velocity is close to the calculated threshold mass velocity for lead [4]. The difference in these velocities does not exceed 10% (Table 4.2).

Similar data were obtained in experiments with cadmium and tin targets. The difference in the experimental and calculated threshold velocities again does not exceed 10 - 12% (Table 4.2).

/228

TABLE 4.2. SOME TARGET METAL CHARACTERISTICS AND THRESHOLD VELOCITY DETERMINATION RESULTS

Metal			Tin	Cadmium	Lead	Zinc	Zinc
Initial target temp., T_0 , °C			20	20	20	20	250
Melting point, T_m , °C			232	321	327	419	419
Specific heat, c_p , cal/g·deg			0.054	0.055	0.030	0.092	0.092
Threshold mass velocity V_t , m/sec	Calculated [4]		800	940	715	1315	925
	Experi- mental	With massive targets	700	880	650	-	910
		With thin screens	770	890	700	-	-

In order to show in a direct experiment that the bottom part of the cavity of Figure 4.21b actually was formed by target metal ejection from the cavity in the unloading wave, a pulsed radiographic study of the collision process was made for various body encounter velocities. Figure 4.22 shows a series of radiograms which characterize the process occurring in a lead target with impact on it of an aluminum disk with velocity about 2.4 km/sec. Here, dispersed target matter ejection from the cavity is clearly seen (Figure 4.22, frames e and f). It is significant that ejection takes place at impact velocities of 1.7 - 1.8 km/sec and higher, when the cavity



Figure 4.22 Radiograms of aluminum disk impact on a massive lead target with velocity V about 2.4 km/sec: a) 7 μ sec prior to encounter; b) 14; c) 27; d) 81; e) 620; and f) 1070 μ sec after encounter [85]

has the form of Figure 4.21b and its bottom part has definite traces of melting, and does not occur at lower velocities. Measurements show that the matter is ejected with a velocity of 30 - 40 m/sec, which also agrees well in order of magnitude with the results of calculation [4].

/229

Similar results were obtained in experiments with the tin and cadmium targets.

Experiments were also conducted with massive zinc targets. The maximal velocity imparted to the aluminum disk (about 2.4 km/sec), as would be expected, was not adequate to cause the subject effects in the zinc target. However, impact on a zinc target heated to 250° C led to results qualitatively similar to the results of the experiments with lead, tin, and cadmium. The threshold velocity established in these experiments again agrees well with the calculated estimate (Table 4.2).

The threshold velocity measurement results obtained in experiments with massive targets were confirmed by the results of a separate series of experiments involving flat impact at the end of a copper cylinder on thin (thickness about 0.1 of the cylinder diameter) shields, fabricated from lead, tin, and cadmium. It was found that, if the shield material in the circular region subjected to impact loading remains solid after impact, then in the free motion the front of the region and the fragments appearing along its

/230

contour will have clear outlines. However, if the material melts during impact loading, it is found that in the free motion the front of the region will become blurred and jet flow will arise on the contour of this region, which is subjected to lateral unloading.

Radiograms obtained in experiments with thin shields at different impact velocities showed that, in fact, near some velocity the behavior of the circular region, which is ejected during impact, changes as expected. As an example of the experimental data, Figure 4.23 shows radiograms obtained in experiments with a lead shield at subthreshold and superthreshold impact velocities. We note that the mass velocities at the front of the shock waves arising in the lead shield during colliding body encounter differ only by 40 m/sec in the experiments for which the radiograms are shown in Figure 4.23.



Figure 4.23. Typical radiograms of copper cylinder impact on a thin lead shield for encounter velocities 1.2 km/sec (a), and 1.3 km/sec (b); time from instant of encounter in both cases is about 25 μ sec

The threshold velocities established in the experiments with the thin shields are presented in the last line of Table

4.2. They are close to the calculated values, and also to the values which were determined in the experiments with the massive targets.

In these experiments, the threshold velocities were measured only for the low-melting alloys. However, it is natural to expect that the residual heating of the target metal after shock loading and the subsequent unloading will obey the same relationship for all the metals. It follows from dimensional considerations that this will be a relation of the form:

$$\frac{\Delta Q}{a^2} = f\left(\frac{U}{a}\right), \quad (4.36)$$

where $\Delta Q = c_p(T - T_0)$ — amount of heat required to warm unit mass of a metal with specific heat c_p from the initial temperature T_0 to the temperature T ; U — mass velocity in the shock wave which leads after unloading to the given residual heating; a — sound speed in the metal.

Experiment [85] showed that in the dimensionless coordinate system $(\frac{U}{a}, \frac{\Delta Q}{a^2})$, the calculated data [1, 4] actually satisfy a single relationship (Figure 4.24). As for the data of Table 4.2, which show /232 the residual heating up to the melting point in targets made from low-melting metals, they confirm this relation very well (Figure 4.25).

This result can be considered proof of the validity of the approximate threshold velocity calculations, not only for the low-melting metals, but also for the refractory metals. This confirms experimentally the conclusion drawn above on the possibility of reliable predictions based on model representations of the results of the collision of a sphere with a massive target of the same metal as the sphere for encounter velocities up to $(3 - 3.5)a$.

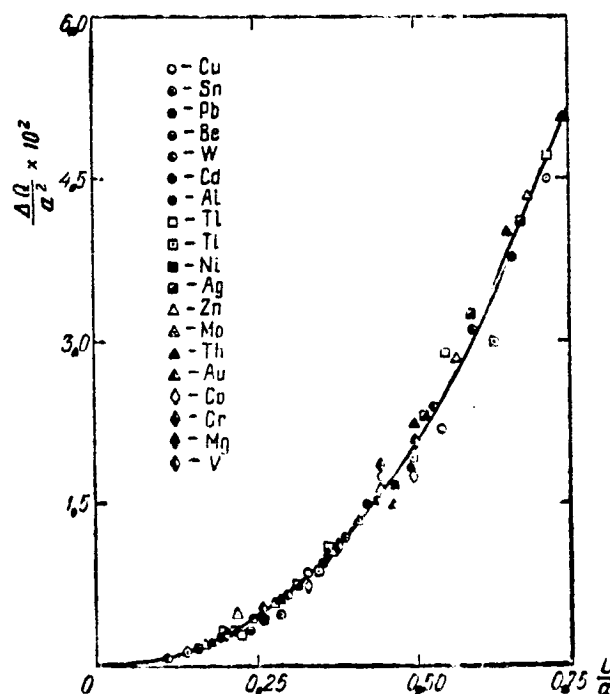


Figure 4.24. Residual heating of various metals versus mass velocity in loading wave from calculated data of [1, 4]

A very good illustration of these concepts and conclusions are the results of experiments with massive lead targets and aluminum disks whose thickness was increased gradually [85]. The experiments were made with impact velocity ~ 2.4 km/sec, which exceeds by nearly

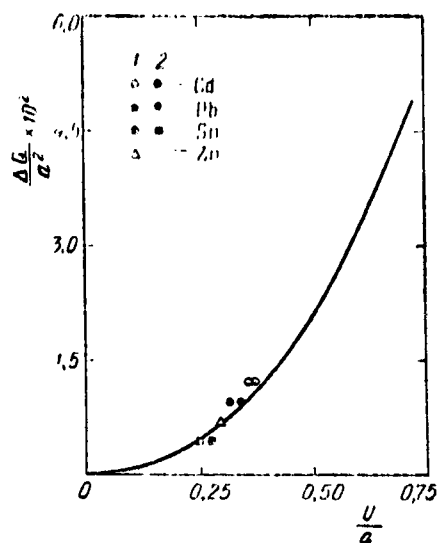


Figure 4.25. Comparison of the relation of Figure 4.24 with experimental data of Table 4.2: 1 — data of experiments with massive targets, and 2 — data of experiments with thin shields [85]

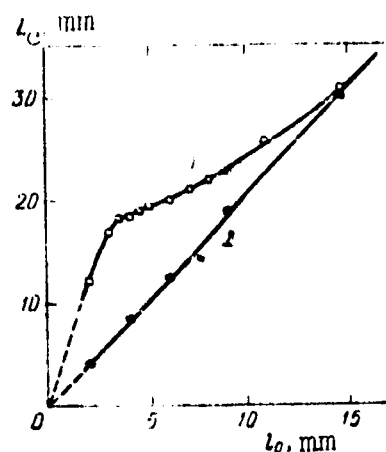


Figure 4.26. Total depth of cavity in massive lead target versus thickness l_0 of impacting aluminum disk (1), and height of upper part of the cavity (see Figure 4.21b) versus the same parameter (2) for encounter velocity $V_0 \approx 2.4$ km/sec [85]

1.5 times the threshold impact velocity ($\sim 1.7 - 1.8$ km/sec). In Figure 4.26, curve 1 reflects the total cavity depth L_c dependence on the disk thickness l_0 , and curve 2 shows the dependence on the same parameter of the height of the upper part of the cavity — that part which is due to target plastic flow (Figure 4.21b). The difference between the ordinates of these curves then characterizes the thermal effect influence.

We see from Figure 4.26 that, for an impact velocity exceeding considerably the threshold value, the thermal effects no longer have any influence on the final cavity depth when the dimensions of the impacting body in the direction of motion and in the transverse direction become approximately the same.

It was shown in the preceding section that the obtained modeling curve (Figure 4.19) makes it possible to formally predict the result of collision of iron (steel) and aluminum (duraluminum) spheres with

a massive target of the same metal as the sphere for encounter velocities of 30 - 50 km/sec. Since these velocities exceed considerably $(3 - 3.5)a$, it is interesting to estimate how significantly the result of collision at the indicated velocities can differ from the value predicted using the modeling curve of Figure 4.19.

Unfortunately, we can present here only very general and purely qualitative arguments, which reduce to the following.

The thickness of the target metal layer located between the contact surface of the colliding bodies and the head wave will be close to the diameter of the impacting sphere [86]. During unloading, which will begin when the instantaneous cavity depth is approximately equal to the diameter of the sphere, part of this layer may be ejected from the cavity. It is quite obvious that this ejection for final cavity depth L_c , on the order of $(4 - 6)d_0$ (Figure 4.19), can lead to increase of L_c only by a few percent. /233

However, we must recall that ejection of the material is necessarily accompanied by removal of some energy, which under other impact conditions is, in the final analysis, expended on cavity formation. Hence, it follows that the possible slight increase of the final cavity depth, owing to target metal ejection from the cavity, will be partially or entirely compensated or even exceeded by the cavity depth reduction owing to energy removal.

Thus, these qualitative arguments lead to the conclusion that, for the processes taking place in the steady state (or quasi-steady state) flow regime, the estimate of the final cavity depth using the modeling curve of Figure 4.19, even for encounter velocities $V_0 > (3 - 3.5)a$, will be close to the actual collision result, and in any case will not be too low.

§ 4.8. Failure of Metal Bodies During "Short" Impact

The study of the first stage of deformable body dynamic interaction — the stage taking place in the unsteady regime — is particularly important, since it makes it possible to obtain interesting information on those laws governing the process due to wave phenomena and change of the thermodynamic parameters of the colliding body materials. An example of this are the results of study of the thermal effects presented in the preceding section. Therefore, it is advisable to examine in greater detail the characteristic features of the phenomena which arise in the massive metallic target during "short" impact, for example, during flat impact of a thin disk on the target surface (Figure 4.27a).

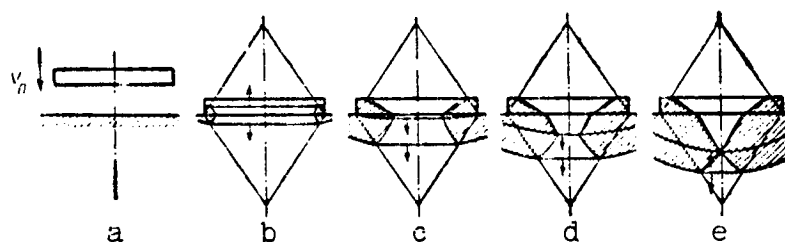


Figure 4.27. Schematic of wave processes arising during flat impact of a thin disk on a massive target [87]

At the instant of body encounter, there arise in both bodies shock waves, the mass velocities at the front of which are determined by the encounter velocity V_0 and the shock adiabats of the metals of the two bodies. At the same time, centered unloading waves arise along the contour of the contact surface of the bodies. As a result of this, the shock waves in both bodies will retain a plane front only within cones whose apex angle is equal to approximately $70 - 90^\circ$ [9, 25]. In the target and disk volumes, which undergo unload and are bounded by a toroidal surface (Figure 4.27b), the particles of both bodies acquire a radial (in relation to the disk axis) velocity component. At that instant when the shock wave propagating through

the disk reaches its free rear surface, a centered unloading wave also arises on this surface, and the unloading wave velocity vector will coincide with the velocity vector of the shock wave propagating through the target. In the disk and target volumes affected by this axial unloading (Figure 4.27c), the particles of both bodies will essentially lose their axial velocity component. Consequently, the metals of both bodies will be under the influence of tensile radial stresses in the volumes adjacent to this toroidal surface. We can expect that under certain body encounter conditions, the target and disk metals will experience failures under the influence of these stresses (Figure 4.27c - e)*. The cavity, whose formation is accompanied by fracture onset and opening, will obviously be characterized by a depth markedly exceeding the depth of the cavity which can be created in a target under the same impact conditions, but whose formation is not accompanied by fractures. /235

In the experiments of [87], conducted to verify this conclusion, the targets were massive blocks made from lead, lead-antimony alloy ($\sim 3\%$ antimony), cadmium, zinc, tin, and copper. The aluminum strikers were plane-parallel disks of diameter $d_0 = 15$ mm and height $l_0 = 4$ mm. These disk dimensions and selection of the cited metals for the striker and targets ensured quite short duration of the pulse experienced by the target (~ 1.5 μ sec), and maximal approach of the pulse to a Π shape (see, for example, [4], and also Figure 4.16).

As an example of the experimental data obtained, Figure 4.28 shows the results of the experiments with the tin and copper targets in the coordinate system "maximal final cavity depth L_c versus impact velocity V_0 ", and Figures 4.29 and 4.30 show photographs of axial sections of the typical cavities developed during impact in these same targets. In the experiments with targets of the other metals listed above, relations $L_c(V_0)$ analogous to those shown in /236

* Joint movement of the colliding bodies is not shown in Figure 4.27 in order to simplify the diagram.

Figure 4.28 were obtained, and the axial sections of the cavities in the targets made from these metals are similar to the sections of the cavities formed in lead (Figure 4.29).

It is not difficult to see that the experimental data are in good agreement with the results of the above analysis. In the case of interaction of bodies in the unsteady regime, beginning with some velocity which is unique for each target metal, cavity formation is accompanied by the onset and opening of fractures. The cavity depth changes abruptly at this velocity. It is essential to emphasize that fracture onset is independent of the massive block shape and size (if the latter is not less than some minimal dimension, naturally). This means that fracture formation is not associated with the unloading waves which arise on the side and back surfaces of the blocks.

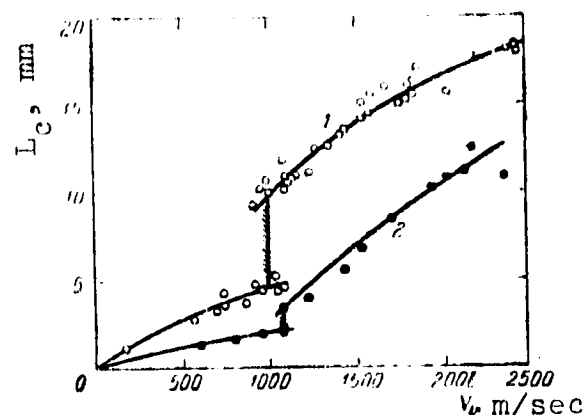


Figure 4.28. Dependence of finite depth of cavity L_c , produced in lead (1) and copper (2) targets in the case of a plane collision by a thin aluminum disc, on the encounter velocity V_0 [87].

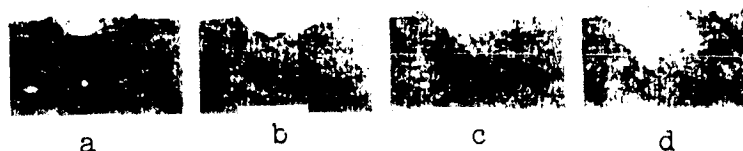


Figure 4.29. Sections of typical cavities obtain in massive lead target as a result of aluminum disk impact with encounter velocities: a) 920; b) 1000; c) 1130; and d) 1700 m/sec [87]

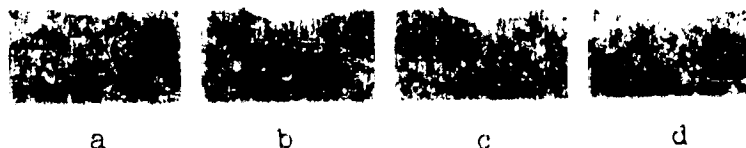


Figure 4.30. Sections of typical cavities obtained in massive copper target as a result of aluminum disk impact with encounter velocities: a) 960; b) 1440; c) 1540; and d) 1930 m/sec [87]

We need to examine some specific features of the cavities obtain in the experiments.

First of all, we note that, for impact velocities of 1.7 - 1.8 km/sec and higher, the cavities in the lead, tin, lead-antimony alloy, and cadmium targets have obvious traces of melting (Figure 4.29d). Since this effect was discussed previously (§ 4.7), there is no need to dwell on it here.

Next, we note the difference in the outlines of the cavities formed in lead (and also in lead-antimony alloy, tin, cadmium, and zinc), on the one hand, and in copper, on the other hand. Comparison of the cavities shown in Figures 4.29 and 4.30 leads to the conclusion that, in the first case, a conical volume of the target metal is ejected when the cracks open up, while in the second case, such ejection does not take place. This effect can be related with the difference between the disturbance propagation velocities in the disk and target metals. In targets made from metals with low sound speed in comparison with aluminum (lead, lead-antimony, tin, cadmium, zinc), for the selected disk dimensions the centered unloading wave, which arises on the free rear surface of the disk, will reach the contact surface of the bodies at an instant when the centered unloading wave arising along the contact surface contour has not yet encompassed the entire contact surface. Therefore, in the subject targets, in accordance with the scheme of Figure 4.27, some conical volume will be separated by the fractures. In copper targets, however, in which the sound speed is close to the sound speed in aluminum, at this instant nearly the entire surface will be encompassed by the unloading wave which arises along the contact surface contour. Therefore, the fractures in the copper target are located near the cavity axis and are approximately parallel to this axis. /237

In analyzing the experimental data obtained, it was shown [87] that the relations established in the experiments with the various targets correlate in the dimensionless coordinates $(\frac{c_0 U_1}{H_1}, \frac{L_0}{a_1 t_0})$, where a_0 , c_0 , and H_1 are, respectively, the sound speed in the target metal,

its density at normal pressure, and dynamic hardness; U_1 is the mass velocity, which characterizes the shock wave arising during body encounter in the target; and t_0 is the duration of the pressure pulse, determined by the ratio of twice the impacting disk thickness to the sound speed in aluminum. The possibility of modeling the described process is thereby shown.

The above problem naturally leads to formulation of the inverse problem — the problem of impact of a body of limited dimensions on a thin shield. While in the case of "short" impact, fractures (cracks) arise in the massive target, we would expect that, under certain conditions of encounter with a thin shield (Whipple problem [238] [88]), a body of limited dimensions would fracture completely.

It is not difficult to transform the scheme of Figure 4.27 to apply to the case of impact of the flat end of a cylinder on a thin shield. The scheme is proposed and analyzed in precisely this transformed form in [79]. On the basis of the analysis results, which are entirely analogous to the results presented above, the conclusion is drawn in [79] that, after encounter with a thin shield — as a result of interference between the loading and unloading waves, not only the cylindrical body, but also bodies of other form — spherical, for example — will fracture. [239]

Experiment confirms this conclusion well. Radiograms of the fracture of a cylinder and sphere after encounter with a thin shield*, analogous to the radiograms obtained in [79, 93], are shown in Figures 4.31 and 4.32.

We note the conical core which separates under the selected collision conditions during failure of the cylinder (Figure 4.31). The mechanism of the formation of such a core was explained above

* Experiments made by V. P. Valitskiy, N. A. Zlatin, and S. M. Mochalov.

In discussing the shapes of the cavities formed in massive lead targets under the action of "short" impact (Figure 4.29).

Analysis of the problem and the experimental data presented make it possible to consider that a thin shield located ahead of the target will lead to considerable reduction of the target damage parameters. Therefore, studies [79] were undertaken whose objective was to clarify what the shield thickness and its distance from the target should be for given impacting body material, shape, and dimensions, in order that the target damage parameters be minimal.

As an example of the data obtained, Figure 4.33 shows the results of experiments [79], in which the impacting bodies were aluminum spheres of diameter $d_0 = 3.2$ mm, and the targets were massive duraluminum blocks; duraluminum shields of different thickness δ were located at the distance $f \approx 51$ mm ahead of the targets.

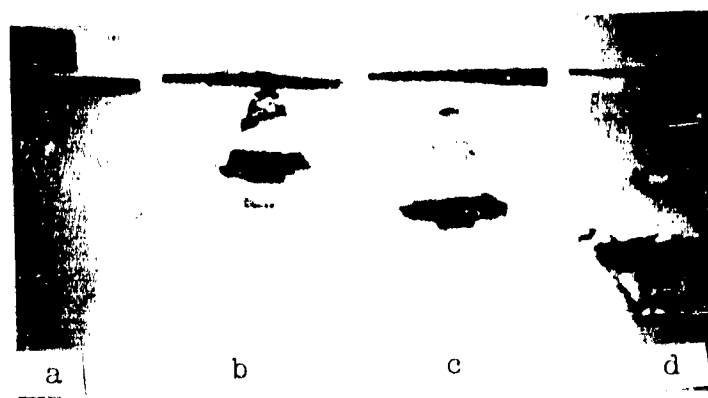


Figure 4.31. Sequential radiograms of copper cylinder ($d_0 \approx 15$ mm, $l_0 = 9$ mm) failing after collision with thin cadmium shield ($\delta = 0.8$ mm) with velocity $V_0 = 1.55$ km/sec: a) 2 μ sec prior to encounter; b) 17; c) 25; and d) 32 μ sec after encounter

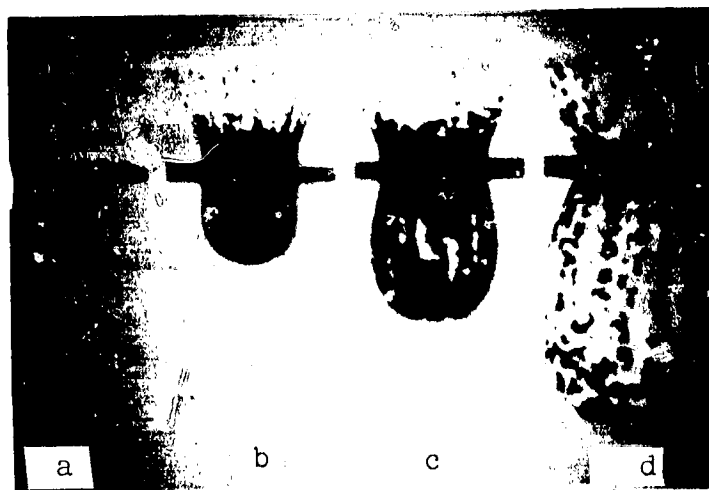


Figure 4.32. Sequential radiograms of lead sphere ($d_0 = 9.4$ mm) failing after collision with lead shield ($\delta = 4$ mm) with velocity $V_0 = 1.1$ km/sec: a) 7 μ sec prior to encounter; b) 25; c) 46; and d) 75 μ sec after encounter

The curves of Figure 4.33, and also the other experimental data [89 - 92, 94] indicate that:

a) other conditions being the same, use of the shield leads to very significant reduction of the damage depth L_c in the semi-infinite target [79, 88 - 91]; the damage is less, the higher the striker velocity [79];

b) between the shield and the target, the striker and target fragments travel within a cone with apex angle $\sim 60 - 80^\circ$ [89 - 91];

c) other conditions being the same, target damage is minimal if the distance between the shield and target $f \geq 5d_0$ [90];

d) other conditions being the same, the optimal shield thickness decreases with increase of the impact velocity V_0 , and at high velocities amounts to tenths of d_0 [79];

e) for impact velocities above the threshold value, when the striker metal and shield region ejected by the striker will melt or vaporize, the target depth will approach zero with increase of the velocity [79]; however, the impulse experienced by the target will have a finite value under these conditions, and increases with increase of the velocity [92, 94].

Thus, the data presented in this section, along with the data of the preceding section, have made it possible to identify very interesting behavior patterns of massive metal bodies and metal

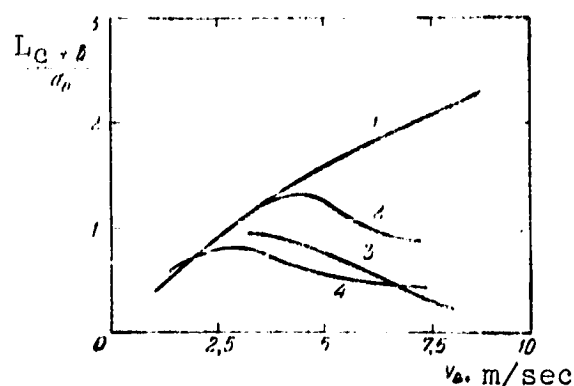


Figure 4.33. Damage to system "duraluminum screen δ thick — massive duraluminum target" ($f \approx 51$ mm) by aluminum sphere ($d_0 = 3.2$ mm) for various impact velocities: 1 — $\delta = 0$; 2 — $\delta = 0.13$ mm; 3 — $\delta = 0.40$ mm, and 4 — $\delta = 1.22$ mm [79]

bodies of limited dimensions under the action of a short-term impulse ("short" impact). It has been shown that these behavior patterns are determined primarily by the wave phenomena which arise in the colliding bodies during their encounter.

--	--	--	--	--	--	--	--	--

CHAPTER V

AEROBALLISTIC INVESTIGATION METHODS

§ 5.1. Preliminary Remarks

In spite of the fact that wind tunnels are the basic tool for studying supersonic aerodynamics, the aeroballistic research methods have taken on increasing importance in recent years. The ballistic method is used with particular success in modeling transonic and hypersonic flight velocities, and also when the presence of supports is not permissible (wake flow, base pressure, and so on).

/241

Tests using free-flying models have required the development of unique specific techniques which differ fundamentally from the wind tunnel techniques. For example, aerodynamic forces are determined in the wind tunnel by direct measurements, while in the ballistic experiment the aerodynamic forces are determined indirectly. Therefore, the technique for determining the aerodynamic coefficients from the flying model trajectory parameters constitutes an independent branch of ballistics. In the last two decades, experimental ballistics has advanced considerably. A large number of ballistic stands have been constructed in which flight of various flight vehicles has been simulated over a wide range of altitudes. Here, it became possible to alter M and Re independently. Aeroballistic tunnels have appeared in which the wind tunnel testing technique is combined with the ballistic experiment technique.

At the present time, the aeroballistic method is widely used to study aerodynamic and aerophysical characteristics on models of various flight vehicles.

In the present chapter, we examine various aspects of the aeroballistic experiments: the operating principle and construction of the experimental facilities, experiment planning, technique for 7242 determining aerodynamic characteristics, the simulation region, and also the results of some studies.

Because of the diversity of the material, it is not possible to examine in detail all of these questions within the space of a single chapter. Some of the questions are covered in greater detail; others are covered rather lightly. Therefore, the material of this chapter should be considered only an introduction to the aeroballistic experiment techniques.

§ 5.2. Characteristics of the Ballistic Method of Aerodynamic Investigation

Wind tunnels are the classical tool of experimental aerodynamics. In many laboratories, wind tunnels have been and are being used to study the aerodynamic characteristics of airplanes at both subsonic and supersonic speeds. However, the development of rocket and space technology has presented experimental aerodynamics with a new task — study of the laws governing the motion of bodies at hypersonic speeds. For many reasons, the use of wind tunnels for the solution of this problem involves serious difficulties.

One such factor was the need for creating extremely high working gas pressure differentials. For example, when creating an air stream with $M = 20$, the losses in the tunnel chamber are so large that the ratio of the pressure at the tunnel entrance to the pressure at the exit must be on the order of a million. In this case, it is necessary to maintain in the forechamber a high absolute air pressure, reaching hundreds and even thousands of atmospheres, in order that

the flow in the tunnel working section not be excessively rarefied and the flow conditions not correspond to very low Re .

A second factor is the necessity for preheating the air in order to avoid condensation of the air or of its components, because of the considerable cooling during expansion in the nozzle. For example, air flowing through a nozzle at $M = 20$ must be preheated to about $3000^\circ K$.

The new practical problems have led to the development of such experimental facilities as the pulse, shock, and adiabatic tunnels and the ballistic ranges.

The basic difference between experiment in ballistic ranges and experiment in wind tunnel is that, in the first case, the model is launched and is in free flight, while in the second case the model is mounted on supporting devices in the tunnel working section.

This fact gives rise to almost complete difference in the technique for determining the aerodynamic coefficients, the experimental methodology, and the equipment used. Each of these experimental methods has its own particular characteristics and its particular drawbacks, so that they do not in any way exclude, but rather complement, one another. /243

The primary advantage of ballistic ranges for studying flight at hypersonic speeds lies in the possibility of simulating the actual stagnation temperatures (enthalpies), since at hypersonic speeds the stagnation temperature becomes just as important a simulation parameter as M and Re .

In addition, we can vary M and Re comparatively easily in the ballistic ranges, and it is easy to realize large Re at high M .

At supersonic flight speeds, the Reynolds numbers in the ballistic ranges have larger values than in wind tunnels, even for very

small model dimensions. We also note that the model motion in experiments in ballistic stands takes place in an undisturbed gas with precisely known parameters.

The ballistic method provides a comparatively simple means for obtaining hypersonic speeds. Even with the use of powder guns with initial velocity 2000 m/sec, when firing into stationary air, Mach numbers of 5 - 6 are reached, and when firing into a supersonic stream with $M = 2 - 3$ (without preheating), it is very easy to obtain $M \sim 15$.

In order to obtain this M in a wind tunnel, it is necessary to preheat the air to 2500°K and provide an air compression ratio on the order of 10^6 .

The disadvantages of the ballistic method include the following. The model is usually destroyed after each firing, and it is more difficult to ensure the desired angular position of the model in space than when using the wind tunnel. The forces and moments acting on the models are determined by calculation from the trajectory measurement data. Because of the small model dimensions, it is difficult to locate the instrumentation within the ballistic model.

The essence of the aerodynamic ballistic experiment reduces to recording by some method or other the flying model coordinates continuously or at sequential discrete points along the trajectory. The resulting dependences of the model center-of-gravity coordinates and angles of attack on time or longitudinal coordinate are the basic data for calculation of the aerodynamic coefficients.

In spite of the considerable variety of ballistic range configurations and designs, they are basically constructed using the same principle, and consists of a powder or light-gas launcher which imparts the required initial velocity to the models, and the instrumented segment in which the model flight space-time parameters are recorded. These segments differ in construction and dimensions in the various ballistic ranges; their length may be from several

kilometers to one meter. The facility may be a test range of the open type, the barochamber of a ballistic stand, or the working section of a wind tunnel or shock tube with a nozzle.

Systems for decelerating and catching the models are located at the exit from the instrumented ballistic range segment.

The availability of a high-velocity launcher is not in itself a sufficient condition for the realization of ballistic experiments. It is necessary that the models not be damaged or deformed during acceleration in the barrel chamber. When conducting aerodynamic studies, it is also necessary that the model travel along a specified trajectory, and in this connection it is necessary in certain cases to impart to the model a definite angular orientation at the exit from the barrel channel.

Various technical model firing techniques have been developed in order to satisfy these requirements. When designing and constructing the models, we must consider the necessity for ensuring model strength and stability in flight.

For illustration, Figure 5.1 shows a photograph of model specimens used for aeroballistic tests.



Figure 5.1. Various model shapes for aeroballistic tests.

Extremely large load factors, whose magnitudes must be known when designing the models, act on the model at the moment of firing.

Taking for the analysis the simplest law of motion with constant acceleration, we have the following connection between the acceleration A , velocity V , and barrel length l :

$$A = \frac{V^2}{2l}. \quad (5.1)$$

Thus, the acceleration at the instant of firing will be defined by the square of the model velocity at the barrel exit. The greater the barrel length, the lower is the model acceleration for the same initial velocity. In reality, because of the fact that the acceleration in the barrel is not constant, its maximal value will always be greater than the value calculated using (5.1). In practice, the model accelerations during firing reach several hundred thousand, and even several million, times the free-fall acceleration g .

The following condition must be satisfied to assure model integrity during firing: the stresses arising in the model because of its acceleration must be in the model material strength limits. Experience shows that models deform or fail when the stresses in them exceed the allowable static stresses. Damage to the base of the model is most frequently encountered. As an example, we shall consider the case when a conical model accelerating along its axis is made from homogeneous material:

$$A = \frac{3\sigma}{l\rho_m}. \quad (5.2)$$

The acceleration at which damage occurs depends on the cone length l and the ratio of the allowable stress σ to the material density ρ_m . Figure 5.2 shows the limiting allowable acceleration as a function of cone length and the model material used. We see that the MA-4 magnesium alloy is the most suitable material.

For a cone 25 mm long, failure occurs at a load factor exceeding $2 \cdot 10^6$. The models may fail at even lower accelerations —

for example, because of local loss of stability, poor quality of the barrel inner surface, and so on.

As for aerodynamic stability, to ensure stability, the model center of gravity is shifted forward by locating ballast in the nose of the model or lightening the aft segment. When designing the models, it is necessary to maintain definite relationships between the aerodynamic forces and the model moments of inertia.

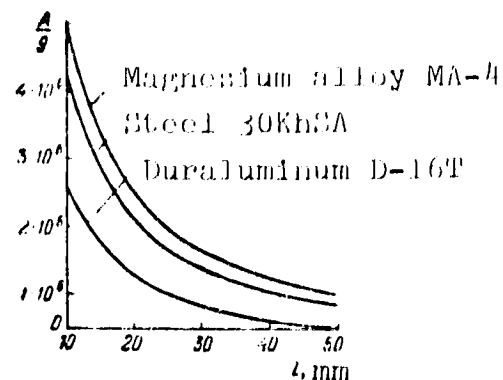


Figure 5.2. Limiting allowable load factor versus cone length

In order to prevent model failure during its travel in the barrel bore, the models are made somewhat smaller in diameter than the barrel and are inserted into protective casings, termed sabots.

The sabots are usually made from quite strong and light materials, such as resin-impregnated plywood, kapron, polyethylene, and aluminum alloys. Figure 5.3 shows a typical polyethylene sabot intended for launching small-caliber models. Polyethylene is easily stamped; because of its plasticity, it may smooth somewhat the action on the model of the acceleration peaks, and it seals the launch gases well. In order to facilitate separation of the models from the sabots, the latter are made from two halves with a transverse locking device.

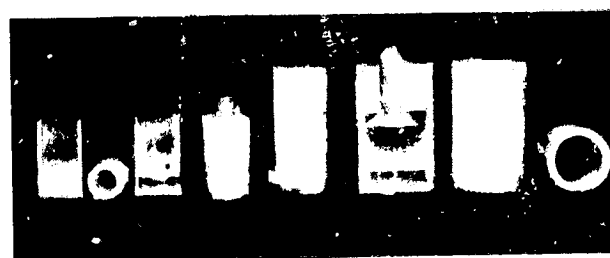


Figure 5.3. One technique for loading model into cartridge using sabots

quite varied sabot types are used, whose shape and construction are determined by the model configuration and the test program. For example, "suction" sabots have been used. In this case, the model

is mounted on the end surface of the cylindrical sabot, and slots between the sabot and the model are sealed tightly. The air is removed from the space between the model and the sabot through a hole in the sabot. Then the hole is sealed by a special plastic. During firing, the plastic bursts, and the powder gases enter the cavity between the model and the sabot. At the muzzle, the gas pressure aids in separating the model from the sabot. The sabot of this type operates reliably, and withstands transverse load factors up to 10.

For measurement of the drag coefficient at zero angle of attack, it is desirable to have a sabot design which will permit separation of the sabot from the model with minimal influence on the latter. In this case, the model is not disturbed, and travels along a practically rectilinear trajectory.

Perturbed model motion is required in order to determine the lift and pitching moment coefficient, and in order to ensure high accuracy, it is necessary that the plane in which the model oscillatory motion takes place not rotate. Figure 5.4 shows a typical recording of model angle-of-attack and center-of-gravity variation as functions of time for the two-dimensional oscillatory motion case. Such trajectory measurement data serve as the basis for obtaining

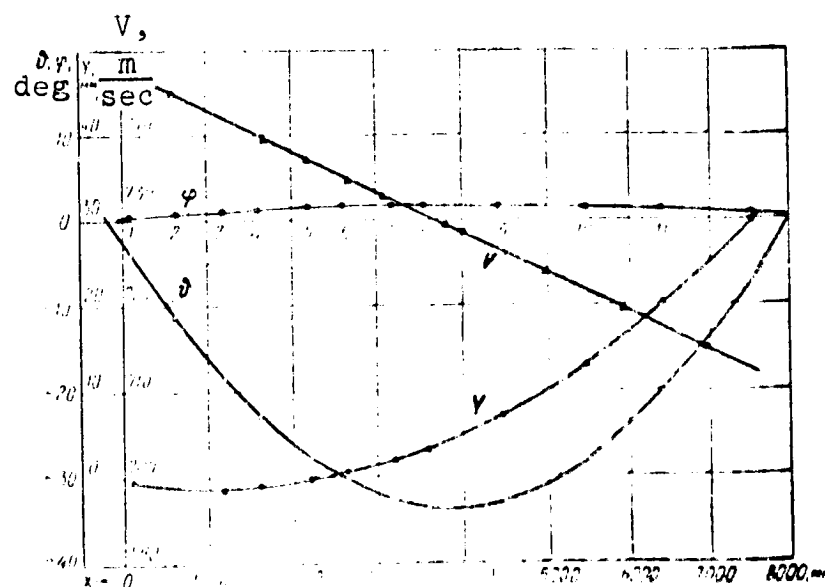


Figure 5.4. Typical recording of two-dimensional oscillatory model motion parameters

the aerodynamic coefficients. Figure 5.5 shows a typical recording of three-dimensional oscillatory motion in the coordinates: angle of attack α and sideslip angle β . The technique for determining the trajectory parameter of flying bodies was discussed in § 3.5.

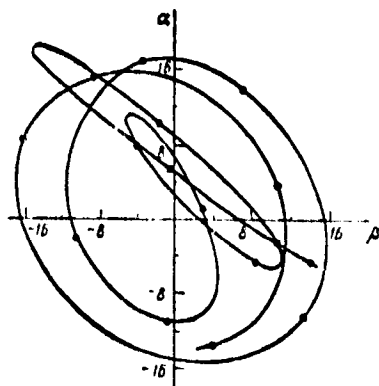


Figure 5.5. Typical three-dimensional model motion recording

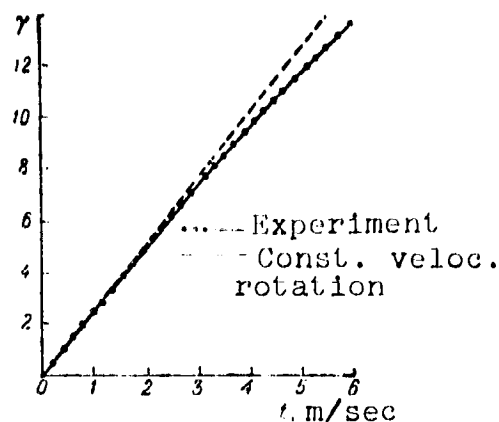


Figure 5.6. Typical recording of model roll angle variation with time

Either sabots in which the model is installed at an angle to the barrel axis, special devices in the form of asymmetric attachments on the muzzle which disturb the model motion, or other techniques are used to give the model an initial angle of attack.

Figure 5.6 shows a recording of angular rotation in roll of a finned projectile model. These data were obtained by analyzing the results of high-speed cinematography, conducted from the end section of the model.

These examples show that the aeroballistic experiment involves determining the time-varying trajectory parameters of the model being studied. The forces which give rise to this motion (or the sought aerodynamic coefficients) are then calculated using the expressions relating the motion characteristics with the aerodynamic characteristics. Sections 5.6 and 5.7 are devoted to finding these expressions.

Thus, in general, in the ballistic investigation method, we solve the first dynamics problem — determining the forces acting

on the model from the given motion. After obtaining the aerodynamic coefficients from the model experiment, we can solve the second dynamics problem — finding the full-scale vehicle motion for the corresponding flight conditions.

§ 5.3. Ballistic Stands

The ballistic stands in their present-day form stem from the artillery ranges. Usually, the open range scheme included three basic elements: the firing system, the instrumented range — whose length could reach several kilometers, and the system for catching the projectiles (butt, deflection plate, and so on) [1].

/249

However, the difficulties associated with conducting experimental studies under various weather conditions, particularly with use of the electron-optical equipment developed in recent years, have forced us to seek other solutions when designing experimental ballistic ranges. Enclosed ranges have been constructed in which the instrumented range or all the component elements of the facility are located in a special building (Figure 5.7). The length of the buildings used for the enclosed ranges reaches several hundred meters, several dozen instrument stations are used, and the caliber of the guns used reaches 150 mm.



Figure 5.7. Building housing Aberdeen Proving Grounds enclosed ballistic range, intended for studies at transonic flight speeds

Figure 5.8 shows a photograph of a ballistic range for operation at atmospheric pressure, located inside a building. The range length is 150 m, width — 12.2 m, height — 9.45 m.

The arrangement of the typical instrumentation station equipment is seen in the photo. Flight of the models along the range is photographed sequentially every 1.5 m by special photocameras, positioned so that the adjacent station

fields overlap. During passage through the viewing field of each photocamera, the projectile is photographed six times, and six silhouette images of the flying model are obtained on each photographic plate. Analysis of the photos on comparators makes it possible to determine the model center-of-gravity coordinates and the location of its axes in space. From these data, we calculate the aerodynamic characteristics of the model.

Since the air pressure and temperature in such ranges are practically constant, the Reynolds number will be a function of the flight speed, and can be varied by

varying the model size. Consequently, for given M , the Re can be varied essentially in the limits of one order of magnitude.

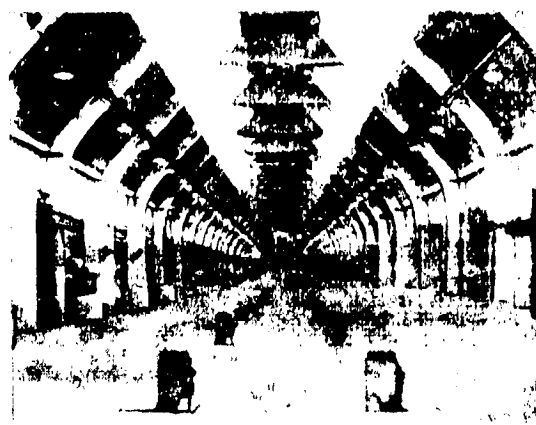


Figure 5.8. Interior view of NOTS ballistic range

Table 5.1 shows the data for several research ranges [2, 3].

More advanced research facilities — ballistic stands — have been developed in order to broaden the experimental capabilities. The essence of the improvement lies in the fact that the segment in which recording of the model trajectory parameters is carried out is enclosed in a sealed chamber. A photo of such a facility can be seen in Figure 5.9.

The use of barochambers makes possible considerable expansion of the ballistic experiment limits of the experimental capability. By altering the pressure in the barochamber from several atmospheres to hundredths of an atmosphere, it is possible to vary Re in wide limits, and simulate flight conditions at various altitudes. Use of the barochamber also makes it possible to conduct experiments in an atmosphere of various gases or gaseous mixtures.

/250

/251

TABLE 5.1. DATA OF SOME FOREIGN RESEARCH RANGES

No.	Organization	Constructed	Length	Section	Additional data
1	Aberdeen	Before 1959	87 m	-	50 instrument stations
2	Aberdeen	Before 1959	305 m	6.7x6.7 m	-
3.	NOL	Before 1957	150 m	12x9.5 m	127 mm, 76 mm, 40 mm calibers
4	Canadian Westinghouse	Before 1958	229 m	-	76 mm caliber
5	DTMA	Before 1955	111 m	6 x 5 m	-
6	CARDE	Before 1958	230 m	6 x 6 m	-

In ballistic stands which are somewhat more complex in construction, both the gas pressure and temperature are varied.

Figure 5.10 shows a typical ballistic stand with barochamber. For operating convenience, the model launcher is usually located outside the barochamber. A vacuum chamber (sometimes termed a receiver or silencer) is installed between the launcher and the barochamber. Its basic functions are to suppress the shot noise and block the driver gas. In this chamber, the model separates from the sabot, and the sabot pieces are trapped by special devices (Figure 5.11), usually a set of diaphragms. In the silencer of more complex construction, a local chamber with elevated air pressure is installed in order to strengthen the effect of sabot separation from the model.

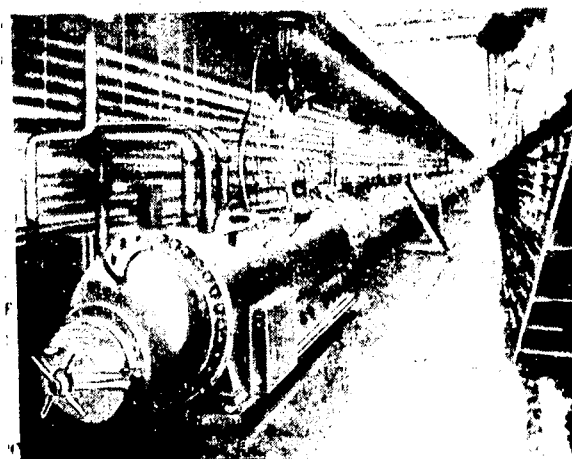


Figure 5.9. Barochamber of NOL ballistic stand

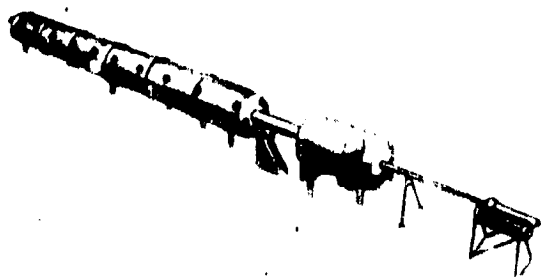


Figure 5.10. Mockup of AEDC ballistic stand

In order to provide the desired conditions in the barochamber, the silencer is separated from the chamber by a film diaphragm (for example, a cellophane film) which does not offer significant resistance to model flight. If the pressure differential across the diaphragm is large — and it must be made quite thin, several diaphragms are used, between which stepwise varying gas pressure is established.

The barochamber, in which the model motion studies are made, has an elongated form with suitable number of optical windows for model photography and installation of the synchronizing and measuring equipment. The chamber cross section is usually circular or rectangular. Sometimes, internal positioning of the equipment, installed in special pressure-sealed pockets, is used. The barochambers are equipped with fittings for connecting vacuum pumps to evacuate the chamber, or compressors to create excess pressure, and also a system for gas supply and mixing of gases for conducting experiments in media simulating the atmospheres of the various planets.

Figure 5.12 shows a ballistic stand for physics research, operated by General Motors. In addition to measurements of the flying model trajectory parameters, this stand is used to make measurements of the intensity of the luminous radiation behind the bow wave, gas ionization behind the shock wave and in the wake behind the model,



Figure 5.11. Separation of model from sabot after exit from launcher system barrel. Model flies through frame-target, breaking the wires

and thermal fluxes to the model. The stand also has a special compartment for radar measurements.

A bunker is installed at the end of the barochamber to catch the models. The bunker is packed with retarding materials (plastic foam, rubber, fiber packing, and so on) and terminates in an armored plate.

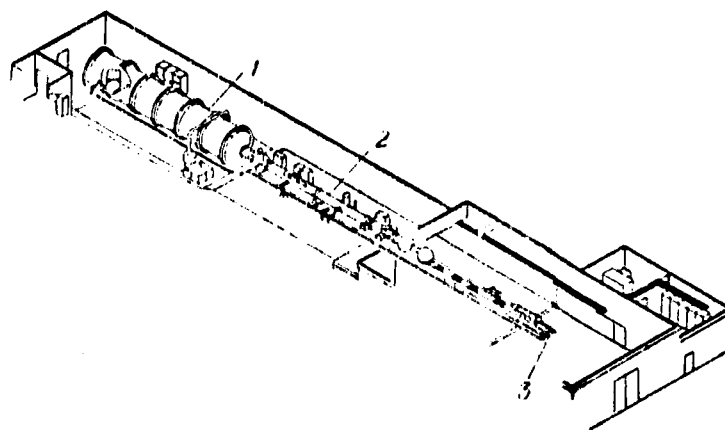


Figure 5.12. Schematic of GM ballistic stand for physics studies:

1 — radar chamber; 2 — working section; 3 — gas gun used to launch the model

Depending on the research objectives, the barochamber length varies from several meters to several hundred meters. Table 5.2 shows the data for several ballistic stands.

The need for the construction of large stands (length up to 300 meters) is indicated by the fact that, when conducting experiments in rarefied gases, the influence of the medium on variation of the model flight trajectory decreases. Therefore, in order to obtain significant changes in the trajectory, as a result of which it is possible to determine the aerodynamic characteristics, long hermetic chamber lengths are required.

Figure 5.13 shows a photo of the giant NOL ballistic stand in the process of construction.

We shall consider, as examples, two ballistic stands of the A. F. Ioffe Physico-Technical Institute of the AN SSSR. The first stand [4] has comparatively small dimensions, and consists (Figure 5.14) of a launcher, shot silencing chamber with attachments for model sabot separation, and also the pressure-sealed instrumented working chamber.

TABLE 5.2. DATA ON SOME FOREIGN RESEARCH BALLISTIC STANDS

No.	Organization	Constructed	Length	Section	Additional data
1	NOL, White Oaks	Before 1957	100 m	0.96 m	25 instrumentation stations. Calibers 20 mm 40 mm. Gas guns. Muzzle velocity to 5 km/sec
2	NOL Silver Spring	Before 1959	300 m	3.05 m	25 instrumentation stations. Caliber 100 mm. Gas gun. Muzzle velocity 3.5 km/sec
3	NOL, Silver Spring	1959	108 m		Working chamber filled with various gases and their mixtures
4	Ames	Before 1956	61 m	0.45 x 0.45 m	Gas (helium) guns 6 mm; muzzle velocity 5 km/sec
5	Ames	Before 1959	152 m	2.4 m	Gas (helium) guns 61 m long — model 19 mm, weight 10 g, muzzle velocity 7 km/sec
6	Aberdeen	1957	13.7 m	0.76 m	5 instrumentation stations. Stand with temperature variation from -188 to +127° C. Calibers, 7.6 mm, 12.7 mm, 19 mm; muzzle velocity 3.6 km/sec
7	Convair	1960	152 m	2.4 m	Caliber 76 mm, gas gun 20 m long. Muzzle velocity to 7 km/sec
8	AEDC	Before 1959	32 m	1.8 m	Used to develop equipment and gas guns

(Table continued on following page)

TABLE 5.2. (continued)

No.	Organization	Constructed	Length	Section	Additional data
9	AEDC	1960	305 m	3.05 m	Gas gun, caliber 15.8 mm; muzzle velocity to 8 km/sec
10	NOL, Washington	1961	22.5 m		16 instrumentation stations, gas gun, caliber 7.6 mm, muzzle velocity 6.8 km/sec
11	CARDE		18 m	0.61 m	Caliber 12 mm

The launcher 1 is a revolver-type mechanism on which four barrels from 16 mm to 32 mm caliber are installed simultaneously. The barrel caliber required for the given test is selected by rotating the drum. The drum mounting makes it possible to displace the drum in the longitudinal and transverse directions relative to the range centerline, and also permits varying the elevation and azimuth angles. Firing is controlled from the console 3. The triggering mechanism of the guns 2 operates automatically after opening of the photo cassettes 13, which are mounted on the barochamber and are controlled by a pneumatic drive.

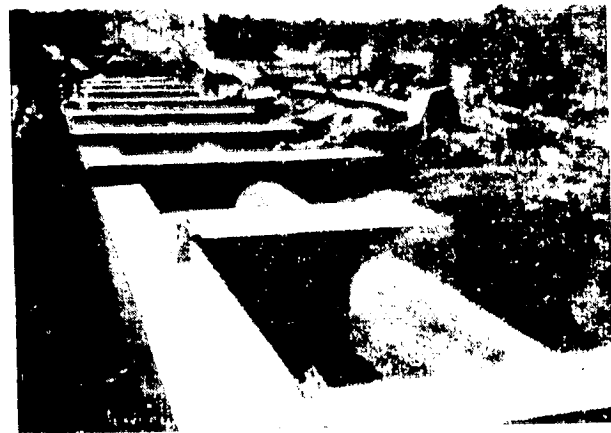


Figure 5.13. Giant NOL ballistic stand under construction

Equipment located in the region where the model separates from the sabot makes it possible to shield the photoelectronic instruments and photo materials from the flash during firing, and also serves for catching the sabot fragments and components.

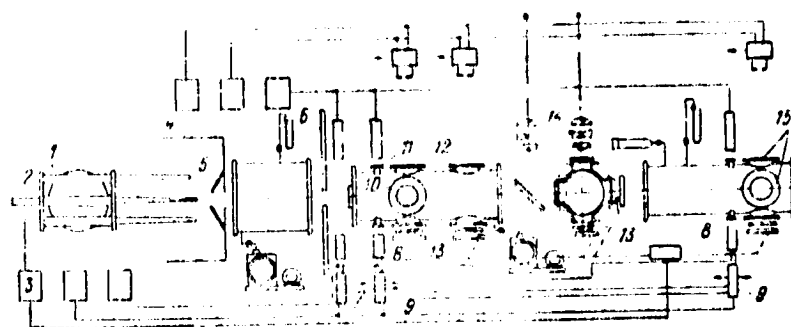


Figure 5.14. Schematic of ballistic stand at the A. F. Ioffe Physico-Technical Institute of the AN SSSR

On the shielding board 4, there are installed adjustable shutters 5 which actuate under the influence of the gases escaping from the barrel, and thus block part of the combustion products. After passing the shutters, the model and pieces of the sabot enter the pre-evacuated shot silencing chamber. The ports at the entrance to and exit from the shot silencing chamber are covered with an easily ruptured film. When necessary, the shot silencing chamber can be hermetically connected to the launcher barrel and to the stand working chamber. Downstream of the silencer is located the armored plate 6, which protects against fragments ricocheting from the edges of the opening in the shot silencing chamber flange.

The hermetically sealed working chamber is a steel tube consisting of eight sections. The section inner diameter is 300 mm, and the length of each section is one meter. The sections have ports 12 through which the flying models are photographed in a transmitted light beam. The ports are covered by plane-parallel optical glasses with rubber seal and rubber shock absorbers on the clamping flange side. Two ports 11 in each section, in the form of narrow slots, permit passage of a narrow light beam to the photoelectronic multipliers 8 which control the electronic synchronizing apparatus 7, 9. When it is necessary to vary the pressure or composition of the gas in the working chamber, its end flanges are sealed by nonmetallic diaphragms.

/256

Two pairs of horizontal windows and one pair of vertical windows 10 are located in the first four sections of the working chamber. A pair of horizontal windows and a pair of vertical windows 15 are located in the following sections. Thus, twelve photographs of the projection of the flying model on the vertical plane and eight on the horizontal plane can be obtained on the stand.

The stand is equipped with shadow instruments 14 with parallel light beams and cassettes 13, mounted directly behind the glass flanges which seal the chamber ports, or at twice the focal length from the auxiliary objectives.

Mercury thermometers and manometers are used to measure the parameters of the gas in the chamber. During filling of the chamber with the gas, measurements are made of the gas density by the pycnometric method, and the sound speed is measured using an acoustic interferometer.

Sequencing of all the operations when conducting the experiment is provided by automatic controls located at the firing console 3.

The large ballistic stand described in [5] has a barochamber 18 m long and 1 m in diameter (Figure 5.15). The model is photographed at fourteen sections uniformly spaced along the length in two mutually perpendicular directions. The maximum launcher caliber is 83 mm, and the pressure in the barochamber can reach 5 atm.

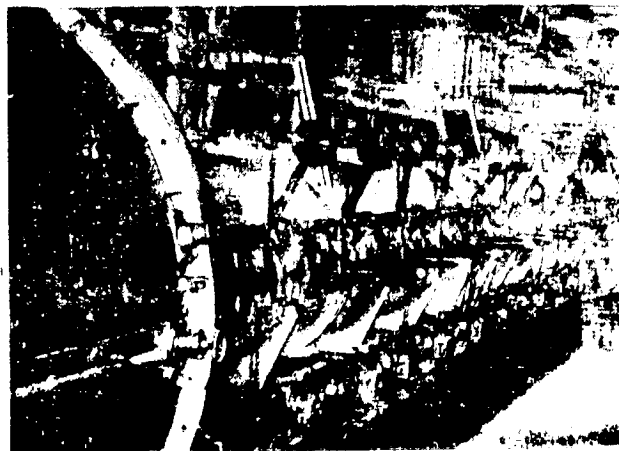


Figure 5.15. Barochamber of ballistic stand at the A. F. Ioffe Physico-Technical Institute of the AN SSSR

1258

The stand is configured with internal arrangement of the equipment for recording model passage and photography. This configuration creates certain difficulties in servicing the facility and requires equipment protection from damage by the sabot fragments and the model; however, it avoids the necessity for using protective glasses of large diameter and thickness, which are capable of withstanding the large pressure differentials.

Table 5.2 presents data on some foreign ballistic stands [2, 3].

§ 5.4 Aeroballistic Tunnels

The next step in ballistic experiment technique development was the appearance of the aeroballistic tunnels. Their operating principle is based on firing models into an opposing supersonic stream. In this case, the wind tunnel working section is used as the segment in which the measurement are made. The appearance of aeroballistic tunnels was the result of the need for experimental facilities which would permit determining the aerodynamic characteristics of models at hypersonic speeds. Prior to the appearance of the light-gas launchers using powder drive systems, it was possible to obtain in practice an initial velocity on the order of two km/sec. This provided $M = 5 - 6$ on the ballistic stands. In the aeroballistic tunnels using the same powder launchers, it was possible to obtain resultant Mach numbers of $M \sim 15$. Thus, at the expense of complicating the experimental facility configuration, it was possible to increase the Mach number by a factor of two to three. /259

In this section, we shall examine various aeroballistic tunnel schemes based on launching models into an opposing supersonic stream.

The simplest facility is the aeroballistic tunnel for determining model drag coefficients and the flow pattern around models [6]. Because of this narrow objective of the facility, it can be constructed with minimal dimensions. Thus, the length of the segment in which the model motion parameters are recorded is 1200 mm, and the maximal caliber of the models tested is 15 mm. Three

instrumentation stations — the minimal possible number for determining the drag coefficient — are located along the model trajectory.

Figure 5.16 shows a schematic of this aeroballistic range.

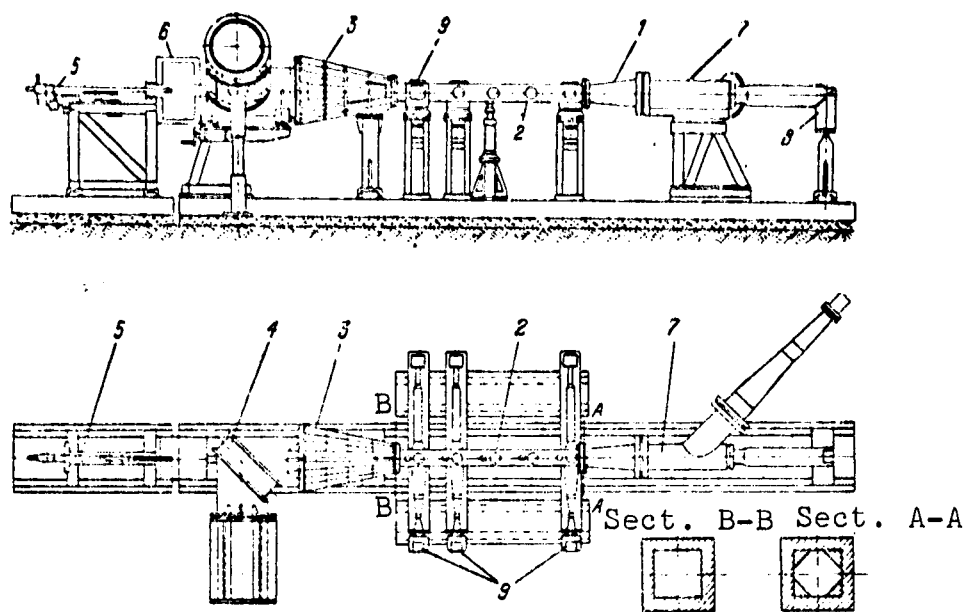


Figure 5.16. Schematic of aeroballistic tunnel designed for measuring drag coefficients

The opposing stream is created in an intermittent operation supersonic wind tunnel. The tunnel is equipped with three interchangeable nozzles 1 with flow Mach numbers $M_F = 2.5, 3.0, \text{ and } 3.5$, and exit section diameter 74.5 mm. Thanks to the use of high-pressure (to 100 atm) compressed air, it was possible to construct a tunnel for measuring C_x with short working section 2 length (1800 mm). Deceleration of the air stream is accomplished in the subsonic diffuser 3, and the air is exhausted through the pivoting elbow 4 and ducting into the silencer shaft. Powder and light-gas guns of 15 mm caliber are used as the launchers 5. The launchers are located outside the supersonic tunnel in order to provide easy access to them and operating convenience. The launchers are installed on recoilless mounts which permit precise regulation for aiming. A vacuum chamber 6 is located between the launcher and the wind tunnel in order to attenuate the shot noise and block the sabots.

One of the characteristic features of the aeroballistic tunnel used for measuring drag coefficients is its supersonic nozzle 7, developed by O. S. Vorob'ev, whose section has the form of a regular octahedron. A characteristic drawback of all aeroballistic tunnels is the very small dimension of the supersonic nozzle throat through which the model must pass. Because of this, it was not possible to use two-dimensional nozzles, which would have had a slot at the throat. For equal throat area, the regular octahedron shape is preferable from the viewpoint of model passage through the throat. With diameter of the inscribed circle at the nozzle exit equal to 74.5 mm and $M = 2.5$, the diameter of the inscribed circle at the throat is 44 mm and, for $M = 3.5$, this diameter is only 27 mm. The nozzle section in the form of a regular octahedron is also convenient for another reason. A characteristic feature of the aeroballistic ranges is the long relative length of the tunnel working section. It reaches several tens of calibers. At these lengths, the boundary layer on the tunnel walls has a significant influence. With increasing boundary layer thickness, the area of the section occupied by potential flow decreases, and therefore the flow Mach number decreases along the working section length. /260

In order to ensure constant Mach number along the working section length, it is necessary to provide boundary layer compensation by increasing the working section area along its length 2. When using a nozzle with octahedral cross section, compensation is accomplished by reducing the diagonal faces of the octahedron with gradual transition from the octahedral section to a square (see section A-A and section B-B in Figure 5.16). In this case, the side walls and upper and lower walls 9 of the working section remain pairwise parallel, which is very convenient for locating the horizontally and vertically positioned optical shadow instruments. /261

Figure 5.17 shows the Mach number distribution along the working section length of an aeroballistic tunnel without compensation, and after use of compensation.

Still another characteristic feature of the aeroballistic range is the method used to catch the models. With a model flight speed of several thousand meters per second, they may cause severe damage when striking an obstacle. Compressed air is used in the fore-chamber '7 to provide considerable model deceleration, and the fore-chamber is specially elongated for this purpose. As a result, the models decrease their velocity by 5 - 10 times prior to striking the deflector 8.

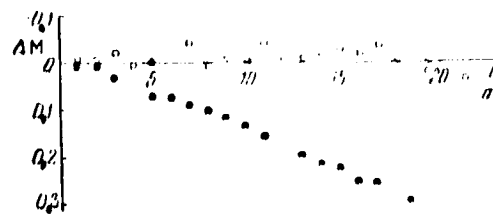


Figure 5.17. Influence of boundary layer compensation on Mach number along aeroballistic tunnel working section length:

- — without compensation;
- o — with compensation

Along the tunnel working section, there are located three instrumentation stations 9, which consist of a complex of electronic and optical apparatus for shadow photography, synchronization, and time measurement.

The basis of the instrumentation station is a schlieren instrument with 70 mm field, through which the model shadow spectra are photographed. Reference points are located in the photographic field so that it is possible to measure the model coordinates (to within 0.1 - 0.2 mm) from the picture. Photography is accomplished with the aid of a flashlamp, with exposure time 0.2 μ sec. Synchronization is provided by a light beam located in the camera field and directed onto a photocell. The signal from the photocell triggers the flashlamp without a delay line. The time between photographs is measured by an electronic chronometer to within 0.25 μ sec.

/262

Figure 5.18 shows the apparatus near the working section of the aeroballistic tunnel. Figure 5.19 shows a schematic of the instrumentation of an aeroballistic tunnel used to measure drag coefficients.

After the wind tunnel reaches the specified operating regime, the pressure on the working section wall is measured, and the model is launched. As the model passes through the working section 1, it sequentially crosses the light beams of the photo recording systems 2 of the three stations. The signal which appears in the photodetector 3 as the model

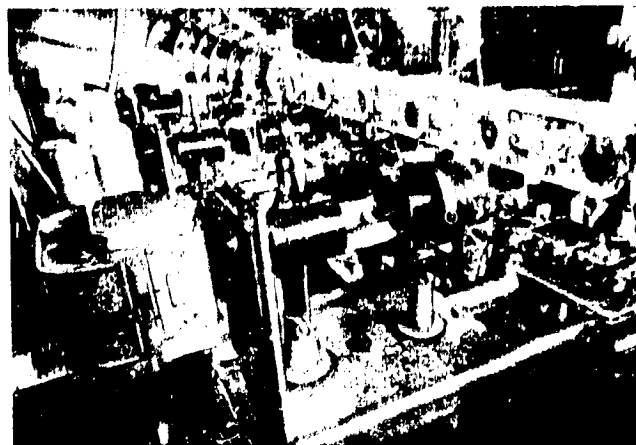


Figure 5.18. Arrangement of equipment at working section of aeroballistic tunnel used to measure drag coefficients

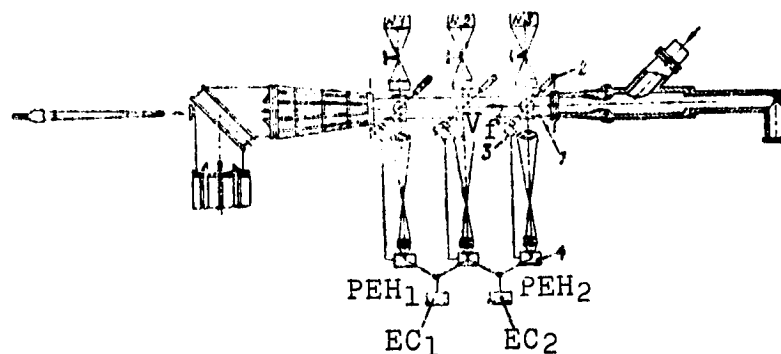


Figure 5.19. Arrangement of instrumentation of aeroballistic tunnel used to measure drag coefficients

crosses the light beam travels by cable into the unit which controls the spark light source 4. A light flash takes place, and the model is recorded on the first station photocamera N1. At the same time, the spark source light pulse strikes the photoelectric head PEH_1 , consisting of the STsV-4 vacuum photocell and a cathode follower. The electrical signal of the photoelectric head triggers the first electronic chronometer EC_1 . The second station operates similarly to the first with the sole difference that, at the same time the first chronometer is stopped, the second is started, and the second is stopped by the flash of the light source at the third station.

In an aeroballistic tunnel of approximately an order of magnitude larger size [7], in addition to drag, it is possible to measure several other aerodynamic characteristics: lift and pitching moment coefficients, rotary derivative coefficients and so on. Figure 5.20 shows a schematic of this aeroballistic tunnel. It is similar in operating principle to the

/263

aeroballistic tunnel described above. However, there are definite differences in the construction. An intermittent operation wind tunnel with rectangular working section 0.51 x 0.43 m and length 7.3 m is used. The tunnel is equipped with two supersonic $M = 2$ and 3 two-dimensional nozzles. The flow is created by air coming from a forechamber 4.8 m long at 6 - 9 atm pressure.

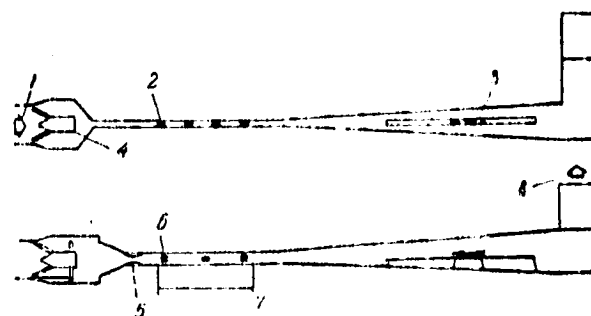


Figure 5.20. Ames Laboratory aeroballistic tunnel [USA]:

- 1 — compressed air; 2 — vertical optical stations; 3 — launcher; 4 — model catcher; 5 — supersonic nozzle; 6 — horizontal optical stations; 7 — working section; 8 — exhaust to the atmosphere

The model catcher, consisting of a 0.75 m-diameter steel cylinder 2 m long, which is tightly packed with fiber packing, is located in the forechamber. The launcher is located in the subsonic diffuser of the tunnel.

The dimensions of this tunnel make it possible to conduct experiments using perturbed model motion. As the models, having longitudinal static stability, fly through the working section, they perform oscillations, describing a halfwave or a complete wave. The primary information in the form of shadow graphs, obtained by seven vertically and horizontally positioned schlieren instruments, is used to calculate the aerodynamic characteristics.

/264

While examining the aeroballistic ranges, we shall discuss the technique for studying the flow around the model and determining the aerodynamic characteristics at fixed angles of attack. The free-flying model is exposed to the approaching flow at some angle not equal to 0 or 180° to the model line of flight. As a result of

combining the model and stream velocities, flow around the model takes place at some angle of attack. The model velocity relative to the medium is equal to the sum of the model and stream velocity vectors. We assume that the model does not alter its orientation in space significantly during the experiment — for example, the model axis remains at all times colinear to the model flight velocity vector. Figure 5.21 shows a schematic characterizing the experimental technique — the diagram for combining the model and stream velocity vectors.

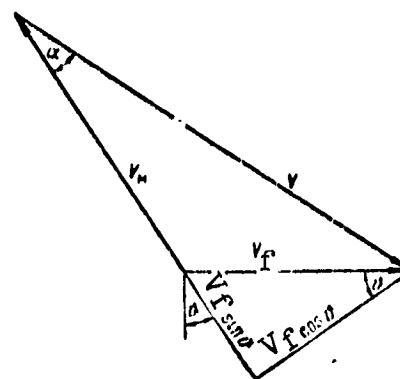


Figure 5.21. Velocity triangles for conducting ballistic tests at fixed angles of attack

Here, V_M is the vector of model velocity relative to the Earth, V_F is the vector of the flow velocity relative to the Earth, V is the resultant vector of the flow velocity approaching the model, θ is the angle between the perpendicular to the local flow and the stream direction.

We see from Figure 5.21 that the angle α is the angle of attack, since by definition the angle of attack is the angle between the resultant velocity vector V and the model axis.

From the velocity vector triangle, we obtain the relation for the angle of attack:

$$\alpha = \arctg \left(\frac{1}{\frac{V_M}{V_F} \cos \theta + \operatorname{tg} \theta} \right), \quad (5.3)$$

from which it follows that the angle of attack α depends on the ratio 265 of the model launch velocity to the approaching stream velocity and the angle θ . The angle of attack will be the larger, the smaller the ratio V_M/V_F . For $V_M/V_F \gg 1$, the angle of attack has a maximum in

the region of negative θ values. Figure 5.22 shows the relation $\alpha=f(\theta)$ for various values of the ratio V_M/V_f .

From the velocity vector triangle, it is also easy to obtain the expression for the magnitude of the resultant velocity V , which will depend on the model velocity V_M , the ratio V_f/V_M and θ :

$$V = V_M \sqrt{1 + \left(\frac{V_f}{V_M}\right)^2 + 2 \frac{V_f}{V_M} \sin \theta}. \quad (5.4)$$

Figure 5.23 shows the relation $\frac{V}{V_M} = f(\theta)$ for various values of the ratio V_M/V_f . For negative values of θ , we have a smaller resultant velocity V than for positive values.

Thus, this experimental technique makes it possible to obtain flow around models at constant angle of attack. If we make trajectory measurements at three points, it is possible to measure the drag coefficient and the lift coefficient simultaneously in a single experiment, and therefore determine the magnitude of the aerodynamic efficiency for the given angle of attack.

Still another aeroballistic range variant has been proposed for simulating the aerodynamic processes involved in flight vehicle entry into the dense layers of the atmosphere [8]. The operating principle of this range involves launching models into an opposing stream in a long supersonic nozzle. Since there is considerable flow density variation along the length of the nozzle, it is possible to simulate model flight with conditions close to full-scale, when

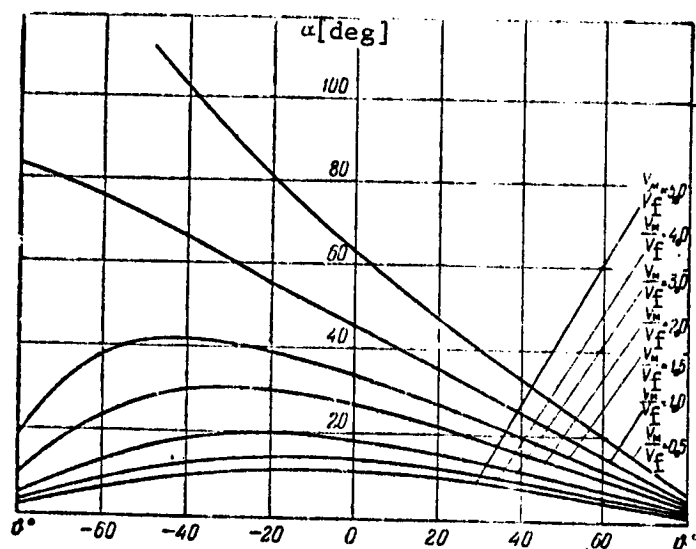


Figure 5.22. Angle of attack as function of the launch angle θ and the ratio V_M/V_f

the vehicle passes through various layers as it enters the atmosphere, from highly rarefied to dense. In this case, the supersonic nozzle is used not so much for creating the flow, whose velocity is an order of magnitude less than the model velocity, rather, it is used as a gas-dynamic range which makes it possible to create an air medium with given distribution of the density and pressure along its length.

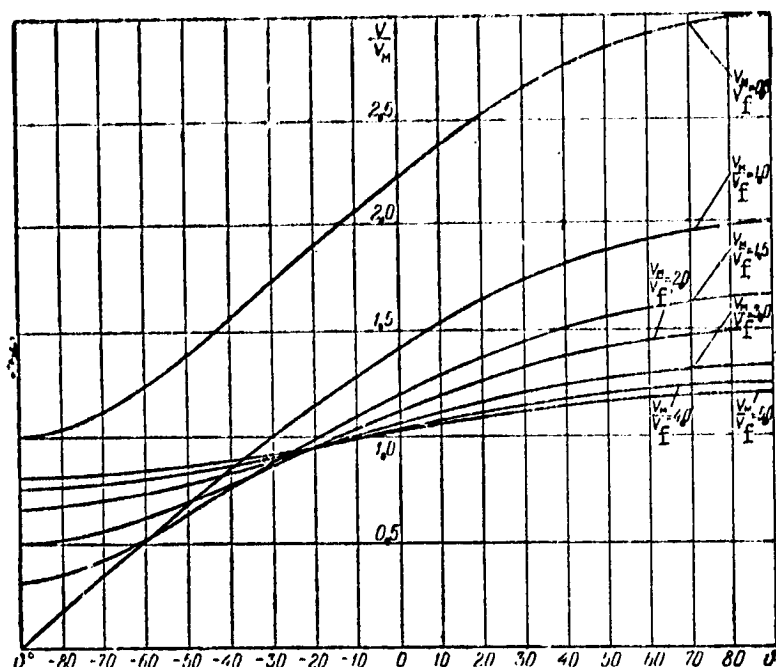


Figure 5.23. Ratio V/V_M as a function of the launch angle ϑ and the ratio V_M/V_f

In order to realize this modeling principle, it is necessary to use light-gas launchers with muzzle velocities no less than 5 km/sec, which corresponds to the entry velocities of ballistic rockets designed for flight ranges of 3000 km or more. In order to simulate the lower layers of the atmosphere from 0 to 30 - 35 km, it is necessary to create a density ratio ρ/ρ_0 in the supersonic nozzle on the order of 10^{-2} . This ratio of the density in the forechamber and at the exit section of the supersonic nozzle holds for a nozzle with Mach number $M = 5$. The model is launched into the stream in the nozzle along the nozzle centerline. The supersonic nozzle is designed so that the density variation along the axis obeys an exponential law.

In practice, the facility is arranged as shown in Figure 5.24. Between the high-pressure vessel and the vacuum receiver, there is a supersonic nozzle with a large number of windows for model photography. The model catcher is located in the forechamber, and the

launcher is located in the vacuum receiver. The total flow duration is about one second. The air is heated in the forechamber to prevent condensation. The nozzle has a smooth expansion, in order that the flow not differ markedly from one-dimensional flow. The facility is equipped with apparatus for recording the trajectory parameters and spectrometers.

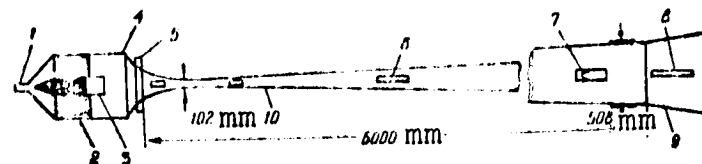


Figure 5.24. Aeroballistic tunnel for simulating parameters during atmospheric entry:

1 — high-pressure air supply; 2 — recuperator preheater; 3 — model catcher; 4 — forechamber with $p_0 = 10 - 15$ atm; 5 — quick acting valve; 6 — window for photography; 7 — flying model (diameter 8.5 mm) in window; 8 — gas gun barrel; 9 — exhaust into vacuum chamber, 10 — asymmetric or square nozzle.

Figure 5.25 shows a photograph of this facility.

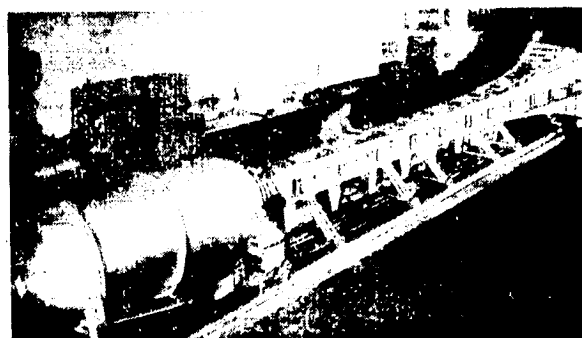


Figure 5.25. Photograph of aeroballistic tunnel for simulating atmospheric entry parameters

A combination of a shock tube and light-gas gun launcher has been used to increase the gasdynamic parameters markedly [9]. While it was previously possible to obtain an increase of 600 - 700 m/sec in the velocity by cooling supersonic flow in a wind tunnel, the use of a shock tube with nozzle has made it possible to obtain a velocity increase of up to 4000 m/sec. These high parameters have made it possible to conduct experiments under conditions in which the intramolecular processes manifest themselves significantly in flow around models.

A schematic of such a facility and its model are shown in Figure 5.26. The facility consists of a shock tube, supersonic nozzle, long working section, vacuum receiver, and light-gas launcher,

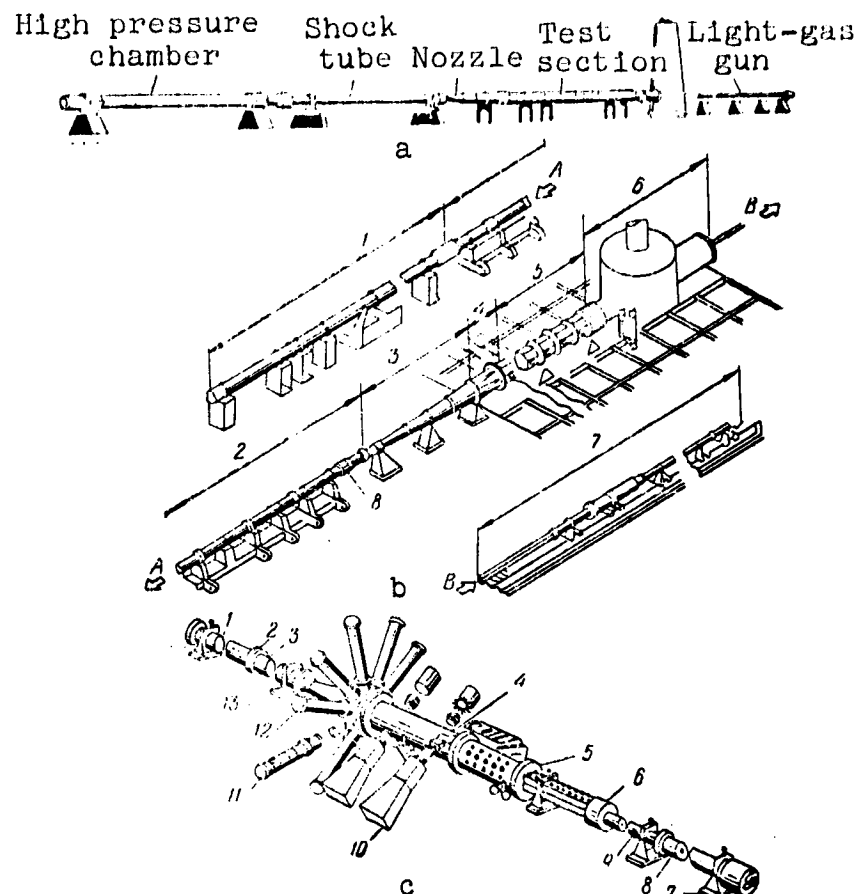


Figure 5.26. General view of Ames Laboratory shock-ballistic tunnel (a, b) and its model (c)

a, b) ballistic tunnel schematic:

1 — driver gas chamber; 2 — working gas chamber;
3 — nozzle; 4 — intermediate section; 5 — working
section; 6 — vacuum chamber; 7 — gas gun; 8 —
fast-acting valve

c) schematic of shock-ballistic tunnel model:

1 — high pressure chamber; 2 — diaphragm; 3 —
shock tube; 4 — working section; 5 — shock wave
attenuation chamber (shock wave exit); 6 — gun bar-
rel; 7 — first compression stage; 8 — light-gas
gun; 9 — second compression stage; 10 — setup for
shadow photography; 11 — spectral radiation pickups;
12 — nozzle for $M = 6$; 13 — nozzle diaphragm

which fires against the stream in the working section. The overall length of the facility is about 70 meters. The shock tube high- and low-pressure chambers both have inner diameter 152 mm and length 12 meters. The pressures in the shock tube reach 1400 atm. An axisymmetric supersonic nozzle with design Mach number $M = 7$ is used. A light gas system with deformable piston is used as the launcher. The launcher piston chamber diameter is 57.2 mm and its length is 11 m. The barrel caliber is 12.7 mm. The model velocity reaches 10,000 m/sec.

Because of the short duration of the shock tube operation, particular attention in designing the shock-ballistic range was devoted to ensuring synchronization.

Figure 5.27 shows the working cycle of this combined range on a time-distance diagram. Range operation begins with ignition of the powder charge of the light gas launcher. After six milliseconds,

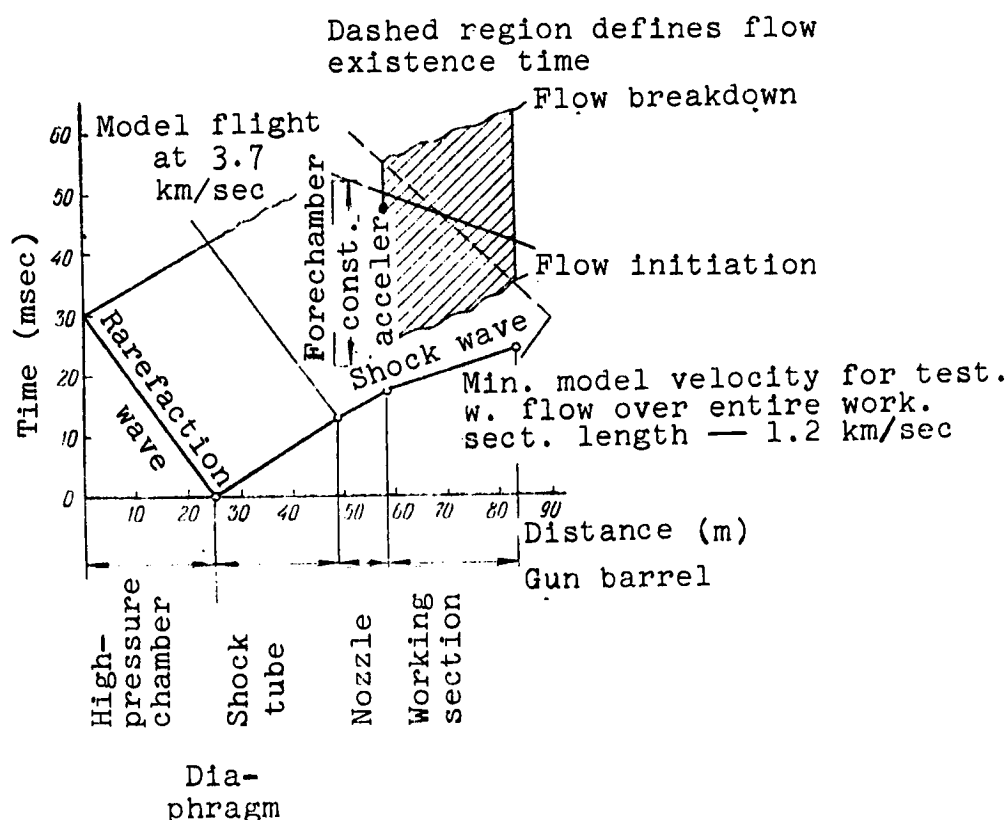


Figure 5.27. Operating cycle of the shock-ballistic tunnel

the gas mixture (hydrogen, oxygen, helium, and nitrogen) in the shock tube high-pressure chamber explodes. A hole is punched in the diaphragm installed between the high- and low-pressure chambers, and the diaphragm bursts. The traveling shock wave compresses the air,

which then discharges into the supersonic nozzle of the shock tube. With flow velocity in the range working section equal to 4000 m/sec, a Mach number $M = 7.3$ is provided in the nozzle, and the air discharge time through the nozzle is 18.8 msec. The regime in the working section is established as this section fills with the approaching stream, and is recorded when the static pressure reaches the design value. The light-gas launcher working cycle terminates when the flow is established at the end of the working section and the model enters the working section. Breakdown of the flow in the tunnel working section takes place after passage of the reflected rarefaction wave. The model flies through the working section approximately 5 msec prior to breakdown of the operating regime. This time margin is necessary for reliable shock tube operating process synchronization and light-gas launcher triggering. This coordination does not cause any particular difficulties, since the operating time of both components of the facility is characterized by repeatability to within one millisecond. /270

Photographs of various shock-ballistic tunnel components are shown in Figures 5.28 and 5.29. Figure 5.28 shows the high-pressure (background) and low-pressure chambers of the shock tube. In the open high-pressure chamber, we see the mechanism for punching the hole in the diaphragm.

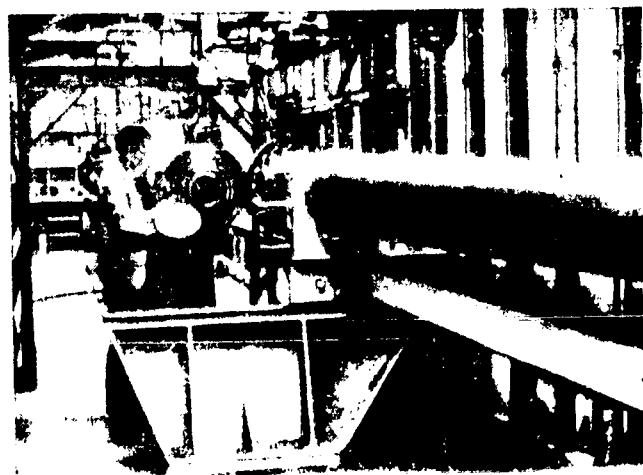


Figure 5.28. Photograph of shock-ballistic tunnel pressure chambers

Figure 5.29 shows a photograph of the shock tube working section taken from the nozzle end, and the 11 optical stations for shadow photography of the model. We see in the background the vacuum receiver, beyond which there is the light-gas launcher.

§ 5.5. Gasdynamic Parameters of Ballistic Ranges. Modeling Region

The existing high-velocity launchers make it possible to obtain quite high model flight velocities. Therefore, aeroballistic ranges have found application for simulating flight regimes in the range from transonic to hypersonic velocities. A characteristic feature of the aeroballistic range is the possibility of obtaining high values (and in the ballistic stands, both high and low values) of the Reynolds number. In order to picture the requirement for modeling with respect to M and Re , let us examine the regions of values of these parameters corresponding to the motion of various flight vehicles along their characteristic trajectories (Figure



Figure 5.29. Photograph of shock-ballistic tunnel working section

5.30). We see that M up to 25 and Re up to 10^7 and higher are required to simulate the flight of vehicles descending from orbit and of intermediate-range and long-range ballistic rocket nose cones. Figures 5.31 to 5.34 show the parameter variation regions which can be obtained in the various aeroballistic ranges. The Reynolds number for the ballistic stands (Figure 5.31) was calculated for models with diameters from 10 mm to 100 mm. The pressure in the ballistic stands varies from 0.1 to 10 ata. We see that for a comparatively high static pressure (10 ata) Re up to 10^8 can be achieved when using 100 mm-caliber launchers. But even with small calibers (10 mm) and normal atmospheric pressure, $Re \sim 10^6 - 10^7$ can be obtained with $M \sim 15 - 20$. In wind tunnels, the Reynolds numbers which can be obtained at these high Mach numbers are lower by two or three orders of magnitude.

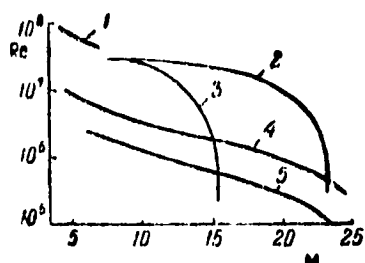


Figure 5.30. Modeling parameters with respect to Re and M for flights of various hypersonic flight vehicles:

1 — airplanes; 2 — long-range ballistic missiles; 3 — medium-range ballistic missiles; 4 — aerospace plane; 5 — orbital vehicle

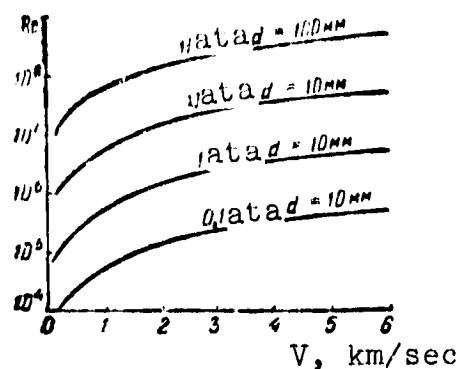


Figure 5.31. Re as function of velocity, pressure, and model diameter for tests in ballistic stands

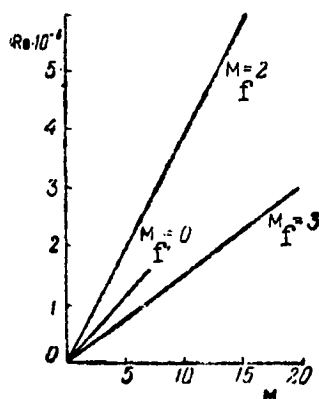


Figure 5.32. Re versus M for tests in the Ames Laboratory aeroballistic tunnel

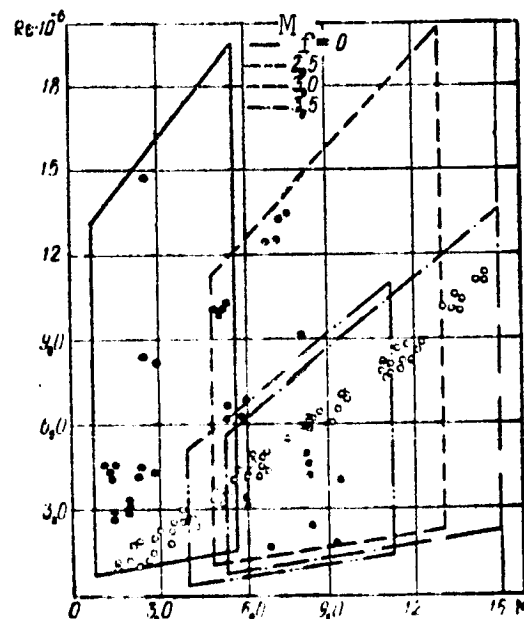


Figure 5.33. Re versus M for tests in aeroballistic tunnel designed for measuring drag coefficient

Figures 5.32 and 5.33 show the modeling regions of a large aeroballistic tunnel [7] and a small aeroballistic tunnel [6]. We see that both facilities have Reynolds numbers of the same order of magnitude, and even in the small tunnel they are larger by 2 - 3 times. The primary factor affecting Re in this case is the pressure in the tunnel forechamber. In the large tunnel, the operating

pressure range is 6 - 9 ata, while in the small tunnel the pressure in the forechamber can reach 100 ata.

Figure 5.34 shows the region of Re variation of the shock-ballistic tunnel [9, 10].

When modeling hypersonic flight regimes, particularly, there enter new modeling parameters, associated primarily with the stagnation temperature.

Beginning at some value of the stagnation temperature, the gas is no longer ideal. Phenomena such as excitation of the vibrational degrees of freedom of the molecules, dissociation, and ionization, accompanied by radiation of the gas, manifest themselves. In order to study these phenomena, we must introduce new modeling parameters, including consideration of the nonequilibrium process characteristic time.

Since complete modeling can never be accomplished in practice in an aerodynamic experiment, the problem becomes still more complicated at hypersonic velocities with the appearance of a large number of parameters. Therefore, before conducting experiments in ballistic ranges, it is necessary to select the definitive modeling parameters as a function of the objectives being sought.

We mentioned previously that the aeroballistic tunnels provide broad capabilities for achieving hypersonic velocities. Their operating principle is based on launching models against the supersonic flow in the wind tunnel working section. The following expression holds for the resultant Mach number M_∞ :

$$M_\infty = M_f + \frac{V_f}{a_f}$$

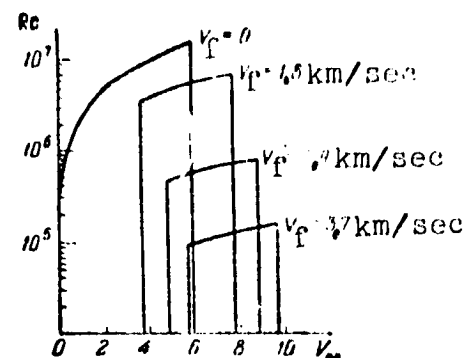


Figure 5.34. Re as function of resultant velocity V_∞ for tests in shock-ballistic tunnel

/274

(5.5)

where M_f is the Mach number of the flow in the wind tunnel, V is the model flight velocity, a_f is the sound speed in the tunnel working section.

Thus, high resultant M_∞ are obtained in the aeroballistic tunnels, first, as a result of combining the velocities of the flow and the model and, second, as a result of reduction of the sound speed in the supersonic wind tunnel working section because of cooling of the air as it passes through the nozzle. In the aeroballistic tunnels, the gas cooling effect is obtained, so to speak, "automatically", while in the ballistic stands the use of a quite complex system for cooling the gas is required.

Figure 5.35 shows M_∞ as a function of model velocity for several M_f . We see that even for low launch velocities, about 2000 m/sec, in the supersonic nozzle designed for $M = 3.5$, the resultant $M_\infty = 15$. For launch velocity 6000 m/sec into an opposing flow with $M = 2.5 - 3.5$, the resultant Mach numbers reach thirty or more.

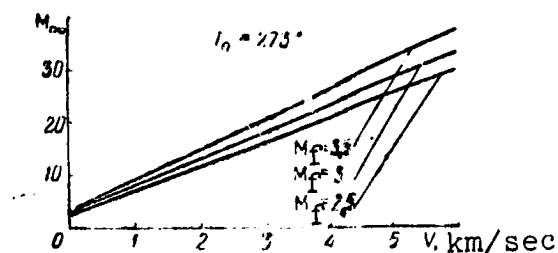


Figure 5.35. Resultant Mach number M_∞ versus initial model velocity for tests in aeroballistic tunnels

Usually, the aeroballistic tunnels are constructed so that the model passes through the nozzle throat. This condition limits M_f , since for excessively large values of M_f , the throat area will be inadequate for model passage. On the other hand, the minimal flow stagnation temperature is selected to avoid condensation of the air. We must also keep in mind that, with increase of M_f , the flow density in the working section decreases markedly, and the force action of the medium becomes too small for the existing instruments to be able to determine the aerodynamic characteristics with satisfactory accuracy. With account for all these limitations, we find that the optimal nozzles in the aeroballistic tunnels are those with $M = 2.5 - 3.5$.

Using the known formulas:

$$a = \sqrt{\gamma R T} \text{ and } T = T_0 \frac{1}{1 + \frac{\gamma-1}{2} M^2},$$

we can represent M_∞ in more general form by an expression in terms of the flow parameters M_f , T_0 in the wind tunnel and the model flight velocity V :

$$M_\infty = M_f + \frac{V}{\sqrt{\gamma R T_0}} \sqrt{1 + \frac{\gamma-1}{2} M_f^2}, \quad (5.6)$$

or

$$M_\infty = M_f + M_0 \sqrt{1 + \frac{\gamma-1}{2} M_f^2} \quad (5.7)$$

where M_0 can be interpreted as the model flight Mach number in a medium corresponding to the gas state in the forechamber.

Figure 5.36 shows the relation $M_\infty = f(M_f)$ for various values of M_0 .

Thus, M_∞ will be larger, the larger the flow Mach number (M_f) and the model velocity V and the lower the flow stagnation temperature in the wind tunnel.

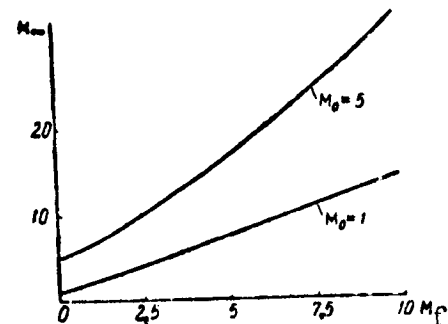


Figure 5.36. M_∞ versus M_f for tests in aeroballistic tunnels

Another distinctive feature of the ballistic ranges is the possibility of obtaining large Re values, which can exceed by several tens of times the Re values which can be realized in wind tunnels at the same Mach numbers. This is achieved primarily as a result of significant reduction of the static density of the flow in the wind tunnel at hypersonic velocities. /276

High Mach numbers are achieved in aeroballistic tunnels with comparatively low flow Mach numbers when the flow density is still high. The Reynolds number formula for the aeroballistic range has the form:

$$Re_{\infty} = \frac{V_{\infty}}{\nu/\rho_F} + \frac{V_F}{\nu/\rho_F} + \frac{V}{\nu/\rho_F}. \quad (5.8)$$

The first term corresponds to the Re number of the model at zero flight velocity, i.e., for conventional wind tunnel tests. The second term is obtained with account for flight of the model with the velocity V relative to the Earth.

Expressing R_{∞} in terms of the stagnation and wind tunnel flow parameters, we obtain:

$$Re_{\infty} = \frac{l \rho_0 a_0}{\mu_0} \frac{1}{\left(1 + \frac{\gamma-1}{2} \cdot M_F^2\right)^{\frac{2\gamma-1}{2(\gamma-1)}}} \left(M_F + \frac{V}{a_0} \sqrt{1 + \frac{\gamma-1}{2} \cdot M_F^2}\right). \quad (5.9)$$

Here, μ was calculated from the formula $\mu = cT^{\eta}$. The relation $Re = F(M_F)$ is shown in Figure 5.37.

The stagnation temperature T_T on the model in aeroballistic tunnel experiments can be represented by the following expression in terms of the wind tunnel flow parameters:

$$\frac{T_T}{T_0} = 1 + \frac{(\gamma-1) M_F^2}{\sqrt{1 + \frac{\gamma-1}{2} \cdot M_F^2}} \cdot M_0 + \frac{\gamma-1}{2} \cdot M_0^2. \quad (5.10)$$

For model velocity corresponding to $M_0 = 0$, we find that the stagnation temperature on the model is equal to the stagnation temperature in the ballistic range wind tunnel. The dependence of the stagnation temperature T_T on flow Mach number M_F shows up in the second term of (5.10). It is not difficult to see that, for large values of M_F , the temperature is independent of

the flow Mach number. This fact can be seen in the graph of $T_T = f(M_F)$, shown in Figure 5.38. Figure 5.39 shows T_T versus M_0 for aeroballistic tunnels. These calculations of the stagnation

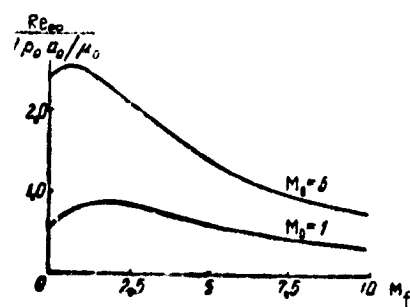


Figure 5.37. Re versus M_F for tests in aeroballistic tunnels

temperature were made under the assumption that the working gas used in the ballistic ranges is a perfect gas. Undoubtedly, in reality, the absolute stagnation temperatures are lower.

However, the high stagnation temperature level (several thousand degrees) favors the use of ballistic ranges from the viewpoint of modeling the processes taking place in flow about full-scale hypersonic objects. For these stagnation temperatures, the ballistic experiment basically reflects properly the processes which depend on viscosity variation with temperature and manifestation of the real gas properties.

Still another characteristic property associated with the ballistic ranges is the low value of the temperature factor. During the ballistic experiment, because of the very short experiment time, the model will not be heated to a significant degree, and its walls will essentially remain "cold" in comparison with the high stagnation temperature, which will correspond to the full-scale flight conditions.

§ 5.6. Technique for Determining Drag Coefficient

In artillery firing range practice, the simplest technique for determining drag is the method based on application of the kinetic energy variation theorem. This theorem says: the increment of the kinetic energy of a material point over a finite path segment is equal to the sum of the works of all the forces acting on the point along the path segment. Thus, the velocity V of the body in question must be determined by one method or another at two points of a rectilinear horizontal trajectory in order to determine the drag force.

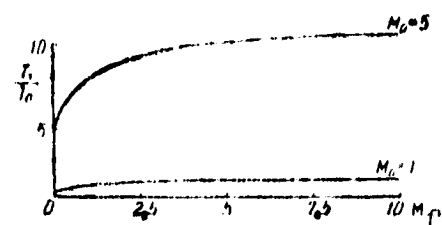


Figure 5.38. Model stagnation temperature versus M_F for tests in aeroballistic tunnels

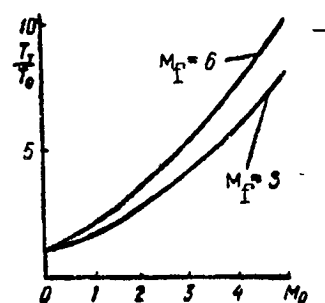


Figure 5.39. Model stagnation temperature versus generalized parameter M_0

Writing the kinetic energy equation for the trajectory segment x , and bearing in mind that the work of the gravity force is equal to zero, we obtain:

$$\frac{mV_e^2}{2} - \frac{mV_0^2}{2} = \int_0^x C_x \frac{\rho V^2}{2} S dx, \quad (5.11)$$

where $C_x \frac{\rho V^2}{2} S$ is the air resistance force, V_0 and V_e are the initial and end velocities on the trajectory segment x .

We remove the expression for the resistance force from under the integral sign, replacing it by the average value over the trajectory segment x . For this, we assume that the drag coefficient $C_x = \text{const.}$ and that V remains constant on the trajectory segment x and equal to $V_{av} = (V_0 + V_e)/2$. Then:

$$\frac{m}{2} (V_e^2 - V_0^2) = -C_x \frac{\rho S}{2} V_{av}^2 x. \quad (5.12)$$

Substituting the expression for V_{av} into (5.12), we obtain:

$$C_x = \frac{4m(V_0 - V_e)}{\rho S(V_0 + V_e)} \frac{1}{x}. \quad (5.13)$$

The basic drawback of this method is that it does not determine the drag force at any definite point, but rather its average value over some trajectory segment. The calculated average drag relates to the average velocity V_{av} , which is also a source of error.

The numerical differentiation technique is somewhat more precise, but also more laborious in comparison with the method based on using the kinetic energy theorem.

On the rectilinear horizontal model trajectory, we note the sequence of points A_0, A_1, \dots, A_k , equidistant from one another at the distance h . The model flight times to the points A_0, A_1, \dots, A_k are denoted by $t_0, t_1, t_2, \dots, t_k$. The times of model travel between the noted points are known from experiment: /279

$$\begin{aligned}\Delta t_0 &= t_1 - t_0, \\ \Delta t_1 &= t_2 - t_1, \\ &\dots \dots \dots \\ \Delta t_{k-1} &= t_k - t_{k-1}.\end{aligned}$$

This means that, as a result of the experiment, we can formulate a table of $\Delta t = f_1(x)$, with step equal to h . Differentiating numerically, we obtain the table of $\left(\frac{dt}{dx}\right) = f_2(x)$, and then the table of $V = f_3(x)$, since:

$$V = \frac{dx}{dt} = \left(\frac{dt}{dx}\right)^{-1}. \quad (5.14)$$

In order to determine the drag at the points A_0, A_1, \dots, A_k , it is necessary to differentiate numerically the tabulated function $V = f_3(x)$.

Having the tables of the values of $\left(\frac{dV}{dx}\right) = f_4(x)$, it is easy to formulate the tables of the values for $C_x = f_5(x)$.

Then, for the point n :

$$C_{x_n} = \frac{2m}{\rho S} \frac{1}{V_n^2} \left(\frac{dV}{dx}\right)_n, \quad (5.15)$$

or, considering that:

$$\frac{dV}{dt} = \frac{dV}{dx} \frac{dx}{dt} = \frac{dV}{dx} V, \quad (5.16)$$

we finally obtain:

$$C_x = \frac{2m}{\rho S} \frac{1}{V_n} \left(\frac{dV}{dx}\right)_n. \quad (5.17)$$

The advantage of this method lies in the fact that, in a single experiment, we determine several values of C_x , and each pair of V_n and C_{x_n} values corresponds to the same trajectory point.

The disadvantage of the method is its complexity, and also the need to use numerical differentiation of the tabulated functions, which is, in itself, a very delicate operation and can lead to large errors in the case of careless handling of the tables.

In order to avoid the inexact operation of numerical differentiation when calculating the drag coefficient, let us examine the method based on integrating the equation of model motion under definite assumptions in regard to the aerodynamic drag coefficient. In this case, we obtain easily visualized analytic expressions relating the drag coefficient with the experimentally measured parameters. /280

For greater generality, we shall examine the motion of a body launched into an opposing stream. Then, we obtain the results for motion in a quiet atmosphere as a particular case, setting the velocity of the approaching uniform stream equal to zero.

Let a uniform stream with velocity V_f and density ρ approach along the abscissa axis, whose origin is fixed with the Earth, and in the opposite direction let there approach a body of mass m with cross section area S and drag coefficient $C_x = f(V)$. The initial model velocity relative to the Earth at some point and at the moment of time t_0 is equal to V_0 (Figure 5.40).

The velocity of the resultant flow approaching the body at the point x_0 and at the moment of time t_0 is equal to $V_{00} = V_0 + V_f$.

The equation of model motion in the axis system fixed with the approaching uniform flow will be:

$$m \frac{d^2 x}{dt^2} = - \frac{C_x \rho S}{2} \left(\frac{dx}{dt} \right)^2, \quad (5.18)$$

where the following relation holds for the flow coordinate x_f :

$$x_f = x + V_f t. \quad (5.19)$$

Let the law of drag coefficient variation with velocity have the form:

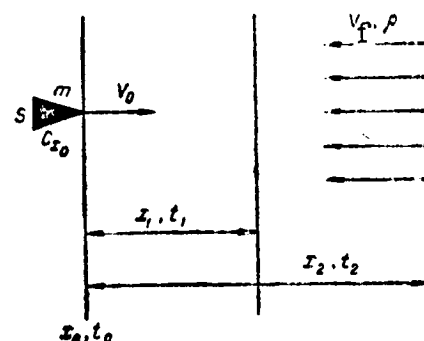


Figure 5.40. Illustration for formulating the problem of calculating model drag coefficient in aeroballistic tests

$$\frac{C_x}{C_{x_0}} = \left(\frac{V}{V_{00}}\right)^\alpha. \quad (5.20)$$

Then, for velocity V equal to the initial velocity V_{00} , the drag coefficient will be equal to the initial value C_{x_0} . For $\alpha = 0$, we have the case when $C_x = C_{x_0}$. For $\alpha > 0$, the drag coefficient decreases with decrease of the velocity. For $\alpha < 0$, the drag coefficient increases with reduction of the velocity. A plot of the relation (5.20) is shown in Figure 5.41.

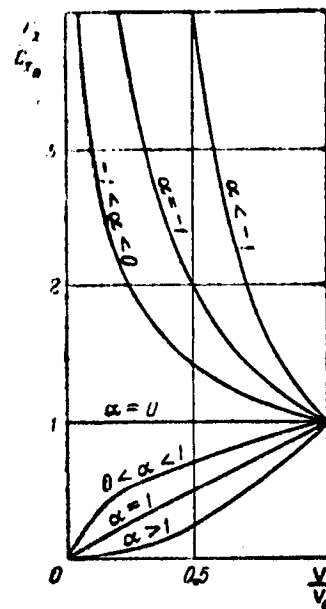


Figure 5.41. Relation $\frac{C_x}{C_{x_0}} = f\left(\frac{V}{V_{00}}\right)$

Thus, setting $dx_f/dt = V$, we integrate the equation:

$$\frac{dV}{V^{\alpha+2}} = -k \frac{1}{V_{00}} dt, \quad (5.21)$$

where

$$k = \frac{\rho S C_{x_0}}{2m} \quad (5.22)$$

is a similarity criterion, whose physical meaning we shall examine below.

After the first integration, the body velocity variation with time ($t_0 = 0$) has the form:

$$V = \frac{V_{00}}{[1 + (\alpha + 1) V_{00} k t]^{1/(\alpha+1)}}. \quad (5.23)$$

For $\alpha = -1$, (5.23) has a singularity, and is expressed in the form:

$$V = \frac{V_{00}}{e^{k V_{00} t}}. \quad (5.24)$$

Integrating a second time, we obtain the variation of the flying body coordinate with time:

$$x_f = \frac{1}{k^2} \{ [1 + (\alpha + 1) V_{00} k t]^{1/(\alpha+1)} - 1 \}. \quad (5.25)$$

Substituting (5.19) into (5.25), we obtain:

$$x = \frac{1}{k^{\alpha}} \{ [1 + (\alpha + 1) \times \\ \times V_{\infty} k t]^{\alpha/(\alpha+1)} - 1 \} - V_{\infty} t. \quad (5.26)$$

The points $\alpha=0$ and $\alpha=-1$ are singular points of the Solution (5.26). To find the solutions of the equation of motion at these points, we expand (5.26) into an infinite series:

$$x_F = \frac{1}{k} \left(V_{\infty} k t - \frac{1}{2} V_{\infty}^2 k^2 t^2 + \frac{\alpha+2}{2 \cdot 3} V_{\infty}^3 k^3 t^3 + \dots + (-1)^{n+1} \times \right. \\ \left. \times \frac{(\alpha+2)(\alpha+3) \dots [\alpha(n-2) + n - 1]}{n!} V_{\infty}^n k^n t^n \pm \dots \right). \quad (5.27)$$

The case $\alpha=0$ corresponds to the solution $C_x = C_x = \text{const.}$ Letting α in (5.27) go to zero, we obtain the logarithmic series: /282

$$x_F = \frac{1}{k} \left(V_{\infty} k t - \frac{1}{2} V_{\infty}^2 k^2 t^2 + \frac{1}{3} V_{\infty}^3 k^3 t^3 - \dots \right. \\ \left. \dots + (-1)^{n+1} \frac{1}{n} V_{\infty}^n k^n t^n \pm \dots \right) = \frac{1}{k} \ln(1 + V_{\infty} k t). \quad (5.28)$$

In the Earth-fixed axis system:

$$x = \frac{1}{k} \ln(1 + V_{\infty} k t) - V_F t. \quad (5.29)$$

Now let us examine the case when $\alpha=-1$. As $\alpha \rightarrow -1$, the Series (5.27) becomes the exponential expression:

$$x_F = \frac{1}{k} \left(V_{\infty} k t - \frac{1}{2} V_{\infty}^2 k^2 t^2 + \frac{1}{2 \cdot 3} V_{\infty}^3 k^3 t^3 - \dots \right. \\ \left. \dots + (-1)^{n+1} \frac{1}{n!} V_{\infty}^n k^n t^n \pm \dots \right) = \frac{1}{k} (1 - e^{-V_{\infty} k t}) \quad (5.30)$$

or, with account for (5.19),

$$x = \frac{1}{k} (1 + e^{-V_{\infty} k t}) - V_F t. \quad (5.31)$$

Thus, (5.18) has three different solutions: power-law, logarithmic, and exponential forms. Depending on the value of α , the power law solution may take the form of various expressions resulting from (5.26).

Table 5.3 shows the solutions of (5.18).

TABLE 5.3

Logarithmic solution	
$a = 0$	$x = \frac{1}{k} \ln(1 + V_{00}kt) - V_F t$
Exponential solution	
$a = -1$	$x = \frac{1}{k} (1 - e^{-V_{00}kt}) - V_F t$
Power law solution	
$a > 0$	$x = \frac{1}{ka} \{ [1 + (a+1)V_{00}kt]^{a/(a+1)} - 1 \} - V_F t$
$-1 < a < 0$	$x = \frac{1}{k a } \left\{ 1 - \frac{1}{[1 + (1- a)V_{00}kt]^{1/(1- a)}} \right\} - V_F t$
$a < -1$	$x = \frac{1}{k a } \{ 1 - [1 - (a -1)V_{00}kt]^{1/(a -1)} \} - V_F t$

Thus, these analytic expressions relate the model parameters m and S , the flow parameters ρ and V_F , and the experimentally measured quantities x and t with the drag coefficient C_{x0} . /283

Now, let us examine in more detail the important case of motion when the sought drag coefficient is a constant quantity [Formula (5.29)]. We note that in many cases this assumption is satisfied quite exactly, since in most cases the model deceleration is not large, and consequently the velocity decay in the segment required for measuring C_x is not large. Moreover, in many cases, particularly at hypersonic speeds, the drag coefficient is a weak function of velocity. Thus, following (5.29), we have for the case $C_x = \text{const}$:

$$x = \frac{2m}{\rho S C_x} \ln \left[\frac{\rho S C_x}{2m} (V_0 + V_F)t + 1 \right] - V_F t. \quad (5.23)$$

We cannot obtain from this expression an explicit relation $C_x = f(x, t, m, \rho, S, V_0, V_F)$ in exact form. Retaining quadratic terms in the expansion of (5.31), we obtain the following approximate expression for C_x :

$$C_x = \frac{4m}{\rho S} \frac{V_{00}t - x}{V_{00}^2} - \frac{4m}{\rho S} \frac{V_0t - x}{(V_0 + V_F)^2} \quad (5.33)$$

In this expression, C_x is considered a function of several independent parameters which must be measured experimentally.

In the numerator of (5.33), there appears the difference $V_0t - x$, which, as we shall see later, is a very important characteristic of the motion. This difference is the lag in distance during the time t of a model experiencing the resistance of the medium from a model whose velocity is constant and equal to the initial velocity of the first model. We exclude time from the expression for this difference, which we denote by b . To within second order terms, we obtain:

$$t = \frac{x}{V_0} \left[1 + \frac{k}{2} \left(1 + \frac{V_F}{V_0} \right)^2 x \right]. \quad (5.34)$$

Returning to the expression $b = V_0t - x$, we replace therein t in accordance with (5.34). We obtain

$$b = \frac{1}{2} k \left(1 + \frac{V_F}{V_0} \right)^2 x^2 \quad (5.35)$$

Thus, b depends linearly on the parameter k , the square of the distance, and the velocity ratio V_F/V_0 .

Let us turn to a more detailed explanation of the nature of the parameter k . This parameter appears in the basic equation of motion and in its solution. The model motion trajectory will depend on the value of k . We shall see in the following that its value also has a significant influence on the drag coefficient measurement error. We shall hereafter term the coefficient k the deceleration parameter. /284

The physical meaning of the parameter k is that it is proportional to the model deceleration resulting from the action on the model of the drag force of the medium at the given flight velocity. In fact, if we denote the deceleration by A , it follows from (5.18) that:

$$A = kV^2.$$

We can also show the physical parameters on which the value of k depends. For this, we represent its expression in the form:

$$k = \frac{\rho S C_x}{2m} = \frac{\rho C_x}{2 \frac{m}{S} \frac{l}{l}},$$

where the referred length l is selected from the condition that the product of this length by the model will be equal to the volume U of our model (i.e., $l = U/S$). Then the expression $\frac{m}{Sl} = \rho_M$ is simply the density of the material from which the model is made, or in the more general case, if the model is made from several materials or has an internal cavity, ρ_M is the model structural density. The expression for the deceleration parameter is written in the form:

$$k = \frac{1}{2} \frac{\rho}{\rho_M} \frac{C_x}{l}, \quad (5.36)$$

with the dimension $\left[\frac{1}{x}\right]$. Thus, the deceleration parameter is proportional to the ratio of the stream density to the model structural density and the drag coefficient, and is inversely proportional to the model reduced length, which depends on the model shape. For example, in the case of a cylinder, its physical length will coincide with its reduced length, $l = l$. For a sphere, the reduced length is equal to $4/3$ the radius of the sphere, $l = \frac{2}{3}l$, for the cone the reduced length is equal to $1/3$ the physical length, $l = \frac{1}{3}l$.

Since the deceleration parameter k is a universal similarity parameter, it is not necessary to vary all the quantities on which it depends in order to change its value. This is very convenient, since we cannot always alter without limit the magnitudes of the physical parameters which determine the deceleration parameter. For example, the density of the medium, determined for a given temperature by the static pressure (the pressure has an upper limit based on strength), and the densities of the materials vary in a limited range, and the model structure is directly related with its strength.

/265

Figure 5.42 shows the velocity decay as a function of the deceleration parameter and measurement base length. Figure 5.43 shows the relation $x = f(t, k)$ (5.29) — the second integral of (5.18). Also shown for comparison is the curve $x = V_0 t$ of uniform motion

($k = 0$). For various values of the parameter k , there is a family of curves which differs from the uniform motion curve the more, the larger the parameter k .

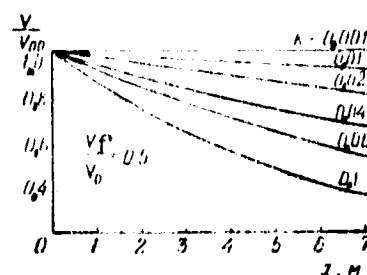


Figure 5.42. Relation

$$\frac{v}{v_0} = f(t, k)$$

Now, let us examine the question of determining the drag coefficient from experimental data. Solution (5.32) contains two unknown quantities: drag coefficient C_x and initial velocity V_0 .

Generally speaking, in experiments conducted to determine the drag coefficient, V_0 is not given and cannot be measured directly, since this requires determination of the instantaneous velocity at a point, and measurement of the velocity on a finite base for the case of large k may lead to significant errors. Thus, for the two unknowns C_x and V_0 , we must write a system of at least two algebraic equations (5.31):

$$\left. \begin{aligned} x_{F1} k &= \ln(1 + V_0 k t_1), \\ x_{F2} k &= \ln(1 + V_0 k t_2). \end{aligned} \right\} \quad (5.37)$$

The system of equations (5.37) corresponds to the conditions of the experiment in which time measurements are made on two bases having different lengths, and the initial reading is taken from a common point of space. In this case, the initial model velocity is the same on both bases (Figure 5.44).

We potentiate (5.37):

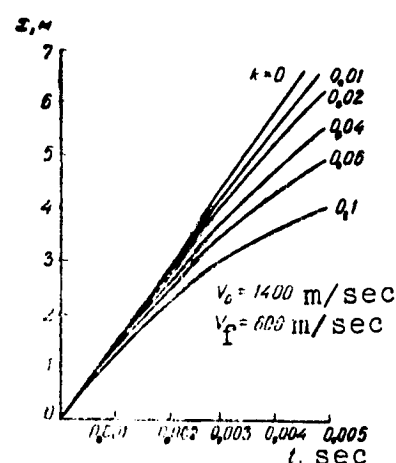


Figure 5.43. Relation

$$x = f(t, k)$$

$$\begin{aligned}
 1 + V_{00} k t_1 &= e^{x_{f1} k}, \\
 1 + V_{00} k t_2 &= e^{x_{f2} k}.
 \end{aligned}
 \tag{5.38}$$

We multiply the first equation (5.38) by t_2 , and the second by t_1 ; after subtracting the second from the first, we obtain the expression:

$$\frac{t_2}{t_1} - 1 = \frac{t_2}{t_1} e^{x_{f1} k} - e^{x_{f2} k}.
 \tag{5.39}$$

Another equation is obtained by subtracting the second equation (5.38) from the first:

$$t_{00} k (t_1 - t_2) = e^{x_{f1} k} - e^{x_{f2} k}
 \tag{5.40}$$

Using the equalities $x_f = x + V_f t$ and $V_{00} = V_0 + V_f$, we can write (5.39) and (5.40) in the final form:

$$\left. \begin{aligned}
 \frac{t_2}{t_1} - 1 &= \frac{t_2}{t_1} e^{k(x_1 + V_f t_1)} - e^{k(x_2 + V_f t_2)}, \\
 V_0 &= \frac{1}{k(t_1 - t_2)} [e^{k(x_1 + V_f t_1)} - e^{k(x_2 + V_f t_2)}] - V_f.
 \end{aligned} \right\}
 \tag{5.41}$$

This system of equations serves for determining the drag coefficient C_x and the initial velocity V_0 in terms of the measurements t_1, t_2, x_1, x_2 , the model parameters S and m , and the flow parameters ρ and V_f .

The first equation (5.41) does not contain V_0 , and the equations can be solved independently, initially the first, and then the second, containing V_0 and C_x . The initial velocity V_0 is expressed in explicit form from the second equation (5.41). As for the first equation, it cannot be transformed to a

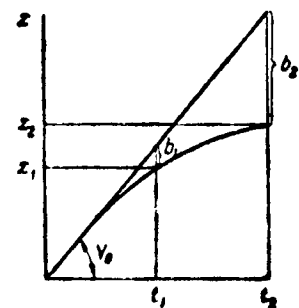


Figure 5.44. Illustration explaining the parameter b

form expressing C_x explicitly, and the drag coefficient must be found by numerical or graphical solution of this equation.

Expanding the exponential functions into a series, we can find the approximate expressions for C_x .

If we retain quadratic terms in the expansion:

287

$$C_x = \frac{4m}{\rho S} \frac{\frac{t_2}{t_1} x_1 - x_2}{\frac{t_2}{t_1} (x_1 + V_F t_1)^2 - (x_2 + V_F t_2)^2} \quad (5.42)$$

If we retain third-order terms in the exponential function expansion:

$$C_x = \frac{4m}{\rho S} \frac{\frac{t_2}{t_1} x_1 - x_2}{\frac{t_2}{t_1} (x_1 + V_F t_1)^2 - (x_2 + V_F t_2)^2} \times \left\{ 1 + \frac{2}{3} \frac{\left(\frac{t_2}{t_1} x_1 - x_2 \right) \left[\frac{t_2}{t_1} (x_1 + V_F t_1)^3 - (x_2 + V_F t_2)^3 \right]}{\left[\frac{t_2}{t_1} (x_1 + V_F t_1)^2 - (x_2 + V_F t_2)^2 \right]^2} \right\} \quad (5.43)$$

If C_x depends on the velocity in accordance with the monomial power law (5.20), the problem of determining the drag coefficient becomes more complicated, since in this case there are now three unknowns: C_x , V_0 and α . The time measurements must be made using three independent bases (four pictures), and the system for determining the unknowns will consist of three equations.

Let us examine the error sources and evaluate the C_x measurement errors. We shall use the simplified expression (5.42), which is valid for small values of x . The following parameters must be measured in order to determine the drag coefficient: model mass m , characteristic area S , stream density ρ in the wind tunnel working section, velocity V_F in the wind tunnel working section, length of the first x_1 and second x_2 bases, the time the model travels the

first base t_1 and the second base t_2 . The measurement of each of these parameters will be made with some error, which depends on the measuring instrument and the experimental conditions. Let us see how errors in the measured parameters influence the error in the magnitude of the drag coefficient.

We obtain the expressions for the errors by taking increments of the drag coefficient with respect to the various parameters of (5.42). It is easy to see that the error in C_x will depend linearly on the magnitudes of the error in the measurement of the mass m , flow density ρ , and area S :

$$\overline{\delta C}_{x|m} = \pm \frac{\delta m}{m} = \pm \overline{\delta m}, \quad (5.44)$$

$$\overline{\delta C}_{x|\rho} = \pm \frac{\delta \rho}{\rho} = \pm \overline{\delta \rho}, \quad (5.45)$$

$$\overline{\delta C}_{x|S} = \pm \frac{\delta S}{S} = \pm \overline{\delta S} = \pm 2 \frac{\delta r}{r}. \quad (5.46)$$

We can also obtain more complex expressions for the dependence of the C_x errors on time, distance, and velocity. Omitting the elementary calculations, we obtain the expression for the error in C_x for the distance measurement error Δx : /288

$$\overline{\delta C}_{x|\Delta x} = \frac{1}{n(1-n)} \frac{\Delta x_1}{b_2}; \quad (5.47)$$

here, n = ratio of the shortest measurement base to the longest measurement base $n = x_1/x_2$. The expression will have a minimum for $n = 0.5$. In the denominator of (5.47) there is the parameter b_2 — the distance decrement, whose magnitude is defined by (5.35). Thus, $\overline{\delta C}_x$ will be inversely proportional to the deceleration parameter k and, what is most important, to the square of the facility working section length x . Consequently, the geometric parameters (facility working section length, location of the windows for model recording) and the instrumental error of the instrument used to measure the distance Δx_1 will have considerable influence on the drag coefficient error.

The expression for the error $\delta \bar{C}_{x|t}$ — the drag coefficient measurement error as a function of the time measurement error — has a similar form:

$$\delta \bar{C}_{x|t} = \pm \frac{V_0}{n(1-n) \cdot b_2} \Delta t_1. \quad (5.48)$$

Comparing the expressions for the time and distance errors under the condition:

$$\delta \bar{C}_{x|t} = \delta \bar{C}_{x|z},$$

we obtain the equality:

$$\Delta t = \frac{\Delta z}{V_0}, \quad (5.49)$$

i.e., for the given distance measurement accuracy, the required time measurement accuracy will depend on the model flight velocity, namely: with increase of the velocity, the requirements on time measurement accuracy will become more severe (see § 3.6).

The error in C_x owing to inexact measurement of the flow velocity in the wind tunnel has the form:

$$\Delta \bar{C}_{x|V_F} = \frac{2}{V_0 + V_F} \Delta V_F. \quad (5.50)$$

and, consequently, decreases with increase of the flow velocity.

The expression for the total differential dC_x , referred to C_x , /289 yields the total relative drag coefficient error:

$$\delta \bar{C}_x = \pm \left[\frac{1}{m} \Delta m + \frac{1}{p} \Delta p + \frac{2}{r} \Delta r + \frac{2}{V_0 + V_F} \Delta V_F + \right. \\ \left. + \frac{2}{n(1-n)} \frac{1}{b_2} \Delta r_1 + \frac{2V_0}{n(1-n)} \frac{1}{b_2} \Delta t_1 \right]. \quad (5.51)$$

The factors 2 which appear in the time and distance error expressions are used here because of the fact that, in the process of determining C_x , the base and time are measured twice.

From this analysis of the estimate and the measurement error, we can extract practical recommendations on measurement of the particular physical parameters. For example, it is clear that model weighing should be accomplished with accuracy to tenths of a percent of the weight, so as to practically exclude in the experiment the error in C_x from inexact mass measurement. The formulas presented above make it possible to give detailed recommendations with respect to the other parameters as well. Certain errors depend through b on the measurement base length and the deceleration parameter k . It is convenient to use this circumstance in designing facilities of this kind. If the measurement methods are not sufficiently accurate to ensure determination of C_x with small error, this error can be reduced by using a longer working section or by changing the value of k — for example, by increasing the static pressure.

Returning to the method based on use of the kinetic energy change theorem, we shall indicate a more exact formula for determining the drag coefficient in terms of the initial V_0 and end V_e velocities on some segment x . Using (5.23) and (5.29), for the case $C_x = \text{const}$ and $V_f = 0$, we can obtain:

$$\frac{V_0}{V_e} = e^{kx}. \quad (5.52)$$

Hence,

$$C_x = \frac{2m}{\rho S} \frac{1}{x} \ln \frac{V_0}{V_e}. \quad (5.53)$$

This formula is more exact than (5.13), since it was obtained under only the single assumption $C_x = \text{const}$. Formula (5.13) for determining C_x can be obtained from (5.53) if, in the expansion of $\ln V_0/V_e$ into a series, we retain only the first term.

In conclusion, we note the studies [11, 12], in which methods are described for calculating the drag coefficient from trajectory measurement data which are based on use of (5.53) and provide determination of C_x with any desired approximation accuracy.

§ 5.7. Measurement of Other Aerodynamic Characteristics

In addition to the drag coefficient, the ballistic method can /290 be used to determine any other aerodynamic characteristics, since the aerodynamic forces and moments determine the model flight trajectory. For example, drag causes model deceleration, lift causes model deviation from rectilinear flight, and pitching moment causes angular acceleration relative to the model transverse axis. By recording the model position in space at known time intervals and thus determining the model flight trajectory, we can obtain the basic information for calculating the aerodynamic characteristics. Various methods of mathematical analysis of the measurement results (which were examined in detail in the preceding section) for determining the drag coefficient have been developed for this purpose. The development of the methods for complete analysis of the experimental results constitutes an independent branch of the methodology.

In the general three-dimensional motion case, we write out a system of six equations for determining the three forces and three moments. Then we seek the solution of this system of equations. The solutions obtained relate the basic trajectory measurement data obtained from the ballistic experiment with the sought aerodynamic forces and moments. In order to use partial or approximate solutions, the experiments are conducted under conditions in which we can utilize various assumptions which simplify the problem — for example, the assumption of two-dimensional model motion, linearity of the aerodynamic characteristics (small angles), absence of damping, and others. In this case, the calculation simplifies significantly.

Another approach to solution of the basic system of equations is representation of the sought aerodynamic characteristics by approximating expressions with arbitrary coefficients, so as to satisfy the basic system of equations. In many cases, such an approach can be used with success; however, the solution may not be unique.

As an example of aerodynamic characteristic determination, we shall examine below the very simple problems of finding the lift and pitching moment coefficients and the characteristics associated with model rotation.

We have mentioned previously that the lift force can be measured from the model flight trajectory curvature. We examine the flight of a model performing pitching oscillations relative to a position with zero lift force. We assume that the oscillation amplitude is limited to the region of linear variations of the lift force and pitching moment, so that the oscillations follow a sinusoidal law. For simplicity, we consider undamped oscillations:

/291

$$\alpha = \alpha_M \sin 2\pi ft, \quad (5.54)$$

where α — angle of attack, α_M — angle-of-attack oscillation amplitude; f — oscillation frequency.

Since the lift force:

$$Y = C_y \rho \frac{V^2}{2} S = C_y^* \rho \frac{V^2}{2} S \alpha, \quad (5.55)$$

then, with account for (5.54) and (5.55), the acceleration normal to the trajectory will also vary sinusoidally:

$$\frac{d^2 y}{dt^2} = \frac{Y}{m} = \frac{C_y^*}{m} \rho \frac{V^2}{2} S \alpha_M \sin 2\pi ft. \quad (5.56)$$

Integrating this equation, we obtain the variation with time of the model center-of-mass position relative to the transverse coordinate:

$$y = - \frac{C_y^* \rho \frac{V^2}{2} S \alpha_M}{m (2\pi f)^2} \sin 2\pi ft. \quad (5.57)$$

The derivative C_y^α of the lift coefficient with respect to angle-of-attack can be found from (5.57), and the experimentally measured oscillation frequency f , angle-of-attack amplitude α_M , and the quantity y — the displacement of the model center-of-mass m along the vertical. A typical trajectory measurement record in the experiment for determining α_M and y is shown in Figure 5.45.

Under these same assumptions, it is not difficult to obtain the connection between the longitudinal static stability characteristics and the measured trajectory parameters. In fact,

$$M_z = -\frac{d^2 a}{dt^2} J_z, \quad (5.58)$$

but, since:

$$\frac{d^2 a}{dt^2} = -(2\pi f)^2 a \sin 2\pi ft,$$

then,

$$M_z = m_z q S l = m_z^* a q S l,$$

where M_z — moment about the transverse axis; J_z — moment of inertia about the transverse axis; q — velocity head; l — model length.

Hence, the slope m_z^* of the pitching moment coefficient versus /292 angle of attack will depend on the oscillation frequency f and the moment of inertia J_z about the transverse axis:

$$m_z^* = -\frac{(2\pi f)^2 J_z}{q S l}. \quad (5.59)$$

From the found values of C_y^α and m_z^* , we can determine the stability margin:

$$x_{cp} - x_{cg} = l \frac{m_z^*}{C_y^\alpha}, \quad (5.60)$$

where x_{cp} — center-of-pressure coordinate, and x_{cg} — center-of-gravity coordinate.

The possibilities of determining the rotary derivatives: roll damping coefficient $m_{\dot{r}}$ and control surface effectiveness coefficient m_{δ}^* , can be illustrated by the following example, in which we examine the

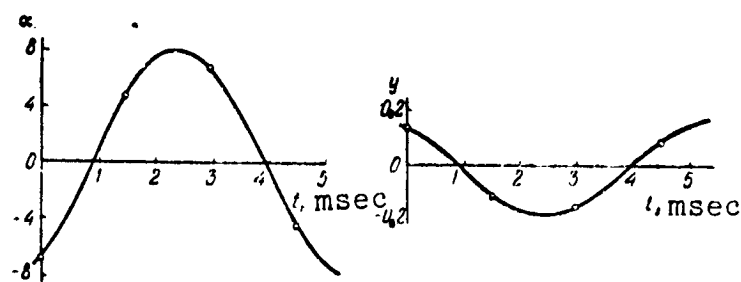


Figure 5.45. Typical record of angle-of-attack α and model center-of-gravity coordinate variation in the plane disturbed motion case

flight of a model of a particular missile with rotation about its longitudinal axis. In this case, we can use the following rotational motion equation:

$$J_x \frac{d^2\gamma}{dt^2} = m_x^\delta \cdot \delta + m_x^{\omega_x} \frac{d\gamma}{dt}, \quad (5.61)$$

where J_x — moment of inertia about the longitudinal axis; γ — roll angle; δ — control surface deflection angle.

Expression (5.61) defines the angular acceleration as a result of control surface deflection and aerodynamic damping. The solution of this equation is an expression of the form:

$$\gamma = C_1 + C_2 t + C_3 t^{-0.1}, \quad (5.62)$$

where C_1, C_2, C_3, C_4 depend on the experimental conditions and the magnitudes of the rotary derivatives $m_x^{\omega_x}$ and m_x^δ . Although the determination of the sought coefficient $m_x^{\omega_x}$ and m_x^δ is possible in principle, it is a very complex operation. /293

Since there are two unknowns in (5.62), we must write a system of two such equations, and then find the sought coefficients.

For simpler determination of the sought coefficients, it is better to reduce the problem to two limiting cases. In the first case, we proceed as if the term $m_x^\delta \delta$ in (5.61) could be neglected. For this, the test model must have zero control surface deflection angle. Then, the equation of motion takes the form:

$$\frac{d\gamma}{dt} m_x^{\omega_x} = J_x \frac{d^2\gamma}{dt^2}, \quad (5.63)$$

and its solution is

$$\gamma = \frac{\omega_0 J_x}{m_x^{\omega_x}} e^{\frac{m_x^{\omega_x}}{J_x} t} + \gamma_0. \quad (5.64)$$

This expression contains a single unknown sought roll damping coefficient $m_x^{\omega x}$. Having the experimental record of $\gamma = f(t)$, we can easily determine $m_x^{\omega x}$ with the aid of (5.64).

In order to determine m_x^{δ} , it is necessary to make a model with deflected control surfaces, and launch it so that the angular rotation velocity will be small, and so that the term containing $m_x^{\omega x}$ will be negligibly small in comparison with the term containing m_x^{δ} . This experiment can be planned with model launch from a rifled barrel with model rotation in the direction opposite that imposed by the control surface deflection. Then the model rotation slows down as it leaves the barrel. The experimental conditions must be selected so that model rotation stops near the middle of the working section. The following equation of motion holds for these experimental conditions:

$$m_x^{\delta} \ddot{\gamma} = J_x \frac{d^2 \gamma}{dt^2}. \quad (5.65)$$

Its solution will have the form:

$$\gamma = \frac{m_x^{\delta} \ddot{\gamma}}{J_x} t^2 + \omega_0 t + \gamma_0. \quad (5.66)$$

Hence, we can find the sought quantity m_x^{δ} with an error arising as a result of the presence of low roll damping with low rotational velocity.

These are some particular examples of aerodynamic characteristic /294 determination by the ballistic method.

More general methods for determining the aerodynamic characteristics can be found, for example, in [13 - 16, 54]. However, discussion of these general methods goes beyond the framework of the problems posed in the present book.

§ 5.8. Results of Some Aerodynamic Studies

In this section, we examine the results of some aerodynamic studies made using the ballistic method. Measurements of the aerodynamic coefficients, determination of the flow pattern around the body, study of the near and far wake behind models constitute the majority of ballistic studies. There have been a large number of ballistic studies in which measurements were made of thermal fluxes, radiation characteristics in the layer behind the shock wave, and model melting. We should also mention studies to measure the base pressure, determine the point of laminar boundary layer transition into turbulent, measure the friction coefficient, and certain other studies.

1) Flow patterns around bodies. The primary experimental data obtained in aeroballistic ranges in the form of photographs of the flow patterns around models make it possible to obtain many data useful for the development of theory and for practical needs. Many studies have been made of the various characteristics of the flow around models, such as shock wave standoff near the stagnation point, shock wave shape, position of the sonic points on the body surface, and others. /295

In certain cases, special techniques have been developed for study of these characteristics, for example, the photoelectron method [53] for measuring shock wave standoff near the stagnation point.

Figures 5.46 - 5.48 show shadow graphs of the flow around models of very simple bodies of revolution.

Figure 5.49 shows the dependence of the shock wave standoff Δ , referred to the model diameter d , near the stagnation point of a sphere on Mach number. With increase of M , the value of Δ/d decreases: sharply for small M , and weakly for large M . In the hypersonic region, the shock wave standoff amounts to 0.065 times the model diameter. Figure 5.50 shows the relative magnitude of the /296

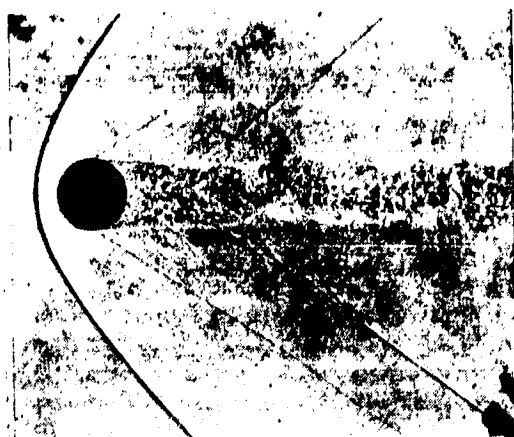


Figure 5.46. Shadowgraph of flow around sphere at $M = 1.5$

wave standoff ahead of ellipsoids with different ratio of the longitudinal semiaxis a to the transverse semiaxis b , while Figure 5.51 shows the magnitude of the standoff ahead of the segmental bodies. These data were obtained in an aeroballistic tunnel [6] with an air medium.

The shock wave standoff ahead of ellipsoids of revolution in various gases with constant specific heat ratio was studied in [18]. As an example, Figure 5.52 shows the experimental curves of

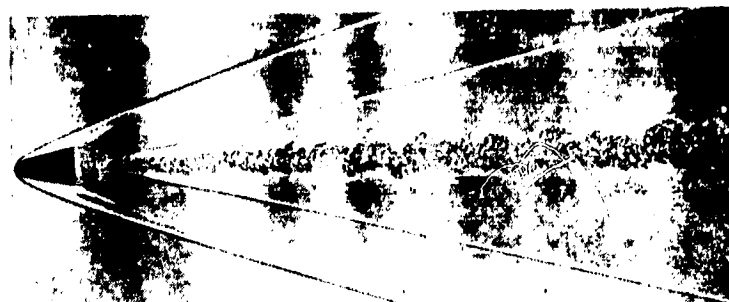


Figure 5.47. Shadowgraph of flow around blunted cone at $M = 4.05$



Figure 4.48. Shadowgraph of flow around model with conical braking skirt at $M = 3.95$

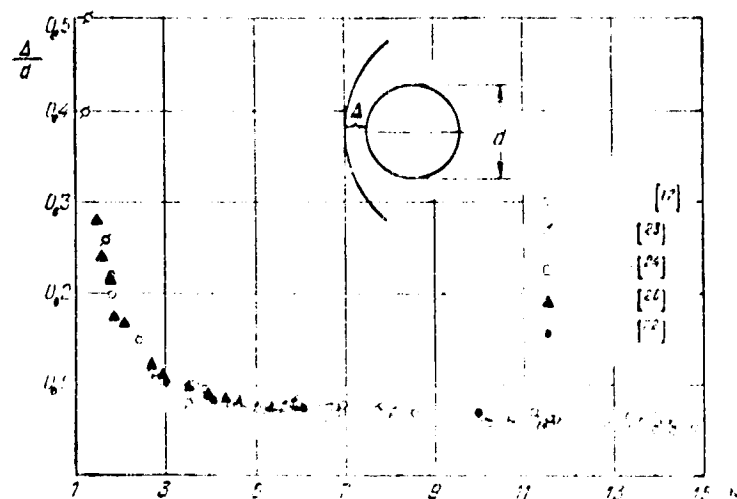


Figure 5.49. Experimental dependence of the relative shock wave standoff Δ/d sphere on M

relative shock wave standoff ahead of ellipsoids of revolution in argon versus M . Figure 5.53 shows the shock wave standoff as a function of a/b for models of ellipsoids of revolution for $M = 4$.

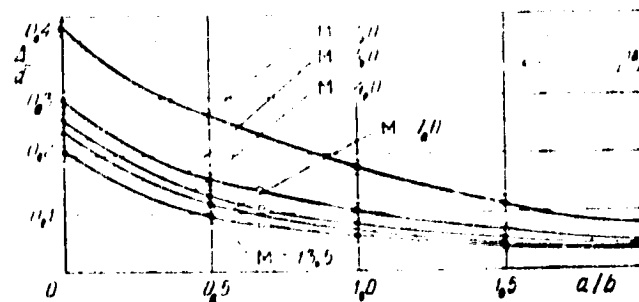


Figure 5.50. Experimental dependence of relative shock wave standoff Δ/d ahead of ellipsoids of revolution on ellipsoid semiaxis ratio

Figure 5.54 shows the results of shock wave standoff

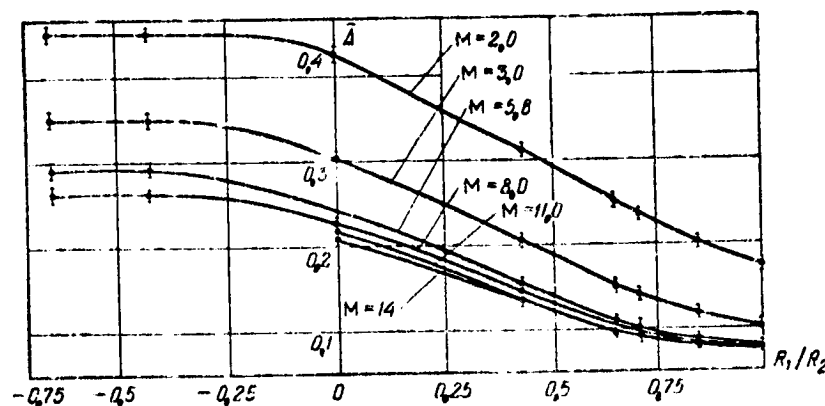


Figure 5.51. Experimental dependence of relative shock wave standoff ahead of segmental front surface on M

measurements on a hemisphere in gases with constant specific heat ratio. In plotting the standoff as a function of the quantity $\frac{x-1}{x+1}$, it was found that in the selected coordinate system, the experimentally measured standoff values for all the model shapes examined lie near straight lines, whose slope is independent of M and varies only with change of the model nose shape. On the basis of this fact, approximating formulas in the following form were proposed in [18]:

$$\Delta = k \left(\frac{x-1}{x+1} \right) + c(M-1)^2$$

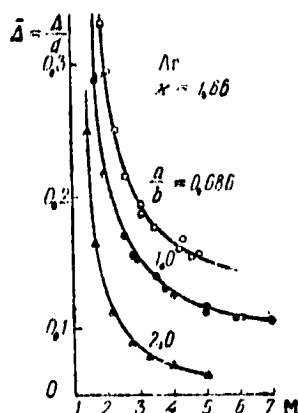


Figure 5.52 Experimental dependence of relative shock wave standoff ahead of ellipsoid of revolution in argon on M

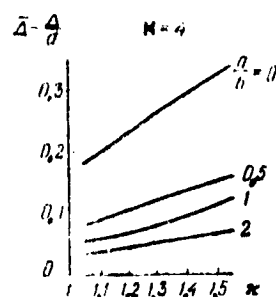


Figure 5.53. Experimental dependence of relative shock wave standoff ahead of ellipsoids of revolution on specific heat ratio κ

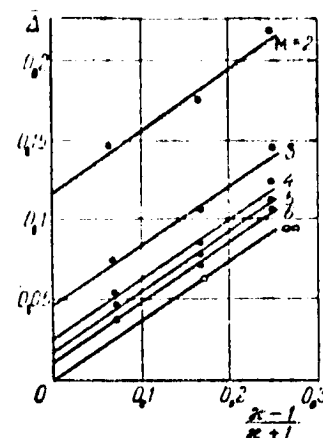


Figure 5.54. Experimental dependence of relative shock wave standoff on hemispherical model on the parameter $\kappa = 1.4$

where α , c , and n depend on the magnitude of the ellipsoid of revolution semi-axis ratio a/b .

It has been established in several studies that the dimensionless bow shock wave standoff is inversely proportional to the gas density ratio in a normal shock wave ρ_2/ρ_1 . The empirical relation for ellipsoids of revolution was obtained in [18]:

$$\bar{\Delta} = \frac{0.8 (b/a)^{0.8}}{\rho_2/\rho_1}, \quad (5.67)$$

which agrees well with the expression for the hemisphere obtained in [19]: $\bar{\Delta} = \frac{0.78}{\rho_2/\rho_1}$.

The magnitude of the specific heat ratio may change at high flight speeds upon passage through a compression shock. Depending on the stagnation temperature, there will be excitation of the vibrational degrees of freedom of the gas molecules, dissociation, and ionization behind the shock wave. These physical processes affect the shock wave standoff near the stagnation point. Figure 5.55 shows data on measurement of the shock wave standoff from an 8 mm-diameter

sphere in a gaseous medium consisting of 60% xenon and 40% nitrogen at a pressure of 20 mm Hg and velocities to 4000 m/sec [20]. The upper theoretical curve 1 corresponds to the "frozen" flow case, when excitation of the vibrational degrees of freedom and dissociation can be neglected.

The lower curve 2 corresponds to fast excitation of the vibrational degrees of freedom and dissociation of the gas, so that an equilibrium process

is realized. The experimental values 3 lie between these theoretical curves. The results show that delay of dissociation and excitation of the vibrational degrees of freedom is observed in this case for $M < 17$. For $M > 17$, this lag is considerably shorter than the gas particle residence time in the space between the shock and the front of the sphere.

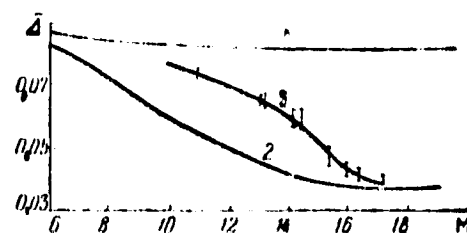


Figure 5.55. Influence of vibrational degrees of freedom and dissociation on shock wave standoff

In addition to shock wave standoff, the shadowgraphs were used to measure shock wave radius of curvature near the stagnation point. Figures 5.56 and 5.57 show the results of measurements of this parameter for various ellipsoids of revolution and bodies of revolution with segmental nose of different radius. Figure 5.58 shows the shock wave shape ahead of a sphere for several values of M .

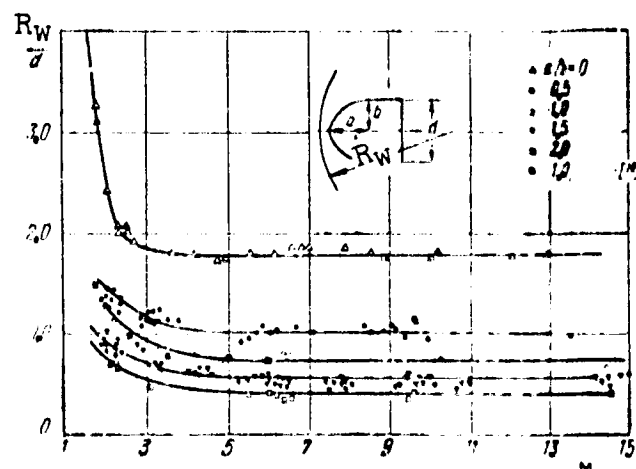


Figure 5.56. Experimental dependence of shock wave radius of curvature near stagnation point ahead of ellipsoids of revolution on M

Measurements were made in [21] in free flight of the sonic point location on the model surface. Flow visualization was achieved by creating

artificial roughness on the smooth model in the form of scribe lines about 0.05 mm deep. Disturbance lines were clearly visible on the shadowgraphs of the flow around the model in the local supersonic flow regions. The sonic point location on the model was determined on the basis of the appearance of the first disturbance lines.



Figure 5.59. Shadowgraph of flow around nose in the form of an ellipsoid of revolution with disturbance lines

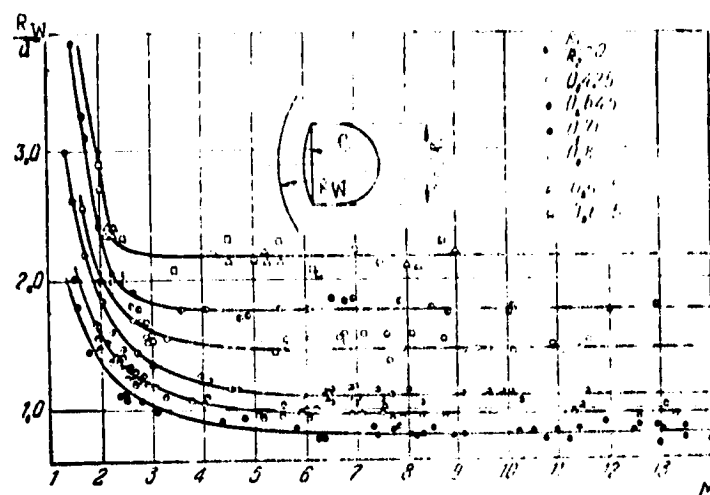


Figure 5.57. Experimental dependence of shock wave radius of curvature near stagnation point of segmental front surface on M

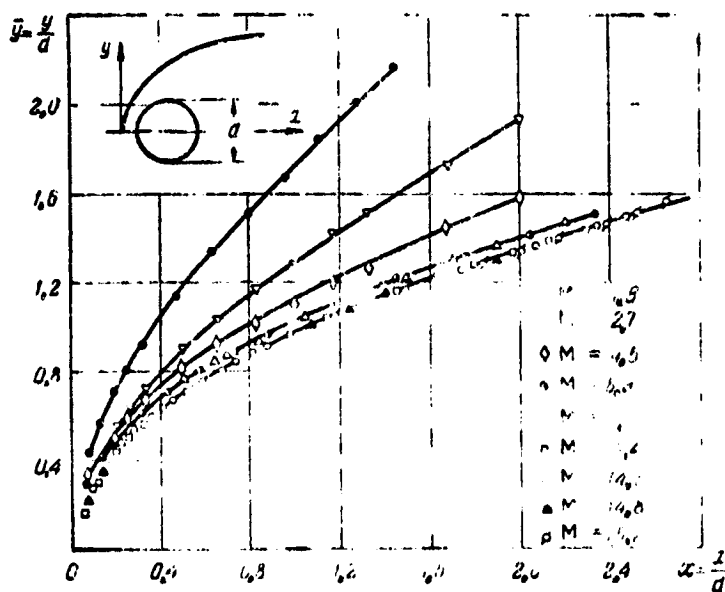


Figure 5.58. Shape of shock wave ahead of sphere for various M

Figure 5.59 shows a photograph of the shadow pattern around a rough ellipsoid of revolution model with semiaxis ratio $a/b = 0.667$. The results of sonic point location measurement on ellipsoids of revolution from tests in air are shown in Figure 5.60. The sonic point location data obtained by ballistic method and from measurement

/301

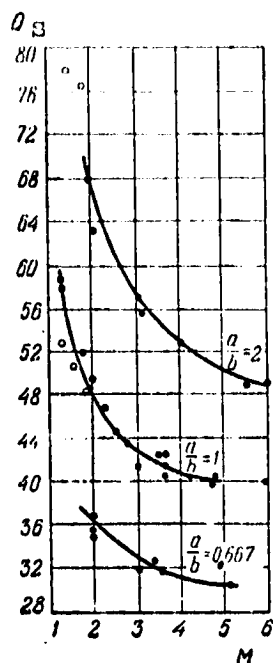


Figure 5.60 Experimental dependence of sonic point location on ellipsoid of revolution as function of M

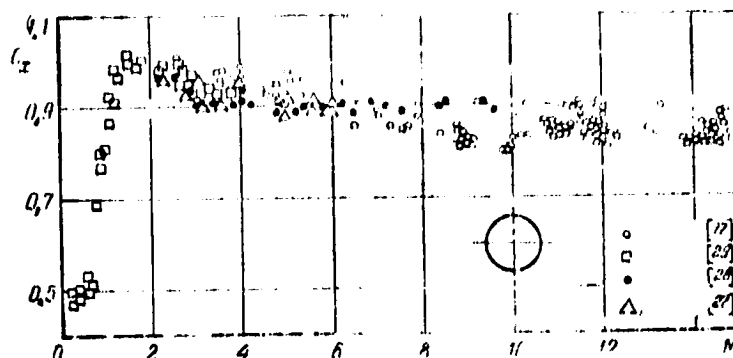


Figure 5.61. Experimental dependence of sphere drag coefficient on M

of the pressure distribution in wind tunnels yield satisfactory agreement.

2) Drag coefficient. The drag coefficient is easier to measure in ballistic experiments than the other aerodynamic characteristics. A large number of studies have been made of models of quite diverse shapes, from very simple bodies to models of flight vehicles of complex form. We shall present data from systematic studies of the drag coefficient of spherical, ellipsoidal, segmental, and conical models.

The largest amount of data has been collected on the aerodynamic characteristics of the sphere, whose form has become traditional for the basic calibrational models in various aerodynamic laboratories.

Figure 5.61 shows the results of a study of the relation $C_x f(M)$, [302] obtained independently in several laboratories by the ballistic method. In [27, 28, 29], the experiments were conducted by launching spheres into air at rest, while in [17] the experiments were conducted in an aeroballistic tunnel. The data shown correspond to the high Re range (10^6 and up). The relation $C_x f(M)$ has the characteristic form with marked increase of the drag coefficient in the M

region and smooth decrease of C_x for $M > 2$. For $M > 8$, the sphere drag coefficient is practically independent of M .

Measurements were made in [27] of the drag coefficient of a sphere in various gases. As a result of these measurements, it was possible to plot the experimental curves as a function of the specific heat ratio $\kappa = c_p/c_v$ (Figure 5.62). Argon ($\kappa = 1.67$) was used as the monatomic gas, air ($\kappa = 1.4$) was used as the diatomic gas, CO_2 ($\kappa = 1.29$) was used as the triatomic gas, and Freon-12 ($\kappa = 1.139$) was used as the polyatomic gas.

The experimental results indicate that at supersonic velocities the blunt body drag coefficient depends significantly on the magnitude of the specific heat of the medium.

The results of ellipsoid of revolution drag measurements are shown in Figure 5.63. These measurements were made on models with ellipsoid semiaxis (a/b) in the range from zero to two.

The experimental data on the drag coefficient of segmental bodies of revolution are shown in Figure 5.64. The drag of models with various ratio of the frontal surface radius to the radius of the cylindrical part of the model was measured in the experiments. The most rounded model was the hemisphere, then the blunting was increased; for $R_1/R_2 = 0$, the model was the flat end of a cylinder, and for negative values of R_1/R_2 , the frontal surface was concave. The drag increases monotonically with

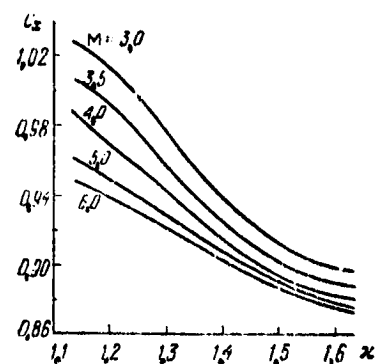


Figure 5.62. Experimental dependence of sphere drag coefficient on κ

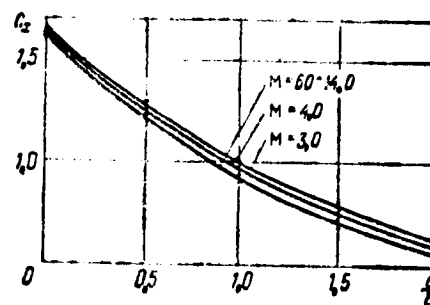


Figure 5.63. Experimental dependence of ellipsoid of revolution drag coefficient on semiaxis ratio

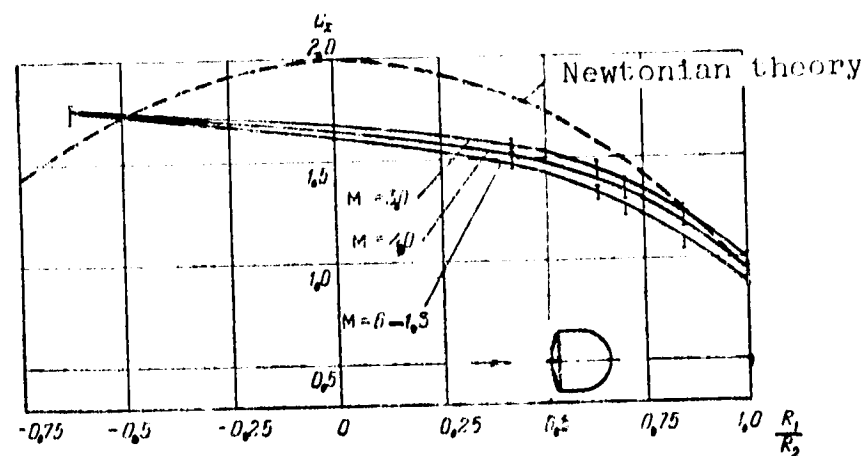


Figure 5.64. Experimental dependence of the drag coefficient on the radius of curvature of a segmental frontal surface

reduction of the ratio R_1/R_2 . The concave surface has somewhat higher drag in comparison with the flat face.

If we relate the drag of the segmental body to the drag of the sphere, then in the region of positive values of the ratio R_1/R_2 we obtain a universal curve which depends only on R_1/R_2 . /304

This curve can be approximated by the expression:

$$\frac{C_{x_s}}{C_{x_N}} = 1.77 + 0.128 \frac{R_1}{R_2} - 0.898 \left(\frac{R_1}{R_2} \right)^2. \quad (5.68)$$

This expression is valid for supersonic and hypersonic velocities, corresponding to $3 < M < 15$.

Figure 5.65 shows systematic results of a study of the drag coefficient of the sharp and spherically blunted circular cones whose geometric data are given in Table 5.4. Re was of the order of $(7 - 12) \cdot 10^6$, i.e., corresponding to the flow region in which viscous interaction is negligibly small. These results were obtained in [30], and are compared with the data of subsequent theoretical calculations [31, 32, 33].

TABLE 5.4*

θ_s	λ	r/D	h/D	θ_s	λ	r/D	h/D
15°	1,0	0	0	35°	1,0	0	0
15°	0,8	0,131	0	35°	0,8	0,19	0,533
15°	0,6	0,261	0,533	35°	0,6	0,38	0,533
15°	0,4	0,391	0,533	50°	1,0	0	0,533
24°	0,8	0,153	0,533	50°	0,8	0,275	0,533
24°	0,6	0,306	0,533	50°	0,6	0,549	0,533
24°	0,45	0,422	0,533	70°	1,0	0	0,533

*Translator's note. Commas in numbers represent decimal points.

The experimental grids are presented in the form of cone C_x versus semivertex angle θ_s for various values of the aspect ratio λ in the range $M = 8 - 14$, when the drag coefficient is stabilized with respect to M . These curves form the region of drag coefficients for any possible pointed or blunted cones. The solid curves are drawn through the experimental values and the values obtained by interpolation of experimental data; the dashed curves are the experimental values of the drag coefficients of the spherical segments, into which the blunted cones degenerate in the limit.

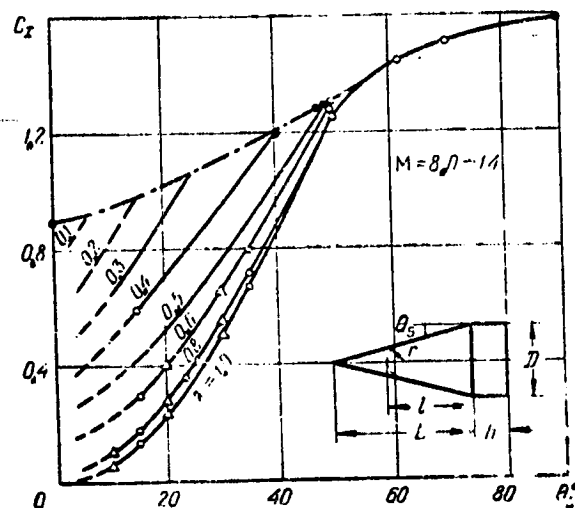


Figure 5.65. Experimental dependence of cone drag coefficient on semivertex angle and bluntness

The dashed curves correspond to the blunted cone drag coefficient, obtained as the sum of experimental drag coefficients of the spherical segment and the conical surface. These values may differ somewhat from the actual values because of interference between the blunting and the spherical surface. However, in most cases, this interference is small, and amounts to 10% only for a few configurations. Since the base pressure drag contribution is less than 3%

for large M and Re , good agreement was found between the experimental data and the theoretical values obtained without account for friction and base pressure.

In the range of moderate cone semivertex angles (up to $40 - 50^\circ$), two parameters — cone semivertex angle θ_s and aspect ratio λ — have a significant influence on the drag coefficient. For large values of θ_s , there is very little influence of the aspect ratio on the drag coefficient. In this case, the pointed cone drag agrees with the drag of the corresponding spherical segment inscribed in the cone. For $\theta_s > 50^\circ$, the flow around the pointed cones is similar to that around blunt bodies. This is seen in Figure 5.66, which shows a shadowgraph of the flow around a sharp cone with $\theta_s = 70^\circ$ for $M = 9.8$.

3) Pressure measurement. The method of measuring the pressure on free flying bodies with the use of a rubber membrane, which has shown good results, was used to measure the base [34] and the stagnation point [35] pressures.

The method amounts to the following. A cavity located in the base of the model is sealed by a rubber diaphragm. In flight, under the action of the difference between the cavity pressure p_c and the base pressure p_b , the rubber diaphragm deflects, and this deflection is recorded on a photograph of the flying model. (Figure 5.67). The models with the rubber diaphragm are calibrated versus pressure difference prior to the experiment, as a result of which we obtain the diaphragm deflection dependence on the pressure difference Δp . In analyzing the experimental data, the inertial and frequency characteristics

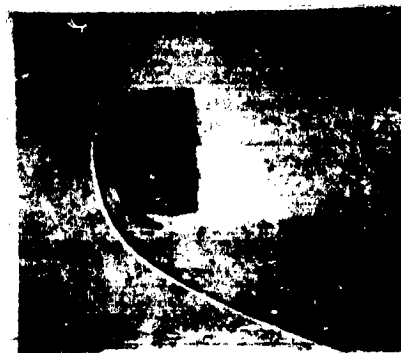


Figure 5.66. Shadowgraph of flow around narrow cone model with large semivertex angle by departing shockwave ($\theta_s = 70^\circ$ with a cylinder at $M = 9.8$ and $Re = 9.4 \cdot 10^6$)



Figure 5.67. Shadowgraph of hemisphere-cylindrical model with diaphragm-type pickup for measuring base pressure

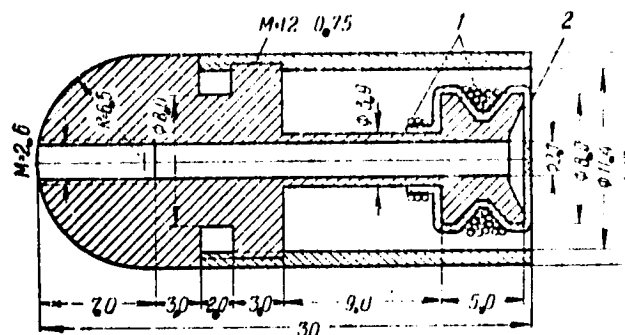


Figure 5.68. Construction of model with diaphragm-type pickup for measuring stagnation point pressure:

1 — winding; 2 — diaphragm

of the diaphragm and also the deviation of the gas expansion

process in the cavity from an isothermal process were taken into consideration.

For measurement of the stagnation point pressure, the cavity in the base of the model, covered by the rubber diaphragm, was connected by a passage with a pressure pickup at the stagnation point (Figure 5.68). Since the magnitudes of the measured pressures amounted to several atmospheres, it was necessary to use rubber diaphragms of greater thickness than when measuring the base pressure. In this case, the pressure difference Δp is determined by the difference between the stagnation point pressure p_0 and the base pressure p_b , with 307 account for the correction δp due to the inertial forces acting on the membrane:

$$\Delta p = p_0 - p_b - \delta p.$$

The quantity Δp was determined from the calibration curve as a function of diaphragm deflection, and the base pressure was determined from previously conducted experiments for the same M and Re conditions.

Figure 5.69 shows the ratio of the stagnation point pressure to the static pressure p_1 as a function of M . The experimental

points were obtained for Re on the order of 10^6 . The dashed curve corresponds to calculation using the Rayleigh formula. Figure 5.70 shows the base pressure measurement results.

4) Study of the staging process.

In analyzing the separation of parts or individual stages of flight vehicles in supersonic flow, it was found that the flow characteristics obtained in wind tunnel flow tests of stationary models spaced at various distances do not reflect certain essential characteristics of the staging process, particularly for small distances between the separating bodies. Specifically, marked change of the static pressure — increase of the rarefaction in the separation zone — in comparison with the flow around the stationary bodies was noted. The gas parameters in the separated flow region between the bodies depend on the rate of separation, even for a very small magnitude of this in comparison with the approaching flow velocity. A theoretical

explanation of the phenomena in the stage separation case and experimental data obtained using the aeroballistic method are presented in [36, 37]. If two bodies positioned coaxially in a supersonic stream separate with small velocity u_s , and the distance between them does not exceed some value L_* (on the order of several calibers), depending basically on the transverse dimensions of both bodies and M_∞ , the flow around the bodies takes place with the formation of a single separation region. The supersonic flow separating from the forward body attaches to the second body near its outer edge, and a free boundary layer develops between the outer inviscid flow and the gas

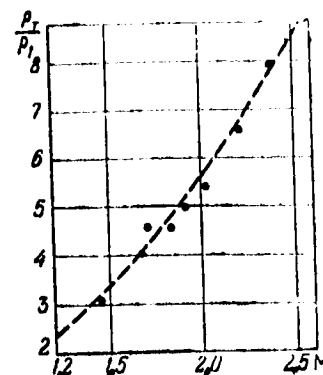


Figure 5.69. Experimental hemisphere stagnation point pressure dependence on M

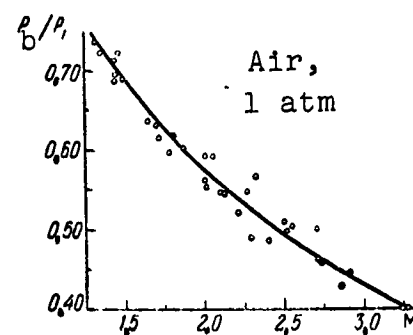


Figure 5.70. Experimental dependence of hemisphere-cylinder model base pressure on M

in the separation zone. If there is relative velocity of the bodies the flow between them will be unsteady. When modeling the staging process, it is necessary to maintain, in addition to geometric similarity, a constant ratio of the separation velocity to the free-stream velocity u_s/v_∞ .

Figure 5.71 shows sequential pictures of the staging of a composite model fired from a 100 mm-caliber gun with velocity corresponding to $M = 3$. The model consisted of a conical forebody and a

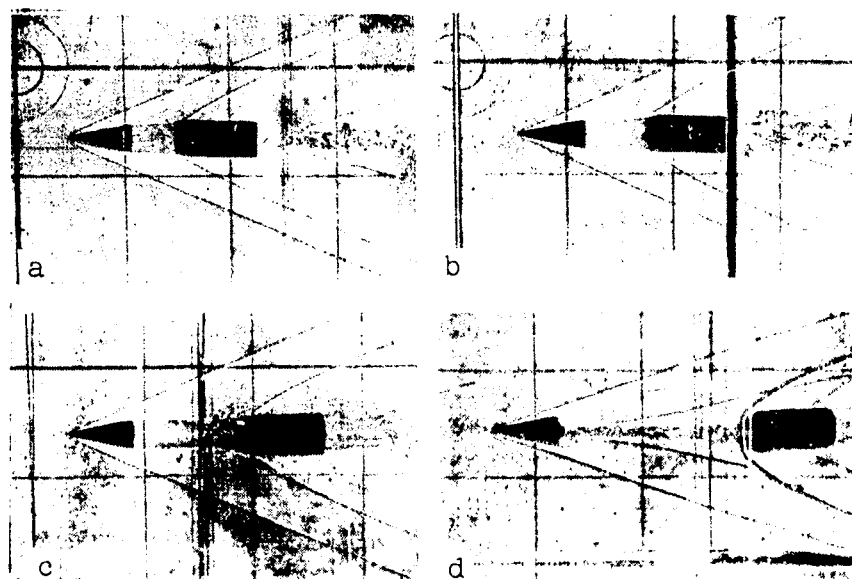


Figure 5.71. Shadowgraphs of flow around cone at various instants of time as the cone separates from a cylinder

cylindrical afterbody. The afterbody, having higher drag (per unit mass), gradually lagged behind the forebody in flight. Measurements were made of the base pressure on the cone using a rubber membrane transducer. Figure 5.72 shows the results of measurement of the base pressure coefficient C_p as a function of the relative distance l/l_0 between the stages. We see that there is a minimum C_p of the base pressure for small distances between the separating stages.

As is well known, with increase of the distance between the separating stages up to some value, there is restructuring of the flow, accompanied by closure of the boundary layer on the axis of symmetry, disruption of the single separated zone between the bodies, and formation of the conventional base flow behind the first body.

Figure 5.71 shows various phases of the flow restructuring: deflection of the visible edge of the separation zone toward the axis of symmetry, closure of the edges at the centerline near the second body, and formation of the base flow. Here, the restructuring distance l_* is equal to 5 - 6 calibers or more, while in flow tests of stationary models for the same conditions $l_* = 3.5 - 4$ calibers.

In many practical problems, it is necessary to examine the process of separation from a flight vehicle of a comparatively lightweight and small structural elements — for example, the plate covering the flight vehicle afterbody hatch. The positively ejected coverplate travels in the base flow region, experiencing very low drag, with nearly constant absolute velocity. The vehicle body experiences considerable deceleration under the action of the aerodynamic forces, and its absolute velocity decreased markedly. Therefore, after some time the coverplate may again begin to approach the main body. This convergence has been observed repeatedly in conducting aeroballistic experiments. However, if the initial impulse is sufficiently great, the coverplate will begin to experience considerable deceleration at some distance and will lag behind the body.

Figure 5.73 shows shadowgraphs of a flying model with a separating coverplate. Experiments showed that the required initial coverplate ejection velocity for the model tested amounted to 2% of the flight velocity. It is obvious that the magnitude of the

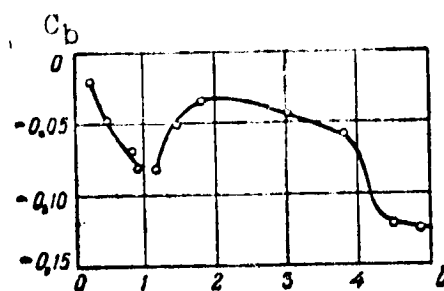


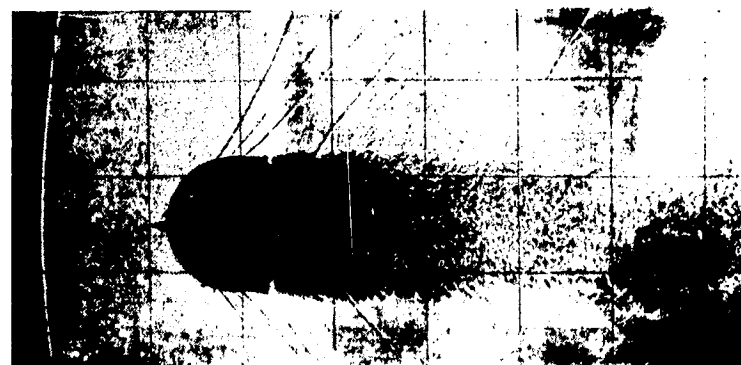
Figure 5.72. Experimental variation of coefficient of base pressure on cone as it separates from a cylinder

required ejection velocity depends on the ratio of the transverse dimensions and the masses of the separating bodies.

5) Measurement of thermophysical characteristics. In this section, we shall present some examples of measurement of the thermal fluxes, melting, and gas radiation characteristics for model flight at high speeds. There are three techniques for measuring thermal fluxes on free flying models — using telemetry, calorimetry, and determining material melting onset.



a



b

Figure 5.73. Shadowgraphs of flow around model with attached (a) and separating (b) coverplate in the base region

The first technique is based on using thermocouple measurements on the flying model (see §3.11).

Figure 5.74 shows the thermal flux as a function of velocity from measurements made in air [38]. Also shown are the theoretical curve from [40], and the experimental data obtained in shock tube experiments.

The second technique for measuring thermal fluxes involves measuring the amount of heat required by the model during flight along the ramp as a result of aerodynamic heating [39]. After recombination in the catcher, the model enters a calorimeter, in which the total amount of heat is measured.

The drawback of the method is the measurement of only the average thermal flux, and the primary limitation is the high velocity, when the model loses some of its mass in flight as a result of melting or ablation. Figure 5.75 shows the thermal flux, referred to the hemisphere frontal surface area, as a function of velocity, which is compared with the theoretical calculations from [40].

Finally, the third method, based on indirect thermal flux determination, involves determining the onset of model melting [39]. The calculations of the thermal flux are made in accordance with the path (and therefore time) traveled prior to the beginning of melting. Figure 5.76 shows the thermal flux parameter $q \sqrt{\frac{R}{p_0'}}$ (where R — hemisphere radius, p_0' — total pressure at the stagnation point) as a function of the difference $(h_0 - h_w)$ between the stagnation enthalpy and the wall enthalpy. Also shown are the points obtained by passive telemetry and from shock tube experiments.

The ballistic test method has been used to conduct experiments and determine the initiation of model melting. The authors of [41] obtained such results on hemispherical models made from Wood's alloy.

Figure 5.77 shows shadowgraphs of the flow around a model at the beginning and end of the test range. While no change of the model nose shape is observed in the first picture, in the last

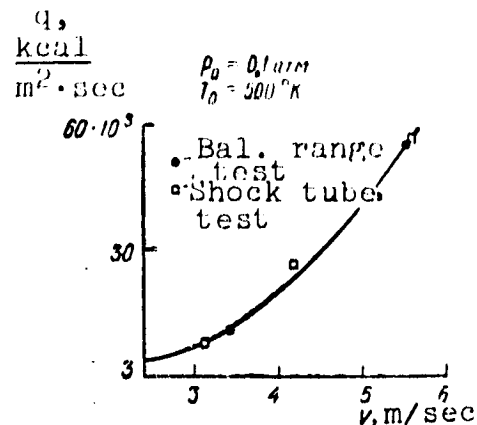


Figure 5.74 Experimental dependence of thermal flux at stagnation point of hemisphere on the velocity, obtained by passive telemetry

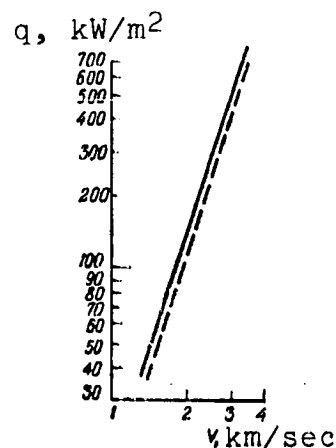


Figure 5.75. Experimental dependence of average thermal flux, referred to a hemisphere, on the velocity, obtained by calorimetry

pictures we see the melting process. A film of molten metal flows from the trailing edge of the model, and is drawn into the base region. We also see the characteristic dust-like wake leaving the model surface in the region of angular coordinate values $\theta = 50^\circ$. K. Toward the end of the flight, the model acquires the characteristic spherically blunted cone shape.

Figure 5.78 shows the curve of mass ablation (along the normal to the model surface) as a function of the angular coordinate θ . The ablation magnitude is nonuniform along the contour, and has a peak at $\theta = 23^\circ$. According to the authors of [41], the ablation peak indicates the turbulent nature of the heat transfer at small distances from the stagnation point.

Results were presented in [9] on melting of aluminum models and models made from materials with quite high melting points. Interesting phenomena were discovered, associated with interaction of the test model material with the hypersonic air stream. For example, in the aluminum model melting case, the beginning of material ablation from the model surface was accompanied by a bright flash, which was seen on the pointed cones with weak air radiation intensity. The brightness of the flash exceeded by about a factor of 1000 the air radiation intensity in the shock layer.

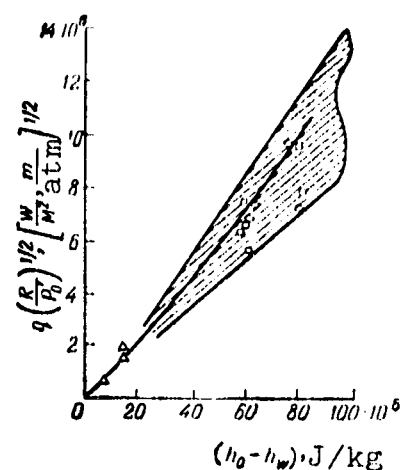


Figure 5.76. Experimental dependence of the parameter $q \sqrt{\frac{R}{R_0}}$ on the difference between the stagnation enthalpy and the wall enthalpy

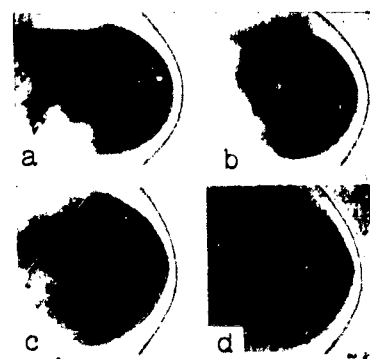


Figure 5.77. Shadowgraphs of flow around hemisphere models melting in flight

/313

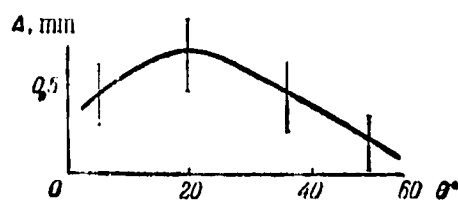


Figure 5.78. Experimental dependence of mass ablation from hemisphere model on angular coordinate

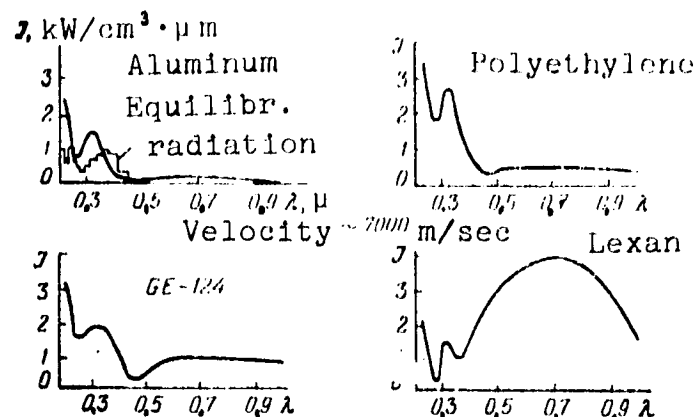


Figure 5.79. Radiation spectra in shock layer near models made from different materials

Comparison of the radiation spectra in the shock layer for four

different materials: aluminum, polyethylene, GE-124, and lexan (polycarbonate) (Figure 5.79) at launch velocity 7000 m/sec, and static density 0.02 times the atmospheric density, showed that the differences in the radiation spectra in the shock layer are due to differences in the model materials. The difference in the IR part of the spectrum is particularly strong. These data indicate that for a definite flight speed and altitude, ablation product radiation may be a source of considerable heating, in certain cases even greater than the heating owing to air radiation, particularly for materials similar to lexan. The radiation spectra of the ablation products in the shock layer and in the wake behind a model made from GE-124 are qualitatively the same (Figure 5.80). These spectra were obtained by excluding the air radiation spectrum from the overall radiation spectrum in the shock layer and in the wake. The radiation spectrum of the air in the shock layer was determined in experiments with aluminum models, for which there was no ablation at the given temperatures.

/314

/315

Figure 5.81 shows the total radiation energy behind a detached shock wave for high model flight velocities in the thermodynamic equilibrium case [42]. A more detailed study of the radiation spectra in the shock layer and in the wake behind the body was made in [43]. Figure 5.82 shows the radiation spectrum for a typical model

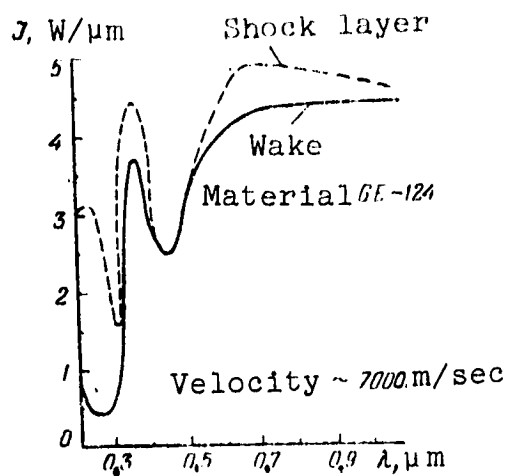


Figure 5.80. Comparison of radiation spectra of model material ablation products in the shock layer and in the wake behind the model

subjected to ablation. The spectrum consists of continuum radiation due to free electron interaction with atoms and ions, and the continuum radiation owing to the ablation products. The molecular spectrum was represented by the

$N_2^+(1-)$ and $N_2(2+)$ band systems and by the CN band (violet and red) systems, which are usually present in the boundary layer or in the wake behind the body. Moreover, there are also atomic lines. For example, the bright hydrogen line 2478 \AA and the strong nitrogen atom line located in the red part of the spectrum were recorded. This spectrum was recorded during flight of a sphere with velocity 6.6 km/sec in air, with static density ρ amounting to 8% of atmospheric density. The characteristic spectrum recording time was only 0.05 m sec .

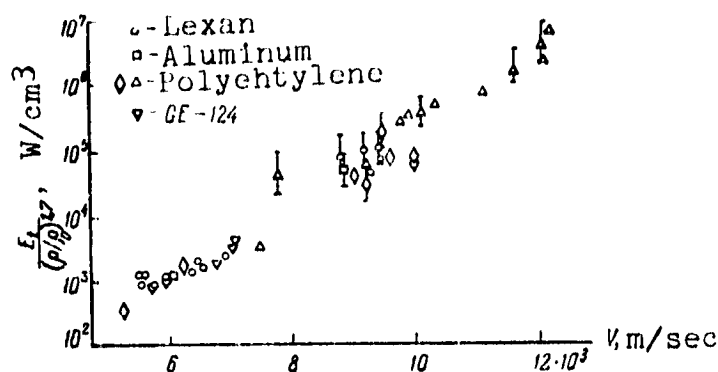


Figure 5.81. Dependence of total radiation energy behind shock wave on velocity for the thermodynamic equilibrium case

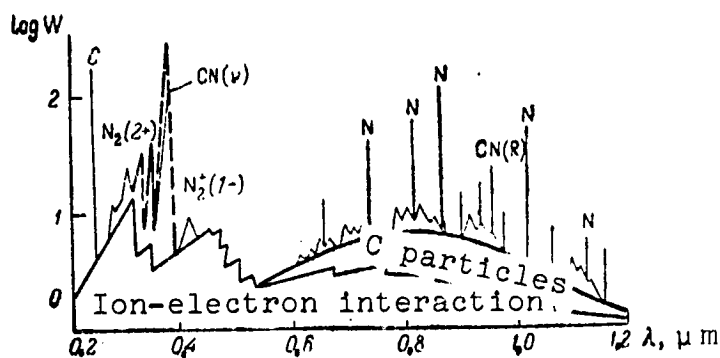


Figure 5.82. Radiation spectrum near spherical model subjected to ablation for flight velocity 6.6 km/sec

6) Study of wake characteristics. In recent years, the wake problem has raised considerable interest among gasdynamicists. While

previously this problem was important only in astronomy in connection with study of the wake behind meteoritic bodies, in recent years it has taken on great practical importance in detecting ballistic missile nosecones, and in radio communication with spacecraft during their entry into the dense layers of the atmosphere. One of the basic methods for studying the wake is the aeroballistic method, since the supports required when conducting tests in wind tunnels introduce considerable distortions into the wake flow.

The wake of a body traveling at supersonic speed is usually considered to be that part of the flow which passes through the boundary layer on the surface of the body and then enters the region behind the body (Figure 5.83). This part of the flow is the primary

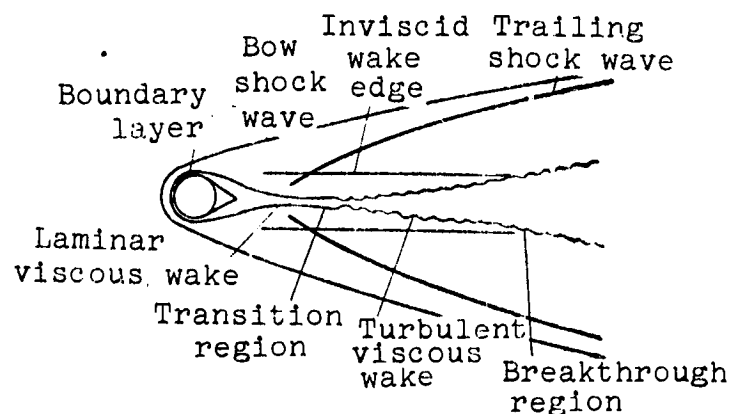


Figure 5.83. Flow in wake of model traveling at supersonic speed

source of radiation and free electrons. In the case of very slender bodies, the wake generated by the boundary layer is primary from the viewpoint of optical and radar observations of the flowfield. On the other hand, in the case of blunt bodies, the strong bow shock wave ahead of the body is a second significant source of electrons and radiation.

At supersonic speeds, the wake subdivides into two parts — the viscous wake arising as a result of viscous interaction with the body, and the inviscid wave arising as a result of heating in the

shock wave, primarily in the inviscid part of the flow. At comparatively high Re (above 10^5), the viscous wake becomes unstable and, at some distance downstream of the body, transitions to turbulent flow. At some moment of time, the inviscid wake is completely filled by the viscous wake, which breaks through into the surrounding cold gas. This leads to changes of the physical processes which influence the reflection of radar signals and the visible radiation level.

At the present time, various methods have been developed for studying the gasdynamic and electrophysical characteristics of the wake on models in free flight: measurement of the wake geometric characteristics and the velocities on the centerline and across the wake, determination of the region laminar wake transition to turbulent, measurement of the electron concentration and temperature in the wake, and so on.

Figure 5.84 and 5.85 show shadowgraphs of the flow around a sphere with segments of the wake at various distances from the model [55]. Such photos are the basic experimental data from which we can determine by measurement

such wake geometric characteristics as, for example, the wake width at various distances behind the model. Figure 5.86, taken from [44], shows the development of the wake width behind



Figure 5.84. Shadowgraph of flow around sphere with large turbulent wake segment for $M = 2.8$ and $Re = 2 \cdot 10^5$

spheres for different M numbers. The width and length of the wake behind the model are referred to the sphere D diameter. The experimental values correspond to turbulent flow conditions in the far wake, where, according to [46], the following wake width growth law holds:

$$\frac{b}{D} = \text{const} \left(C' \frac{x}{D} \right)^{1/2}. \quad (5.69)$$

Good confirmation of this result is shown in Figure 5.87, taken from [45], in which the experimental data for the far wake width in air

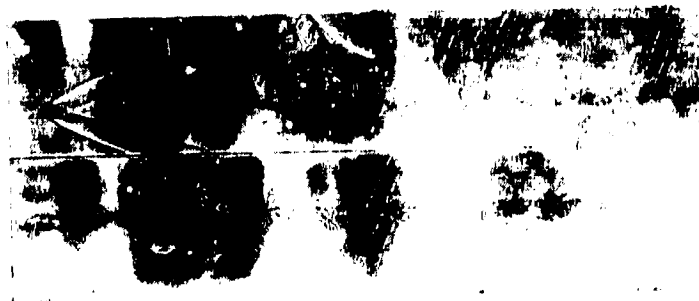


Figure 5.85. Shadowgraphs of flow around sphere with wake segments at different distances from the model. $M = 2.65$. Second photo with far wake segment was obtained 234 msec after the first photo

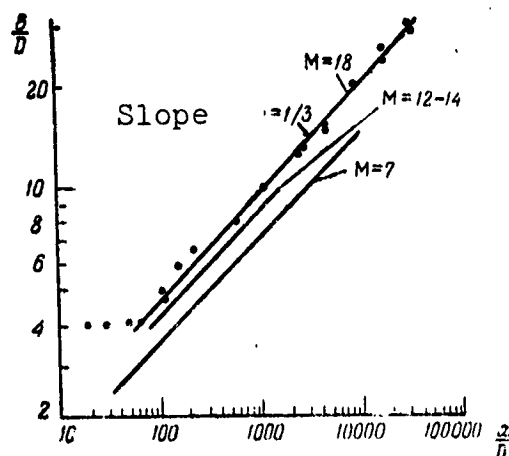


Figure 5.86. Experimental dependence of wake width behind spheres for different M

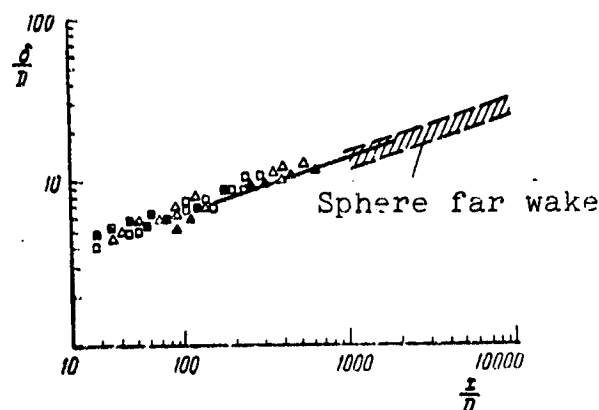


Figure 5.87. Wake development behind sphere and cone models in models in far wake

behind cones and spheres are presented — these data obey the expression:

$$\frac{\delta}{D} = 1.4 \left(C_x \frac{x}{D} \right)^{1/3}. \quad (5.70)$$

Measurements were made of the gas velocities in the wake at various distances behind the sphere. Figure 5.88 shows these results. The filled triangles in Figures 5.87 and 5.88 denote the maximal velocities in the wake. The remaining experimental points were obtained by the time-scan method, which defines the average gas particle velocities in the wake. We note the rapid decrease of the gas

velocity in the wake. Thus, at a distance of 100 calibers, the velocity in the wake is 5 - 10% of the model flight velocity, while at a distance of 1500 calibers, the wake velocity is only 1% of the model flight velocity.

Figure 5.89 shows data from measurement of the velocity profile across the wake. These results were obtained using the tracer particle method; the particle travel during a short time Δt characterizes the local velo-

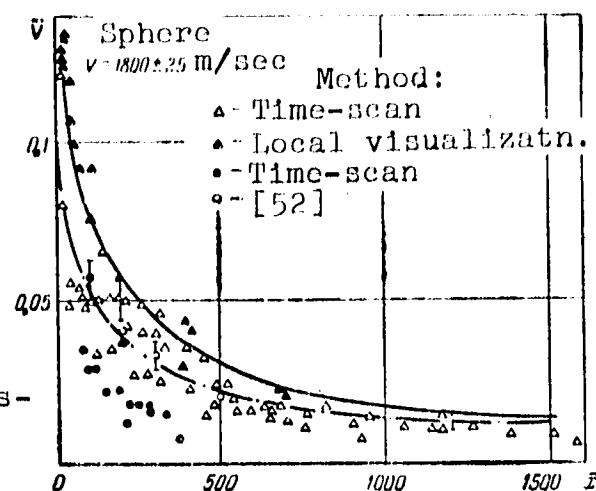


Figure 5.88. Results of average gas velocity measurement in the wake at different distances behind the model

/320

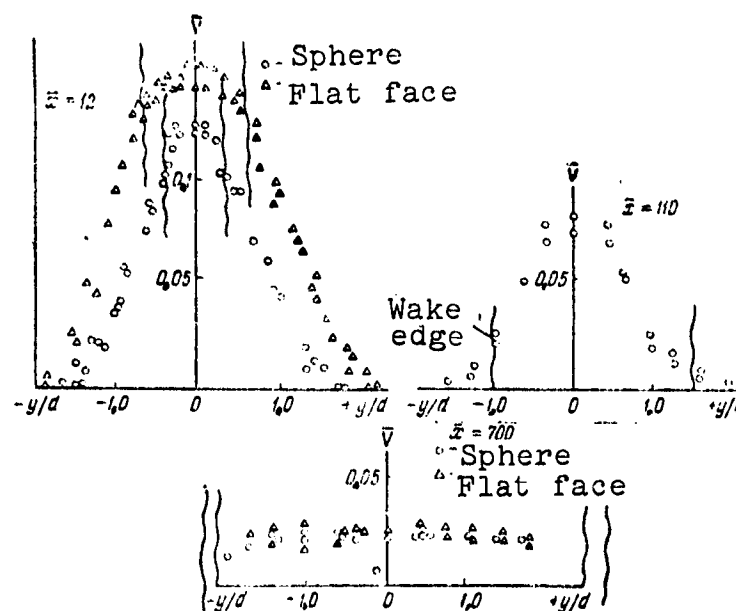


Figure 5.89. Results of velocity profile measurement across the wake at various distances behind the models

city at various points across the wake [47]. At small distances from the model, there is a highly developed velocity profile with maximal value on the wake centerline and decreasing magnitude toward

the edge of the wake. At large distances (700 calibers), the velocity profile becomes more uniform and its magnitude reaches only 2% of the model velocity.

Studies have been made of transition of laminar flow in the wake into turbulent flow [44, 48]. Figures 5.90 and 5.91 present the results of some such studies.

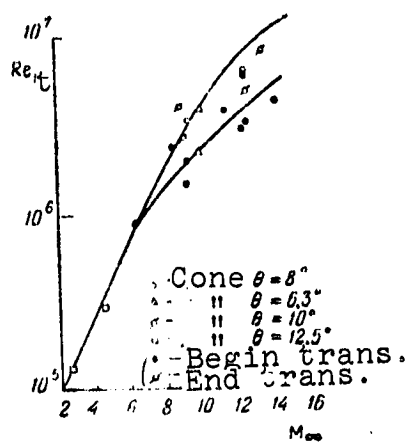


Figure 5.90. Experimental dependence of Re_t of laminar flow transition into turbulent flow in wake behind models as function of M_∞

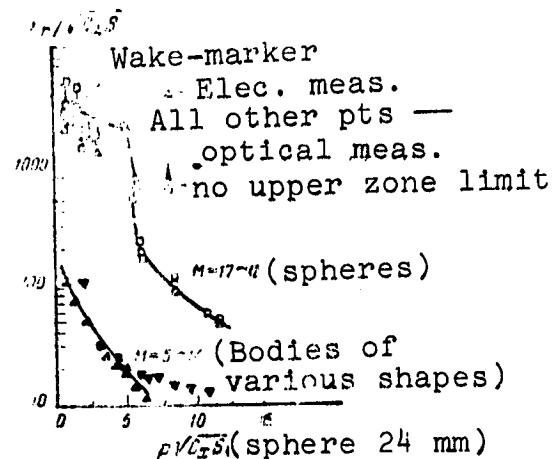


Figure 5.91. Results of transition measurement in wake behind models

Measurements were made of the electron density in the wake behind 4.75 mm-diameter aluminum and copper spheres at velocities 5360 - 6440 m/sec [49], with the aid of a microwave cavity resonator, in which TM_{010} mode oscillations with frequency 441 Hz were excited. The presence of the ionized wake in the resonator changed its complex admittance. The linear electron density (number of electrons per unit length along the resonator axis) in the 10^{12} - 10^6 electrons/cm range) was determined from the output signal phase and amplitude change.

The static pressure has a significant influence on electron density decay. Figure 5.92 shows the results of electron density measurement behind copper spheres in air at flight speeds 4880 - 6160 m/sec for five pressures, from 10 to 160 torr. The electron

density decay curves depend monotonically on the pressure, and the rate of decrease of the number of electrons increases with pressure increase. This indicates the significant importance of the electron capture reaction.

Interesting results were obtained in experiments with aluminum and copper spheres. Figures 5.93 and 5.94 compare the linear electron density behind aluminum

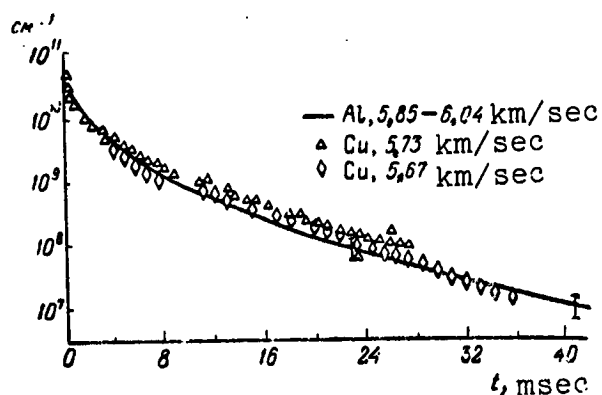


Figure 5.93. Experimental variation of electron density decay with time behind aluminum and copper spheres for 10 torr pressure

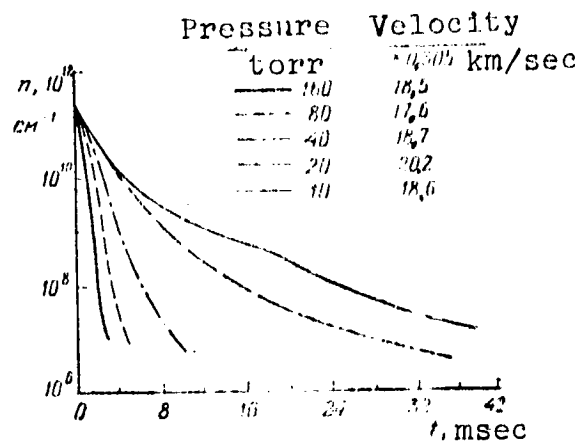


Figure 5.92. Experimental electron density decrease with time for various static pressures

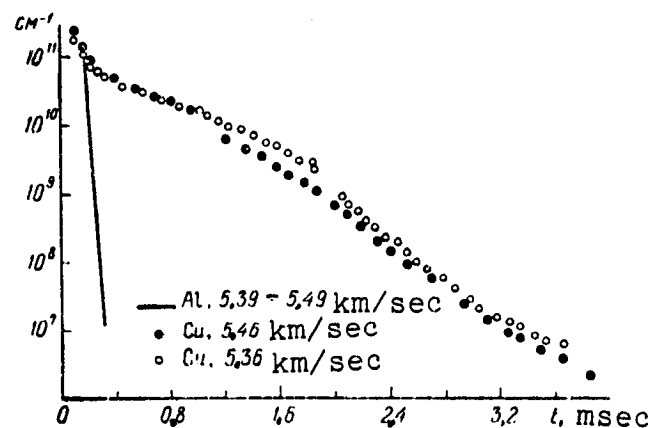


Figure 5.94. Experimental variation of electron density decay behind aluminum and copper spheres for 80 torr pressure

and copper spheres in air for 10 torr and 80 torr pressures, respectively. While in the first case we do not observe any difference in the nature of the curves, there is considerable difference in the second case. The reason is that, at pressures exceeding 40 torr, ablation of the aluminum begins, and this leads to increase of the electron density decay rate.

Measurements based on IR radiation were made in [50] of the temperature in the laminar wake behind 5.6 mm-diameter nylon spheres traveling at 3960 m/sec. The ballistic stand working chamber was filled with 95% N_2 and 5% CO_2 . The CO_2 radiation, which played the role of a gaseous temperature indicator, was recorded by a gold-plated germanium IR radiation sensor and a narrow-band filter with 4.39-micron wavelength. Figure 5.95 shows the wake temperature along its axis. After reaching magnitudes of the order of 2000° K at a distance of twenty calibers from the sphere, the temperature decreases monotonically, and at 200 calibers is equal to 1230° K.

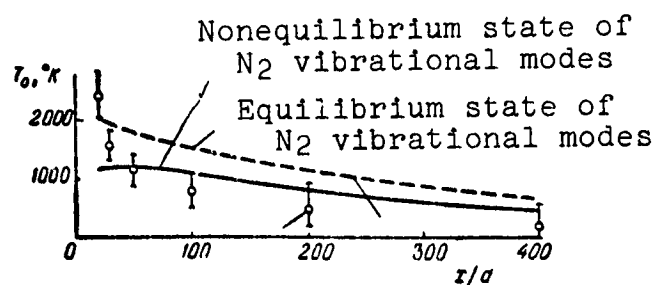


Figure 5.95. Experimental variation of temperature on wake centerline with wake length

7) Shock wave impact.

The ballistic investigation method is used successfully

in studying the characteristics of shock wave impact or the result of incident shock wave interaction with a screen or a model. Moreover, this method approaches most closely the full-scale flight experiment conditions.

Figure 5.96 shows shadowgraphs of shock wave reflection from a screen simulating the Earth's surface. The nature of the reflection changes significantly, depending on the relative model flight trajectory height \bar{h} above the screen. Thus, for sphere flight at $M = 1.35$ and relative height $\bar{h} = 2.26-2.36$ above the screen, the bow wave had a low slope. Near the screen, the wave is transformed so that its front becomes perpendicular to the screen. At this same M , but with increase of the relative height to $\bar{h} = 2.54$, there occurs the so-called irregular (Mach) reflection with a triple point. With further increase of the relative height, regular reflection in the form of an oblique incident shock and an oblique reflected shock is established. It is obvious that to each type of reflection there corresponds its particular characteristic pressure differential at

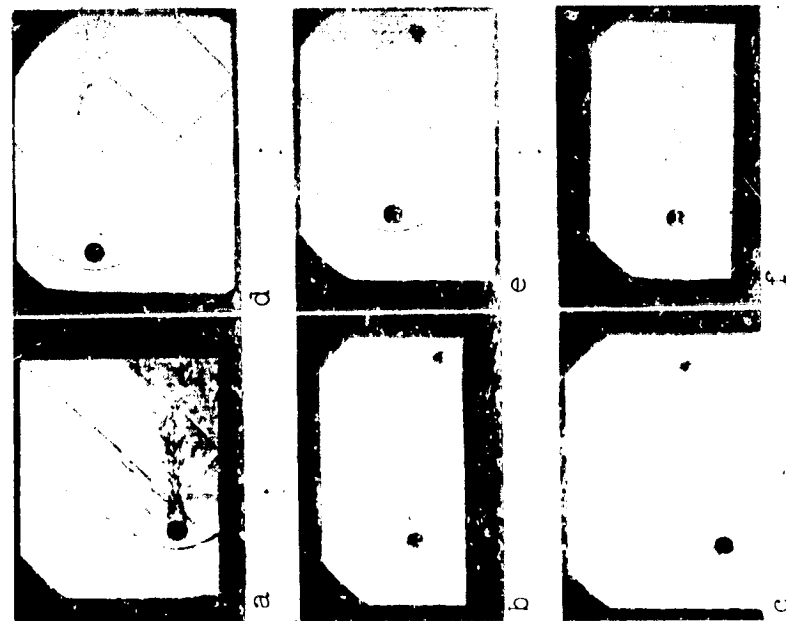


Figure 5.96. Shadowgraphs of shock wave reflection from screen simulating the Earth's surface during sphere flight

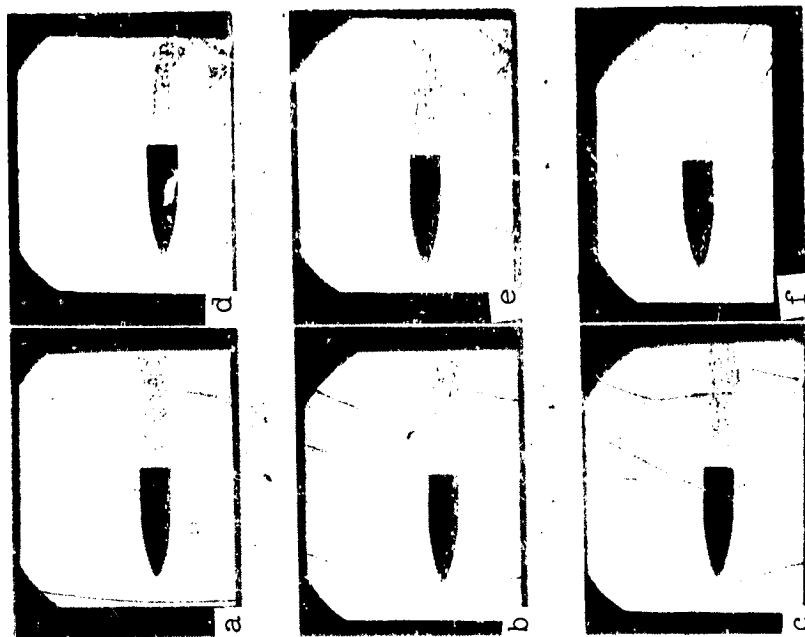


Figure 5.97. Shadowgraphs of shock wave reflection from screen simulating the Earth's surface for flight of 7.62 mm bullet

the point of shock wave reflection. The nature of the shock wave reflection from the screen also changes with change of M . This can be seen in shadowgraphs of the flow around a rifle bullet, shown in Figure 5.97.

We shall present some data obtained in [51] in studying the effect of shock waves which arise during the flight of a bullet, using the notations shown in Figure 5.98. Figures 5.99 - 5.101 show the shock wave intensity at the point of its incidence on the screen, relative length of the N-wave, and pressure gradient in the N-wave. These results were obtained at Mach numbers from 1.1 to 2.6 for relative heights $3 < h < 10$.

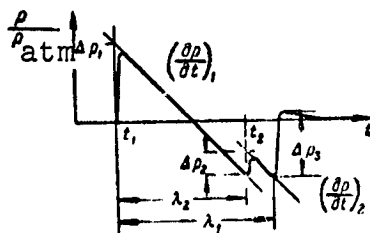


Figure 5.98. N-wave parameter notations

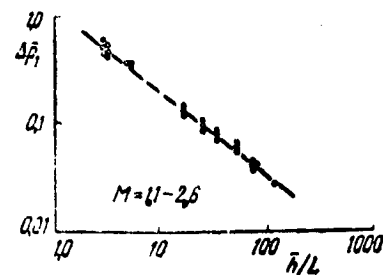


Figure 5.10. N-wave intensity at point of incidence on screen

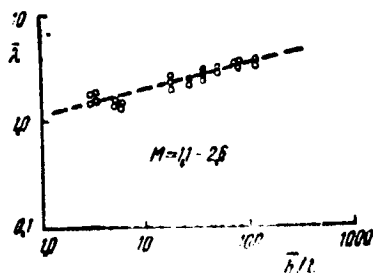


Figure 5.100. Relative length of N-wave

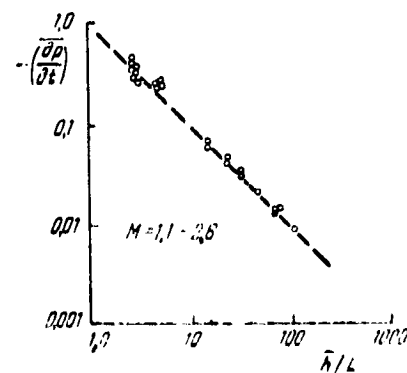


Figure 5.101. Pressure gradient in N-wave

The examples considered in this section demonstrate convincingly 4326 the capabilities and advantages of the aeroballistic study method for the solution of a wide range of gasdynamic problems.

Aeroballistic tests make it possible to determine aerodynamic characteristics by an independent (in comparison with wind tunnel experiment) method. Moreover, the aerodynamic characteristics can be obtained at large M and Re , simultaneously.

Thanks to the absence of supports and flow nonuniformity, the aeroballistic research method offers great possibilities for studying the wake and base region flow characteristics.

Staging, shock wave impact, and several other gasdynamic phenomena are most successfully simulated in ballistic ranges.

The aeroballistic research method plays an important role in studying high-temperature phenomena associated with intramolecular processes and radiation.

REFERENCES

CHAPTERS I AND II

1. Aerofizicheskiye issledovaniya sverkhzvukovykh techeniy (Aero-dynamic Studies of Supersonic Flows). Collection of articles. Moscow, Nauka Press, 1967. /327
2. Serebryakov, N. Ye. Vnutrennyaya ballistika stvol'nykh sistem i porokhovykh raket (Interior Ballistics of Gun Systems and Solid Propellant Rockets). Moscow, Oborongiz Press, 1957.
3. Tekhnika giperzvukovykh issledovaniy (Supersonic Study Techniques). Collection of translated articles. Moscow, Mir Press, 1964.
4. Sovremennaya tekhnika giperzvukovykh issledovaniy (Modern Supersonic Study Techniques). Collection of articles. Moscow, Mashinostroyeniye Press, 1965.
5. Stanyukovich, K. P. Neustanovisheyeya dvizheniye sploshnoy sredy (Unsteady Motion of a Continuum). Moscow, Nauka Press, 1971.
6. Stanyukovich, K. P., M. S. Gorokhov, et al. Gazodynamicheskiye osnovy vnutrenney ballistiki (Gasdynamic Fundamentals of Interior Ballistics). Moscow, Oborongiz Press, 1957.
7. Chislennyye metody v gazovoy dinamike (Numerical Methods in Gasdynamics). Transactions of the Computer Center, Moscow University Press, 1965.
8. Popov, N. N. Imparting High Flight Speed to Bodies. Vestnik MGU, No. 4, 1962.
9. Jones, A. H., W. M. Isbell and C. J. Maiden. J. Appl. Phys., Vol. 37, No. 9, 1967, pp. 3493-3499.
10. Charters, A. C. and G. S. Curtis. The High Temperature Aspects of Hypersonic Flow. AGARDograph 68, Pergamon Press, 1964.
11. Baer, P. G. and H. C. Smith. Proceedings of the Sixth Symposium on Hypervelocity Impact. Cleveland, Ohio, August, 1963.
12. Baker, G. R. Proceedings of the Seventh Symposium on Hypervelocity Impact. Tampa, Florida, November, 1964.
13. Likashewicz, I. The High Temperature Aspects of Hypersonic Flow. AGARDograph 68, Pergamon Press, 1964.

14. Godfrey, Charles S. Technol. Rev., Vol. 72, No. 3, 1970, pp. 41-47.
15. Grozier, W. D. High Velocity Light Gas Gun. J. Appl. Phys., Vol. 28, No. 8, 1957, p. 892.
16. Selected Topics on Ballistics. Pergamon Press, 1959.
17. Titov, V. M., Yu. I. Fadeyenko, and N. S. Titova. Acceleration of Solid Bodies by a Shaped Charge. Reports of the Academy of Sciences SSSR, Vol. 180, No. 5, 1968, pp. 1051-1052.
18. Bomelburg, H. J. J. Appl. Phys., Vol. 30, No. 9, 1959, p. 1467.
19. Physics of High Speed Processes. Vol. 2. Translated from English. Mir Press, 1971.
20. Crosby, J. K. Aeronautics, Vol. 48, No. 7, 1968, p. 107.
21. Zel'dovich, Ya. B. and Yu. P. Rayzer. Fizika udarnykh voln i vysokotemperaturnykh gidrodinamicheskikh yavleniy (Physics of Shock Waves and High-Temperature Hydrodynamic Phenomena). Moscow, Nauka Press, 1966.
22. Grozier, W. D. and W. Hume. Some Historical Highlights of Hypervelocity Techniques Symposium. Denver, Colorado, October, 1960.
23. Osnovnyye dannyye aerodinamicheskikh trub i gazodinamicheskikh ustanovok SShA (Basic Performance of U.S.A. Wind Tunnels and Hydrodynamic Test Facilities) (Survey). TsAGE Press, 1968.
24. Wilenius, G. P. I. ARGMA Symposium on Aeroballistic Ranges. CADRE IM Q-646/61, 1961. /328
25. Kochin, N. Ye., N. A. Kibel and N. V. Roze. Teoreticheskaya gidromekhanika (Theoretical Hydromechanics), Vol. 2. 1963.
26. Swift, H. F. Proceedings of the Sixth Symposium on Hypervelocity Impact. Cleveland, Ohio, August, 1963.
27. Sedov, L. I. Metody podobiya i razmernosti v mekhanika (Similarity and Dimensional Methods in Mechanics). Nauka Press, 1967.
28. Curtis, I. S. Third Hypervelocity Techniques Symposium. Denver, Colorado, March, 1964.
29. Swift, H. F. Proceedings of the Seventh Symposium on Hypervelocity Impact. Tampa, Florida, November, 1964.
30. Barbarek, I. A. C. Proceedings of the Sixth Symposium on Hypervelocity Impact. Cleveland, Ohio, August, 1963.

31. Godfrey, C. S. Ordnance, Vol. 51, No. 279, 1966, p. 312.
32. Volpe, V. F. and F. J. Zimmerman. Proceedings of the Hypervelocity Techniques Symposium, Denver, Colorado, October, 1960.
33. Courant, R. and K. O. Friedrichs. Supersonic Flow and Shock Waves. Moscow, Foreign Literature Press (IL), 1950.
34. Fundamentals of Gasdynamics. Collection of translated articles. Moscow, IL, 1963.
35. Osnovnyye dannyye inostrannykh aerodinamicheskikh trub i gazodinamicheskikh ustanovok (Basic Performance of Foreign Wind Tunnels and Gasdynamic Test Facilities) (Survey). TsAGI Press, 1968.
36. Richtmyer, R. D. Difference Methods for Initial Value Problems. New York, Interscience Publishers, 1957.
37. Evans, C. and F. Evans. J. Fluid Mechanics, No. 399, October, 1956.
38. Ferri, A. Fundamental Data Obtained from Shock Tube Experiments. Translated from English. Moscow, IL, 1963.
39. Shock Tubes. Collection of translated articles. Moscow, IL, 1962.
40. Popov, N. N. Determination of Contact Discontinuity Motion in a Gas with Heat Addition. Vestnik MGU, No. 4, 1960.
41. Popov, N. N. On Application of the Limiting Solution of the Equations of One-Dimensional Motion to the Problem of Heated Gas Expansion. Vestnik MGU, No. 2, 1960.
42. Enkenhus, K. R. AIAA Paper, No. 169, 1969.
43. Fizicheskaya gazodinamika (Physical Gasdynamics). Collection of articles. Moscow, Press of the Academy of Sciences SSSR, 1959.
44. Popov, N. N. Unsteady One-Dimensional Gas Flow with Heat Addition in a Channel of Variable Section. Vestnik MGU, No. 3, 1959.
45. Popov, N. N. On Unsteady One-Dimensional Gas Motion in a Variable-Section Channel with Heat Addition. Vestnik MGU, No. 2, 1961.
46. Richtmyer, R. D. Difference Methods for Initial Value Problems. Translated from German. Moscow, IL, 1960.

47. Berezin, I. S. and N. P. Zhidkov. Chislennoye resheniye uravneniy v chastnykh proizvodnykh (Numerical Solution of Partial Differential Equations). Moscow, Fizmatgiz, 1959.
48. Panov, D. Yu. Chislennoye resheniye uravneniy v chastnykh proizvodnykh (Numerical Solution of Partial Differential Equations). Moscow, Gostekhizdat, 1957.
49. Kottenstette, G. and W. G. Howell. Proceedings of the Seventh Symposium on Hypervelocity Impact. Tampa, Florida, November, 1964.
50. Scully, C. N. Proceedings of the Seventh Symposium on Hypervelocity Impact. Tampa, Florida, November, 1964.

CHAPTER III

1. Hodges, A. J. JAS, Vol. 24, No. 10, 1957, p. 755.
2. Seiff, A. A Free-Flight Tunnel for Aerodynamic Testing at Hypersonic Speeds. NACA Report 1222, 1951.
3. Bull, G. V. IAS Paper, No. 59-143, Seventh Anglo-American Aeronautical Conference, 1959. /329
4. Mishin, G. I. and N. P. Mende. Collection: Aerofizicheskiye issledovaniya sverkhzvukovykh techeniy (Aerophysical Studies of Supersonic flows). Moscow, Nauka Press, 1967, p. 163.
5. Basargin, I. V., I. M. Dement'yev and G. I. Mishin. Collection: Aerophysical Studies of Supersonic Flows. Moscow, Nauka Press, 1967, p. 168
6. Berezkin, A. N., V. N. Bykov, A. P. Gordeyev, V. G. Maslennikov, A. M. Studenkov and S. N. Palkin. Collection: Aerophysical Studies of Supersonic Flows. Moscow, Nauka Press, 1967, p. 218.
7. Clemens, P. L. and M. K. Kingery. Supersonic Study Techniques. Moscow, Mir Press, 1964*, p. 124.
8. White, E. L. and J. N. Fedenia. IEEE Transactions on Aerospace and Electronic Systems. AES-2, Vol. 13, No. 1, 1966.
9. Cords, P. N., W. R. Noyes and P. A. Thurston. Proceedings of the Fifth International Congress on High-Speed Photography, 1960.

*Translator's note. AIAA Journal, Vol. 5, 1967, p. 1999.

10. Wall, C. R. Proceedings of the Sixthe International Congress on High-Speed Photography, 1962, p. 566.
11. Charters, A. Collection: Issledovaniye giperzvukovykh techeniy (Supersonic Flow Studies). Moscow, Mir Press, 1964, p.433.
12. Murphy, C. H. Selected Topics on Ballistics. AGARDograph 32, Pergamon Press, 1959, pp. 145-167.
13. Davis, J., J. Dehnell and D. Hall. Proceedings of the Seventh International Congress on High-Speed Photography, 1967, p. 319.
14. Holder, D. W. and R. J. North. Schlieren Methods in Aerodynamics. Moscow, Mir Press, 1966.
15. Adams, G. K. J. Sci. Inst., Vol. 28, 1951 p. 379.
16. Mishin, G. I. and I. N. Rodicheva. Collection: (Aerophysical Studies of Supersonic Flows). Moscow, Nauka Press, 1967, p.184.
17. Dunayev, Yu. A. and G. I. Mishin. Izvestiya Academy of Sciences SSSR, Mekhanika i Mashinostroyeniye, No. 2, 1959, p.188.
18. Berezkin, A. N. and M. K. Berezkina. Collection: (Aerophysical Studies of Supersonic Flows). Moscow, Nauka Press, 1967, p. 227.
19. Koch, B. and G. Simon. Proceedings of the Sixth Intern. Congress on High-Speed Photography, 1962, p. 409.
20. Girand, M., B. Koch and G. Simon. Proceedings of the Seventh Intern. Congress on High-Speed Photography, 1965, p. 225.
21. Hall, D. A., W. W. Atkins. Proceedings of the Fifth Intern. Congress on High-Speed Photography, 1962, p. 372.
22. Blizard, G. F. J. SMPTE, Vol. 71, No. 12, 1962, p. 925.
23. Theophanis, G. A. Rev. Sci. Inst., Vol 31, No. 4, 1960, p. 427.
24. Eckerman, V., et al. Collection: (Hypersonic Study Techniques). Moscow, Mir Press, 1964, p. 52.
25. Palkin, S. N, B. I. Reznikov, A. M. Studenkov and V. N. Bykov. Collection: (Aerophysical Studies of Supersonic Flows). Moscow, Nauka Press, 1967, p. 274.
26. Mishin, G. I. and I. V. Basargin. Author's Certificate No. 168797, Bulletin of Inventions, April, 1966.
27. Bedin, A. P. and N. P. Mende. Collection: (Aerophysical Studies of Supersonic Flows). Moscow, Nauka Press, 1967, p. 178.

28. Pavlenko, P. I. Schetno-impul'snyi khronometr (Pulse-Counting Chronometer). Fizmatgiz Press, 1963.
29. Mirskiy, G. Ya. Time Interval Measurement (extensive bibliography), No. 11. Moscow, Energiya Press, 1964, p. 511.
30. Christensen, A. B. and W. V. Isbell. Rev. Sci. Inst., Vol. 37, No. 5, 1966, p. 559.
31. Sokolik, A. I. and V. M. Bortsov. IV-I Z, IV-I ZM, IV-I ZMA Timers. VINITI (All-Union Institute of Scientific and Technical Information) Press, Theme 31, No. P-58-22/4, 1958. /330
32. Ronssellet, M. Mesures, Vol. 192, 1953, p. 271.
33. Kondurov, I. A. and V. B. Chernyayev. PTE (Experimental Instruments and Techniques), No. 1, 1956, p. 54
34. Ostretsov, L. A., G. D. Latyshev, V. D. Leonov and N. M. Shirshov. PTE, No. 2, 1956, p. 72.
35. Kolpakov, I. F. PTE, NO. 6, 1962, p. 55.
36. Shvetskiy, B. I. Elektronnye izmeritel'nye pribory s tsifrovym otshchetom (Electronic Meters with Digital Readout). Tekhnika Press, 1964.
37. Izokh, V. V. and M. K. Yefimchik. PTE, No. 3, 1962, p. 86.
38. Predein, B. A. PTE, No. 2, 1958, p. 31.
39. Borlinger, L. E. Austral. J. Inst. Tech., Vol. 13, No. 3, 1957, p. 37.
40. Kerwin, W. J. Electronics, April 1, 1957, p. 152.
41. Mishin, G. I. PTE, No. 5, 1960, p. 56.
42. Pelykh, N. A. and A. V. Pronyushkin. PTE, No. 4, 1961, p. 83.
43. Pelykh, N. A., A. V. Pronyushkin, V. P. Golovkov and G. V. Dobrovol'skiy. PTE, No. 2, 1962, p. 76.
44. Mishin, G. I. PTE, No. 5, 1962, p. 106
45. Mishin, G. I. and A. V. Fedorov. Collection: (Aerophysical Studies of Supersonic Flows). Moscow, Nauka Press, 1967, p. 188.
46. Stevens, V. J. J. Appl. Phys, Vol. 21, No. 11, 1950, p. 1150.
47. Barnes, N. F. J. SMPTE, Vol. 61, 1953, p. 487.
48. Hilton, W. F. High-Speed Aerodynamics. Moscow, IL, 1955.

49. Physical Measurements in Gasdynamics and Combustion. Translated from English. Moscow, IL, 1957.
50. Abrukov, S. A. Tenevye i interferentsionnye metody issledovaniya opticheskikh neodnorodnostey (Shadow and Interference Methods of Studying Optical Nonhomogeneities). Kazan, 1962.
51. Dubovik, A. S. Fotograficheskaya registratsiya bystroprotekayushchikh protsessov (Photographic Recording of High-Speed Processes). Moscow, Nauka Press, 1964.
52. Salamandra, G. D. Vysokoskorostnye s"yemki shliren-metodom (High-Speed Schlieren Photography). Moscow, Nauka Press, 1965.
53. Schardin, H. Ergebn. exakt. Naturw., Vol. 20, 1942, p. 303.
54. Nesterikhin, Yu. Ye. and R. I. Soloukhin. Metody skorostnykh izmerenii v gazodinamike i fizike plazmy (Velocity Measurement Methods in Gasdynamics and Plasma Physics). Moscow, Nauka Press, 1967.
55. Vasil'yev, L. A. Tenevye metody (Shadow Methods). Moscow, Nauka Press, 1968.
56. Suchorukich, V. S. Proceedings of the Eighth Intern. Congress on High-Speed Photography, 1968, p. 341.
57. Bedin, A. P., I. M. Dement'yev and G. I. Mishin. PMTF (Applied Mechanics and Technical Physics), No. 2, 1968, p. 95.
58. Maslennikov, V. G. Collection: (Aerophysical Studies of Supersonic Flows). Moscow, Nauka Press, 1967, pp. 241, 256, 265.
59. Clay, W. G., M. Labbit and R. E. Slattery. AIAA Journal, No. 5, 1965, p. 47.
60. Royer, H. Proceedings of the Ninth Intern. Congress of High-speed Photography, 1971, p. 410.
61. Syshchikova, M. P., M. I. Berezkina and A. N. Semenov. Collection: (Aerophysical Studies of Supersonic Flows). Moscow, Nauka Press, 1967, p. 13.
62. Semenov, A. N. Inzhenernyy Zhurnal, Vol. 4, No. 4, 1964, p. 743.
63. Semenov, A. N. Collection: (Aerophysical Studies of Supersonic Flows). Moscow, Nauka Press, 1967, p. 28.
64. Hall, L. S. Rev. Sci. Inst., No. 12, 1966, p. 1735.

65. Paikin, S. N., B. I. Reznikov, A. M. Studenkov and V. I. Bykov.
Collection: (Aerophysical Studies of Supersonic Flows).
Moscow, Nauka Press, 1967, p. 274.
66. Schardin, H. Zeitschrift für Instrumentenkunde, Vol. 9, 1933, 1331
p. 388.
67. Kinder, W. Optik, Vol. 1, No. 6, 1946, p. 413.
68. Goldstein, R. J. Rev. Sci. Inst., No. 10, 1965, p. 1408.
69. Bennet, F. D., W. C. Carter and W. E. Bergdolt. J. Appl.
Phys., Vol 23, No. 4, 1952, p. 453; Vol 24, No. 11, 1953,
p. 1389.
70. Sedney, R. and G. D. Kahe. Planetary and Space Science, No.
4, 1961, p. 337.
71. Cranz, C. Lehrbuch der Ballistik, Vol. 3, 1927, p. 277;
Ergänzungsband, 1936, p. 173.
72. Giese, J. H., F. D. Bennett and V. E. Bergdolt. J. Appl.
Physics., Vol. 21, 1950, p. 1226.
73. Belotserkovskiy, S. M., V. S. Sukhorukikh and V. S. Tataren-
chik. PMTF, No. 3, 1964, p. 95.
74. Belotserkovskiy, S. M., V. S. Sukhorukikh and V. S. Tataren-
chik. Sbornik dokladov na II Vsesoyuznom s'yezde po teoreti-
cheskoy i prikladnoy mekhanike (Collection of Reports to
Second All-Union Meeting on Theoretical and Applied Mech-
anics), 1964.
75. Belotzerkovsky, S. M. Proceedings of the Eighth Intern. Con-
gress on High-Speed Photography, 1958, p. 410.
76. North, R. J. and C. M. Stuart. Proceedings of the Sixth
Intern. Congress on High-Speed Photography, 1962, p.470.
77. Nagel, M. R. Proceedings of the Seventh Intern. Congress on
High-Speed Photography, 1965, p. 485.
78. Schardin, H. Proceedings of the Sixth Intern. Congress on
High-Speed Photography, 1962, p. 1.
79. Physics of High-Speed Processes. Translated from English.
Moscow, Mir Press, 1971.
80. Wilson, L. H. AIAA Journal, Vol. 5, No. 7, 1967, p. 29.
81. Borisov, V. N. and G. I. Mishin. PTE, No. 4, 1971, p. 184.
82. Brewster, J. L., J. P. Barbour, F. M. Charbonnier and F. J.
Grundhauser. Proceedings of the Ninth Intern. Congress on
High-Speed Photography, 1971, p. 303.

83. Schardin, H. Proceedings of the Seventh Intern. Congress on High-Speed Photography, 1965, p. 17.
84. Thorwart, W., J. F. Suarez and H. G. Patzke. Proceedings of the Seventh Intern. Congress on High-Speed Photography, 1965, p. 51.
85. Thorwart, W. and J. F. Suarez. Proceedings of the Eighth Intern. Congress on High-Speed Photography, 1968, p. 157.
86. Schardin, H. Proceedings of the Fifth Intern. Congress on High-Speed Photography, 1962, p. 329.
87. Schardin, H. VRT, No. 5, 1953, p. 127.
88. Garg, S. K. and J. Siekmann. Rev. Sci. Inst., Vol. 37, No. 8, 1966, p. 1032.
89. Stenzel, A. Proceedings of the Eighth Intern. Congress on High-Speed Photography, 1968, p. 153.
90. Marshak, I. S. Impul'snye istochniki sveta (Pulsed Light Sources). Moscow, Gosenergoizdat Press, 1963.
91. Marshak, I. S. PTE, No. 3, 1962, p. 5.
92. Andreev, S. I. and M. P. Vanyukov. Proceedings of the Sixth Intern. Congress on High-Speed Photography, 1962, p. 166.
93. Fischer, H. J. Opt, Soc. of America, Vol. 47, No. 11, 1957, p. 981.
94. Schardin, H. and E. Fuenfer. Zeitschr. für angew. Physik, Vol. 4, No. 5, 1952, p. 185; Vol. 4, No. 6, 1952, p. 224.
95. Fruengel, F. Pulse Technology. Moscow, Energiya Press, 1965.
96. Fischer, H. J. Opt. Soc. of America, Vol. 51, No. 5, 1961, p. 543.
97. Andreyev, S. I. and M. P. Vanyukov. PTE, No. 4, 1961, p. 76.
98. Vul'fson, K. S., I. Sh. Libin and F. A. Charnaya. Izvestiya AN SSSR, Physics Series, No. 19, 1955, p. 61.
99. Vanyukov, M. P., A. A. Mak, N. V. Parazinskaya. Optika i spektroskopiya, Vol. 1, No. 5, 1956, p. 642.
100. Charnaya, F. A. Optika i spektroskopiya, Vol. 1, No. 7, 1956, 1332 p. 857.
101. Vanyukov, M. P., A. A. Mak and A. I. Sadykova. DAN SSSR, Vol. 135, No. 3, 1960, p. 537.
102. Kirsanov, V. P., V. A. Gavanin and I. S. Marshak. Optika i spektroskopiya, Vol. 13, No. 2, 1962, p. 276.

103. McMahon, D. H., A. R. Franklin and H. R. Carleton. Rev. Sci. Inst., No. 9, 1966, p. 1142.
104. Fitzpatrick, I. A., J. C. Hubbard and W. J. Thaller. J. Appl. Phys., Vol. 21, 1950, p. 1269.
105. Fischer, H. and W. Schwanzer. Proceedings of the Eighth Intern. Congress on High-Speed Photography, 1968, p. 215.
106. Pollack, S. A. J. Appl. Phys., Vol. 36, 1965, p. 3459.
107. Mackey, R. C., S. A. Pollack and R. S. Witte. Rev. Sci. Inst., Vol. 36, No. 12, 1965, p. 1715.
108. Vvedenskiy, Ya. V. PTE, No. 3, 1967, p. 165.
109. Onuchin, A. P. PTE, No. 6, 1961, p. 100.
110. Witte, A. B. and R. F. Wuerker. AIAA Paper, No. 69-347, April, 1969.
111. Vorob'yev, G. A. and G. A. Mesyats. Formirovaniye vysokovol'tnykh impul'sov nanosekundnoy dlitel'nosti (Forming High Voltage Nanosecond Pulses). Moscow, Gosatomizdat Press, 1963.
112. Theophanis, G. A. Rev. Sci. Inst., Vol. 31, No. 4, 1960, p. 427.
113. Magyar, C. Rev. Sci. Inst., Vol. 38, 1967, p. 517.
114. Witte, A. B., J. Fox and H. Rungaldier. AIAA Paper, No. 71-564, 1971.
115. Christie, R. H. Proceedings of the Seventh Intern. Congress on High-Speed Photography, 1965, p. 215.
116. Martellucci, S. and E. Mazzucato. Proceedings of the Seventh Intern. Congress on High-Speed Photography, 1965, p. 144.
117. Ascoli-Bartoli, V. Proceedings of the Seventh Intern. Congress on High-Speed Photography, 1965, p. 29.
118. Oppenheim, A. K., P. A. Yrtiew and F. J. Weiberg. Proc. Roy. Soc. S. A., Vol. 291, 1966, pp. 1425, 279.
119. Tanner, L. N. J. Sci. Inst., Vol. 43, No. 10, 1966, p. 677.
120. Presby, H. M. and D. Finkelstein. Rev. Sci. Inst., No. 11, 1967, p. 1563.
121. Basov, N. G., O. N. Krokhin and G. V. Sklizkov. Proceedings of the Eighth International Congress on High-Speed Photography, 1968, p. 272.

122. Bagshaw, J. R. and D. Pitton. J. Photog. Sci., Vol. 15, No. 4, 1967, p. 197.
123. Ellis, A. T. and M. E. Fourny. Proc. IEEE, Vol. 51, No. 6, 1963, p. 942.
124. Ebeling, D. Proceedings of the Seventh Intern. Congress on High-Speed Photography, 1965, p. 554.
125. Holland, T. E. and J. K. Landre. Proceedings of the Seventh Intern. Congress on High-Speed Photography, 1965, p. 105.
126. Rowlands, R. E., C. E. Taylor and I. M. Daniel. Proceedings of the Eighth Intern. Congress on High-Speed Photography, 1968, p. 275.
127. Alfs, A. Proceedings of the Eighth Intern. Congress on High-Speed Photography, 1968, p. 281.
128. Vollrath, K. and M. Hugenschmidt. Proceedings of the Eighth Intern. Congress on High-Speed Photography, 1968, p. 284.
129. Clay, W. G., R. E. Slattery, A. P. Ferdinand and C. R. Kiline. AIAA Journal, Vol. 5, No. 2, 1967, p. 364.
130. Slattery, R. E., W. G. Clay and A. P. Ferdinand. Proceedings of the Eighth Intern. Congress on High-Speed Photography, 1968, p. 351.
131. Yajima, T., F. Shimizu and K. Shimoda. J. Appl. Optics, Vol. 1, No. 6, 1962, p. 770.
132. Shimoda, K., T. Yajima and F. Shimizu. Sci. Papers Inst. Phys. a. Chem. Research, Vol. 56, No. 3, 1962, p. 201.
133. Trammell, W. V. Rev. Sci. Inst., Vol. 36, No. 11, 1965, p. 1551.
134. Brooks, R. E., L. O. Heflinger, R. F. Wuerker and R. A. Briones. Appl. Phys. Letters, Vol. 7, No. 4, 1965, p. 92. /333
135. Brooks, R. E., L. O. Heflinger and R. F. Wuerker. IEEE Journal Quantum Electronics QE-2, No. 8, 1966, p. 275.
136. Dunaev, Yu. A., W. M. Ovchinnikov, A. N. Berjiozkin, Yu. E. Kamatch and E. N. Koslovsky. Proceedings of the Eighth Intern. Congress on High-Speed Photography, 1968, p. 328.
137. Brooks, R. E. and L. O. Heflinger. J. Appl. Phys., Vol. 37, No. 2, 1966, p. 642.
138. Gehring, J. W. and D. R. Christman. Proceedings of the Seventh Intern. Congress on High-Speed Photography, 1965, p. 365.

139. Tanner, L. N. J. Sci. Inst., Vol. 43, No. 10, 1966, p. 677.
140. Leith, E. N. and J. Upatnieks. J. Opt. Soc. Amer., Vol. 52, No. 10, 1962, p. 1123; Vol. 54, No. 11, 1964, p. 1295.
141. Leith, E. N. and J. Upatnieks. Scientific Amer., Vol. 212, No. 6, 1965, p. 24.
142. Collier, R. J., C. B. Burkhardt and L. H. Lin. Optical Holography. Moscow, Mir Press, 1973.
143. Denisjuk, Yu. N. DAN SSSR, Vol. 144, No. 6, 1962, p. 1275.
144. Thompson, B. J., J. H. Ward and W. R. Zinky. J. Appl. Opt., Vol. 6, No. 3, 1967, p. 519.
145. Collier, R. J., E. T. Doherty and K. S. Pennington, Appl. Phys. Letters, Vol. 7, No. 8, 1965, p. 223.
146. Mannheim, J. A. Phototechnik und Wirtschaft, Vol. 16, No. 4, 1965, p. 131.
147. Movotny, G. V. Electronics, No. 37, 1964, p. 30.
148. Ostrovskiy, Yu. I. Golografiya i yeye primeneniye (Holography and Its Application). Leningrad, Nauka Press, 1973.
149. Leith, E. N. J. Opt. Soc. Amer., Vol. 55, No. 8, 1965, p. 981.
150. Berezkin, A. N., Yu. E. Kamach, Ye. N. Kozlovskiy and A. I. Razumovskaya. ZhTF (Journal of Technical Physics), Vol. 42, 1973, p. 219.
151. Brooks, R. E., L. O. Heflinger and R. E. Wuerker. Appl. Phys. Letters, Vol. 7, No. 9, 1965, p. 248.
152. Hormann, M. H. J. Appl. Opt., Vol. 4, No. 3, 1965, p. 333.
153. Belozerov, A. F., A. N. Berezkin, A. E. Razumovskaya and N. M. Spornik. ZhTF, Vol. 43, 1973, p. 777.
154. Mustafin, K. S., V. A. Seleznev and Ye. I. Shtyrkov. Optika i spektroskopiya, Vol. 22, No. 2, 1967, p. 319.
155. Gates, J. W. C., R. G. N. Hall and I. N. Ross. Proceedings of the Eighth Intern. Congress on High-Speed Photography, 1968, pp. 299, 304.
156. Ostrovsky, Yu. and A. N. Zaidel. Proceedings of the Eighth Intern. Congress on High-Speed Photography, 1968, p. 309.
157. Reid, C. D. Proceedings of the Eighth Intern. Congress on High-Speed Photography, 1968, p. 314.
158. Redman, J. D. and M. A. Lowe. Proceedings of the Eighth Intern. Congress on High-Speed Photography, 1968, p. 317.

159. Courrier, M. G. and M. Leblanc. Proceedings of the Eighth Intern. Congress on High Speed Photography, 1968, p. 321.
160. Buzzard, R. O. Proceedings of the Eighth Intern. Congress on High Speed Photography, 1968, p. 335.
161. Smiglielski, P. and H. Royer. Proceedings of the Eighth Intern. Congress on High-Speed Photography, 1968, p. 324.
162. Jacobson, A. D. and F. G. McClung. J. Appl. Opt., Vol. 4, No. 11, 1965, p. 1509.
163. Presby, H. M. and D. Finkelstein. Rev. Sci. Inst., Vol. 38, No. 11, 1967, p. 1563.
164. Collins, D. J., A. C. Charters and D. K. Sangster. Rev. Sci. Inst., Vol. 38, No. 8, 1967, p. 1076.
165. Edgerton, H. E. and Ch. W. Wyckoff. J. SMPTE, No. 56, 1951, p. 398.
166. Elle, D. Zeitschr. angew. Physik., Vol. 6, No. 2, 1954, p. 49.
167. Dugual, N. A. and J. W. Hansen. Proceedings of the Ninth International Congress on High-Speed Photography, 1971, p. 124.
168. Zarem, A. M., F. R. Marshall and S. M. Hauser. Rev. Sci. Inst., Vol. 29, No. 11, 1958, p. 1041.
169. Persson, A. Proceedings of the Seventh Intern. Congress on High-Speed Photography, 1965, p. 123.
170. Hull, J. A. and G. A. Theophanis. J. SMPTE, Vol. 69, No. 5, 1960, p. 355.
171. Theophanis, G. A. Proceedings of the Fifth Intern. Congress on High-Speed Photography, 1960, p. 129.
172. Lunn, G. H. and E. D. Menzies. Proceedings of the Fifth Intern. Congress on High-Speed Photography, 1960, p. 127.
173. Goss, W. C. Proceedings of the Fifth International Congress on High-Speed Photography, 1960, p. 135.
174. Liebing, L. and F. Fruengel. Proceedings of the Fifth Intern. Congress on High-Speed Photography, 1960, p. 138.
175. Prime, H. A. and R. C. Thurnock. Rev. Sci. Inst., Vol. 20, 1949, p. 830.
176. Hermann, W. Proceedings of the Seventh Intern. Congress on High-Speed Photography, 1965, p. 443.

177. Bang, B. A. Proceedings of the Fifth Intern. Congress on High-Speed Photography, 1960, p. 141.
178. Maslennikov, V. G., I. G. Paritskiy, S. I. Rozov and A. M. Studenkov. PMTF, No. 1, 1965, p. 98.
179. Blanchet, M. Proceedings of the Eighth Intern. Congress on High-Speed Photography, 1968, p. 64.
180. Karolus, A. Proceedings of the Second Intern. Congress on High-Speed Photography, 1956, p. 78.
181. Michon, M. and Guillet. Proceedings of the Eighth Intern. Congress on High-Speed Photography, 1968, p. 71.
182. Butslov, M. M. Kaskadnye elektronno-opticheskiye preobrazovateli i ikh primeneniye (Cascade Electron-Optical Converters and Their Application). Moscow, Mir Press, 1965.
183. Gavganen, L. V., L. M. Diamant, A. M. Iskoldsky, Y. E. Nesterikhin and V. M. Fedorov. Proceedings of the Eighth Intern. Congress on High-Speed Photography, 1968, p. 41.
184. Eschard, G. and R. Polaert. Proceedings of the Eighth Intern. Congress on High-Speed Photography, 1968, p. 54.
185. Korobkin, V. V., A. A. Malyntin and M. Ya Schelev. Proceedings of the Ninth Intern. Congress on High-Speed Photography, 1971, p. 232.
186. Christie, R. H. Proceedings of the Seventh Intern. Congress on High-Speed Photography, 1965, p. 151.
187. Arpishkin, V. M., M. P. Vanjukov and O. B. Danilov. Proceedings of the Eighth Intern. Congress on High-Speed Photography, 1968, p. 401.
188. Wilenins, G. P. T. and G. W. Wheeler. Proceedings of the Seventh Intern. Congress on High-Speed Photography, 1965, p. 47.
189. Huston, A. E. Proceedings of the Ninth International Congress on High-Speed Photography, 1971, p. 182.
190. Dyke, W. P., F. J. Grundhauser, F. M. Collins and N. W. Stunkard. In: Modern Aerodynamic Study Techniques at Hypersonic Speeds. Moscow, Mashinostroyeniye Press, 1965, p. 173.
191. Hall, D. A. Proceedings of the Seventh Intern. Congress on High-Speed Photography, 1965, p. 49.
192. Tsukerman, V. A. and N. A. Monakova. ZhTF, Vol. 27, No. 2, 1957, p. 391.

193. Thomer, G. and F. Jamet. Proceedings of the Eighth Intern. Congress on High-Speed Photography, 1968, p. 256.
194. Grundhauser, F. J., J. P. Barbour, M. P. Hafner, J. L. Brewster, F. M. Charbonnier and W. P. Dyke. Proceedings of the Seventh Intern. Congress on High-Speed Photography, 1965. /335
195. Grundhauser, F. J., J. P. Barbour, M. P. Hafner and J. L. Brewster. Proceedings of the Eighth Intern. Congress on High-Speed Photography, 1968, p. 237.
196. Brewster, J. L., J. P. Barbour, F. J. Grundhauser and W. P. Dyke. Proceedings of the Eighth Intern. Congress on High-Speed Photography, 1968, p. 240.
197. Glyden, N., L. Hoegberg, R. Nilsson and A. Svedberg. Proceedings of the Eighth Intern. Congress on High-Speed Photography, 1968, p. 249.
198. Jamet, F. and G. Thomer. Proceedings of the Eighth Intern. Congress on High-Speed Photography, 1968, p. 259.
199. Dyke, W. P. Scientific American, Vol. 210, No. 1, 1964, p. 108.
200. Barbour, J. P., F. J. Grundhauser and W. P. Dyke. Proceedings of the Seventh Intern. Congress on High-Speed Photography, 1965, p. 292.
201. Ebeling, D. Proceedings of the Eighth Intern. Congress on High-Speed Photography, 1968, p. 245.
202. Winter, D. T. F and C. R. Wall. Collection: Modern Aerodynamic Study Techniques at Hypersonic Speeds. Moscow, Mashinostroyeniye Press, 1965, p. 402.
203. McDevitt, J. B., D. B. Harrison and W. K. Lockman. IEEE Transaction on Aerospace and Electronic Systems AES-2, Vol. 2, No. 1, 1966.
204. Letarte, M. and L. Ye. Moir. Collection: Modern Aerodynamic Study Techniques at Hypersonic Speeds. Moscow, Mashinostroyeniye Press, 1965, p. 524.
205. Finger, D. V. Collection: Sovremennaya tekhnika aerodinamicheskikh issledovaniy pri giperzvukovykh skorostyakh (High Temperature Aspects of Hypersonic Flow). Moscow, Mashinostroyeniye Press, 1965, p. 163.
206. Letarte, M., M. Gravel and L. E. Moir. The High Temperature Aspects of Hypersonic Flow. Pergamon Press, 1964, p. 404.
207. Lobb, R. K. Hypersonic Research at the Naval Ordnance Laboratory, Hypersonic Flow. London, 1960.

208. Nadtochiy, B. F. and N. M. Lobasheva. Collection: (Aerodynamic Studies of Supersonic Flows). Moscow, Nauka Press, 1967, p. 198.
209. Peters, C. J. Proc. IEEE, Vol. 53, No. 5, 1965, p. 455.
210. Ley, J. M. Electronics Letters, Vol. 5, No. 4, 1966, p. 12.
211. Healey, T. J. and H. M. Owren. Proceedings of the Seventh Intern. Congress on High-Speed Photography, 1965, p. 531.
212. Hadland, R. Proceedings of the Ninth Intern. Congress on High-Speed Photography, 1971, p. 510.
213. Tsukerman, V. A., L. V. Tarasova and S. I. Lobov. UFN (Progress of Physical Sciences), Vol. 103, No. 2, 1971.
214. Baikov, A. P., V. A. Belago, L. M. Diamant, V. I. Dotsenko, A. M. Iskol'skii, E. M. Kurashov and A. F. Shestak. Proceedings of the Ninth Intern. Congress on High-Speed Photography, 1971, p. 283.

CHAPTER IV

1. Walsh, J. M. and R. H. Christian. Phys. Rev., Vol. 97, No. 6, 1955, p. 1544.
2. Walsh, J. M., M. H. Rise, R. G. McQueen and F. L. Yarger. Phys. Rev., Vol. 108, No. 2, 1957, p. 196.
3. Rise, M. H., R. G. McQueen and J. M. Walsh. Solid State Physics, Vol. 6. Eds. F. Seitz and D. Turnbull, 1958.
4. McQueen, R. G. and S. P. Marsh. J. Appl. Phys., Vol. 31, No. 7, 1960, p. 1253. /336
5. Goranson, R. W., D. Bancroft, B. L. Burton, T. Blechar, E. E. Hauston, E. F. Gittings and S. A. Landeen. J. Appl. Phys., Vol. 26, No. 12, 1955, p. 1472.
6. Mallory, M. D. J. Appl. Phys., Vol. 26, No. 5, 1955, p. 555.
7. Al'tshuler, L. V., K. K. Krupnikov, B. N. Ledenev, V. I. Zhuchikhin and M. I. Brazhnik. ZhETF (Journal of Experimental and Technical Physics), Vol. 34, No. 4, 1958, p. 874.
8. Al'tshuler, L. V., K. K. Krupnikov and M. I. Brazhnik. ZhETF, Vol. 34, No. 4, 1958, p. 886.
9. Al'tshuler, L. V., S. B. Kormer, A. A. Bakanova and K. F. Trunin. ZhETF, Vol. 38, No. 3, 1960, p. 790.
10. Al'tshuler, L. V., S. B. Kormer, M. I. Brazhnik, L. A. Vladimirov, M. P. Speranskaya and A. I. Funtikov. ZhETF, Vol. 38, No. 4, 1960, p. 1061.

11. Al'tshuler, L. V., L. V. Kuleshova and M. N. Pavlovskiy. ShETF, Vol. 39, No. 1(7), 1960, p. 16.
12. Al'tshuler, L. V., A. A. Bakanova and R. F. Trunin. ZhETF, Vol. 42, No. 1, 1962, p. 91.
13. Krupnikov, K. K., A. A. Bakanova, M. I. Brazhnik and R. F. Trunin. DAN SSSR, Vol. 148, No. 6, 1963, p. 1302.
14. Al'tshuler, L. V. and A. P. Petrunin. ZhTF, Vol. 31, No. 6, 1961, p. 717.
15. Al'tshuler, L. V., A. A. Bakanova and R. F. Trunin. DAN SSSR, Vol. 121, No. 1, 1958, p. 4.
16. Kormer, S. B. and V. D. Urlin. DAN SSSR, Vol. 131, No. 3, 1960, p. 542.
17. Kormer, S. B., V. D. Urlin and L. T. Popova. Fizika tverdogo tela, Vol. 3, No. 7, 1961, p. 2131.
18. Kormer, S. B., M. V. Sinitsyn, A. E. Funtikov, V. D. Urlin and A. I. Blinov. ZhETF, Vol. 47, No. 4 (10), 1964, p. 1202.
19. Kormer, S. B., M. V. Sinitsyn, G. A. Kirillov and V. D. Urlin. ZhETF, Vol. 48, No. 4, 1965, p. 1033.
20. Dremine, A. N., and G. A. Adadurov. DAN SSSR, Vol. 128, No. 2, 1959, p. 261.
21. Dremine, A. N. and I. A. Karpukhin. PMTF, No. 3, 1960, p. 184.
22. Zel'dovich, Ya. B., S. B. Kormer, M. V. Sinitsyn and A. I. Kuryapin. DAN SSSR, Vol. 122, No. 1, 1958, p. 48.
23. Zlatin, N. A. Collection: Nekotoryye problemy prochnosti tverdogo tela (Some Problems of Solid Body Strength). Moscow, Press of the AN SSSR, 1959, p. 222.
24. Al'tshuler, L. V. UFN, Vol. 85, No. 2, 1965, p. 197.
25. Zel'dovich, Ya. B. and Yu. P. Rayzer. Fizika udranykh voln i vysokotemperaturnykh gidrodinamicheskikh yavlenii (Physics of Shock Waves and High-Temperature Hydrodynamic Phenomena). Moscow, Nauka Press, 1966.
26. Orlenko, L. P. Povedeniye materialov pri intensivnykh dinamicheskikh nagruzkakh (Behavior of Materials under Intense Dynamic Loads). Moscow, Mashinostroyeniye Press, 1964.
27. Baum, F. A., K. P. Stanyukovich and B. I. Shekhter. Fizika vryva (Physics of Explosions). Moscow, Fizmatgiz Press, 1959.

47. Fabrikant, N. Ya. Aerodinamika (Aerodynamics). Moscow, Gostekhizdat Press, Moscow, 1949.
48. Chernyy, G. G. Tekheniya gaza s bol'shoi sverkhzvukovoy skorost'yu (Gas Flow at High Supersonic Velocity). Moscow, Fizmatgiz Press, 1959.
49. Vitman, F. F. and V. A. Stepanov. ZhTF, Vol. 9, No. 12, 1939, p. 1070.
50. Taylor, G. A. C. Whiffin, W. E. Carrington and M. L. V. Gayler. Proc. Roy. Soc., Vol. 194, No. 1038, 1948, p. 289.
51. Kolsky, H. Stress Waves in Solids. Moscow, IL, 1955.
52. Stepanov, G. V. Problemy prochnosti, Vol. 1, No. 3, 1969, p. 78.
53. Rinehart, J. S. Popular Astron. Vol. 58, 1950, p. 458.
54. Rostoker, N. Meteoritics, Vol. 1, No. 1, 1953, p. 11.
55. Valeknborg, M. E., M. G. Clay and J. H. Huth. J. Appl. Phys., Vol. 27, No. 10, 1956, p. 1123.
56. Huth, J. H., J. Thompson and M. E. Valkenburg. J. Appl. Mech., Vol. 24, No. 1, 1957, p. 65.
57. Partridge, W. S., H. B. Vanfleet and C. R. Whited. J. Appl. Phys., Vol. 29, No. 9, 1958, p. 1332.
58. Charters, A. C. and J. L. Summers. Proceedings of the Third Symposium on Hypervelocity Impact, Chicago, 1959, p. 2.
59. Charters, A. C. Sci. Amer., Vol. 203, No. 4, 1960, p. 128.
60. Wall, J. K. AIAA Journ., Vol. 2, No. 7, 1964, p. 1242.
61. Rolsten, F. G. AIAA Journ, Vol. 3, No. 11, 1965, p. 2149.
62. Rolsten, R. F. and H. H. Hunt. J. Spacecraft and Rockets, Vol. 2, No. 1, 1965, p. 38.
63. Mar'yamov, A. N. PMTF, No. 2, 1967, p. 83.
64. Lenskiy, V. S. Materialy Vsesoyuznogo simpoziuma po rasprostrnleniyu uprugoplasticheskikh voln v sploshnykh sredakh (Reports of All-Union Symposium on Elastoplastic Wave Propagation in Continua). Baku, October, 1964. Baku, Press of the AS of the Azerb. SSR, 1966, p. 26.
65. Andriankin, E. I. and Yu. S. Stepanov. Iskusstvennye sputniki zemli. (Artificial Earth satellites), No. 15, 1963, p. 44.

66. Christman, D. R. and J. W. Gehring. J. Appl. Phys., Vol. 37, No. 4, 1966, p. 1579.
67. Cook, M. A. Science of High Explosives. New York, Reinhold Publishing Corporation, 1958.
68. Cook, M. A. J. Appl. Phys., Vol. 30, No. 5, 1959, p. 725.
69. Zlatin, N. A. ZhTF, Vol. 31, No. 8, 1961, p. 982.
70. Zlatin, N. A. ZhTF, Vol. 33, No. 2, 1963, p. 231.
71. Stanyukovich, K. P. Neustanovivsheyesya dvizheniye sploshnoy sredy (Unsteady Motion of a Continuum). Moscow, Gostekhizdat Press, Moscow, 1955.
72. Belyakov, L. V. and N. A. Zlatin. ZhTF, Vol. 37., No. 10, 1967, p. 1933.
73. Sedov, L. I. Metody podobiya i razmernosti v mekhanika (Similarity and Dimensional Methods in Mechanics). Moscow, Nauka Press, 1967. /338
74. Vitman, F. F. and N. A. Zlatin. DAN SSSR, Vol. 146, No. 2, 1962, p. 337.
75. Vitman, F. F. and N. A. Zlatin. ZhTF, Vol. 33, No. 8, 1963, p. 982.
76. Belyakov, N. V., F. F. Vitman and N. A. Zlatin. ZhTF, Vol. 34, No. 3, 1964, p. 519.
77. Belyakov, L. V., F. F. Vitman and N. A. Zlatin. ZhTF, Vol. 33, No. 8, 1963, p. 990.
78. Stephenson, W. H. Aerospace Engineering, Vol. 21, No. 11, 1962, p. 10.
79. Maiden, C. J. and A. R. McMillan. AIAA Journ., Vol. 2, No. 11, 1964, p. 1992.
80. Bjork, R. L. Proc. Tenth Intern. Astronaut. Congress (London, 1959). Vienna, 1960.
81. Stanyukovich, K. P. and V. V. Fedynskiy. DAN SSSR, Vol. 57, No. 2, 1947, p. 129.
82. Stanyukovich, K. P. Artificial Earth Satellites, No. 4, 1960, p. 86.
83. Stanyukovich, K. P. ZhETF, Vol. 36, No. 5, 1959, p. 1605.
84. Belyakov, L. V., V. P. Valitskiy and N. A. Zlatin. DAN SSSR, Vol. 160, No. 2, 1965, p. 314.

85. Belyakov, L. V., V. P. Valitskiy and N. A. Zlatin. ZhTF, Vol. 36, No. 10, 1966, p. 1875.
86. Sagomonyan, A. Ya. DAN SSSR, Vol. 156, No. 5, 1964, p. 1053; Vestnik MGU, Series 1 (Mathematics and Mechanics), No. 5, 1964, p. 39.
87. Belyakov, L. V. and N. A. Zlatin. ZhTF, Vol. 36, No. 2, 1966, p. 358.
88. Whipple, F. L. Astronom. Journ., Vol. 52, 1947, p. 131.
89. Eichelberger, R. J. and J. W. Gehring. ARS Journ., Vol. 32, No. 10, 1962, p. 1583.
90. Olshaker, A. E. J. Appl. Phys., Vol. 31, No. 12, 1960, p. 2118.
91. Wallace, R. R., J. R. Vinson and M. Cornhauser. ARS. Journ., Vol. 32, No. 8, 1962, p. 1231.
92. Andriankin, E. K. Kosmicheskiye issledovaniya, Vol. 4, No. 2, 1966, p. 280.
93. Technical Bulletin Field Emission Corporation 6, No. 1, 1967.
94. Bezgin, L. S. and M. I. Ivashchenko. Izvestiya AN SSSR, Division of Technical Sciences, Mechanic and Machine Design, No. 1, 1963, p. 127.

CHAPTER V

1. Okunev, B. N. Osnovy Ballistiki (Fundamentals of Ballistics). Vol. 1, Book 1. Military Press of the People's Defense Commissariat, 1943.
2. Osnovnyye dannyye aerodinamicheskikh trub i gazodinamicheskikh ustanovok SSHA (Performance of U.S.A. Wind Tunnels and Gasdynamic Test Facilities). TsAGI Press, 1968.
3. Osnovnyye dannyye inostrannykh aerodinamicheskikh trub i gazodinamicheskikh ustanovok (Performance of Foreign Wind Tunnels and Gasdynamic Test Facilities). TsAGI Press, 1968.
4. Mishin, G. I. and N. P. Mende. Hermetically Sealed Ballistic Range. Collection: (Aerophysical Studies of Supersonic Flows). Moscow, Nauka Press, 1967.
5. Basargin, I. V., I. M. Dement'yev and G. I. Mishin. Range for Aerodynamic studies. Collection: (Aerophysical Studies of Supersonic Flows). Moscow, Nauka Press, 1967.

6. Gur'yashkin, L. P., A. P. Krasil'shechikov and V. P. Podobin. Aeroballistic Tube for Measuring Model Drag in Free Flight at Hypersonic Speeds. Uchenyye zapiski TsAGI, Vol. 1, No. 2, 1970.
7. Seiff, A. A Free-Flight Wind Tunnel for Aerodynamic Testing at Hypersonic Speeds. NACA Report, 1955, p. 1222.
8. Eggers, A. J. A Method for Simulating the Atmospheric Entry of Long-Range Ballistic Missiles. NACA Report, 1958, p. 1378.
9. Seiff, A. A Progress Report on the Amer Hypervelocity Free Flight Facilities and Some of the Current Research Problems Being Studied in Them. AIAA Report, 1963, pp. 63-162. /339
10. Seiff, A. Ames Hypervelocity Free Flight Research, Astronautics and Aerospace Engineering, No. 12, 1963.
11. Seiff, A. A New Method for Computing Drag Coefficients from Ballistic-Range Data. JAS, Vol. 25, No. 2, 1958.
12. Mishin, G. I. Simple Method for Calculating the Drag Coefficient from Space-Time Relationship Data. Collection: (Aerophysical Studies of Supersonic Flows). Moscow, Nauka Press, 1967.
13. Nicolaides, J. D. On the Free Flight Motion of Missiles Having Slight Configurational Asymmetries. JAS Preprint No. 395, 1953.
14. Murphy, C. H. The Prediction of Non-Linear Pitching and Yawing Motion of Symmetric Missiles. JAS Preprint No. 677, 1957.
15. Chapman, G. T., D. B. Kirk and G. N. Malcolm. A New Method for Extracting Aerodynamic Coefficients from Free-Flight Data. AIAA Paper 69-134, 1969.
16. Chapman, G. T., D. B. Kirk and G. N. Malcolm. Aerodynamics of Bodies from Motion Analysis. Ballistic Range Technology, AGARD-AG, No. 138, 1970.
17. Krasil'shechikov, A. P. and V. P. Podobin. Experimental Study of the Aerodynamic Characteristics of a Sphere in Free Flight to $M \sim 15$. MZhG, No. 4, 1968.
18. Maslennikov, V. G. Study of Detached Shock Wave Position with Supersonic Motion of Ellipsoids of Revolution in Gases with different Intermolecular Structure. Collection: (Aerophysical Studies of Supersonic Flows). Moscow, Nauka Press, 1967.
19. Seiff, A. Recent Information on Hypersonic Flow Fields, Gas Dynamics in Space Exploration. NASA, SP-24, 1967.

20. Thurston, P. A. Research in the U. S. Naval Ordnance Laboratory Ballistic Ranges. AGARD Report No. 137, 1957.
21. Maslennikov, V. G. Determining the Position of Sonic Points on the Bow Shock Wave and on the Surface of a Blunt Body in Ballistic Studies. Collection: (Aerophysical Studies of Supersonic Flows). Moscow, Nauka Press, 1967.
22. Belotserkovskiy, O. M. Calculating Flow Around Axisymmetric Bodies with Detached Shock Wave on an Electronic Computer. PMM (Applied Mathematics and Mechanics), Vol. 24, No. 3, 1960, issue 3.
23. Liepman, H. W. and A. Roshko. Elements of Gasdynamics.
24. Fraasa, D. An Experimental Investigation of Hypersonic Flow over Blunt-Nosed Bodies at a Mach Number of 5, 8. GALCIT, No. 2, 1957.
25. Belotserkovskiy, O. M. Calculation of Flow Around Axisymmetric Blunt Bodies with Detached Shock Wave. Moscow, Press of the Computer Center of the AN SSSR, 1961.
26. Maslennikov, V. G. On the Shape of the Detached Shock Wave Formed During Supersonic Motion of a Hemisphere and Blunt Cylinder in Various Gases. Collection: (Aerophysical Studies of Supersonic Flows). Moscow, Nauka Press, 1967.
27. Mishin, G. I. Study of the Drag Coefficient of a Sphere at Supersonic Speeds in Gases with Different Specific Heat Ratios. ZhTF, Vol. 31, No. 4, 1961.
28. Hodges, A. J. The Drag Coefficient of Very High Velocity Spheres. JAS, Vol. 24, No. 10, 1957. /340
29. Charters, A. C. and R. N. Thomas. The Aerodynamic Performance of Small Spheres from Subsonic to High Supersonic Velocities. JAS, Vol. 12, No. 4, 1945.
30. Krasil'shchikov, A. P., V. P. Podobin, and V. V. Nosov. Systematic Experimental Data on the Drag of Sharp and Blunt Cones at Hypersonic Speeds. MZhG, No. 3, 1969.
31. Kopal, Z. Tables of Supersonic Flow Around Yawing Cones. Massachusetts Inst. Technology, Tech. Reports, No. 1, 1947.
32. Chushkin, P. I. and N. P. Shulishina. Table of Supersonic Flow Around Blunt Cones. Moscow, Press of the Computer Center of the AN SSSR, 1961.
33. Lyubimov, A. N. and V. V. Rusanov. Tekheniya gaza okolo tupykh tel (Gas Flow Around Blunt Bodies). Moscow, Nauka Press, 1970.

34. Mishin, F. I. and Yu. V. Shelud'ko. Dependence of Base Pressure on Specific Heat Ratio. ZhTF, Vol. 42, No. 10, 1972, p. 2208.
35. Mishin, G. I. Pressure Measurement at the Stagnation Point on Free-Flying Bodies. Collection (Aerophysical Studies of Supersonic Flows). Moscow, Nauka Press, 1967.
36. Karpov, Yu. L., Yu. P. Semenkevich and A. Ya. Cherkez. On the Calculation of Separation Flow between Two Bodies. MZhG, No. 3, 1968.
37. Kudryavtsev, V. N., A. Ya. Cherkez and V. A. Shilov. Study of Supersonic Flow Around Two Separating Bodies. MZhG, No. 2, 1969.
38. Charters, A. C. The Free-Flight Range: A Tool for Research in Physics of High-Speed Flight, Hypersonic Flow Research. New York - London, Academic Press, 1962.
39. Compton, D. L. and G. T. Chapman. Two New Free-Flight Methods for Obtaining Convective-Heat-Transfer Data. AIAA Aerodynamic Testing Conference, Washington, D. C., March 9 - 10, 1964.
40. Fay, J. A. and F. R. Riddell. Theory of Stagnation Point Heat Transfer in Dissociated Air. JAS, Vol. 25, No. 2, 1958.
41. Palkin, S. N., B. I. Reznikov, A. M. Stedenkov and V. N. Bykov. Study of Ablation of Low-Melting Models in Ballistic Range. Collection: (Aerophysical Studies of Supersonic Flows). Moscow, Nauka Press, 1967.
42. Page, W. A. Shock-Layer Radiation of Blunt Bodies Traveling at Lunar Return Entry Velocities. JAS Paper, 63-41, 1963.
43. Page, W. A. Techniques for Optical Radiation Studies in the Ballistic Range. Ballistic-Range Technology, AGARD-AG, No. 138, 1970.
44. Clay, W. G., M. Labitt and R. E. Slattery. Measured Transition from Laminar to Turbulent Flow and Subsequent Growth of Turbulent Wakes. AIAA Journ., No. 5, 1965.
45. Wilson, L. N. Far-Wake Behavior of Hypersonic Blunted Cones. AIAA Journ, Vol. 3, No. 8, 1967.
46. Hromas, L. and L. Lees. Effect of Nose Bluntness on the Turbulent Hypersonic Wake. Ballistic Systems Div., U. S. Air Force, BSD-TDR-62-354, 1962.
47. Gur'yashkin, L. P., I. M. Surikova and V. P. Podobin. Experimental Study of Velocities in the Turbulent Wake Behind Bodies of Revolution. MZhG, No. 3, 1973.

48. Lyons, W. D., J. J. Brady and Z. J. Levensteins. Hypersonic Drag, Stability, and Wake Data for Cones and Spheres. AIAA Preprint, No. 64-44, 1964.
49. Kornegay, W. M. Electron Density Decay in Wakes. AIAA Journ., Vol. 3, No. 10, 1965. /341
50. Young, L. A. Infrared Temperature Measurement of the Laminar Wake of a Hypersonic Sphere. AIAA Journ., Vol. 3, No. 4, 1965.
51. Collins, D. J. On the Experimental Determination of the Near Field Behavior of the Sonic Boom and Its Application to Problems of N-wave Focusing. AIAA Paper, No. 71-185, 1971.
52. Hidalgo, H., R. L. Taylor and J. C. Keek. Transition in the Viscous Wakes of Blunt Bodies at Hypersonic Speeds. IAS, No. 11, 1962.
53. Maslennikov, V. G. and A. M. Studenkov. Photoelectric Technique for Measuring Bow Shock Wave Standoff. Collection: (Aerophysical Studies of Supersonic Flows). Moscow, Nauka Press, 1967.
54. Bedin, A. P., V. P. Meleshko, G. I. Mishin, M. V. Chistyakova and J. V. Sheludko. Investigation of the Influence of the Specific Heat Ratio of the Surrounding Medium on the Aerodynamic Characteristics of Blunt Bodies in Free Flight. Report, Twenty-fourth International Astronautical Congress, Baku, 1973.
55. Gulyayev, B. A., L. P. Gur'yashkin, A. P. Krasil'shchikov and K. A. Sumenkov. On the Application of Spark Photography in Studying High-Speed Objects. Collection: Tekhnika kinos'yeye primeneniye v promyshlennosti i nauchnikh issledovaniyakh (Movie Techniques and Their Application in Industry and Scientific Studies), Part 2. Moscow, 1966.